Mechanism of the F_O Motor in the F-ATP Synthase

by

Seiga Yanagisawa

A Dissertation Presented in Partial Fulfillment
of the Requirements for the Degree
Doctor of Philosophy

Approved November 2023 by the
Graduate Supervisory Committee:

Wayne D. Frasch, Chair
Rajeev Misra
Kevin Redding
Abhishek Singharoy
Jeremy Wideman

ARIZONA STATE UNIVERSITY

December 2023

ABSTRACT

The F_OF_1 ATP synthase is responsible for generating the majority of adenosine triphosphate (ATP) in almost all organisms on Earth. A major unresolved question is the mechanism of the F_O motor that converts the transmembrane flow of protons into rotation that drives ATP synthesis. Using single-molecule gold nanorod experiments, rotation of individual F_OF_1 were observed to measure transient dwells (TDs). TDs occur when the F_O momentarily halts the ATP hydrolysis rotation by the F_1-ATPase. The work presented here showed increasing TDs with decreasing pH, with calculated pKa values of 5.6 and 7.5 for wild-type (WT) *Escherichia coli* (*E. coli*) subunit-a proton input and output half-channels, respectively. This is consistent with the conclusion that the periplasmic proton half-channel is more easily protonated than the cytoplasmic half-channel. Mutation in one proton half-channel affected the pKa values of both half-channels, suggesting that protons flow through the F_O motor *via* the Grotthuss mechanism. The data revealed that 36° stepping of the *E. coli* F_O subunit-c ring during ATP synthesis consists of an 11° step caused by proton translocations between subunit-a and the c-ring, and a 25° step caused by the electrostatic interaction between the unprotonated c-subunit and the aR210 residue in subunit-a. The occurrence of TDs fit to the sum of three Gaussian curves, which suggested that the asymmetry between the F_O and F_1 motors play a role in the mechanism behind the F_OF_1 rotation. Replacing the inner (N-terminal) helix of *E. coli* c_{10}-ring with sequences derived from c_8 to c_{17}-ring sequences showed expression and full assembly of F_OF_1. Decrease in anticipated c-ring size resulted in increased ATP synthesis activity, while increase in c-ring size resulted in decreased ATP synthesis activity, loss of Δψ-dependence to synthesize ATP, decreased ATP hydrolysis activity, and decreased ACMA quenching activity. Low levels of ATP synthesis by the c_{12} and c_{15}-ring chimeras are consistent with the role of the asymmetry between the F_O and F_1 motors that affects ATP synthesis rotation. Lack of a major trend in succinate-dependent growth rates of the chimeric *E. coli* suggest cellular mechanisms that compensates for the c-ring modification.

DEDICATION

I dedicate this work to my friends, my family, and my Aubrey, who has given me support and

encouragement throughout my pursuit to complete my degree. I would like to thank them from the

bottom of my heart.

ACKNOWLEDGMENTS

TABLE OF CONTENTS

LIST OF TABLES

LIST OF FIGURES

Chapter 1

INTRODUCTION

The F_OF_1 ATP Synthase

The F-type ATP synthase, also referred to as the F_OF_1 (or F_1F_O) ATP synthase (**Figure 1**), is an enzyme that is responsible for synthesizing the majority of adenosine triphosphate (ATP) in living cells, which serves as an energy currency that fuels a wide range of cellular processes. Because of its essential role in oxidative phosphorylation to synthesize ATP, F_OF_1 is found in almost all organisms on Earth. In eubacteria, this enzyme is found in the inner membrane, and in eukaryotes, it is found in the mitochondria and the chloroplast (Kühlbrandt, 2019).

The F_OF_1 ATP synthase is comprised of two rotary molecular motors that are connected by a central rotor and a peripheral stalk. The transmembrane F_O motor allows the flow of protons (or Na^+ in some species) across the membrane. This flow of protons is driven by the proton motive force (PMF), which powers the rotation of the F_O subunit-c ring in a clockwise (CW) direction relative to the stator subunits-a, as viewed from the bacterial periplasm, the mitochondrial inner membrane space, or the thylakoid lumen (**Figure 1B**). This rotation of the c-ring is transmitted by the central rotor composed of γ and ϵ subunits to the extrinsic F_1 motor, which contains a hexameric $(\alpha\beta)_3$-ring composed of three subunit-$\alpha\beta$ heterodimers. The rotation of the central rotor causes conformational changes of the $(\alpha\beta)_3$-ring, which induces the conversion of ADP and P_i into ATP at the three catalytic sites located between subunits α and β of each heterodimer. Three additional non-catalytic binding sites are also present at the alternate α-β interfaces where residues on subunit-α contribute to nucleotide binding. The δ and b_2 subunits form a peripheral stalk that serves as a stator that holds the F_O and F_1 together. The F-ATP synthase from different species can have additional subunits, such as the extra subunits present in the mammalian mitochondrial F_OF_1 that contribute to the formation of ATP synthase dimers (**Figure 2**). However, all known species of F_OF_1 ATP synthase share the above-mentioned core subunits (Kühlbrandt, 2019).

1
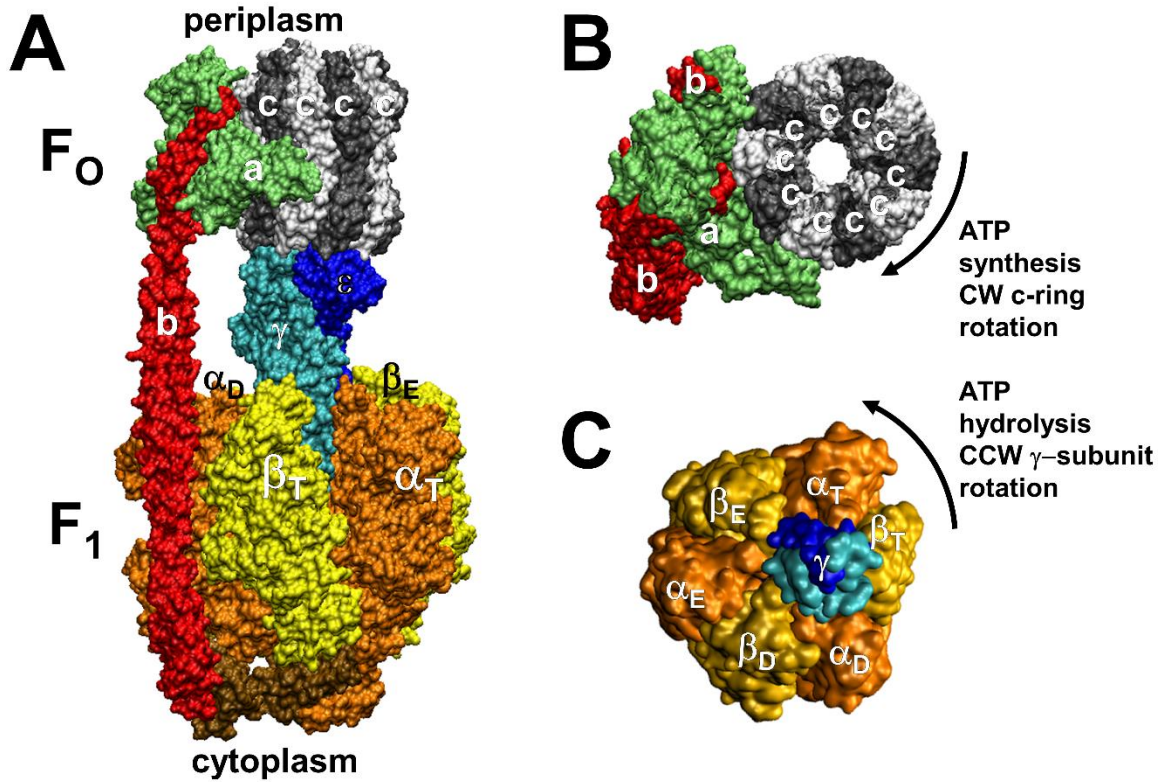
Figure 1. Subunit composition of *Escherichia coli* $F_O F_1$ (pdb-ID 6OQR) from the side (A), of F_O from the periplasm (B), and of solubilized F1 (C) from the periplasm (pdb-ID 3OAA). Peripheral stalk, b-subunits; central stalk, γ– and ε–subunits; rotor subunits, γ–, ε–subunits and the c-ring; catalytic sites, β-subunits; proton-translocating half-channels, subunit-a. Each c-subunit carries one proton between subunit-a half-channels during rotation.

The F_OF_1 ATP synthase belongs in a family of rotary ATPase motor enzymes that include the archaeal A-type (A_OA_1) ATP-synthases, prokaryotic V/A-type ATP synthases, and prokaryotic and eukaryotic vacuolar V-type (V_OV_1) ATPases (**Figure 2**). The F-ATP synthase in mitochondria and chloroplast exclusively synthesizes ATP, but in bacteria, the F_OF_1 can carry out the reverse reaction in which ATP is hydrolyzed to pump protons in the opposite direction (**Figure 1C**). This reversible mechanism allows the bacteria to maintain the PMF during fermentation. The V-type ATPase does not synthesize ATP, but is instead specialized for the ATP hydrolysis-dependent proton pumping function to maintain the pH specific to the requirements of organelles including vacuoles (which V-type is named after), Golgi, endosomes, and lysosomes (Hayek *et al.*, 2019).

A variety of regulatory mechanisms have evolved in different organisms to minimize the wasteful ATP hydrolysis by the F-ATP synthase. Mammalian and yeast F_OF_1 are regulated by an inhibitory protein IF_1 that binds to the DELSEED motif near the C-terminus of the β-subunit and prevents the rotation of the F_1 motor (Pullman and Monroy, 1963; Bason *et al.,* 2014; Gledhill *et al.*, 2007; Cabezon *et al.*, 2003). In bacteria, subunit-ε located adjacent to subunit-γ in the central stalk extends its C-terminal α–helix into the β-subunit to autoinhibit ATP hydrolysis (Sobti *et al.*, 2016; Tanigawara *et al.*, 2012). Plants inhibit the F_OF_1 activity during the night when sunlight is not available to power the redox reactions that generate the PMF necessary to drive ATP synthesis. In this process, the cysteine residues in the two β-hairpins of subunit-γ are oxidized during the night and form a disulfide bond that stabilizes the β-hairpins and binds the DELSEED motif on subunit-β, which prevents the rotation of the F_1. In the morning, the disulfide bond between the two cysteine residues is reduced and the γ-subunit is released from the β-subunit, allowing the F_1 to rotate again (Junesch and Gräber, 1987; Nalin and McCarty, 1984).

Evolutionary variations of F_OF_1 are now known to enable life forms to survive in a wide variety of environmental conditions. The F_OF_1 found in *Mycobacterium tuberculosis* allows the pathogen to survive in a low oxygen environment where oxidative phosphorylation is restricted (Andries *et al.*, 2005). Alkaliphilic bacteria such as *Bacillus pseudofirmus* OF4 can survive despite the external pH value of >10 that necessitates a lower PMF to maintain a cytoplasmic pH that is

below the pH outside (Krulwich, 1995; Hicks *et al.*, 2010). F_OF_1 found in organisms such as

Propionigenium modestum to conduct Na^+ ions rather than H^+ to power the ATP synthase (Hilpert

et al., 1984). Thermophilic bacteria *Geobacillus stearothermophilus* can thrive at 65°C with the

ATP synthase adapted to function at high temperature (Itoh *et al.*, 2004). And a novel type of

F_OF_1 found in *Burkholderia pseudomallei* allows the bacteria to survive in the acidic environment

inside the host phagosome by pumping protons out of the cell (Schulz *et al.*, 2017). In this

organism, the F-ATP synthase may be transitioning from an ATP synthase to an ATPase-

dependent proton pump akin to the V-type ATPase.
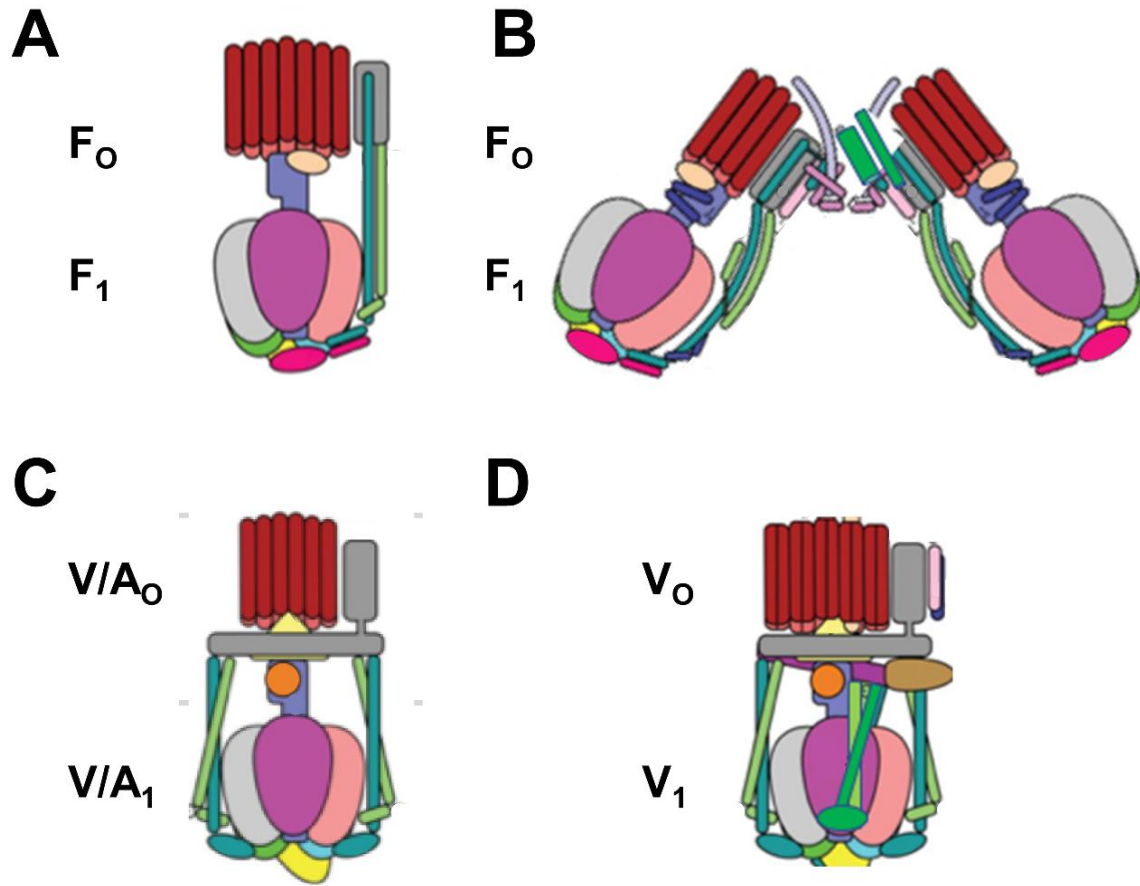
Figure 2. Structural variations among the family of rotary ATP synthases and ATPases that are coupled to transmembrane proton, or rarely sodium, gradients. (A) F-type ATP synthases in bacteria and plant chloroplasts (pdb-IDs 6OQR and 6FKF). (B) F-type ATP synthases in mitochondria (pdb-ID 6B8H). (C) V-type ATPases in some bacteria such as E. hirae and V/A-type ATP synthases in archaebacteria (pdb-ID 6R0Z) (D) V-type ATPases in vacuoles (pdb-ID 3J9V). V-type motors are incapable of synthesizing ATP and are used to pump protons to create a transmembrane pH gradient.

The Discovery and Early Characterization of the F-ATP Synthase

The $F_O F_1$ ATP synthase was first discovered by Racker *et al.* in 1958. A protein was identified in beef heart mitochondria as the "coupling factor" due to its role in coupling the energy from the oxidative electron transport chain to the synthesis of ATP, a process known as oxidative phosphorylation (Pullman *et al.*, 1958). This protein was coined the "F_1", while the membrane counterpart was named "F_O", in which the "O" stands for oligomycin sensitivity.

In oxidative phosphorylation, the electron transport chain transfers electrons from NADH and $FADH_2$ through a series of redox reactions to transfer protons from one side of the membrane to the other and generate the PMF. In 1961, Peter Mitchell hypothesized that the PMF that drives the ATP synthase is composed of pH gradient (ΔpH) and membrane potential ($\Delta\psi$) as shown in Equation 1. (Mitchell, 1961; Mitchell, 1966).

$$\text{PMF (or } \mu_H{}^+) = \Delta\psi - 60 \cdot \Delta pH \text{ (in units of mV)} \qquad \text{Eq. 1}$$

The $F_O F_1$ ATP synthase couples the PMF to ATP synthesis by using the energy from the proton gradient to convert ADP and inorganic phosphate (P_i) into ATP. This increases the concentration of ATP relative to ADP and P_i, which increases the chemical disequilibrium. Cellular processes that require an energy input from ATP take advantage of this disequilibrium by hydrolyzing the ATP back to ADP and P_i, and use the catalytic energy to carry out enzymatic functions (Spetzler *et al.*, 2012; Kühlbrandt, 2019).

In 1977, Boyer *et al.*, showed that the F_1 contains two or three catalytic sites where ATP is synthesized/hydrolyzed (Kayalar *et al.*, 1977). Later, Boyer and Kohlbrenner proposed the Alternating Site hypothesis, or Binding-Change mechanism, in which each of the three catalytic sites in the F_1 motor undergo different stages of catalytic steps in an alternating matter at any given moment. In this model, the binding of ADP and P_i at one catalytic site induces a conformation change of all three catalytic sites, causing one adjacent site to synthesize ATP and

the other to release the ATP (Boyer and Kohlbrenner, 1981; O'Neal and Boyer, 1984; Rao and Senior 1987).

The Alternating Site hypothesis was supported by a study that showed that the nucleotide binding affinities and positions of the catalytic sites in the F_1 changes as the F_1 undergoes ATPase-driven conformational changes (Richter *et al.*, 1985). This hypothesis was also supported by experiments using vanadyl (VO^{2+}) that can substitute for the Mg^{2+} cofactor that is necessary for a nucleotide (e.g. ATP) to bind to the F_1 catalytic site. Like the Mg^{2+} cofactor, VO^{2+} can form a complex with ATP and bind to the F_1 catalytic site, where it can serve as a sensitive probe of the nucleotide-binding environment of the catalytic sites. Unlike Mg-ATP complex, each functional group (e.g., phosphate, carboxyl, hydroxyl) in the VO-ATP complex that are coordinated at the equatorial positions contributes independently and quantitatively to the magnitude of the values that define the Electron Paramagnetic Resonance (EPR) spectrum, which can be measured to determine the conformational changes in the catalytic sites. Vanadyl experiments using the F_1 purified from *Spinacia oleracea* chloroplasts (*So*CF$_1$) showed the staggered conformations of the three catalytic sites, which changed in a concerted, sequential manner through the three conformations, consistent with the Alternating Site hypothesis (**Figure 3**) (Frasch *et al.*, 2000a,b).
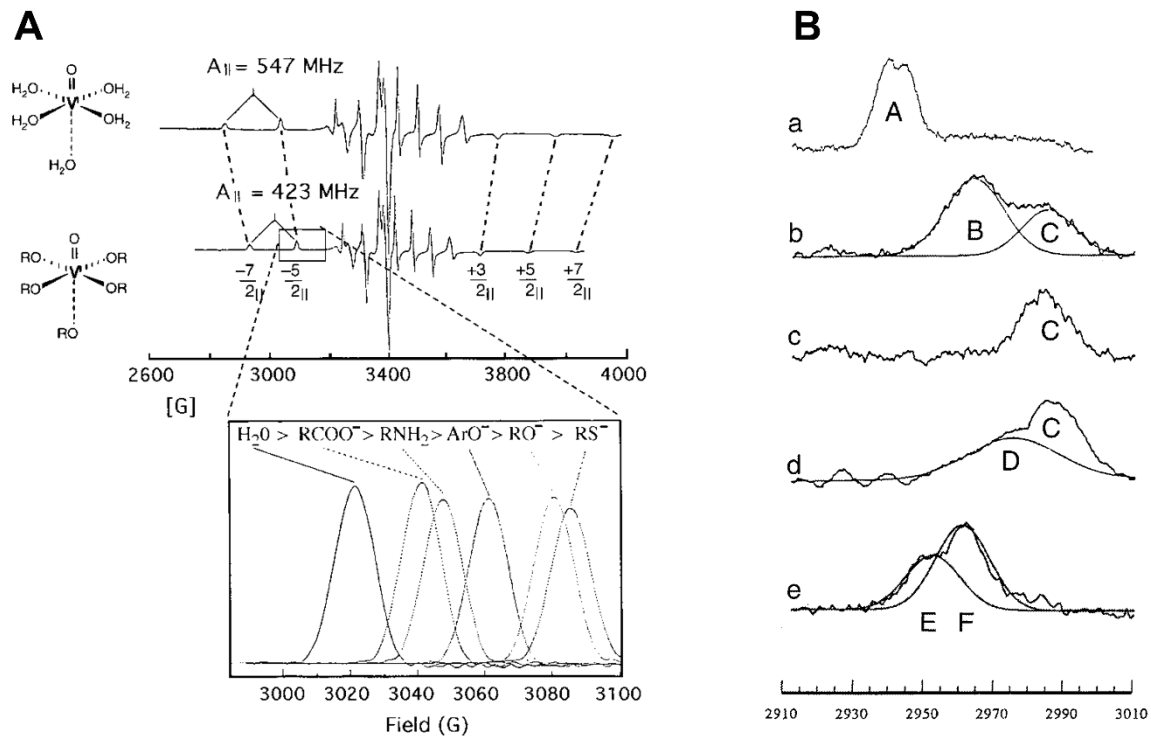
Figure 3. Sequential conformational changes of vanadyl-nucleotides bound to specific F_1-ATPase catalytic sites demonstrate the F_1 binding-change mechanism. (A) Equatorial ligands determine ^{51}V-hyperfine Parameters of VO^{2+}. EPR spectra of VO^{2+} with water (top) or hydroxyl groups (bottom) as equatorial ligands. The parallel transitions ($-7/2_{||}$, $-5/2_{||}$, $+3/2_{||}$, $+5/2_{||}$, and $+7/2_{||}$) that are not superimposed with perpendicular transitions are identified. Inset: dependence of the $-5/2_{||}$ transition on the type of equatorial ligands. (B) The $-5/2_{||}$ transition(s) of VO^{2+} bound to SoF_1 as: (a) VO^{2+}–ATP at latent Site-2, (b) VO^{2+}–ADP bound to latent Site-3, (c) VO^{2+}–ADP bound to activated Site-3, (d) VO^{2+}–ATP bound to activated site 3; and (e) VO^{2+}–ATP bound to Site 1 using SoF_1–ε (Frasch et al., 2000a,b).

8

The first crystal structure of F_1 obtained from bovine mitochondria further confirmed Boyer's Alternating Site hypothesis and the VO^{2+}-nucleotide studies by showing the asymmetric interactions between subunit-γ and the surrounding $(αβ)_3$-ring that result in the three different conformations at the three catalytic sites. This structure showed that at any given moment, one catalytic site contains a Mg-ATP (referred to as $β_T$), the second site contains a Mg-ADP ($β_D$), and the third site is empty ($β_E$) (**Figure 4**) (Abrahams *et al.*, 1994).

This F_1 crystal structure revealed new details of how the protein subunits fold and assemble into an enzyme complex. Each α and β subunit were shown to contain a "crown" domain, a "lever" domain, and a nucleotide binding domain. Both α and β subunits were shown to contain a nucleotide binding domain but the catalytic reaction only occurs in the nucleotide binding site of subunit-β, whereas the same site in subunit-α binds Mg-ATP but does not catalyze the reaction. Of the three F_1 β-subunits, the β-subunit that does not contain the Mg-nucleotide ($β_E$) was shown to have an open lever domain that extends away from the catalytic domain. In β-subunits that contain a nucleotide ($β_T$ and $β_D$), the lever domain was shown to be closed (Abrahams *et al.*, 1994).

This structure also showed that subunit–γ contains a an antiparallel coiled-coil domain, which is comprised of N- and C-terminal α–helices that extend through the core of the $(αβ)_3$-ring. The γ-subunit was also shown to contain a globular "foot" domain that protrudes from the $(αβ)_3$-ring and docks with subunit-ε and the c-ring of the F_O. This foot domain extends over the closed lever domains of $β_T$ and $β_D$ and away from that of $β_E$ (**Figure 4A**). The structure showed that subunit-γ interacts with the $(αβ)_3$-ring at three locations. First, the ends of the six α- and β-lever domains surround and contact the γ-coiled-coil proximal to the globular foot domain. (**Figure 4B**). Second, at the end of the γ-coiled-coil distal from the foot, conserved γ-tether residues (γR268 and γQ269 in *E. coli*) form strong electrostatic interactions with conserved $β_E$- "catch loop" residues ($β_E$301, 302, 304 and 305 in *E. coli*) (**Figure 4C**). Third, the γ-subunit C-terminal α–helix passes through a hydrophobic sleeve formed by loops of the six α- and β-catalytic domains (**Figure 4D**) (Abrahams *et al.*, 1994).

9
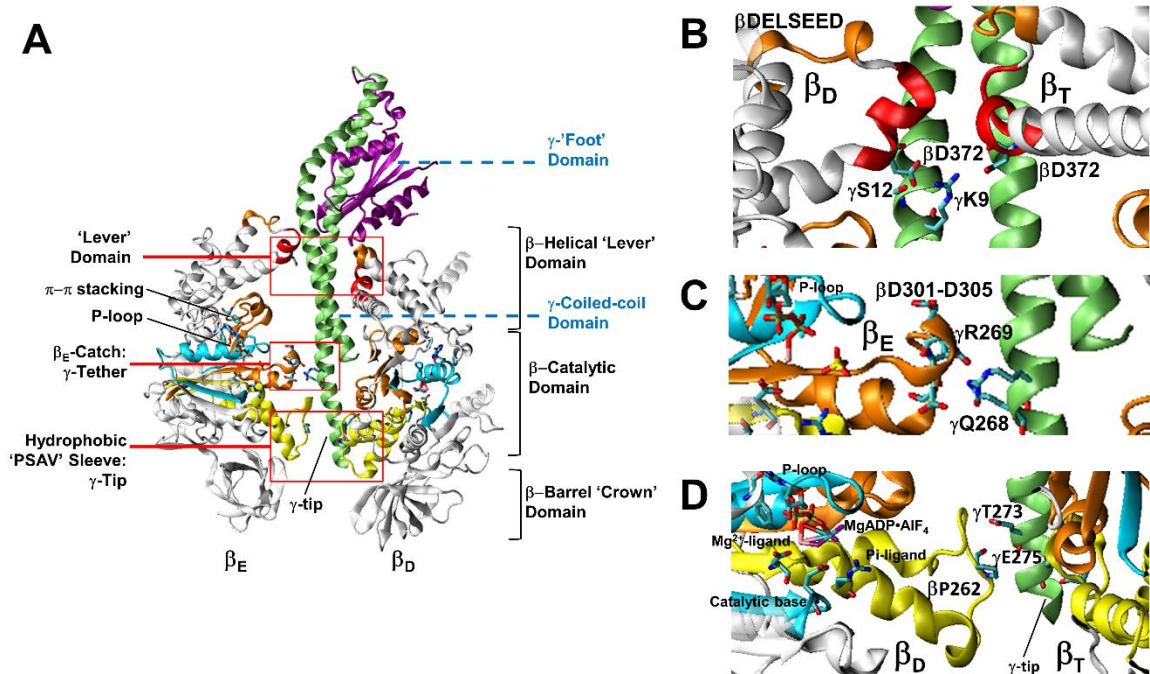
Figure 4. Domain composition of F_1 showing the relationship between Mg-nucleotide binding motifs and the stator-rotor interfaces. (A) Cross-section of F_1 showing the relationship between the β_E and β_D-subunit conformations and subunit-γ. Red boxes are detailed in (B–D) showing subunit-γ and catalytic site interfaces. (B) Interactions between the β_D and β_T-subunit Lever domains and subunit-γ. (C) Electrostatic interactions between the β_E-Catch loop and γ-subunit tether residues. (D) The short β_D and β_T-subunit helices that connect the Mg^{2+} and P_i ligands of bound Mg-ADP·AlF_n transition state analogs with the hydrophobic sleeve surrounding the C-terminal tip of subunit-γ. Images show bovine F_1 structure pdb-ID 1H8E labeled with equivalent *E. coli* F_1 residue numbers to show the location of bound Mg-ADP·AlF_n.

10

Observation of F_1-ATPase Through Single-Molecule Measurements

The first direct evidence that the F_1 motor rotates as it catalyzes ATP hydrolysis was observed in a single-molecule study of *Geobacillus stearothermophilus* F_1 (*Gs*F_1) (previously known as thermophilic *Bacillus* Sp. PS3 F_1). In this experiment, the purified F_1 was immobilized on a Ni-NTA-coated cover slip by six His-tags on the β–subunit N-terminus. A fluorescent-labeled actin filament was attached to the biotinylated γ-subunit (S107C), which allowed the rotary position of the γ-subunit to be determined. Addition of ATP induced the rotation of the F_1 γ-subunit along with the attached actin filament, which was observed under the microscope. The F_1 rotated in discrete 120° steps in the counterclockwise (CCW) direction as viewed from the foot domain of subunit-γ, which is distal from the $(αβ)_3$-ring (Noji *et al.*, 1997).

The CCW rotation of F_1 during ATP hydrolysis was confirmed by subsequent observation of *E. coli* F_1 (*Ec*F_1) rotation using the same method (Müller *et al.*, 2002). And single-molecule FRET measurements of *Ec*$F_O F_1$ in membrane vesicles showed that the enzyme rotates in the opposite, clockwise (CW) direction during ATP synthesis (Diez *et al.*, 2004).

Finer details of the enzyme rotation were characterized by single-molecule experiments carried out by attaching a 40 nm gold bead to the *Gs*F_1 instead of an actin filament. When the rotation of the F_1 was measured at 8000 fps, a 2 ms dwell was observed in between the 120° rotational stepping, and a kinetic profile indicated that there are two successive 1 ms steps (Yasuda *et al.*, 2001). Substituting ATP with ATPγS (adenosine 5′-[γ-thio]triphosphate), which hydrolyzes more slowly than ATP, caused the duration of the first kinetic step of the dwell to be extended, hence, this was designated to be the catalytic dwell (Shimabukuro *et al.*, 2003). Mutation of the catalytic base residue $β_E$190D that slow ATP hydrolysis also caused the same dwell to extend, confirming that this is the catalytic dwell (Enoki *et al.*, 2009). When [ATP] was decreased to a concentration that limits the rate of ATPase activity, a second dwell was observed 30°–40° after the catalytic dwell, which was designated as the ATP-binding dwell (Yasuda *et al.*, 2001). An increase in [P_i] caused the duration of the second kinetic step to extend in duration, indicating that P_i release ends the catalytic dwell (Adachi *et al.*, 2007; Watanabe *et al.*, 2010).

11

Detailed Characterization of F$_1$-ATPase Rotation Through Single-Molecule Gold Nanorod Assays

In 2006, the use of gold nanorods as a probe to measure the rotation of the ATPase in a higher time resolution was developed by Frasch *et al.* In this method, the ATPase is immobilized on a glass slide and the avidin-coated gold nanorod is attached to the biotinylated subunit-γ (**Figure 5A**). What distinguished the gold nanorod experiments from previous single-molecule experiments was that gold nanorods scatter different wavelengths of light through Raman scattering depending on the direction of the incident light relative to the orientation of the gold nanorod. With an 80 X 40 nm gold nanorod, red light is scattered along the long axis of the gold nanorod, and green light is scattered along the short axis of the gold nanorod. By using a polarizer and a red bandpass filter, the orientation of the gold nanorod can be determined by measuring the intensity of the unidirectional red light scattered off the gold nanorod. When the gold nanorod is oriented perpendicular to the incident light, the red light scattering is minimal. When the gold nanorod is oriented parallel to the incident light, the intensity of scattered red light is at a maximum (**Figure 5B**). This property allowed the measurement of the gold nanorod orientation with the standard error of 0.02°–0.12°. Using a single-photon counting avalanche photodiode to measure the intensity of the red light scattered from the gold nanorod, the rotation of the ATPase under hydrolysis can be measured under dark field microscope at rates as high as 400k fps, which achieves the time resolution of 2.5 μs (**Figure 5C**). Additionally, the gold nanorod allowed for an extended observation of the ATPase rotation because the measurement does not depend on fluorescence and does not undergo photobleaching (Spetzler *et al.*, 2006; Hornung *et al.*, 2011).
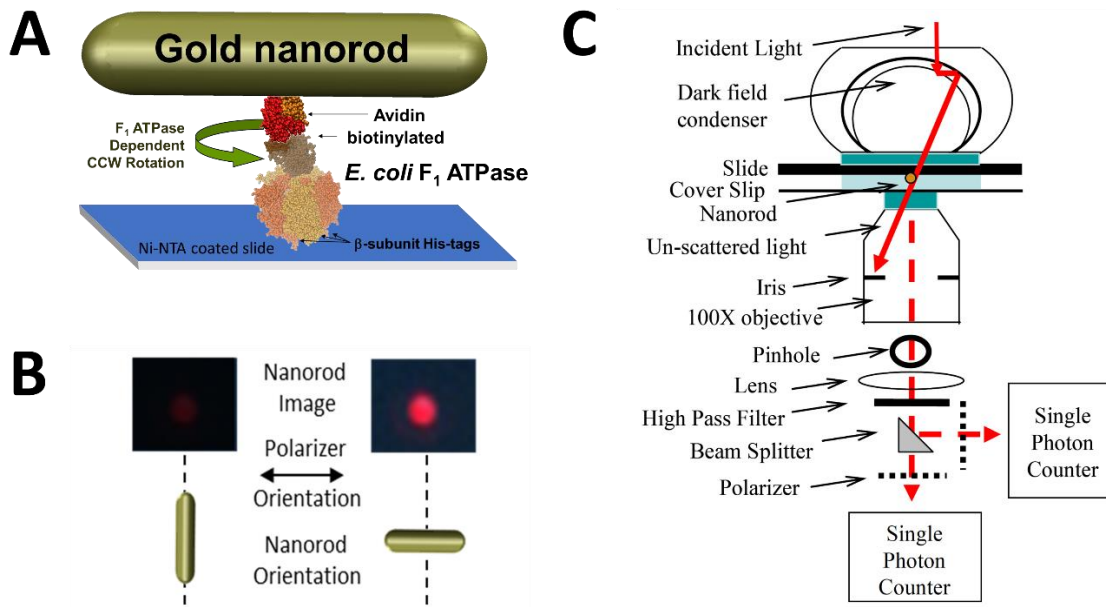
Figure 5. Use of scattered red light intensity from a 80 × 40 nm gold nanorod to measure rotation at the nanoscale. (A) Schematic of the E coli F_1-ATPase immobilized on a glass slide via His-tags on the β-subunits and avidin-coated gold nanorod bound to the biotinylated subunit-γ. Addition of ATP induces hydrolysis-driven CCW rotation of the F_1 and the attached gold nanorod. (B) Color image of gold nanorod -scattered light viewed by dark-field microscopy through a high pass filter to eliminate all but red light and a polarizer filter when the long axis of the gold nanorod is perpendicular and parallel to the plane of polarization. (C) Dark-field microscope design to record changes of scattered red light intensity vs. time from a single gold nanorod capable of determining the direction of rotation using a beam splitter to divert half of the photons through a second polarizer set at a rotational position that will reach a maximum light intensity before the first if the gold nanorod is rotating counterclockwise (CCW).

To measure the rotation of the individual ATPase molecules in the presence of 1 mM Mg-ATP, rotating gold nanorods were identified first by observing the field of view of the microscope through a polarizing lens with a color camera at 50 fps. At this data acquisition rate, rotating gold nanorods blinked red and green as the long and short axes of the nanorods became aligned with the polarizer. Stationary gold nanorods that were not bound to an active enzyme showed no changes in the color of scattered light (Spetzler *et al.*, 2006).

To measure the ATPase-dependent rotation, a 100 μm pinhole was aligned to a rotating gold nanorod-bound F_1, which eliminated all light that was not scattered from the selected molecule. The orientation of the polarizer was adjusted so that the minimum red light intensity aligned with one of the three catalytic dwells. When the intensity of the red light was measured as the 120° power stroke began after a catalytic dwell, the red light intensity increased in a sinusoidal manner as the gold nanorod rotated through the 90° (maximum intensity) position. A power stroke is defined here by the 120° rotation of subunit-γ between catalytic dwells. During the second power stroke, the intensity passed through the minimum but not through the maximum, and during the third, the intensity first passed through the maximum upon rotating 30° and returned to the minimum intensity as a 360° rotation was completed (**Figure 6A**). By using a beam splitter and polarizers set to different rotary positions, the direction of gold nanorod rotation was determined by observing which of the two rotary positions was the first to reach the maximum intensity of scattered light (**Figure 6B**). This showed that EcF$_1$-ATPase rotation is exclusively CCW when actively hydrolyzing ATP (**Figure 6C**) (Spetzler *et al.*, 2009; Hornung *et al.* 2011).

The gold nanorod assay was also used to measure the torque generated by EcF$_1$ during a power stroke, which was determined by increasing the viscous drag on the gold nanorod with an addition of polyethylene glycol. The average torque generated by EcF$_1$ varied as a function of viscous load on the gold nanorod, which averaged 63 ± 8 pN nm (Hornung *et al.*, 2008). A statistically equivalent torque value of 56 ± 6 pN nm was obtained with EcF$_1$ (Junge *et al.*, 2009) and of 50 ± 6 pN nm with EcF$_O$F$_1$ (Pänke *et al.*, 2001) using the extent of deformation of an actin

14

filament attached to the rotor. Torque values of ~80 pN nm and 40-50 pN nm for GsF$_1$ were estimated from actin filament (Yasuda *et al.*, 1998) and duplex bead rotation rates (Usukura *et al.*, 2012).

The rotation of F$_1$ and the three catalytic dwells in between the 120° power strokes were confirmed by the polarizer rotation measurements (**Figure 7**), in which the variation of intensity of red light scattered from a nanorod attached to a single F$_1$ molecule in the presence of saturating Mg-ATP was observed as a function of the stepped rotation of the polarizer by 10°, in 5 s intervals, at a data sampling rate of 1 kHz. This low data acquisition speed reports the positions of the three catalytic dwells because subunit-γ rotation during the power stroke typically occurs too fast (µsec time scale) for the detector to capture most of the intermediate rotational gold nanorod positions. Each dwell contributes a peak in the distribution of the histogram at a given set angle of the polarizer. When viewed as a series of histograms of light intensities at each of 36 polarizer angles covering 360°, three offset sinusoidal curves in scattered light intensities were observed from a nanorod attached to the actively rotating drive shaft of a single F$_1$-ATPase (**Figure 7D,E**). Because the dependence of light intensity versus the gold nanorod orientation relative to the axis of the polarizer is sinusoidal, the three offset sinusoidal curves in the histogram indicated that rotation occurs in 120° power strokes separated by catalytic dwells. Stationary gold nanorod that was not bound to an active F$_1$ showed a single sinusoidal curve as the polarizer was rotated (**Figure 7A,B**). The distribution of light intensities scattered from the gold nanorod was smaller at polarization angles in which the intensity was at a minimum than the distribution at maximum intensities. The standard error in the measurements at each rotary position of the polarizer varied between 0.02° and 0.12° as calculated from the minimum and maximum intensity values, respectively (**Figure 7C**). When the F$_1$ rotation was inhibited by the presence of subunit-ε or Mg-ADP, the three off-set sinusoidal intensity curves were temporarily converted into a single intensity curve until the inhibition was relieved and the rotation was resumed (**Figure 7F**) (Spetzler *et al.*, 2006; Ishmukhametov *et al.*, 2010; Sielaff *et al.*, 2016).

15

To analyze the F_1 rotation at high resolution, data was collected from individual F_1 molecules for 5 s at 200 kHz, and rotation events that began at a minimum light intensity and passed through a maximum were used for further analysis. The minimum and maximum light intensities were defined by determining the lowest and highest 5th percentile of peaks, respectively, which aligned the power strokes and minimized the phase shift when averaging the data from many power strokes. This also established the same minimum and maximum intensity values, $I(t)$, for any one molecule so the normalized value satisfied $0 \leq I(t) \leq 1$, which was required to take note of the relation between the rotational position, $\theta(t)$, and the intensity, $I(t)$. The t_0 was established such that $I(t_0) = 0$ is the first time at which the intensity is zero, and t_{max} was the first time at which $I(t_0) = I_{max}$ (i.e. I is increasing for $t_0 < t < t_{max}$, with $0 < I(t) < 1$). Because the scattered light intensity varies in a sinusoidal manner dependent on the rotational position of the nanorod relative to the direction of polarization, the rotational position during the power stroke was determined from Equation 2 for $t_0 < t < t_{max}$, which is valid for the first 90° of the 120° power stroke ($-\pi/2 < \theta < \pi/2$). To obtain the rotational position from the scattered light intensity for the final 30° of the power stroke, Equation 3 was used for $t > t_{max}$, which is valid for $\pi/2 < \theta < \pi$.

$$\theta(t) = \arcsin^{1/2} I(t) = \arcsin^{1/2}(I(t)) = \arcsin^{1/2}(I(t)) + \theta(t_0) \qquad \text{Eq. 2}$$

$$\theta(t) = \pi - \arcsin^{1/2}(I(t)) + \theta(t_0) \qquad \text{Eq. 3}$$

The rotational position versus time for each 120° power stroke calculated from Equations 2 and 3 was used to determine the average angular velocity as a function of rotational position from thousands of power strokes. The profile of the average angular velocity vs. degrees of rotation showed that the angular velocity is not constant and undergoes a series of accelerations and decelerations during the continuous counterclockwise rotation between the catalytic dwells at saturating Mg-ATP. The power stroke of EcF$_1$ was divided into Phase-1 (0° to 60°) when ATP

binding occurs and Phase-2 (60° to 120°) when ADP release occurs (**Figure 8**) (Martin *et al.*, 2014; Sielaff *et al.*, 2016).
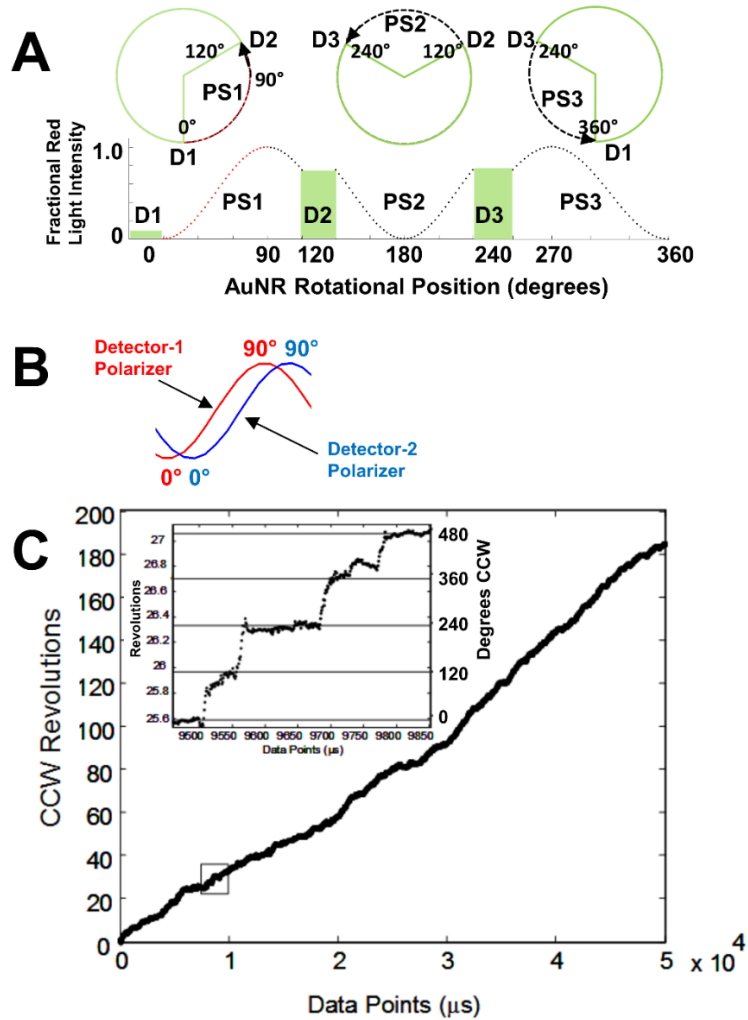
Figure 6. CCW rotation of the F_1-ATPase measured by single-molecule gold nanorod assay. (A) Changes in gold nanorod scattered red light intensity during one complete revolution involving three consecutive power strokes (PS) and three consecutive catalytic dwells (D) separated by exactly 120° when, prior to data collection, the polarizer is rotated such that scattered light intensity is at a minimum during catalytic dwell-1 (D1). (B) Rotational off-set of polarizer positions when two detectors are used to observe the direction of rotation. (C) Counterclockwise rotation observed by EcF$_1$-ATPase-dependent rotation calculated from two detectors with off-set polarizer positions with data acquired at 10 kHz in the presence of 1 mM MgCl$_2$ and 2 mM ATP. (Inset) Detail of the rotational stepping of the boxed region. Horizontal lines show the 120° dwell positions.
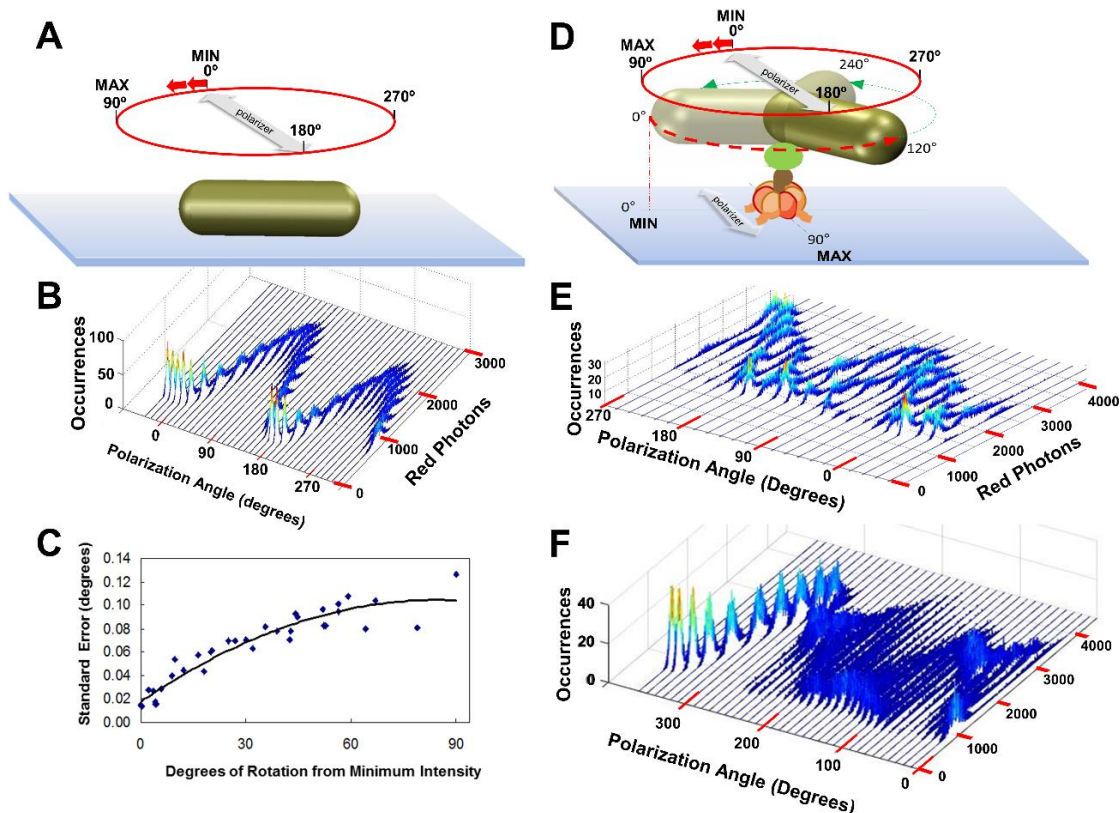
Figure 7. Polarizer Rotation Measurements (PRM) to determine rotational position measurement error and to show F1-ATPase-dependent 120° step rotations. (A) PRM measurement of a nonrotating gold nanorod attached directly to the cover slip. Red photons scattered from the gold nanorod were measured in 5 s intervals at a data sampling rate of 1 kHz (1,000 fps) at each 10° stepped rotational position of the polarizer. (B) PRM-dependent distribution of photons scattered from the non-rotating gold nanorod of A vs. rotary position of the polarizer. (C) Standard error of the gold nanorod rotary position vs. degrees of rotation from the minimum intensity calculated from B. This error is equivalent to that obtained from a data set of 3,250 power strokes. (D) PRM measurement of a gold nanorod attached to an actively rotating subunit-γ of the F$_1$-ATPase in the presence of saturating ATP concentrations. (E) PRM-dependent distribution of photons scattered from the non-rotating gold nanorod of A vs. rotary position of the polarizer. (F) PRM when the gold nanorod is attached to actively rotating F$_1$ subunit-γ, which stops rotating at polarizer angle 260°, likely due to subunit-ε inhibition.
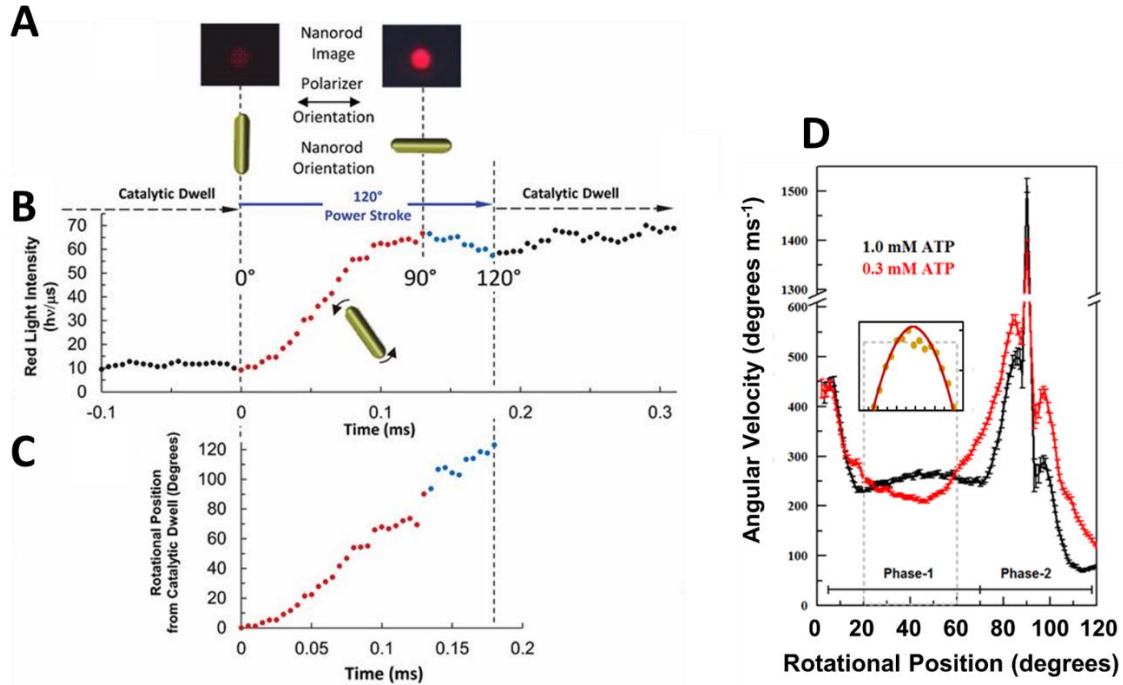
Figure 8. Single-molecule measurements of angular velocity vs rotational position of F1 ATPase-driven rotation during a power stroke. (A) Intensity of scattered red light when the long axis of a gold nanorod is perpendicular and parallel to the direction of incident light. (B) Scattered red light intensity collected at 200 kHz from a gold nanorod attached to F_1 with 1 mM Mg-ATP from the end of one catalytic dwell through a 120° power stroke until the start of the next catalytic dwell. (C) Rotational position for 0° to 90° of the power stroke (red) was determined from minimum to maximum intensity values of B using Eq. 1, and rotational position for 90° to 120° (blue) was determined using Eq. 2. (D) Average power stroke angular velocity vs. rotational position of EcF_1 ATPase-driven γ-subunit rotation binned for every 3° of rotation from the end of the catalytic dwell, which was designated as 0° in the presence of saturating 1 mM Mg-ATP (black) and 0.3 mM Mg-ATP (red). Inset: Distribution of ATP-binding dwells vs. rotational position in the presence of 0.3 mM Mg-ATP, which is proportional to the decrease in average angular velocity vs. rotational position at 0.3 mM Mg-ATP.

The Elastic Coupling Power Stroke Mechanism of F_1-ATPase Powered Rotation

The high-resolution data of ATPase-dependent F_1 rotation acquired from the gold nanorod experiments advanced the understanding of the molecular mechanism behind the interactions between F_1 subunits that generate the rotation of the motor. Before the gold nanorod experiments, it was hypothesized that the interactions between the $(\alpha\beta)_3$-ring and subunit-γ during F_1 rotation involve electrostatic interactions, steric interactions, and/or an elastic spring mechanism between the stator and rotor (Koga and Takada, 2006; Pu and Karplus, 2008; Mukherjee and Warshel, 2011, 2015; Czub and Grubmüller, 2011). Data acquired from measuring the rotation of F_1 mutants indicated that all three components contribute to the rotation mechanism. These studies showed that the key interactions between the $(\alpha\beta)_3$-ring and subunit-γ involve the $(\alpha\beta)_3$-hydrophobic sleeve that surrounds the tip comprised of the C-terminal helical extension beyond the coiled-coil, the β_E-catch loop electrostatic interactions with the γ-tether residues on the C-terminal helix of the coiled-coil distal from the foot, and the $(\alpha\beta)_3$-lever domains that surround the γ-subunit coil-coil proximal to the globular foot domain (Greene and Frasch, 2003; Boltz and Frasch, 2005, 2006; Lowry and Frasch, 2005; Martin *et al.*, 2014, 2018).

Based on these studies, a model of how the $(\alpha\beta)_3$-ring and subunit-γ interact during each catalytic step to induce the rotation has been made (**Figure 9**), which is described as follows: During catalytic dwell, subunit-γ coiled-coil is tightly wound with torsion maintained by restraints at both ends. The restraint that is distal from the subunit-γ foot domain is formed from the electrostatic interactions between the β_E-catch loop and the γ-tether. The proximal restraint is formed by the closed positions of the six lever domains of the $(\alpha\beta)_3$-ring (**Figure 9A**). When the catalytic dwell ends, the β_E and β_D lever domains open to allow the γ coiled-coil to unwind at the start of power stroke Phase-1, which is characterized by negative activation energies (**Figure 9B**). The β_E catch loop remains attached to the γ-tether so that only the foot domain rotates, where the gold nanorod is attached. During Phase-1 of the power stroke, ATP binding to β_E occurs as the activation energy reaches a minimum, which powers the Phase-2 of the power stroke. The binding of ATP induces the β_E-lever domain to close and push the γ-subunit via van

21

der Waals repulsive forces (**Figure 9C-D**). As ADP dissociates during Phase-2 of the power stroke, the β-lever domain closes upon the γ coiled-coil, which traps the tightly wound conformation of the coiled-coil that stores the torsional energy during the catalytic dwell (**Figure 9E**), which is used to power Phase-1 of the subsequent power stroke (Martin *et al.*, 2018).

This mechanism is supported both by crystal structures of the F_1, as well as by mutagenesis experiments. Mutations that disrupt either the interactions between $β_E$ catch loop and γ-tether, or the interaction between the β-lever DIIA motif and the γ coiled-coil causes the torque during power stroke to decrease by half, and causes the ATPase activity of the F_1 to be severely impacted (Greene and Frasch, 2003; Boltz and Frasch, 2005, 2006; Lowry and Frasch, 2005; Martin *et al.*, 2014, 2018).
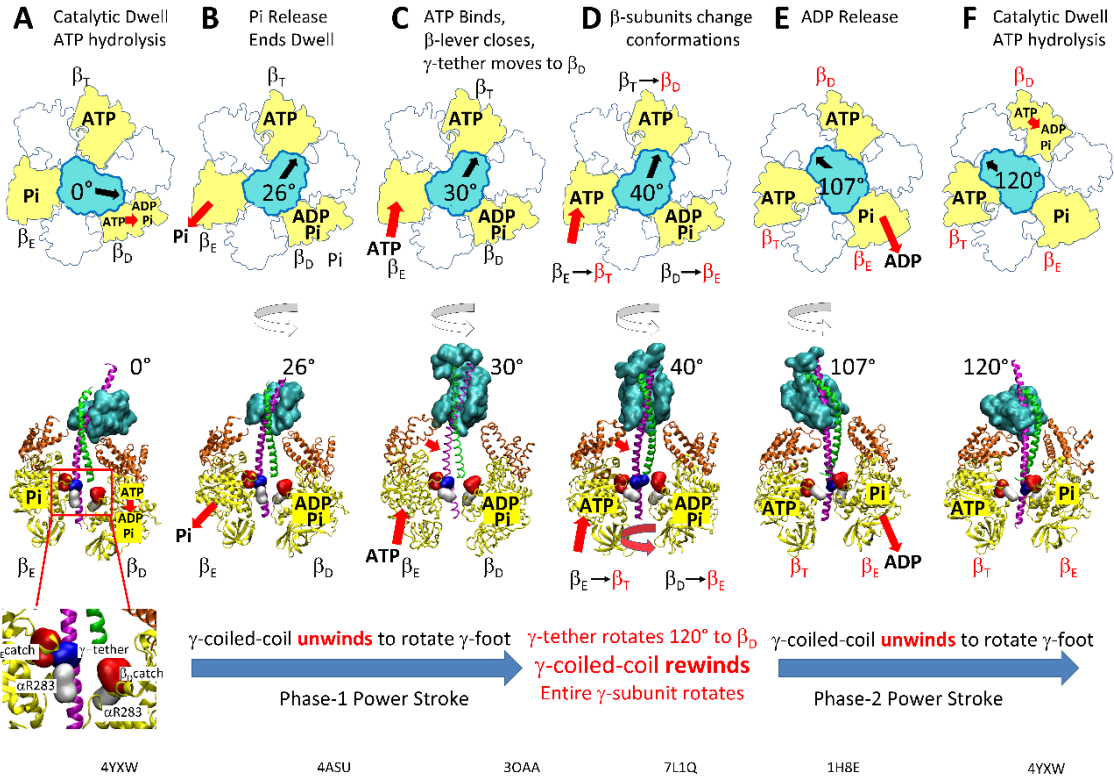
Figure 9. Elastic Coupling Mechanism of the F1-ATPase Power Stroke. (A) Catalytic dwell where ATP hydrolysis occurs at β_D. Inset: residues of the β_E- and β_D- catch loops (red), the γ-tether (blue), and aR283 (white). (B) P_i release from β_D initiates Phase-1 power stroke using torsion energy from tightly wound γ-coiled-coil to rotate γ-foot. (C) As γ-coiled-coil unwinds, ATP binds β_E from 20°–50° (optimally 34°) to force β-lever closed and rotate γ-foot further. (D) γ-tether moves from β_E-catch loop to β_D-catch to rotate γ-coiled-coil 120° and rewind it to initiate Phase-2 power stroke. This initiates catalytic site conformational changes $\beta_E \to \beta_T$, $\beta_T \to \beta_D$, and $\beta_D \to \beta_E$. (E) Release of ADP upon $\beta_D \to \beta_E$ occurs from 78°–110° (optimally 93°). (F) Catalytic dwell state after γ-foot rotates 120°. Structures corresponding to the indicated γ-foot rotation positions are bovine F_1 4YXW at 0° (A) and 120° (F), bovine F_1 4ASU at 26° (B), EcF$_1$ 3OAA at 30° (C), GsF$_1$ 7L1Q at 40°(D), and bovine F_1 1H8E at 110° (E). Top view structures as viewed from γ-foot, while side view structures omitted α-subunits and the rear β-subunit for clarity. White, α-subunits; yellow, β-subunits; orange, β-levers; cyan, γ-subunit foot; green and pink, γ-coiled-coil.

23

Energetics of *Ec*F$_1$ ATPase-Dependent Rotation

The thermodynamic parameters of the *Ec*F$_1$-ATPase power stroke were derived by Årrhenius analysis of the dependence of angular velocity vs. rotational position, as a function of temperature. The temperatures examined ranged from 16.3°C to 44.6°C, which is a range of temperatures that the *Ec*F$_1$-ATPase is believed to remain stable since Årrhenius plots of ensemble ATPase measurements remain linear as high as 55°C. At all temperatures examined, the angular velocity profiles contained a similar pattern of accelerations and decelerations vs. rotational position and differed from each other only in the magnitude of angular velocities at various rotary positions (Martin *et al.*, 2018).

The angular velocity changed inversely with temperature during most of the first 60° of rotation after the catalytic dwell (Martin *et al.*, 2018). As a result, the activation energy (E$_a$) values derived from these Årrhenius plots were negative during Phase-1 of the power stroke and reached a minimum of −3.5 k$_B$T after rotation by 34° from the catalytic dwell. As rotation continued beyond 34°, E$_a$ values increased to zero at 61°, at which point the angular velocity did not change significantly as a function of temperature. The E$_a$ continued to increase during Phase-2 of the power stroke, reaching the first maximum of 4.3 k$_B$T at 79° when subunit-γ rotation was accelerating. At 93°, E$_a$ reached a local minimum of 1.3 k$_B$T, and then increased again to a maximum of 7.5 k$_B$T at 106° during the final deceleration as subunit-γ approached the next catalytic dwell (Martin *et al.*, 2018).

Negative E$_a$ values indicate that the energy used for work during Phase-1 rotation is of entropic origin, which is characteristic of elastic energy (Mark *et al.*, 1993; Bustamante *et al.*, 1994), and is commonly observed in long biological polymers such as a protein coiled-coil (Wolgemuth and Sun, 2006; Neukirch *et al.*, 2008). Twisting a coiled-coil away from its equilibrium position stores elastic energy that can serve as an entropic spring capable of mechanical work when it unwinds (Panyukov and Rabin, 2000). This is thought to occur because fewer conformations are possible when a coiled-coil is twisted, which reduces the entropy significantly (Treloar, 1975). Allowing a coiled-coil to return to its untwisted equilibrium position

exerts a restoring force as the number of possible conformations, and the associated entropy, increases.

The presence of tethers between subunit-γ and the $(\alpha\beta)_3$-ring that give rise to torsional elastic springs (Saita *et al.*, 2015) have been observed at the same rotary positions as those reported by Årrhenius analysis of the power stroke. Additionally, the free energy of activation ($\Delta G^{\ddagger}$) profile of the *Ec*F$_1$-ATPase power stroke and its enthalpic ($\Delta H^{\ddagger}$) and entropic ($T\Delta S^{\ddagger}$) components were derived from the Årrhenius analysis (Martin *et al.*, 2018).

Comparisons of F-, A-, and V-type ATPase Rotation

The gold-nanorod rotational assays have been utilized to study the rotational characteristics of *Ec*F$_1$ (Spetzler *et al.*, 2006; Sielaff *et al.*, 2016), *Gs*F$_1$ (Sielaff *et al.*, 2016), *Mycobacterium smegmatis* F$_1$ (*Ms*F$_1$) (Ragunathan *et al.*, 2017), and *Methanocarcina mazei* Gō1 A$_1$-ATPase (*Mm*A$_1$) (Sielaff *et al.*, 2016). Closely similar profiles of angular velocity vs. degrees of rotation have been observed in power strokes of *Gs*F$_1$, and *Ms*F$_1$, as well as with *Mm*A$_1$ (Sielaff *et al.*, 2016; Ragunathan *et al.*, 2017). Consequently, several steps in the molecular mechanism to drive ATPase-dependent rotation must be shared among this diverse family of motors. It is noteworthy that the angular velocity during Phase-1 is almost 30% slower for *Gs*F$_1$ and *Mm*A$_1$ than that of *Ec*F$_1$. This suggests that the conversion of ATP binding into angular velocity is more efficient for *Ec*F$_1$ than for thermophilic and archaeal rotary motors. Differences in substrate binding affinity and the drag imposed on subunit-γ by the inner surface of the $(\alpha\beta)_3$-ring may explain these effects. The slower angular velocities of *Gs*F$_1$ compared to *Ec*F$_1$ are consistent with the lower torque generated by the former motor.

Decreases in the angular velocity of ITPase-dependent rotation, a substrate with a lower affinity than ATP to *Ec*F$_1$, provided the first direct evidence that angular velocity depends on substrate binding affinity (Martin *et al.*, 2014). The power stroke angular velocity profile vs. rotational position of *Mm*A$_1$ was not altered by rate-limiting concentrations of ATP and did not give rise to ATP-binding dwells during Phase-1 (Sielaff *et al.*, 2016). Although the V$_1$-ATPase from *Enterococcus hirae* V$_1$V$_O$ (*Eh*V$_1$) showed both ATP-binding and catalytic dwells (Iida *et al.*,

2019), the *Paracoccus denitrificans* PdF$_1$, and V/A$_1$-ATPase from the bacterial V/A-type ATP synthase of *Thermus thermophilus* (*Tt*V/A$_1$) did not exhibit an ATP-binding dwell at rate-limiting ATP concentrations (Furuike *et al.*, 2011; Zarco-Zavala *et al.*, 2020), suggesting that ATP binding of these rotary motors occurs at the same rotary position as the catalytic dwell.

Elevated ADP concentrations were found to affect *Ec*F$_1$ ATPase-dependent rotation in two ways (Martin *et al.*, 2014). First, the presence of ADP suppressed the Phase-1 angular velocity by ~30%, maximal at ~36° subsequent to the catalytic dwell, which resulted from competitive inhibition with ATP for binding to β$_E$. Second, elevated ADP concentrations also decreased the average Phase-2 angular velocity with a distribution of rotary positions between 78° and 110° with a maximum of ~93° where there was also an increase in dwells of comparable duration to those during Phase-1. These resulted from the mass action-dependent inhibition of dissociation of ADP from β$_{DP}$ (Martin *et al.*, 2014). By comparison, *Mm*A$_1$ did not exhibit either ADP-inhibition dwells or show any decreases in the angular velocity of the power stroke during either Phase-1 or Phase-2 in the presence of ADP concentrations as high as 250 μM (Sielaff *et al.*, 2016). These results provide further support for the conclusion that for this A-type ATPase, ATP binds to the β$_E$ conformation, and ADP dissociates from β$_D$ conformation during the catalytic dwell.

The F$_O$ Motor Mechanism

The structure and mechanism of the water-soluble F$_1$ motor has been studied extensively, however, membrane-bound F$_O$ motor is less understood. The F$_O$ motor of the F$_O$F$_1$ ATP synthase conducts the protons from one side of the membrane to the other and generates the torque necessary to rotate the central rotor, which powers the F$_1$ motor to synthesize ATP. The F$_O$ contains the oligomeric subunit-c ring that rotates relative to subunit-a, which contains the two proton half-channels facing opposite sides of the membrane (**Figure 10A**). The PMF induces the protons to flow from one side of the membrane to the other through the subunit-a half-channels, but the two half-channels are separated by a highly conserved arginine (aR210 in *E.*

coli) that prevents the protons from being translocated directly from one channel to another (Cain *et al.*, 1986; Lightowlers *et al.*, 1987; Howitt *et al.*, 1992). Because the two half-channels are not directly connected, protons must flow from one channel to the c-ring and released to the other half-channel only after completing a rotation. Each c-subunit contains a carboxyl residue in the middle of the outer helix (cD61 in *Ec*F$_O$) that is responsible for accepting a proton from the subunit-a input half-channel and donating a proton to the output half-channel (Fillingame *et al.*, 1984). The crystal structure of the c-ring revealed that this carboxyl group extends towards the proton half-channels when it is unprotonated and adjacent to the subunit-a, and retracts inward when it becomes protonated and the subunit-c rotates into the hydrophilic, lipid membrane environment away from subunit-a (Meier *et al.*, 2005; Pogoryelov *et al.*, 2010).

In subunit-a, helices 1 – 4 are distal from the c-ring and anchor the b-subunits of the peripheral stalk, while helices 5 and 6 are proximal to the c-ring. The connection between the distal and proximal helices contains two 3$_{10}$-helical segments that vary in conformation among known structures. In *E. coli*, the amino acid residues aN214, aE219, aH245, aQ252 in the proton input half channel and residues aE196 and aS199 in the output channel have been identified to play a role in the proton translocation mechanism through mutation studies that showed effects in ensemble assays of ATP synthesis, ATP hydrolysis, ATPase-dependent proton pumping activity, and single-molecule experiments (Lightowlers *et al.*, 1988; Vik *et al.*, 1988; Howitt *et al.*, 1990; Eya *et al.*, 1991; Hartzog and Cain, 1994; Hatch *et al.*, 1995; Fillingame and Steed, 2014; Martin *et al.*, 2015). These residues are thought to transfer the protons from one to another through protonation-deprotonation process. Recent cryo-EM structures that revealed the details of subunit-a structure confirmed that these residues are positioned at the locations consistent with proton half-channels, with aR210 separating the two half-channels, which is thought to be responsible for the deprotonation of the proton from the subunit-c approaching the proton output channel (Martin *et al.*, 2015; Zhou *et al.*, 2015; Hahn *et al.*, 2018; Pinke *et al.*, 2020; Sobti *et al.*, 2020). Alternatively, it has also been hypothesized that protons flow through the F$_O$ motor through the Grotthuss mechanism, where a single row of water molecules in the proton input and output

27

channels rapidly transfer the protons between H_3O and H_2O (Feniouk $et\ al.$, 2004; Cukierman, 2006). This was first proposed to explain the extremely high proton translocation rates of $R.$ $capsulatus$ F_O motor (Feniouk $et\ al.$, 2004). It was postulated that a ~40 Å diameter Coulomb cage lined with charged and polar groups would be required to serve as a proton antenna to efficiently feed protons from the aqueous environment into the input half-channel to allow for such a fast rate of proton transfer across the membrane (Wraight, 2006).

Single-Molecule Gold Nanorod Experiments to Study the F_O Motor

The F_O motor proton translocation mechanism, as well as the dynamic interactions between the F_O and F_1 motors has been studied using the gold nanorod single-molecule experiments by observing the rotations of fully assembled $E.\ coli$ F_OF_1. The use of single-molecule experiments allowed for the F_O motor mechanism to be studied by observing how the presence of the F_O motor changed F_1-ATPase rotation.

To stabilize the transmembrane F_O motor, the F_OF_1 was embedded into a lipid bilayer nanodisc that mimics the cell membrane. This was achieved by adding the membrane scaffold protein (MSP) along with lipids to EcF_OF_1 that had been purified by detergent solubilization (**Figure 10B**). The F_OF_1 incorporated into a nanodisc showed 1.5-fold higher ATPase activity compared to detergent solubilized F_OF_1 without the nanodisc. The activity did not decline significantly even after the sample was kept at 25°C for 8 h, while detergent solubilized F_OF_1 without nanodisc aggregated and lost most of its activity after a few hours. The ATPase activity of the nanodisc-F_OF_1 decreased 85% upon addition of the F_O inhibitor DCCD, showing that the nanodisc can support the tight coupling between the subunit-c ring and subunit-a (Ishmukhametov $et\ al.$, 2010).
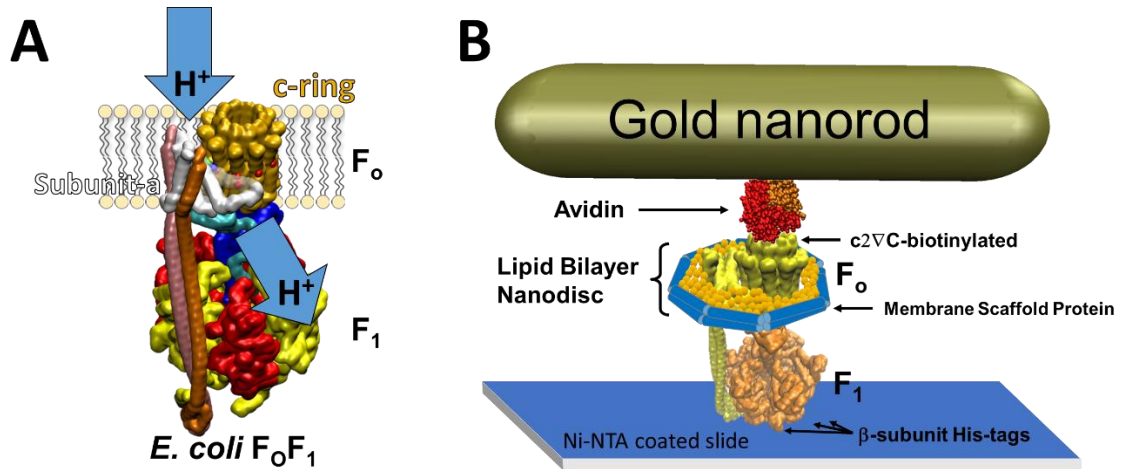
Figure 10. Structure of the *E. coli* FO.(A) Protons flow through the subunit-a half-channels and the subunit-c ring to power the ATP synthesis CW rotation. Red orbs in the subunit-c ring represent the proton-carrying cD61 residue. (B) Microscope slide assembly of $F_O F_1$ embedded in a lipid bilayer nanodisc for rotation measurements. His6-tags on β-subunit C-termini enabled attachment to slide, while the gold nanorod coated with avidin bound to the biotinylated subunit-c ring.

To conduct the gold-nanorod rotation assays, the c2∇C mutation was made to the c-subunit to insert a cysteine residue at the N-terminus for biotinylation, which enabled the attachment of an avidin-coated gold nanorod. The single-molecule experiments using F_OF_1 were conducted in a similar manner as the measurement of the F_1 rotation, with His-tagged β-subunit immobilized on a glass slide and the gold nanorod attached to the c-ring. Rotation of the gold nanorod attached to the F_OF_1 was observed by measuring the intensity of the scattered red light at 5 μsec intervals. Data was collected for 50 s during which ~3,520 power stroke events were monitored (Ishmukhametov *et al.*, 2010).

When the angular position vs. time of the F_OF_1 ATPase rotations were calculated, two different groups of power strokes were observed. One group showed a quick, continuous rotation that progressed from 0° to 90° in ~200 μs without any dwells, in a similar manner to the F_1 power stroke. The other group showed rotation that were interrupted by up to 3 or 4 dwells that each lasted for ~150 μs, which extended the duration of the 0° to 90° rotation to an average of ~650 μs. These dwells observed from F_OF_1 ATPases were designated as transient dwells (TDs) (Ishmukhametov *et al.*, 2010).

The data indicated that these TDs were caused by the interactions between subunit-a and individual c-subunits in the c-ring because: (1) the average space between two TDs were ~36°, which is equivalent to the distance between two c-subunits; and (2) the average number of TDs during the 90° rotation was ~2.5, which equates to 10 TDs for a complete 360° rotation, indicating that each c-subunit in *E. coli* F_O c_{10}-ring was causing the formation of a TD (Ishmukhametov *et al.*, 2010).

To further test the interactions between subunit-a and the c-ring, mutations were made to subunit-a that inserted 14 amino acids to duplicate the sequence in transmembrane helix-4 and converted the aR210 residue into valine and glycine in this duplicate helix. This mutation did not alter the ATPase activity, but it did eliminate the TDs from the power strokes, inhibited the ATPase-dependent proton translocation, and the F_O was no longer susceptible to DCCD

inhibition, all of which indicated that the interactions between the c-ring and subunit-a was disrupted in this mutant (Ishmukhametov *et al.*, 2010).

The viscosity experiment used to study the F_1 mechanism was employed to study the F_OF_1 mechanism as well. Increasing the drag on the gold nanorod by increasing the viscosity of the medium increased the occurrence of TDs, but decreased the duration of the dwells. When the viscosity of the medium was increased from 0.9 cP to 1.8 cP by an addition of 15% PEG400, the angular velocity of the power strokes did not change (Ishmukhametov *et al.*, 2010) as was also observed with F_1 power strokes (Spetzler *et al.*, 2009). However, when the viscosity was increased from 1.8 to 4.3 cP, the angular velocity of the power strokes decreased, the occurrence of TDs increased from 27% of power stokes containing TDs to >80% of power strokes containing TDs, and the TD duration decreased from~200 μs to ~50 μs. When the viscosity was increased even more to 7.5 cP, the angular velocity of the power stroke became so slow that those with and without TDs were indistinguishable. When subunit-a∇14 insertion mutants were examined, none of the power strokes contained TDs regardless of the viscosity of the medium (Ishmukhametov *et al.*, 2010).

The viscosity experiments showed that time constant for TD formation is ~160 μs, and any molecule that rotates 36° in <163 μs does not exhibit transient dwells. The time constant for the termination of the interaction between subunit-a and subunit-c is ~175 μs, which is independent of viscosity. If a TD does occur during a power stroke, the duration of the power stroke is ~338 μs regardless of the viscosity (Ishmukhametov *et al.*, 2010).

In a subsequent study, rotations of 50 nanodisc-F_OF_1 molecules were measured for ten consecutive 5 s intervals, each of which was considered a data set containing ~300 power strokes. The percentage of power strokes that contained TDs was determined in each data set, which were binned into 10% increments. This analysis showed that about 70% of the TDs not only halted the ATP hydrolysis-driven CCW rotation, but also rotated in the CW direction towards ATP synthesis up to 36°, which is equivalent to a rotation of the c-ring by one c-subunit (Martin *et al.*, 2015).

When the occurrences of TDs were measured as a function of viscosity, it was shown that the percentage of power strokes containing TDs increased with the viscosity in a same manner as the data obtained from the average of all power strokes. The distribution of TDs per data set at a viscosity of 4.3 cP showed a curve with a single maximum of ~85% with very few data sets of <50%. When the subunit-c residue D61 responsible for carrying the proton was mutated into a glycine, the distribution of TDs became bifurcated with local maxima of ~20% and 90%. This suggested at high viscosities, TDs can be caused either by the proton translocation-dependent process involving c-ring rotation, or by a second interaction that was independent of proton translocation. Mutation of aR210 into Gly resulted in a similar bifurcation of the TD distribution with local maxima of 50% and 90% (Martin *et al.*, 2015).

These data indicated that there is an interaction between subunit-a and c that forms a "leash" within the first few degrees of CCW rotation. This leash prevents the c-ring from rotating more than 36° by halting the ATP hydrolysis-driven rotation and even pull the c-ring in the CW, ATP synthesis direction. The extent that the c-ring rotates CCW after the 163 μs leash formation time decreases as the angular velocity is slowed by increased viscosity. For example, at viscosities of 3.0 cP and 5.5 cP, the leash forms after the c-ring rotated ~31° and 21°, respectively. There is evidence that the leash formation between subunit-a and subunit-c had both a proton-translocation-dependent and an -independent component (Ishmukhametov *et al.*, 2010; Martin *et al.*, 2015).

Mutations of the aE196 residue into Gln and Leu resulted in a decrease of TDs per data set to local maxima of 30% and 60%, indicating that these residues play a role in the proton translocation mechanism of the subunit-a output half-channel. These mutations decreased the ATP synthesis activity of the F_OF_1 by 11- and 15-fold, respectively, and increased the NADH-dependent ACMA quenching in inverted *E. coli* membrane vesicles, indicating a decrease in the ability by the F_O to translocate protons across the membrane. These data showed for the first time that aE196 residue participates in the F_O proton output channel mechanism (Martin *et al.*, 2015).

Cryo-EM Structure of Subunit-a

In 2015, the structure of intermembrane subunit-a was resolved for the first time by cryo-EM at the resolution of ~7 Å. Surprisingly, the structure showed that the subunit-a helices 5 and 6 that interface with the c-ring are at an oblique angle relative to the membrane, unlike the conventional transmembrane helices that orient perpendicular to the membrane. These structures also revealed the position of amino acids along the putative proton half-channels that connect the aqueous environment on both sides of the membrane to the c-ring (Allegretti *et al.*, 2015; Zhou *et al.*, 2015) (**Figure 11**).

The mechanism of how the interactions between subunit-a and the c-ring generates the torque necessary to overcome the CCW force of F_1-dependent ATP hydrolysis and drive the CW rotation in the ATP synthesis direction is poorly understood. The focus of this dissertation is to gain insight into the mechanism of how protons are conducted through the subunit-a half-channels, the residues involved in the proton half-channel mechanism, and the interactions between subunit-a and the c-ring that drives c-ring rotation.
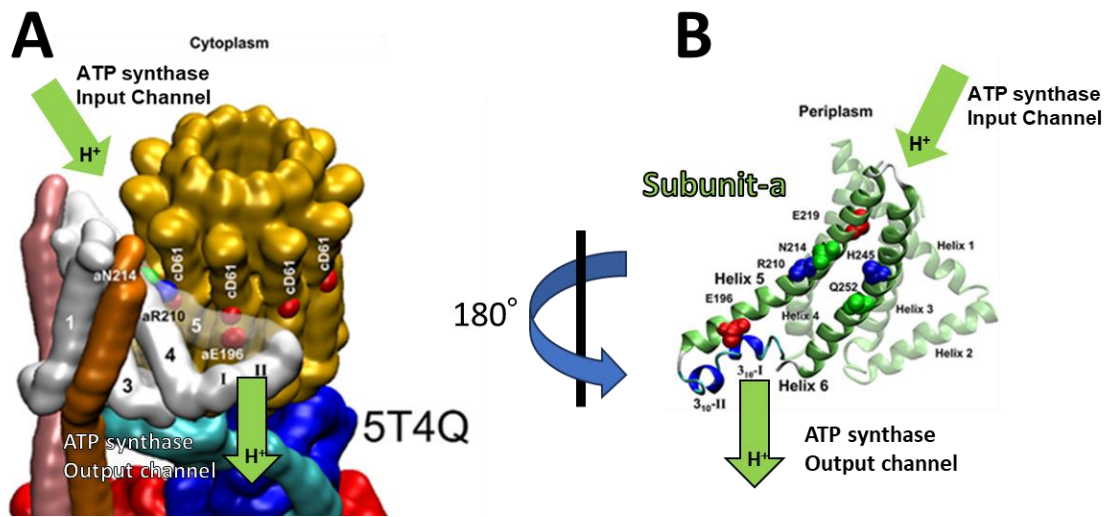
Figure 11. Cryo-EM structure of the *E. coli* ATP synthase showing the subunit organization of the FO motor. (A) Subunit-a contains transmembrane helices V and VI that are oriented at an oblique angle and interface with the proton-carrying cD61 residues in the c-ring. (B) Subunit-a helices contain polar and/or charged residues that are thought to participate in the proton translocation mechanism.

Chapter 2

PROTONATION-DEPENDENT STEPPED ROTATION OF THE F-TYPE ATP SYNTHASE C-RING OBSERVED BY SINGLE-MOLECULE MEASUREMENTS

Abstract

The two opposed rotary molecular motors of the F_OF_1 ATP synthase work together to provide the majority of ATP in biological organisms. Rotation occurs in 120° power strokes separated by dwells when F_1 synthesizes or hydrolyzes ATP. F_O and F_1 complexes connect via a central rotor stalk and a peripheral stator stalk. A major unresolved question is the mechanism in which the interaction between subunit-a and rotating subunit c-ring in the F_O motor uses the flux of H^+ across the membrane to induce clockwise rotation against the force of counterclockwise rotation driven by the F_1-ATPase. In single-molecule measurements of F_OF_1 embedded in lipid bilayer nanodiscs, we observed that the ability of the F_O motor to form transient dwells increases with decreasing pH. Transient dwells can halt CCW rotation powered by the F_1-ATPase in steps equivalent to the rotation of single c-subunits in the c-ring of F_O, and can push the common axle shared by the two motors clockwise by as much as one c-subunit. Since the F_O proton half-channels that access the periplasm and the cytoplasm are exposed to the same pH, these data are consistent with the conclusion that the periplasmic half-channel is more easily protonated in a manner that halts ATPase-driven rotation by blocking ATPase-dependent proton pumping. The fit of transient dwell occurrence to the sum of three Gaussian curves suggests that the asymmetry of the three ATPase-dependent 120° power strokes imposed by the relative positions of the central and peripheral stalks affects c-subunit stepping efficiency.

Introduction

The F-ATP synthases, located in eubacteria, mitochondria, and chloroplasts, are members of a family of rotary molecular motors that also include archaeal A-ATP synthases, bacterial A/V-like ATP synthases, and eukaryotic vacuolar V-ATPases (Spetzler *et al.*, 2012). The

35

F-ATP synthases are composed of two opposed rotary motors known as the membrane-embedded F_O, and the extrinsic membrane protein complex F_1 (**Figure 12**). These motors are connected by a central stalk that serves as the rotor, and a peripheral stalk that is a component of the stator (Stock *et al.*, 1999). In *Escherichia coli*, as in most organisms, the largest single source of cellular ATP is that made by the F_OF_1 ATP synthase.

Synthesis of ATP from ADP and inorganic phosphate (P_i) is catalyzed by F_1 in response to a transmembrane electrochemical gradient used by F_O to force the rotor in the clockwise (CW) direction as viewed from the periplasm of *E. coli* (Diez *et al.*, 2004). In so doing, *E. coli* F_O, which is specific for protons, consumes the gradient by transporting protons across the membrane. The F_1 motor can hydrolyze ATP to drive the rotor counterclockwise (CCW) and pump protons (Noji *et al.*, 1997; Spetzler *et al.*, 2009). However, under steady-state conditions, the F_OF_1 ATP synthase maintains the [ATP]/[ADP][P_i] ratio far from equilibrium (Turina *et al.*, 2003; Kushmerick *et al.*, 1992a,b).

The three catalytic sites for ATP synthesis/hydrolysis are located at the interfaces of α and β-subunit heterodimers that comprise the $(\alpha\beta)_3$-ring of the F_1-ATPase, which serves as the stator (Abrahams *et al.*, 1994). The rotor consists of the γ-subunit that protrudes from the center of the $(\alpha\beta)_3$-ring, the ε-subunit, and the ring of c-subunits of F_O. During ATPase-driven rotation, each 120° power stroke occurs as the result of the binding of an ATP to the empty catalytic site, while product release occurs at an adjacent site (Adachi *et al.*, 2007). Hydrolysis of ATP occurs at the third site during catalytic dwells that separate the power strokes. Three states of the *E. coli* F_OF_1 structure were revealed by single-particle cryo-EM in which the axle subunits $\gamma$and ε were rotated in 120° increments from the peripheral stalk that is a component of the stator (Sobti *et al.*, 2016).
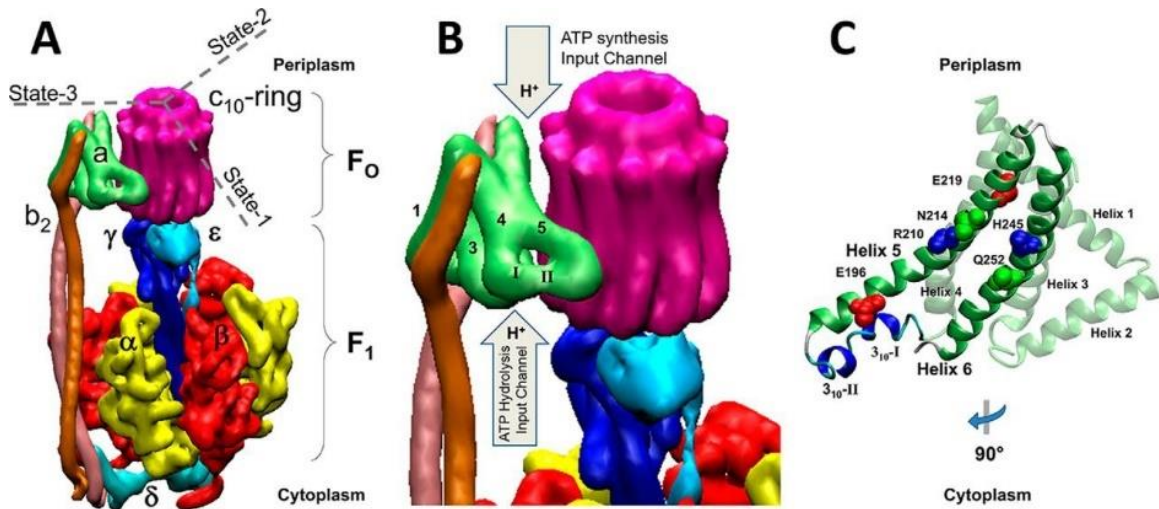
Figure 12. Subunit organization of the *E. coli* FOF1 ATP synthase (Sobti et al., 2016) (pdb code 5T4O). B, Organization of helices in subunit-a and approximate locations of proton translocation half-channels with access for protons from the periplasm and cytoplasm of *E. coli* that serve as the input channels during ATP synthesis and hydrolysis, respectively. Two 3_{10}-helical segments (I and II) in the subunit-a segment that connect helices 4 and 5. C. Structure of subunit-a rotated 90° clockwise from (A) and (B) that shows the position of residues implicated in proton translocation, and 3_{10}-helical segments I and II.

In the F_O motor, proton translocation-dependent rotation of the c-ring results from events in which half-channels in stator subunit-a protonate and deprotonate cAsp61 (cD61) on each c-subunit. Subunit-a of *E. coli* F_OF_1 folds in a manner similar to that observed in F_O structures from other organisms for which the structure is known (Sobti *et al.*, 2016; Zhou *et al.*, 2015; Allegretti *et al.*, 2015; Morales-Rios *et al.*, 2015). Subunit-a helices 1 - 4 anchor the b-subunits of the peripheral stalk, and are distal from the c-ring. Helices 3 - 6 are oriented at an oblique angle to the membrane plane where C-terminal helices (5 and 6) are proximal to the c-ring. The connection between the distal and proximal helices contains two 3_{10}-helical segments (**Figure 12B and C**, helices I and II) that vary in conformation among known structures.

Subunit-a residues aN214, aE219, aH245, and aQ252 on helices 5 and 6 have been implicated in proton translocation as part of the periplasmic half-channel that serves as the import channel during proton gradient-powered c-ring rotation (CW) for ATP synthesis (Cain and Simoni 1988; Cain and Simoni 1989; Vik *et al.* 1988). To date, the only residue known to participate in the cytoplasmic half-channel, which serves as the import channel for ATPase-driven proton pumping, is aE196 (Vik *et al.* 1988; Martin *et al.*, 2015). The two half-channels are separated by aR210 that effectively deprotonates cD61 as each successive c-subunit rotates into close proximity of its resonance-stabilized positive charge (Lightowlers *et al.*, 1987).

Rates of ATP synthesis catalyzed by the F-ATP synthase can approach 400-600 ATP sec^{-1} (Engelbrecht *et al.*, 1989; Fischer *et al.*, 1994; Etzold *et al.*, 1997). This equates to 500-750 µs per proton translocated during the rotational stepping of single c-subunits in *E. coli* that has a c_{10}-ring. The ability to observe single c-subunit stepping of the c-ring on this time scale was first achieved in single-molecule experiments by monitoring ATPase-driven rotation using a gold nanorod attached to the c-ring of F_OF_1 embedded in lipid bilayer nanodiscs (n-F_OF_1) (Ishmukhametov *et al.*, 2010). Although some power strokes rotated CCW in continuous 120° events, many were periodically interrupted by "transient dwells". These dwells occurred at an average interval of ~36° consistent with single c-subunit stepping of the c_{10}-ring of *E. coli* F_OF_1. The duration of transient dwells ranged from 50–175 µs. Although somewhat shorter than the

duration of c-subunit stepping anticipated during ATP synthesis, transient dwells are observed in the presence of high ATP concentrations that optimize ATP hydrolysis in lieu of synthesis. The fraction of power strokes that contain transient dwells can be increased to the point at which they are present in all power strokes of most data sets (~80% average occurrence in all power strokes) through the use of viscosity-dependent drag to decrease the angular velocity of the F_1-ATPase power stroke.

Mutations in subunit-a and subunit-c have been identified that affect the ability to form transient dwells (Martin *et al.*, 2015; Ishmukhametov *et al.*, 2010), indicating that these dwells result when subunit-a forms a 'leash' with the c-ring that limits CCW rotation to a maximum of ~36° while engaged. Subunit-a was not only observed to halt CCW rotation of the c-ring in n-F_OF_1, but in >70% of all transient dwells, was able to push the rotor CW against ATPase-dependent rotation powered by F_1 (Martin *et al.*, 2015). The extent of CW rotation in the ATP synthase direction averaged 11°, but could be as much as ~36°, which is equivalent to rotation of the c-ring by one c-subunit relative to subunit-a.

Using proteoliposomes in which the F_1 complex of F_OF_1 is on the outside, high rates of ATP synthesis require transmembrane proton gradients with a ΔpH = 3. This is typically achieved by equilibrating the pH inside the liposome to 5.5, and then rapidly shifting the outside pH to 8.5 (Turina *et al.*, 2003; Fischer *et al.*, 1994). Thus far, single-molecule rotation studies of F_OF_1 embedded in nanodiscs have been examined only at pH 8.0. We now present a single-molecule study of the pH dependence of transient dwell formation by n-F_OF_1. The occurrence of transient dwells increased inversely with pH over the pH range of 5.0 to 7.0. Transient dwells formed at low pH at intervals of ~36°, lasted an average of 118 – 158 μs, and were able to push the c-ring CW against the force of ATPase-dependent CCW rotation by as much as one c-subunit. These results show that even though both F_O half-channels were exposed to the same pH, the periplasmic half-channel that serves as the ATP synthase proton import channel is more easily protonated in a manner that halted ATPase-driven rotation by blocking ATPase-dependent proton pumping.

Results

Rotation of the c-ring of single n-F_OF_1 molecules was monitored as a function of time by changes in the intensity of polarized red light scattered from a 78 X 34 nm gold nanorod attached to the c-ring (**Figure 13**). For each molecule examined, multiple 5-s data sets of ATP hydrolysis-powered rotation were acquired in the presence of 1 mM Mg-ATP at a data acquisition rate of 100 kHz. At this saturating substrate concentration, *E. coli* F_1 produces power strokes that rotate 120° CCW on a time scale of ~300 μsec, which are separated by catalytic dwells with a duration of a few msec (Spetzler *et al.*, 2006; Spetzler *et al.*, 2009). The intensity of polarized red light that is scattered from the long axis of the nanorod oscillates in a sinusoidal manner as the nanorod rotates relative to the direction of the polarizing filter in the light path of the microscope, which is captured by a single photon detector (Hornung *et al.*, 2011).

Examples of n-F_OF_1 power strokes that contain or lack transient dwells at pH 5.0 are shown in **Figure 14**. Prior to data collection of each molecule, the polarizing filter was rotated to minimize the scattered light intensity from one of the three catalytic dwells. During the subsequent power stroke, the light intensity increased through a maximum as the nanorod rotated CCW 90°. Each data set acquired contained ~300 power strokes that fit to these criteria, and were analyzed for the presence of transient dwells. In the absence of transient dwells, the power stroke rotated CCW continuously at angular velocities that were comparable to that of purified F_1-ATPase (Martin *et al.*, 2014).
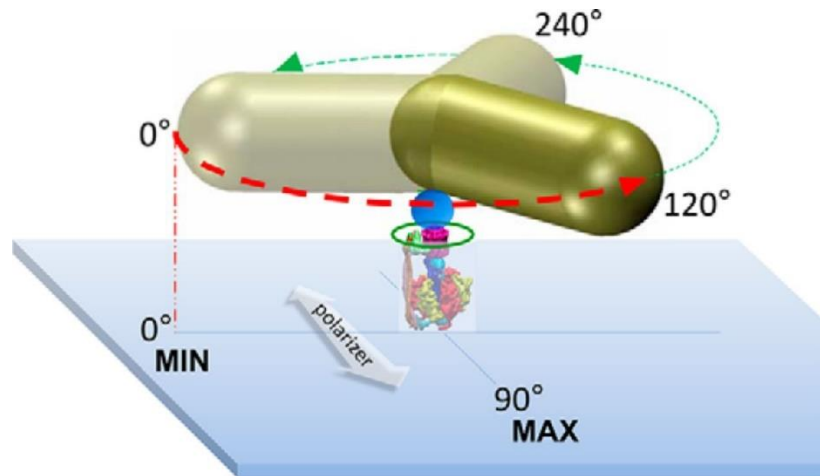
Figure 13. Using a gold nanorod as a probe of rotational position to make single-molecule measurements of FOF1 embedded in lipid bilayer nanodiscs (green circle). Attachment of F_OF_1 to the microscope slide occurred via His6 tags on the N-termini of the F_1 β-subunits. The c2∇C mutation to *E. coli* F_OF_1 was biotinylated to attach the gold nanorod (78 X 34 nm) coated with streptavidin (blue sphere). The 120° power strokes due to F_1-ATPase dependent CCW rotation in the presence of 1 mM Mg-ATP were monitored by the intensity of polarized red light scattered from the long axis of the nanorod as a function of time. Shorter wavelengths were eliminated by a band-pass filter. Prior to data collection, a polarizing filter (white arrow) was aligned for minimum intensity of scattered light at one of the three ATPase-dependent catalytic dwells (0°) such that the intensity during the subsequent power stroke increased and passed through a maximum when the nanorod rotated 90° measured using an avalanche photodiode. These power strokes (red dashed arrow) were analyzed for the presence of transient dwells.
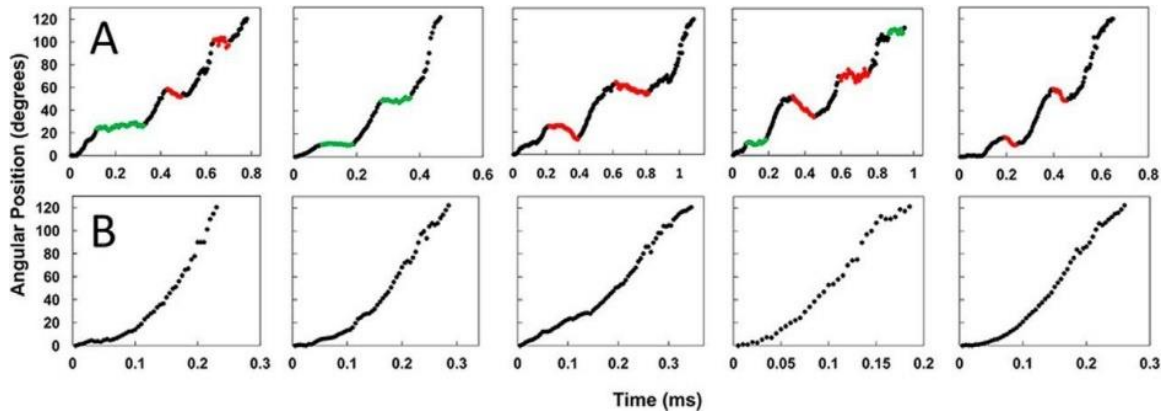
Figure 14. Examples of time-dependent changes in rotational position of n-F_OF_1 during F_1-ATPasedependent power strokes at pH 5.0 where transient dwells are present (A), or absent (B). Transient dwells where rotation was halted, or contained CW rotation are colored green and red, respectively.

Transient dwells that stopped the CCW rotation driven by the F_1-ATPase, and those that rotated the c-ring CW against the force of the F_1 power stroke at pH 5.0 are indicated as green and red data, respectively (**Figure 14A**). The average periodicity of transient dwells as a function of pH is shown in **Figure 15A**. At pH 5.0, transient dwells occurred an average of every 35.3°±0.3 (s.e). This periodicity did not change significantly between pH 5.0 and 9.0, and is consistent with a mechanism in which transient dwells result from stepping by single c-subunits in the c_{10}-ring of *E. coli* $F_O F_1$.

The duration of transient dwells was ~118 μs at pH 5.0 and at pH 9.0, but increased with pH to a maximum value of ~158 μs at pH 8.0 (**Figure 15B**), which amounted to a change of ~25 % over the pH range examined. In the absence of transient dwells, power strokes rotated the first 90° from the catalytic dwell at pH 5.0 in ~250 μs, which was comparable to power strokes of soluble *E. coli* F_1-ATPase (Spetzler *et al.*, 2004; Spetzler *et al.*, 2009). When transient dwells were present, the increase in the time required to rotate 90° resulted from the duration of the transient dwells.

Figure 16 shows the average percent of transient dwells formed per data set during n-$F_O F_1$ power strokes as a function of pH, where each data set contained about 300 power strokes. At pH 9.0, about 23% of the power strokes contained transient dwells, and transient dwell formation did not change significantly from this value between pH 9.0 and pH 7.5. However, the occurrence of transient and dwells increased with decreasing pH between pH 7.5 and pH 5.0 to an average of ~48% at pH 5.0. The fit of these data to the Henderson-Hasselbach relationship suggested that protonation of a group with a pK of 6.3 was necessary to form a transient dwell. However, it is clear that the average changes in transient dwell formation between pH 6.0 and 7.5 did not fit particularly well to the dependence on the protonation of a single group.
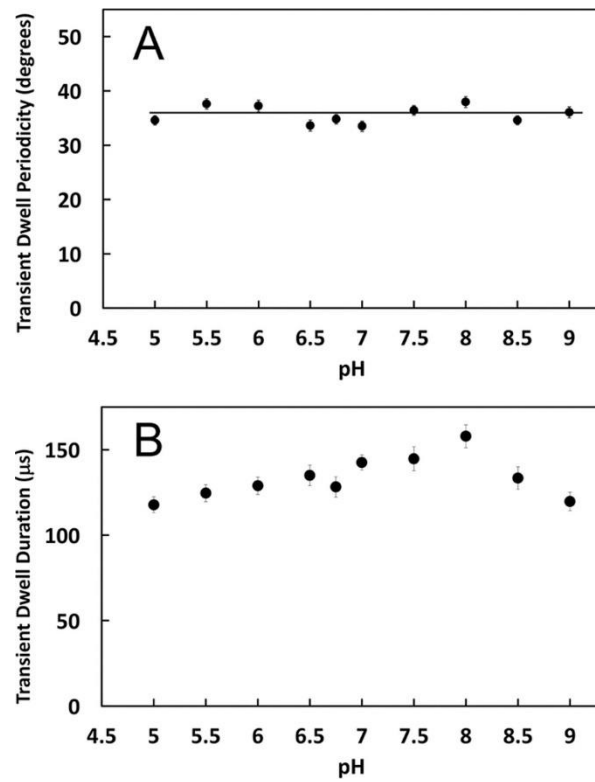
Figure 15. The pH dependence of the average degrees of rotation between transient dwells (A),

or the duration of transient dwells (B). Vertical bars indicate standard error.
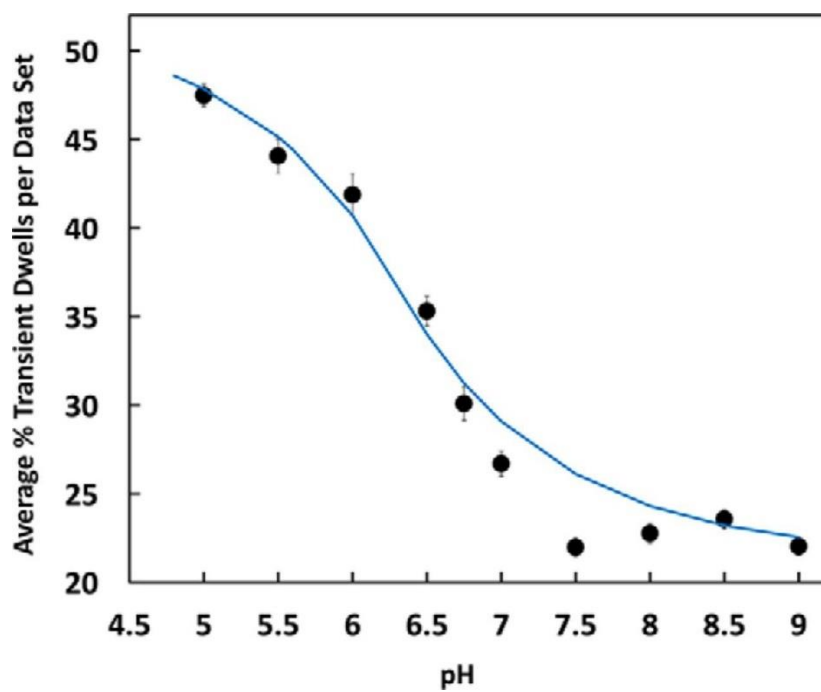
Figure 16. The average percent of transient dwells per data set as a function of pH. Each data set contained ~300 power strokes. The data were fit to a Henderson-Hasselbach dependence for the protonation of a single group with a pK of 6.3 (blue line). Vertical bars indicate standard error determined from the distributions in Figure 6A (gray bars).

The distributions of single-molecule rotation data sets of n-F_OF_1 power strokes at each pH as a function of the percentage of transitions in each data set that contain transient dwells are shown in **Figure 17A** (gray bars). The percent of transient dwells formed per data set that each contained ~300 power strokes was determined, and the data sets were binned into groups for each 10% occurrence of transient dwells formed. Although the percent of transient dwells formed per data set shown in **Figure 16** were taken from the averages of these distributions, it is clear that these data did not fit to a normal distribution over the pH range examined. In several data sets at pH values between 5.0 and 6.0, transient dwells formed in 90%-100% of the power strokes.

The *E. coli* F_OF_1 structure determined by cryo-EM was observed to exist in three states that differed in the rotary positions of the central stalk relative to the peripheral stalk by 120° (Sobti *et al.*, 2016). To test the hypothesis that the distributions of transient dwells observed in **Figure17A** could result differences of the three structural states, three Gaussian curves for which the probability of forming transient dwells was low (blue line), medium (red line), and high (green line) were generated. The sum of the three Gaussians (black line) were fit to the measured distribution at each pH (gray bars).

The average values of transient dwells formed represented by each of the three Gaussian curves increased inversely with pH (**Figure 18**). The Gaussian fit with the highest probability of forming transient dwells (green) increased to the greatest extent, and had an average value of 70% transient dwell formation per data set at pH 5.0.
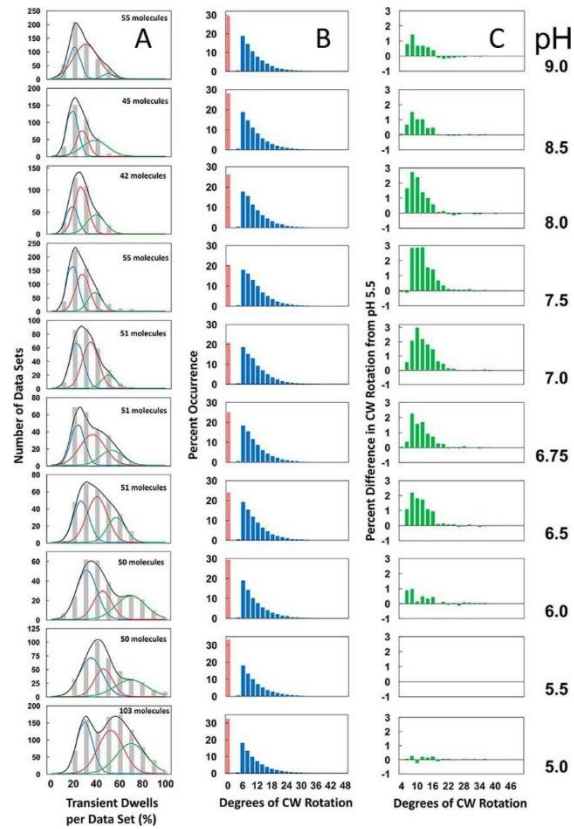
Figure 17. The pH dependence of: (A) the distribution of single-molecule n-$F_O F_1$ power stroke data sets as a function of the percentage of the occurrence of transient dwells per data set, which were binned to each 10 % (gray bar graphs). Each data set contained ~300 power strokes. The fit of the data to the sum of three Gaussians (black line) where the probability of forming transient dwells was low (blue line), medium (red line), and high (green line). The total number of n-$F_O F_1$ molecules examined at each pH is indicated; (B) the distribution of the extent of F_O-dependent CW rotation against the force of F_1-ATPase driven rotation; and (C) the difference in extent of CW rotation at each pH versus that observed at pH 5.5.

47
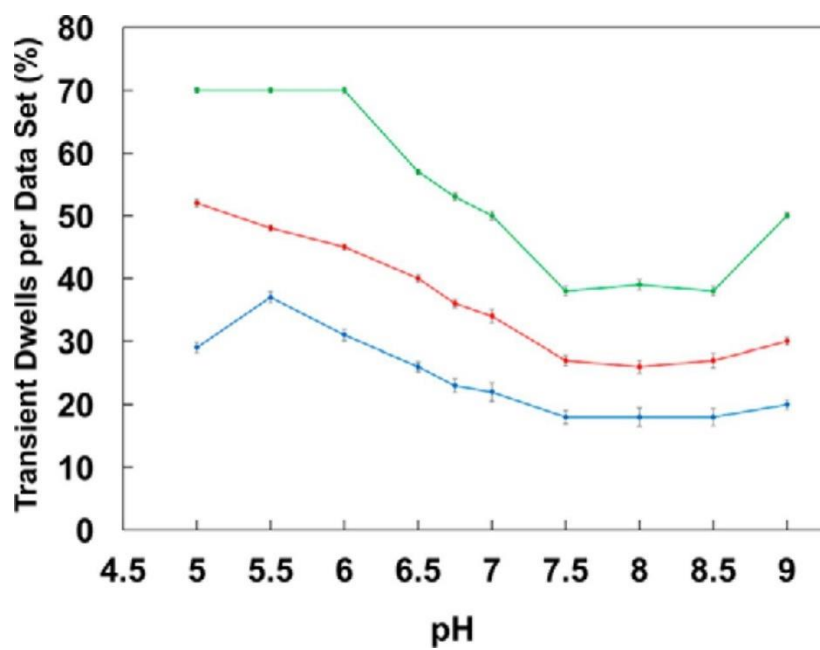
Figure 18. The pH dependencies of the average percent of transient dwells per data set derived

from the Gaussian fits from Fig 17 with low (blue), medium (red), and high (green) probabilities of

transient dwell formation. Vertical bars indicate standard error determined from the Gaussian

curves of Fig. 6A.

The distributions of the extent to which subunit-a was able to force the c-ring to rotate CW against the ATPase-driven CCW power stroke during the transient dwell as a function of pH are shown in **Figure 17B**. The maximal extent of these 'backsteps' in the CW direction was about 36°, equivalent to the rotation of the c_{10}-ring by one c-subunit. The distributions of the extent of the backsteps were plotted as a difference from that of pH 5.5 for which the extent of the backstep was lowest (**Figure 17C**). The average changes in the extent of the backstep as a function of pH were insignificant, ranging from ~11° at pH 5.5 to a maximum of about 13° at pH 7.0. The percent of transient dwells that contained backsteps varied only by ~13% as a function of pH from a minimum to a maximum of 67% to 80% at pH 5.0 and 7.0, respectively (**Figure 19**).
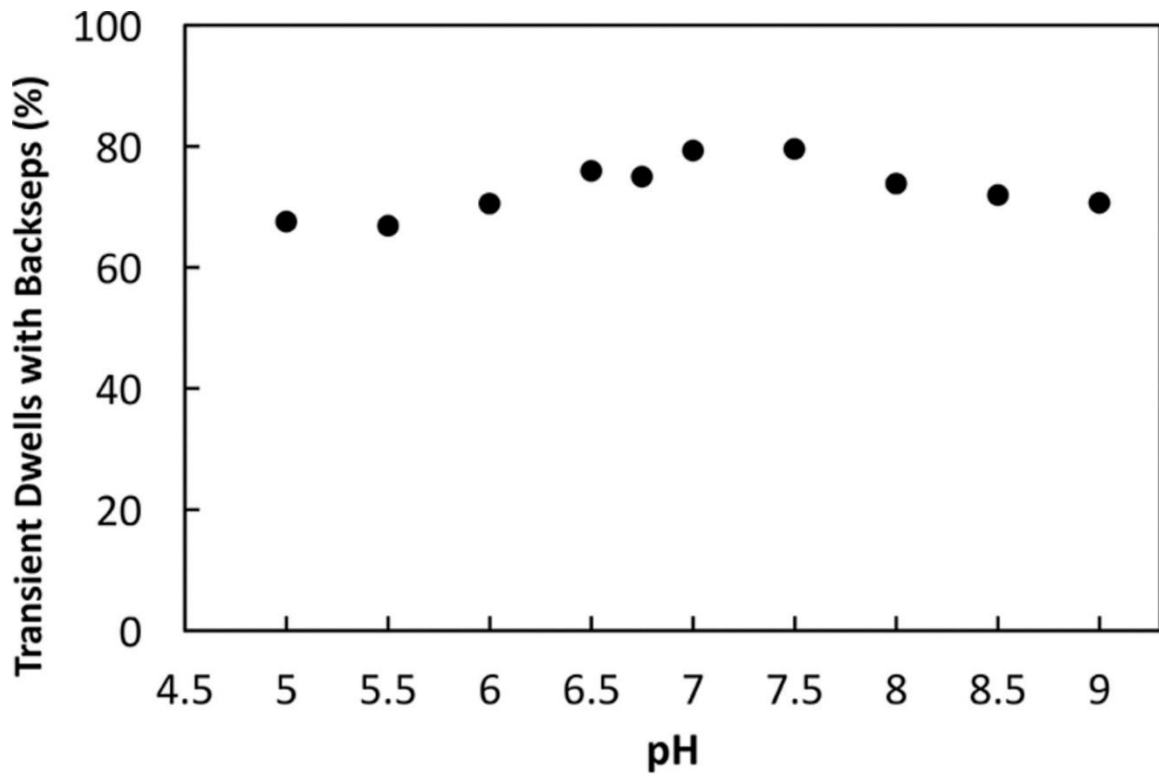
Figure 19. Average percent of transient dwells in which the c-ring rotates CW against the force of F$_1$-ATPase dependent CCW rotation as a function of pH.

Discussion

The results presented here show that the occurrence of transient dwells increases as the pH of the medium becomes more acidic. Subunit-a is the stator component in the F_O complex that contains both half-channels for proton translocation across the membrane (Fillingame *et al.*, 2014). High rates of ATP synthesis are achieved in inverted membrane vesicles of *E. coli* when the periplasmic and cytoplasmic half-channels are exposed to pH 5.5 and pH 8.5, respectively (Turina *et al.*, 2003; Fischer *et al.*, 1994). As a result of this non-equilibrium gradient, protons enter F_O through the periplasmic half-channel (the ATP synthase input channel) to induce CW rotation of the c-ring. Conversely, ATPase-driven proton pumping occurs as the result of protons entering F_O from the cytoplasm as the result of CCW rotation induced by ATP hydrolysis in F_1.

Transient dwells result from the ability of subunit-a to interact with subunit-c in a manner that stops ATPase-dependent CCW rotation of the c-ring, and results in CW rotation in the ATP synthesis direction ~ 80 % of the time (**Figure 19**). Modification of cD61 in the c-ring by N,N'-dicyclohexylcarbodiimide (DCCD) effectively inhibits ATPase activity of F_OF_1 embedded in nanodiscs (Ishmukhametov *et al.*, 2010), indicating that this ATPase-dependent rotation is linked to proton pumping across the lipid bilayer.

A major difference between a membrane and a nanodisc is that in the latter, which was used in the single-molecule experiments here, both half-channels are exposed to the same pH. The rate of F_1-ATPase activity measured in ensemble assays decreases with pH between pH 7.5 and 6.5 by ~2 fold (Wilke-Mounts *et al.*, 1994), during which the increase in transient dwells is the greatest (**Figure 16**). However, it is noteworthy that the rate-limiting step that determines ATPase activity occurs during the catalytic dwell, and not angular velocity of the power stroke (Martin *et al.*, 2014), which can contribute to the formation of transient dwells (Ishmukhametov *et al.*, 2010). Thus, although the potential contribution of the pH dependence to the angular velocity of the F_1-ATPase cannot be ruled out, these data strongly suggest that the periplasmic half-channel is more easily protonated than is the cytoplasmic half-channel.

This preferential protonation of the periplasmic half-channel halts ATPase-driven rotation, and thereby blocks ATPase-dependent proton pumping. Residues that contribute to proton translocation include aN214, aE219, aH245, and aQ252 in the periplasmic half-channel, and aE196 in the cytoplasmic half-channel (Cain and Simoni 1988; Cain and Simoni 1989; Vik *et al.* 1988; Martin *et al.*, 2015). Several additional residues are likely to have a role, especially in the cytoplasmic half-channel that is currently less well defined.

When ATP synthase is driven by a high nonequilibrium pH gradient (ΔpH=3), the periplasmic half-channel is exposed to a proton concentration 1000-fold higher than is the cytoplasmic channel. At such a high concentration, the groups in the former half-channel will be rapidly re-protonated after each donation of a proton to cD61, which induces CW rotation of the c-ring, and minimizes the probability that the c-ring will subsequently rotate CCW. In response to CW rotation, a protonated cD61 moves into proximity of aE196 in the cytoplasmic half-channel. Presumably, the proton concentration is less than the pK of aE196, and the sum of the other groups that participate in this half-channel such that dissociation of the proton into the cytoplasm is favored.

The concentration of protons required to protonate each half-channel is likely to depend on the number of groups that can be protonated, their aggregate accessibility to the adjacent aqueous phase, and their pKs, which depend on the hydrophobicity of their environments. The results presented here show that the ability to protonate the half-channels differ. Mutational studies are required to determine the relative contributions of subunit-a residues. These differences in the two half-channels have likely evolved to favor proton flux in the ATP synthase direction in order to minimize a futile cycle when the system has reached a steady state chemical gradient of ATP to ADP and P_i. In such a futile cycle, an ATP synthesized by proton flow would be immediately hydrolyzed to pump the protons in the opposite direction with no net gain in the storage of energy in the form of ATP. Without a bias that favors protonation of the ATP synthase half-channel, the magnitude of the chemical gradient that can be sustained will be diminished.

Single particle cryo-EM structures of F_OF_1 in the autoinhibited form (Sobti *et al.*, 2016) revealed three states (**Figure 20**). The autoinhibited form of the ATP synthase from *E. coli* results when the C-terminal helix-turn-helix domain of the ε-subunit has become inserted into the core of the $(\alpha\beta)_3$-ring along the shaft of the γ-subunit in a manner that prevents rotation (Cingolani *et al.*, 2011). The three structural states of this F_OF_1 structure are distinguished by the rotary positions of central stalk subunits γ and ε relative to the peripheral stalk that are separated by 120°, which is equivalent to the rotary positions of the drive shaft between ATPase-driven power strokes. It is noteworthy that single-molecule FRET measurements made where the donor and acceptor are attached to the central and peripheral stalks show a sequential low, medium, and high FRET signal when F_OF_1 embedded in proteoliposomes are actively synthesizing ATP in response to a proton gradient (Diez *et al.*, 2004). The correlation between these FRET signals with the relative positions of the central and peripheral stalks in the three states of the *E. coli* cryo-EM structure suggests that the rotary positions of the γ and ε-subunits in these three states resembles that of the functional protein complex during each of the three F_1-ATPase catalytic dwells.
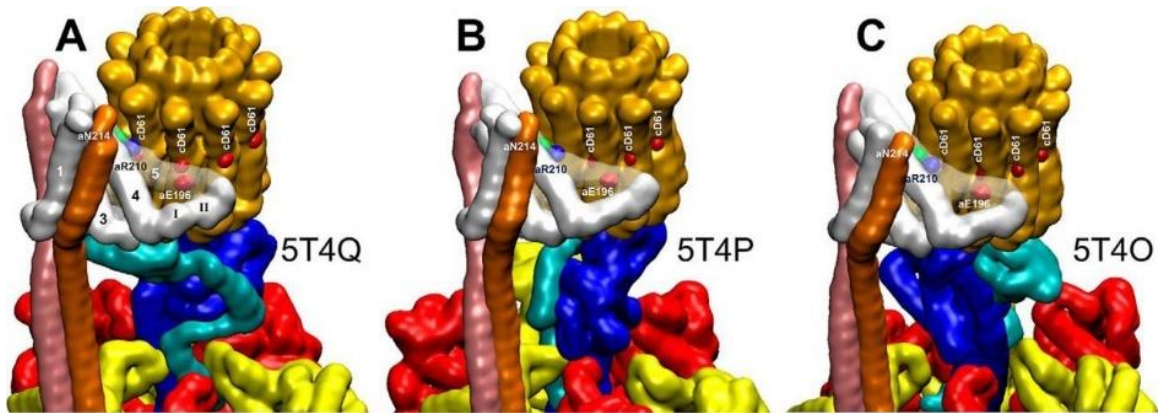
Figure 20. Conformational differences in the subunit-a relative to the c-ring between the three states of autoinhibited *E. coli* F_OF_1 as determined by cryo-EM. States 1 (A), 2 (B), and 3 (C) are defined by the rotational positions of the central stalk relative to the peripheral stalk that result from the 120° power strokes (pdb reference IDs 5T4Q, 5T4P, and 5T4O, respectively). The autoinhibited state results from insertion of the C-terminal domain of subunit-ε into the core of the F_1 (αβ)$_3$-ring.

The data presented at each pH in **Figure 17A** represent the sum of data sets typically from ~50 molecules of F_OF_1. The occurrence of transient dwells was analyzed for each molecule examined only from the power stroke in which the scattered light intensity of the nanorod progressed from a minimum through a maximum (**Figure 13**), and not from the other two power strokes that complete a 360° rotation. For any given molecule, there is an equal probability that the power stroke analyzed corresponds to the rotation from one of the three structural states defined by the relative position of the two stalks. Thus, for every 51 F_OF_1 molecules analyzed for transient dwells, it is likely that the power strokes specific to each of the three different structural states will have been sampled by 17 molecules. This conclusion is supported by the observations that the distributions of transient dwell occurrence at any of the pH values examined do not fit to a single normal distribution, but that good fits to the data were achieved by fitting the distributions to the sum of three Gaussians (**Figure 17A**).

The average values derived from each Gaussian dependence changed by a comparable extent as a function of pH (**Figure 18**), which implies that the Gaussian curves represent molecules in which the probability of forming a transient dwell is low (blue), medium (red), or high (green). This suggests that the ATPase-driven power stroke that follows each of the three structural F_OF_1 states derived from cryo-EM has a low, medium, or high probability of forming transient dwells. In the absence of knowledge of the correlation between the ability to form transient dwells and the structural state of the power stroke examined, it is not possible at this time to know how the probability to form transient dwells in any one structural state changes with pH. It is noteworthy that since the ATPase rotates in 120° power strokes, the c-ring will rotate 4x36° for one of the power strokes, but 3x36° for the other two. Thus, it is possible that the probability of observing transient dwells is more likely for molecules aligned to step by 4 c-subunits per power stroke, although it does not explain the differences in the molecules with a low and medium probability of forming transient dwells.

The three states of *E. coli* F_OF_1 determined by cryo-EM (**Figure 20**) differ not only by the relative position of the central and peripheral stalks, but also by the conformation of subunit-a,

and its position on the c-ring. These differences include the positions of subunit-a residues aN214, aR210, and aE196 involved in proton translocation relative to the cD61 residues on each c-subunit. In addition, the three structural states of *E. coli* F_OF_1 differ in the position of the subunit-a 3_{10}-helix II and its subsequent loop relative to the c-ring. It is noteworthy that similar conformational changes were proposed in the Grab and Push mechanism to explain the basis of transient dwell formation, and the ability of subunit-a to push the c-ring CW against the force of ATPase-dependent rotation (Martin *et al.*, 2015). The cryo-EM structures of *E. coli* F_OF_1 are in the autoinhibited state in which the C-terminus of the ε-subunit has adopted a conformation that prevents rotation. Thus, it is not possible at this time to determine whether subunit-a has been trapped in different functional conformations that represent sequential steps in the Grab and Push mechanism or whether these conformational differences predispose a given rotational state of the complex to have a low, medium, or high probability of forming transient dwells.

Chapter 3

PH-DEPENDENT 11° F_1F_O ATP SYNTHASE SUB-STEPS REVEAL INSIGHT INTO THE F_O TORQUE GENERATING MECHANISM

Abstract

Most cellular ATP is made by rotary F_1F_O ATP synthases using proton translocation-generated clockwise torque on the F_O c-ring rotor, while F_1-ATP hydrolysis can force counterclockwise rotation and proton pumping. The F_O torque-generating mechanism remains elusive even though the F_O interface of stator subunit-a, which contains the transmembrane proton half-channels, and the c-ring is known from recent F_1F_O structures. Here, single-molecule F_1F_O rotation studies determined that the pKa values of the half-channels differ, show that mutations of residues in these channels change the pKa values of both half-channels, and reveal the ability of F_O to undergo single c-subunit rotational stepping. These experiments provide evidence to support the hypothesis that proton translocation through F_O operates via a Grotthuss mechanism involving a column of single water molecules in each half-channel linked by proton translocation-dependent c-ring rotation. We also observed pH-dependent 11° ATP synthase-direction sub-steps of the *Escherichia coli* c_{10}-ring of F_1F_O against the torque of F_1-ATPase-dependent rotation that result from H^+ transfer events from F_O subunit-a groups with a low pKa to one c-subunit in the c-ring, and from an adjacent c-subunit to stator groups with a high pKa. These results support a mechanism in which alternating proton translocation-dependent 11° and 25° synthase-direction rotational sub-steps of the c_{10}-ring occur to sustain F_1F_O ATP synthesis.

Introduction

The F_1F_O ATP synthase (**Figure 21**) that is found in all animals, plants, and eubacteria is comprised of two molecular motors that are attached by their rotors and by their stators (Kühlbrandt, 2019; Spetzler *et al.*, 2012). The F_O motor, which is embedded in bioenergetic

membranes, uses a non-equilibrium transmembrane chemiosmotic proton gradient also known as a proton-motive force (pmf) to power clockwise (CW) rotation of its ring of c-subunits relative to the subunit-a and -b stator proteins as viewed from the *Escherichia coli* periplasm. These subunits contribute to the peripheral stalk bound to one side of the F_1 $(\alpha\beta)_3$-subunit ring where each $\alpha\beta$-heterodimer comprises a catalytic site that synthesizes ATP from ADP and P_i. Subunit-γ, which docks to the c-ring along with subunit-ϵ, extends into the core of the $(\alpha\beta)_3$-ring (**Figure 21B**). The rotary position of subunit-γ within the $(\alpha\beta)_3$-ring causes the conformations of the three catalytic sites to differ such that one site contains ADP and P_i, a second site contains ATP, and the third site is empty. Pmf-powered CW rotation of subunit-γ forces conformational changes to all catalytic sites in the $(\alpha\beta)_3$-ring, which releases ATP from one catalytic site with each 120° rotational step (Kühlbrandt, 2019; Spetzler *et al.*, 2012). In this manner, F_1F_O converts the energy from the pmf ($\Delta\mu H^+$) into energy in the form of a non-equilibrium chemical gradient ($\Delta\mu ATP$) where the ATP/ADP•P_i concentration ratio is far in excess of that found at equilibrium.

When ΔG_{ATP} is significantly higher than n*pmf, the F_1-ATPase motor can overpower the F_O motor and catalyze net ATP hydrolysis (Steigmiller *et al.*, 2008; Fischer *et al.*, 2000). This results in ATPase-dependent power strokes that rotate continuously CCW for 120° at saturating ATP concentrations (Yasuda *et al.*, 2001; Spetzler *et al.*, 2006), and pump protons across the membrane to the periplasm in *E. coli* (Spetzler *et al.*, 2012). Power strokes are separated by catalytic dwells that last a few ms, during which ATP is hydrolyzed (Yasuda *et al.*, 2001; Spetzler *et al.*, 2006; Spetzler *et al.*, 2009). At rate-limiting ATP concentrations, an ATP-binding dwell can interrupt the *E. coli* F_1 power stroke ~34° after the catalytic dwell (Yasuda *et al.*, 2001; Martin *et al.*, 2014). At this same rotary position, high ADP concentrations can compete with ATP to bind to the empty catalytic site resulting in ADP inhibition (Martin *et al.*, 2014). All ATP synthases can catalyze ATP hydrolysis to some extent, although many have evolved regulatory mechanisms to minimize this energy wasteful process (Kühlbrandt, 2019). Under some circumstances, *E. coli* employs F_1F_O as an ATPase-driven H^+ pump to maintain a pmf as an energy source for other metabolic processes (Spetzler *et al.*, 2012).
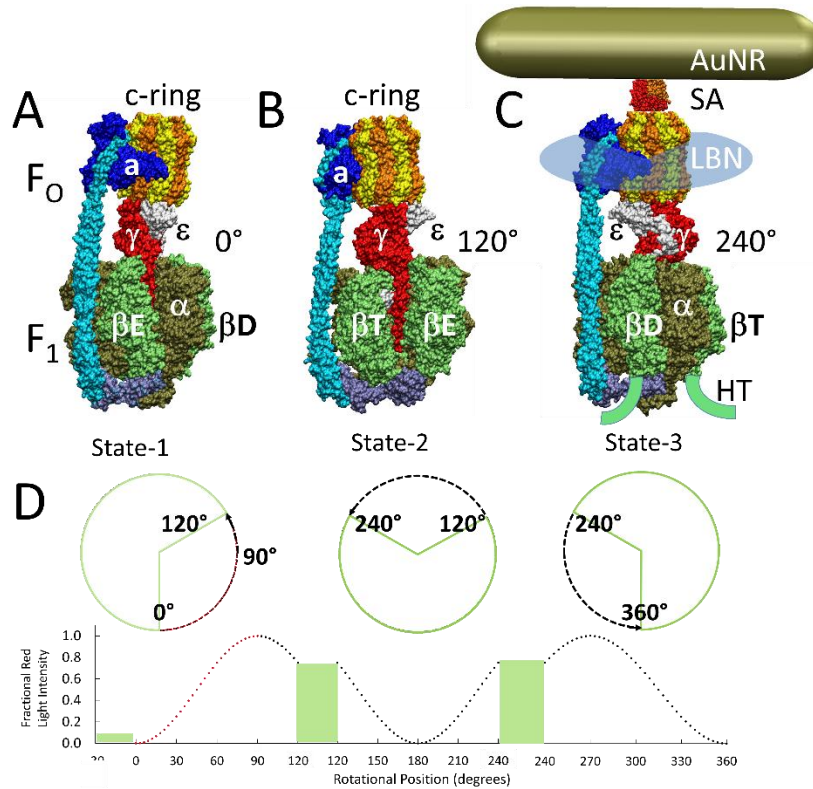
Figure 21. Cryo-EM structures of F_1F_O ATP synthase inhibited by ADP in three rotary states, and measurement of changes in rotational position between catalytic dwells. (A) Rotational state-1, pdb-ID 6OQU (Sobti et al., 2020). (B) State-2, pdb-ID 6OQV, with rotor 120° counterclockwise (CCW) from (A) where subunit-α is not shown to reveal subunit-γ. (C) State-3, pdb-ID 6WNR, with rotor 240° CCW from (A) showing microscope slide assembly of F_1F_O embedded in a lipid bilayer nanodisc (LBN) for rotation measurements. His6-tags (HT) on β-subunit C-termini enabled attachment to slide, while the gold nanorod (AuNR) coated with streptavidin (SA) bound to the biotinylated subunit c-ring. (D) Rotational position of single F_1F_O molecules versus time was monitored by intensity changes of polarized red light scattered from the AuNR in the presence of 1 mM Mg^{2+}ATP, which enabled F_1-ATPase-dependent 120° CCW power strokes between catalytic dwells (green bars). Prior to data collection at 200 kHz, a polarizer in the scattered light path was rotated to minimize intensity during one of the three catalytic dwells. Light intensity increased to a maximum upon rotation by 90° during the subsequent CCW 120° power stroke. For each molecule the angular dependence of these power strokes versus time was analyzed.

59

The means by which H$^+$ translocation from the periplasm generates CW rotational torque on the c-ring is poorly understood. Molecular motors are believed to operate by either power stroke or by a Brownian ratchet mechanism, which has been postulated for F$_O$ (Hwang and Karplus, 2019; Oster *et al.*, 2000). Although evidence clearly supports a power stroke mechanism for F$_1$-ATPase-dependent rotation (Martin *et al.*, 2014; Martin *et al.*, 2018; Pu and Karplus, 2008), there is little direct evidence in support of either mechanism for F$_O$-driven rotation in the ATP synthase direction. Protons enter and exit F$_O$ via half-channels in stator subunit-a. Two c-subunits in the ring contact subunit-a at a time where the leading cD61 during CW rotation (synthase direction) accepts a proton from the input channel, while the lagging cD61 donates its proton to the output channel.

The half-channels are separated by the highly conserved subunit-a arginine (aR210 in *E. coli*), which has long been thought to be responsible for displacing the H$^+$ from cD61 into the output channel during ATP synthesis (Lightowlers *et al.*, 1987; Cain and Simoni, 1989; Cain and Simoni, 1988; Vik *et al.*, 1988). As the result of mutations of *E. coli* subunit-a residues aN214, aE219, aH245, aQ252, and aE196 to other groups including leucine that decreased ATP synthase activity, ATPase-dependent H$^+$ pumping, and altered the ATP hydrolysis activity, these residues were proposed to translocate protons directly along the half-channels (Lightowlers *et al*., 1988; Howitt *et al*., 1990; Eya *et al*., 1991; Hartzog and Cain, 1994; Hatch *et al*., 1995; Hahn *et al*., 2018). Cryo-EM F$_1$F$_O$ structures that reveal details of subunit-a confirmed that these residues are positioned along possible half-channels that are separated by aR210 (Hahn *et al.*, 2018; Zhou *et al.*, 2015; Pinke *et al.*, 2020; Sobti *et al.*, 2020; Martin *et al.*, 2015).

Alternatively, H$^+$ translocation through F$_O$ has also been postulated to occur via a Grotthuss mechanism (Cukierman, 2006) where a column of single water molecules that are hydrogen-bonded to specific protein groups behave in a coherent manner to transfer protonic charge over long distances via rapid exchange of H$^+$ between H$_3$O and H$_2$O (Cukierman, 2006; Wraight, 2006). A recent F$_1$F$_O$ structure from bovine mitochondria was of sufficient resolution to observe density near the input channel residues consistent with Grotthuss-type water molecules

in this half-channel (Spikes *et al.*, 2020). A consequence of this coherent behavior of a Grotthuss water column is that the rate of H^+ transfer can be much faster than the rate via free diffusion (Cukierman, 2006). The possibility that F_O operates via a Grotthuss mechanism was first suggested from the observation of an astounding H^+ translocation rate of 6240 H^+ s^{-1} from a driving force of 100 mV across *Rhodobacter capsulatus* vesicles containing F_O that lacked F_1 (Feniouk *et al.*, 2004). The *R. capsulatus* F_O rates of H^+ transfer exceed the rate of delivery of protons by free diffusion from the bulk aqueous solution at a concentration of 10^{-8} M (pH 8) such that the ability to supply protons to a Grotthuss water column should be rate-limiting (Wraight, 2006). To achieve this rate of H^+ translocation, the existence of a H^+ antenna at the entrance to the F_O input channel has been postulated (Wraight, 2006), which in *R. capsulatus*, was calculated to consist of a hemispherical Coulomb cage with a H^+ capture radius of ~40 Å surrounding the entrance to the input channel.

      Single-molecule studies of F_1F_O molecules embedded in lipid bilayer nanodiscs (**Figure 21C**) revealed that the 120° CCW ATPase power strokes can be interrupted by transient dwells (TDs) at ~36° intervals with a duration of ~150 μs (Martin *et al.*, 2015; Ishmukhametov *et al.*, 2010; Yanagisawa and Frasch, 2017). In more than 70% of TDs, the F_O motor not only halted F_1-ATPase CCW rotation, but the c-ring rotated CW in synthase-direction steps (Martin *et al.*, 2015; Yanagisawa and Frasch, 2017). Complete assembly of F_1F_O nanodisc complexes from the membrane scaffold protein (MSP), lipids, and detergent-solubilized F_1F_O was verified by 2D electrophoresis where the first nondenaturing gel dimension contained a single band, which after the second denaturing dimension, contained bands corresponding to MSP and all F_1F_O subunits (Ishmukhametov *et al.*, 2010). The ATPase activity of nanodisc preparations is DCCD-sensitive, remains unchanged after 8 hr at room temperature, and is 1.5-fold higher than the initial activity of detergent-solubilized F_1F_O, which loses all activity in <4 hr. The observation that a subunit-a insertion mutation, which disrupts the interface between subunit-a and the c-ring, retained ATPase activity but lost the ability to form TDs indicates that these dwells result from an

interaction between subunit-a and successive c-subunits in the c-ring (Ishmukhametov *et al.*, 2010).

The occurrence of TDs was found to increase at pH 8 when viscous drag on the nanorod is sufficient to slow the angular velocity of the F_1 ATPase-driven power stroke (Martin *et al.*, 2015; Ishmukhametov *et al.*, 2010). These results showed that there is a kinetic component that affects the probability that the interaction between subunit-a and the c-ring will occur relative to the F_1-ATPase power stroke. A kinetic dependence for F_1F_O-catalyzed ATP synthesis versus hydrolysis has been theorized based on energetic calculations (Gao *et al.*, 2005). The occurrence of TDs, including those with synthase-direction steps, is also known to increase inversely with pH between pH 5 and pH 7 (Yanagisawa and Frasch, 2017). This suggests that synthase-direction steps depend on H^+ transfer from the protonated groups with a low pKa from the subunit-a input channel to the c-ring, and from the c-ring to unprotonated groups with a high pKa in subunit-a output channel.

Maximal ATP synthase rates in membrane vesicles where *E. coli* F_1F_O is oriented with F_1 on the outer surface are typically achieved with inner and outer pH values of 5.0 and 8.5, respectively (Fischer *et al.*, 2000; Fischer *et al.*, 1994). The pmf can be derived from non-equilibrium differences in pH (ΔpH) or membrane potential (Δψ). Although the energy from ΔpH and Δψ to drive ATP synthesis are interconvertible, the latter is the dominant energy source for *E. coli* in vivo.

Each of the three successive 120° F_1-ATPase power strokes required for a full revolution of the F_1F_O rotor is unique because the rotary positions of subunit-γ differ relative to the peripheral stalk that includes subunit-a (**Figure 21A–C**). These power strokes also differ because the 36° stepping of the c_{10}-ring and the 120° power strokes can only be aligned during one of the three catalytic dwells. As a result, the three power strokes require the translocation of 4 H^+, 3 H^+, and 3 H^+ that result in net c-ring rotations of 144°, 108°, and 108°, respectively. Consequently, the c-ring and subunit-γ become misaligned by +14° and −14° during two of the catalytic dwells.

The elasticities of the peripheral stalk, subunit-δ, and to some extent, subunit-γ accommodate these rotary differences (Sobti *et al.*, 2020; Murphy *et al.*, 2019).

The positive and negative torsion on the c_{10}-ring from the elastic energy needed to accommodate the +14° and −14° misalignments during rotation affects the ability to form TDs and their associated synthase-direction steps (Yanagisawa and Frasch, 2017), which along with their pH dependence and occurrence every 36°, indicate that they correspond to single c-subunit stepping relative to subunit-a. To determine the percentage of power strokes in which TDs were observed, data sets were collected from one of the three 120° power strokes from each single-molecule of nanodisc-embedded *E. coli* F_1F_O examined. For each data set that comprised ~300 power strokes, the percent of power strokes that contained TDs was determined. For each molecule examined there was an equal chance that the c-ring and catalytic dwell was aligned, or subject to the positive or negative torsion from misalignment. The distribution of data sets collected from many molecules versus the percent of power strokes containing TDs fit to the sum of three Gaussians that corresponded to low, medium, and high probabilities of TD formation. The high and low TD percentages were consistent with the torsion from misalignment that provides additional energy to promote TD formation, or to inhibit it when torsion is in the opposite direction (Yanagisawa and Frasch, 2017). Similar effects of the c_{10}-ring and catalytic dwell misalignments have also been observed in other single-molecule F_1F_O measurements (Sielaff *et al.*, 2019).

We have now examined mutations of residues in the putative subunit-a half-channels that have been implicated to participate in H^+ transfer events in both the input and output channels with the goal of distinguishing whether F_O rotation occurs via a Brownian ratchet versus a power stroke mechanism, and whether the half-channel residues transfer protons individually or act together to support water column that transfers protons via a Grotthuss mechanism.

The ability to form ATP synthase-direction steps as a function of pH during ATP hydrolysis-driven CCW power strokes was characterized in single-molecule studies of F_1F_O molecules embedded in lipid bilayer nanodiscs. Formation of synthase-direction steps during a TD was maximal at the pH value when unprotonated and protonated forms of the input and

output channels were optimal such that synthase-direction steps required H^+ transfer both from the input channel to the leading c-subunit and from the lagging c-subunit to the output channel. Mutation of a residue from either the input or output channel altered both the low and high pKa values of TD formation indicating that input and output channels communicate. This is consistent with a Grotthuss mechanism where a water column in each of the two channels is connected by rotation-dependent H^+ transfer to and from the leading and lagging c-subunits in the c-ring, which is also supported by features from a variety of F_1F_O structures.

The extent of rotation during ATP synthase-direction steps was unexpectedly found to rotate 11° in the WT and all mutants. Cryo-EM structures of sub-states with subunit-a: c-ring differences of 11° that position the lagging c-subunit cD61 adjacent to output residues aS199 and aE196 (Sobti *et al.*, 2020) are consistent with the synthase-direction steps observed here. When combined with structural information, the results do not support the hypothesis that the role of aR210 is to displace the H^+ from cD61, but are consistent with a Grotthuss H^+ translocation mechanism involving both half-channels for sustained ATP synthase-direction c-ring rotation that results from successive alternating 11° and 25° synthase-direction sub-steps for each c-subunit in the c_{10}-ring. Direct evidence of a mixed model was observed in which some synthase-direction steps show characteristics of a power stroke while others exhibit oscillations consistent with a Brownian ratchet mechanism.

Results

Contributions of subunit-a residues putatively involved in the ATP synthase H^+ half-channels were assessed by the effects on TD formation caused by mutations that converted charged or polar groups in subunit-a to hydrophobic leucine. Changes in rotational position were measured by a 35 × 75 nm gold nanorod (AuNR) bound to the biotinylated c-ring of individual *E. coli* F_OF_1 molecules embedded in lipid bilayer nanodiscs (Ishmukhametov *et al.*, 2010), hereafter F_1F_O (**Figure 21C**). Changes in rotational position during F_1-ATPase power strokes in the presence of saturating 1 mM MgATP were monitored by the intensity of polarized red light

64

scattered from the AuNR (Spetzler *et al.*, 2006; Hornung *et al.*, 2011). Prior to data collection, the polarizer was adjusted so that the scattered red light intensity was at a minimum during one of the three F_1 catalytic dwells (**Figures 21D and 22A**). The subsequent power stroke caused an increase in light intensity to a maximum when the AuNR had rotated 90° (Ragunathan *et al.*, 2017). Rotational data sets of each F_1F_O molecule examined were collected for 5 s, which included ~300 of these power strokes (Yanagisawa and Frasch, 2017). Ten data sets were collected for each molecule. The number of F_1F_O molecules examined at each pH for WT and mutants is indicated in **Figure 25**. Using WT at pH 5.0 as an example where data from 103 F_1F_O molecules were collected, this was equivalent to 1030 data sets, and ~309,000 power strokes examined. For each molecule examined, rotational position versus time was calculated from scattered light intensity versus time using an arcsine$^{1/2}$ function from which the number of TDs observed during the first 90° of rotation were determined (Ragunathan *et al.*, 2017).

 Example power strokes from WT and mutant F_1F_O molecules at pH 5.0 where TDs were present (black dots) and absent (blue dots) are shown in **Figure 22A** and **Figure 23**, respectively. When present, TDs either stopped F_1-ATPase CCW rotation momentarily (green dots) or exhibited CW rotation in the ATP synthase direction, hereafter synthase-direction steps (red dots). None of the mutations examined eliminated the ability of F_1F_O to form TDs. Power strokes typically contained two to three TDs, when present. These were separated by an average of ~36°, consistent with an interaction between subunit-a and successive c-subunits in the c_{10}-ring of *E. coli* F_1F_O.

 A power stroke mechanism has been defined as the generation of a large free energy gradient over a distance comparable to the step size of the molecular motion so that transition to the forward position occurs nearly irreversibly (Hwang and Karplus, 2019). By contrast, in a Brownian ratchet mechanism the motor is thought to visit previous and forward positions through thermal motion, where stabilization in the forward position results by conformational changes triggered by the fuel processing event. While some synthase-direction steps shown of **Figure 22A** and **Figure 23** rotated CW in a concerted, and apparently irreversible manner characteristic

of a power stroke, others indicated by brackets were observed to oscillate back and forth during the TD. These oscillations most commonly occurred late in the F_1 power stroke (~70–80°) and were more pronounced in all mutations examined except aN214L (**Figure 23**). Such oscillations are direct evidence of a Brownian ratchet mechanism and are likely the result of a close balance between the energy that powers the F_1-ATPases power stroke with the energy that powers synthase-direction rotation, which suggests that these mutations cause a decrease in the energy to power synthase-direction rotation.
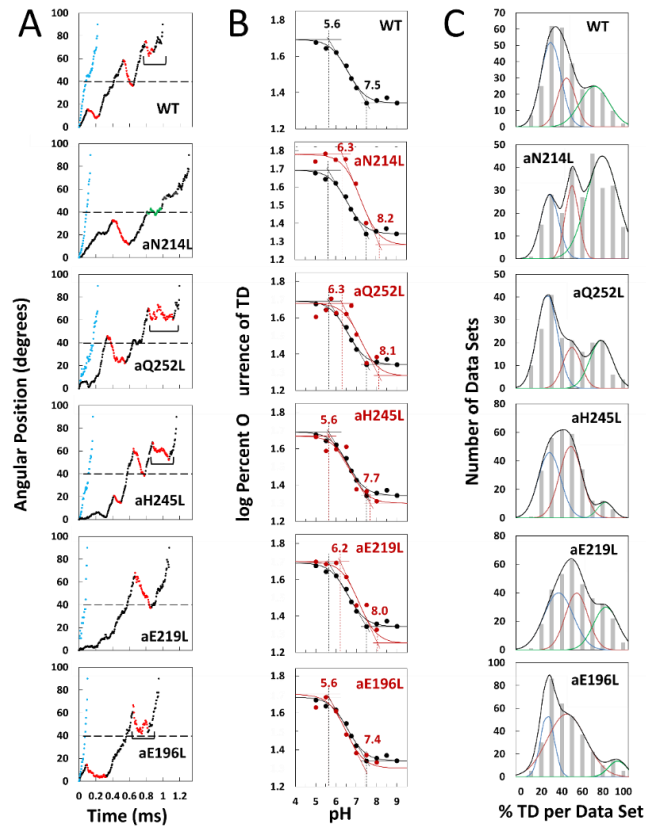
Figure 22. Effects of subunit-a mutations on transient dwells (TDs). (A) Examples of power strokes without TDs (blue), and of power strokes with TDs that lacked (green), or contained clockwise (CW) synthase-direction c-ring rotation relative to subunit-a (red) plotted as degrees of rotation after the catalytic dwell versus time where 40° (dotted line) is the optimal position for binding of ATP or inhibitory ADP (Yasuda et al., 2001; Martin et al., 2014). Brackets indicate Brownian-type oscillations during a TD. (B) Average percent TDs per data set versus pH from which pKa values were derived via intercepts of the slope and plateaus (solid line) of each curve based on the fit of the data to Equation 4 for WT (black line) and subunit-a mutants (red line). (C) Distributions at pH 6.0 of the percent of TDs per data set of power strokes (gray bars) where multiple data sets that each contained ~300 power strokes were collected from each of the total number of the F_1F_O indicated, and data were binned in 10% increments. The data were fit to the sum of three Gaussians (black line) representing low (blue), medium (orange), and high (green) efficiencies of TD formation.

67
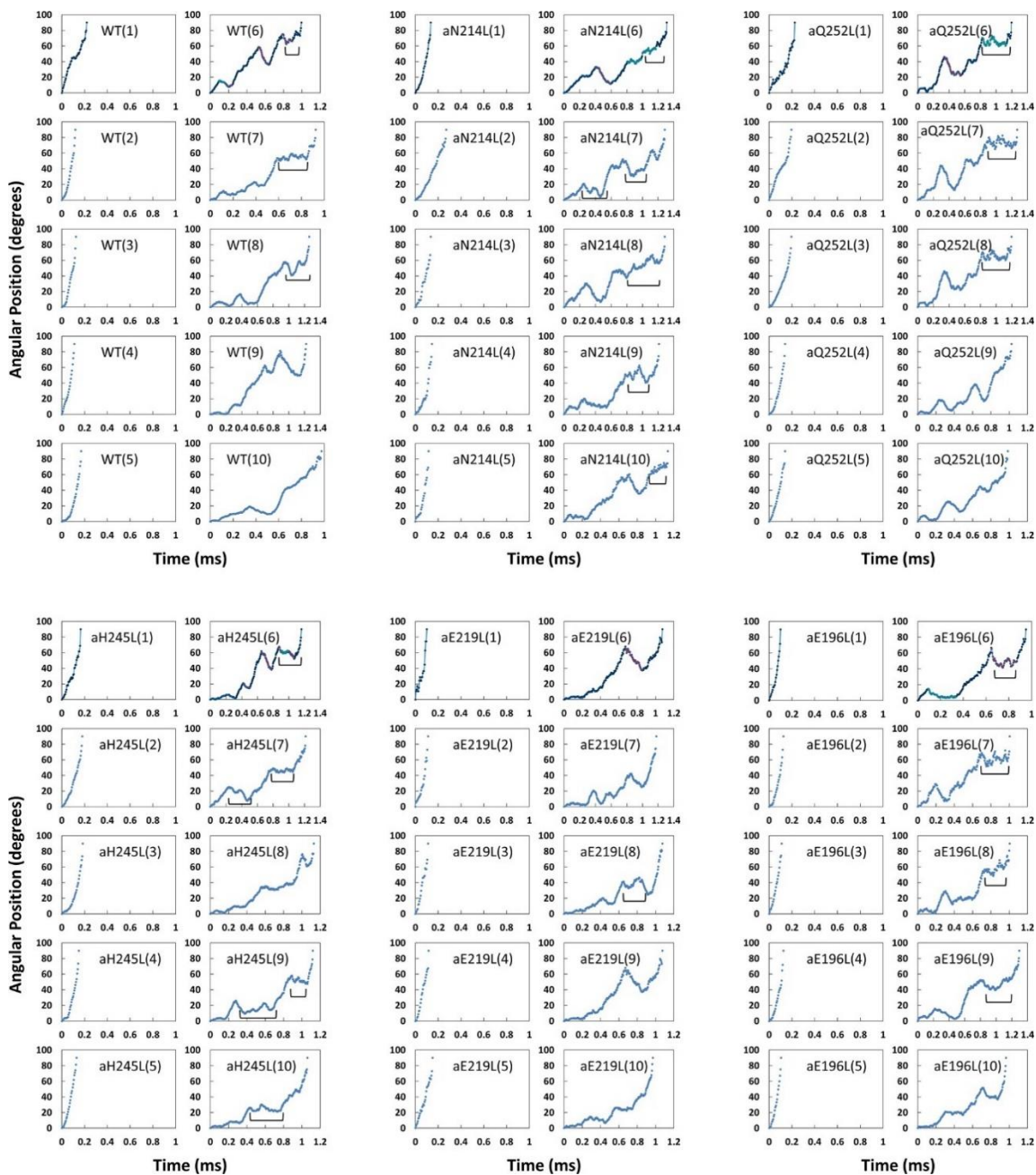
Figure 23. Examples each of the first 90° of ATP hydrolysis-driven power strokes observed using F_OF_1 nanodiscs. In each mutant, examples 1–5 show power strokes without transient dwells (TDs). Examples 6–10 show power strokes with transient dwells where the F_O motor either halts counterclockwise (CCW) rotation or caused clockwise (CW) rotation in the ATP synthase direction (synthase-direction steps). Brackets indicate Brownian-type oscillations during a TD.

68

Change in K_1 causes a change in the maximum TD occurrence.
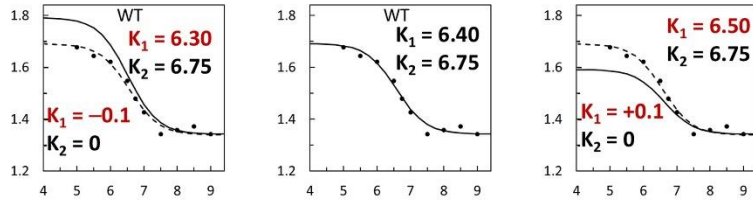
Change in K_2 also changes in the maximum TD occurrence, but in the opposite direction as when K_1 is changed.
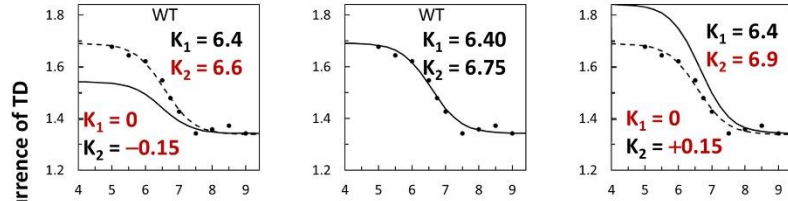
Changing both K_1 and K_2 an equal amount shifts the curve along the x-axis
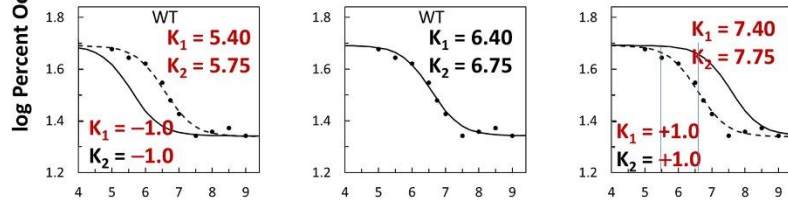
Changing the T_{min} shifts the curve along the y-axis
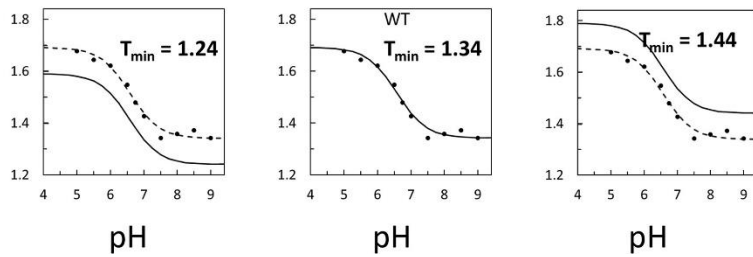
Figure 24. Examples of how changes in the variables in Equation 4 affect the log-log plots that describe the F-ATPase inhibition kinetics of Figure 22B.
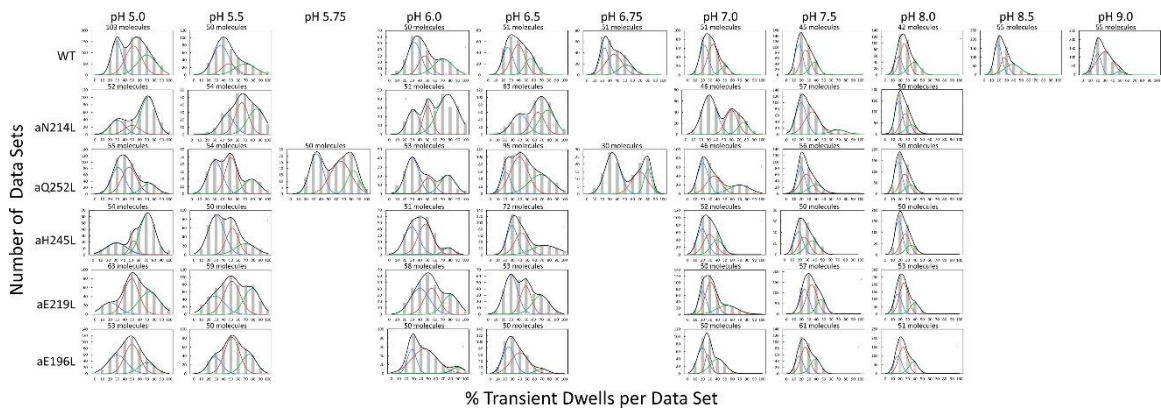
Figure 25. Distribution of power stroke data sets (each set containing ~300 power strokes) at each pH examined versus the percentage of the occurrence of transient dwells (TDs) per data set binned to each 10% (gray bars). The data were fit to the sum of three Gaussians (—) representing low (—), medium (—), and high (—) efficiencies of TD formation. Ten data sets were acquired from each molecule, and the number of molecules examined is shown for each condition.

<u>Subunit-a mutations alter pKas of TD formation</u>

We postulated that mutation of subunit-a residues involved in H$^+$ translocation related to c-ring rotation would alter the pKa of the half-channel in which the is located if each residue contributes independently to the H$^+$ translocation process. Consequently, we precisely determined the pKa values of groups that contribute to TD formation (**Figure 22B**) using Equations applied to the pH dependence of enzyme inhibition kinetics (Cook and Cleland, 2007).

TDs occur when subunit-a binds to the c-ring to stop F$_1$ ATPase-driven rotation for a period of time. Thus, a TD represents an extent that F$_O$ inhibited the F$_1$ATPase motor, which occur as often as 3.6 times per F$_1$ power stroke. Kinetically, the ATPase power stroke duration without TDs is ~200 µs, while the average duration of each TD is ~150 µs (Martin *et al.*, 2015; Ishmukhametov *et al.*, 2010; Yanagisawa and Frasch, 2017). In data sets where TDs occur in 100% of the power strokes, for example, aN214L at pH 6.0, all of the ~300 power strokes in that data set will contain TDs (i.e. they look like the power strokes in **Figure 2A** where TDs are denoted by green or red dots) such that the efficiency of TD formation is 100%. Such a data set represents a 64% inhibition of the F$_1$ ATPase power stroke kinetics. When all ~300 power strokes in a data set look like those in **Figure 2A** represented by blue dots, the efficiency of TD formation in that data set is 0%.

Precise pKa determination depended upon the fits of the efficiency at each pH examined to the pH dependence over the range of pH values in **Figure 22B**. The number of molecules examined for WT and each mutant is indicated in **Figure 25**. For example, a total of 553 F$_1$F$_O$ molecules (~92 million power strokes) were examined to establish the pH dependence of WT. A maximum average of 47.5% of WT power strokes from all three efficiency groups occurred at pH 5.0, which decreased with increasing pH until it plateaued at a minimum of ~22% at pH values > 7.5 (**Figure 22B**). The pH dependences for WT and mutants were fit to Equation 4 where T is the total average TD occurrence, T$_{min}$ is the minimum TD occurrence, and K$_1$ and K$_2$ are inhibition constants that define the increase and maximum TD occurrence versus pH as the result of either a residue that is protonated with pKa$_1$, or unprotonated with pKa$_2$, respectively. It is noteworthy

that K_1 is similar to a dissociation constant because a smaller K_1 increases the ability of subunit-a to bind to, and stop, c-ring rotation with decreasing pH (**Figure 24**). Conversely, a smaller K_2 value decreases TD formation with decreasing pH because it is the unprotonated form of that residue that binds and inhibits.

$$T=\log T_{min}-\log\left(1+\frac{K_2}{[H^+]}\right)+\log\left(1+\frac{K_2}{[H^+]}\right) \qquad\qquad \text{Eq. 4}$$

The fit of the data to Equation 4 defines the slope of the curve as well as the high and low plateau values. Because these are log-log plots, the pKa values (**Figure 22B**, dotted lines) are determined by the intercept of the slope with the high and low plateau values (solid lines). None of the mutations changed T_{min} significantly. Using parameters derived by the fits of the data to Equation 4 for WT and mutants (Table 1), the WT group(s) that must be protonated to induce a TD had pKa_1 and K_1 of 5.6, and 6.4, respectively, while the group(s) that must be unprotonated to induce a TD had pKa_2 and K_2 values of 7.5 and 6.75, respectively.

	K_1	K_2	T_{min} (%)	pKa_1	pKa_2
WT	6.4	6.75	22.0	5.6	7.5
aN214L	7.0	7.50	19.1	6.3	8.2
aQ252L	7.0	7.40	19.5	6.3	8.1
aE219L	6.9	7.35	17.8	6.2	8.0
aH245L	6.5	6.87	20.0	5.6	7.7
aE196L	6.3	6.70	20.0	5.6	7.4

Table 1. pKa Values and Inhibition Constants for WT and Subunit-a Mutants. Values were derived from the fits to Equation 4 of the average percent of TDs per data set versus pH in **Figure 2C**.

The aN214L mutation, which had the greatest effect on the pH dependence of TD formation, increased the maximum percent of TDs formed at low pH to 61% (1.3-fold) and shifted the pH dependence in the alkaline direction from WT. These changes were due to increases in K_1 and K_2 to 6.4 and 6.75, respectively, that increased pKa_1 and pKa_2 by 0.9 and 0.7 pH units. The differential increases in K_1 and K_2 by 0.6 and 0.75 units led to the aN214L-dependent increase in maximum TD formation at low pH because an equal shift of these values in the same direction causes the curve to shift to higher pH values without affecting the maximum occurrence of TDs formed (**Figure 24**). Similar but smaller effects were observed with aQ252L and aE219L (**Figure 22B**) where K_1 increased by 0.6 and 0.5 units, respectively, resulting in a pKa_1 increase of almost 1 pH unit from that of WT. However, aQ252L and aE219L decreased K_2 by 0.35 and 0.40 units from WT such that the increase in pKa_2 was proportionally smaller than that observed for aN214L. Consequently, while both mutants shifted the pH dependence in the alkaline direction from that of WT, only aQ252L showed an increase in the maximum TD occurrence (52%).

Mutations aH245L and aE196L caused the smallest changes in the pH dependence of TD formation. The former increased K_1 and K_2 by 0.1 and 0.12 units, which had no effect on pKa_1, and increased pKa_2 by 0.2 units. The latter was the only mutation to decrease the values of both K_1 and K_2, which decreased pKa_2 by 0.1 pH units from that of WT. It is noteworthy that aE196 is a component of the H^+ output channel.

In summary, mutation of residues examined in either the input or the output channel changed both the high and low pKa values of TD formation. These results support the conclusion that they participate in H^+ translocation as first proposed from ensemble studies (Lightowlers *et al.*, 1987; Cain and Simoni, 1989; Cain and Simoni, 1988; Vik *et al.*, 1988; Lightowlers *et al.*, 1988; Howitt *et al.*, 1990; Eya *et al.*, 1991; Hartzog and Cain, 1994; Hatch *et al.*, 1995), but also show that the two channels communicate via the c-ring, which would occur if the residues in both channels support a Grotthuss-type water column connected by c-ring rotation.

<u>Subunit-a mutations affect TD formation efficiency</u>

The percent of TDs observed per data set was fit to three Gaussian distributions with low (blue), medium (orange), and high (green) efficiencies as shown at pH 6.0 (**Figure 22C**), and at all pH values examined (**Figure 25**). These efficiency differences were proposed to result from elastic energy resulting from the 14° rotational mismatch between two of the three catalytic dwells and the c_{10}-ring that supplements or subtracts from the binding energy required for subunit-a to stop F_1-ATPase- driven rotation momentarily, resulting in a TD. If TDs result from H^+ translocation-dependent interactions between subunit-a and the c-ring, mutations that impact H^+ translocation should alter the TD formation efficiency.

Subunit-a mutations affected the percent of TDs formed per data set during power strokes in each of these efficiencies, which correlate to the three rotary positions of the central stalk relative to the peripheral stalk (Yanagisawa and Frasch, 2017; Sielaff *et al.*, 2019). The proportional differences of efficiencies of TD formation are shown relative to the average low efficiency for WT (**Figure 26**). Medium and high efficiency distributions of TDs in WT increased 1.5-fold and 2.2-fold, respectively, relative to low efficiency. The aN214L mutation increased the percent of TDs per data set for high, medium, and low efficiencies by 3-fold, 2-fold, and 1.2-fold, respectively, from the WT low efficiency. Mutations aQ252L and aE219L also increased TDs per data set for the high (2.7-fold and 2.5-fold) and medium (1.7-fold and 1.6-fold), but not the low efficiency distributions. Mutations aH245L and aE196L either did not increase the efficiency or slightly decreased the efficiency of the distributions of TD formation per data set.
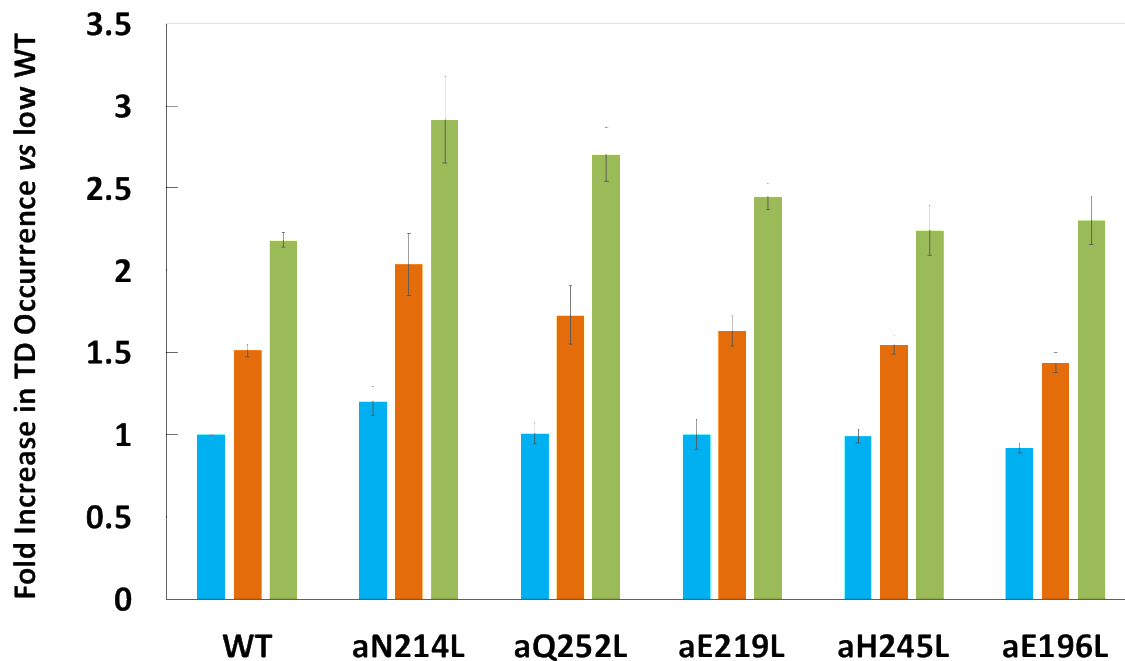
Figure 26. Proportion of low (blue bar), medium (orange bar), and high (green bar) transient dwell (TD) formation efficiencies relative to WT low efficiency TD formation. Each was the average of all pH values examined (**Figure 25**). All of the low, medium, and high efficiencies of TD formation are shown in **Figure 25** from which the averages were taken to calculate **Figure 26**. Vertical bars represent standard error.

<u>Synthase-direction steps rotate CW an average of ~11°</u>

The proportion of TDs with and without a synthase-direction step for WT and mutants are shown in **Figure 27A** at the pH values when the proportion of synthase-direction steps was minimum (black bars) and maximum (red bars), and at all pH values examined in **Figure 28**. The minimum proportion of synthase-direction steps was observed at pH 5.5 for WT and all mutants except aN214L that occurred at pH 6.0. Even at these low pH values, synthase-direction steps accounted for 62–68% of all TDs. In WT, a maximum of ~80% of TDs contained synthase-direction steps at pH 7.0, which was an increase of 13% from the minimum. These plots also show the distributions of the extent of CW rotation during a synthase-direction step, for which the 11° and 9° average and median values of CW rotation, respectively, were not changed significantly by the mutations (**Figure 27B**).

After subtracting the occurrence of the extent of synthase-direction step CW rotation at the pH when it was at a minimum (black bars) from that observed at other pH values (**Figure 28**) including that at its maximum (red bars), a Gaussian distribution of the increase in the extent of synthase-direction step CW rotation was observed (**Figure 27C**). During a synthase-direction step, the mean and standard deviations in the extent of CW rotation (**Figure 29**) was 12° ± 3° for WT, with little variation resulting from the mutations including: 11° ± 3° (aN214L), 11° ± 4° (aQ252L), 11° ± 3° (aH245L), 10° ± 3° (aE219L), and 11° ± 3° (aE196L). In all cases, the distributions were truncated with minimum CW rotational steps of 6°. At their maxima, the extents of CW c-ring rotation during synthase events rotated 25° and 36° about 1% and 0.1% of the time, respectively.
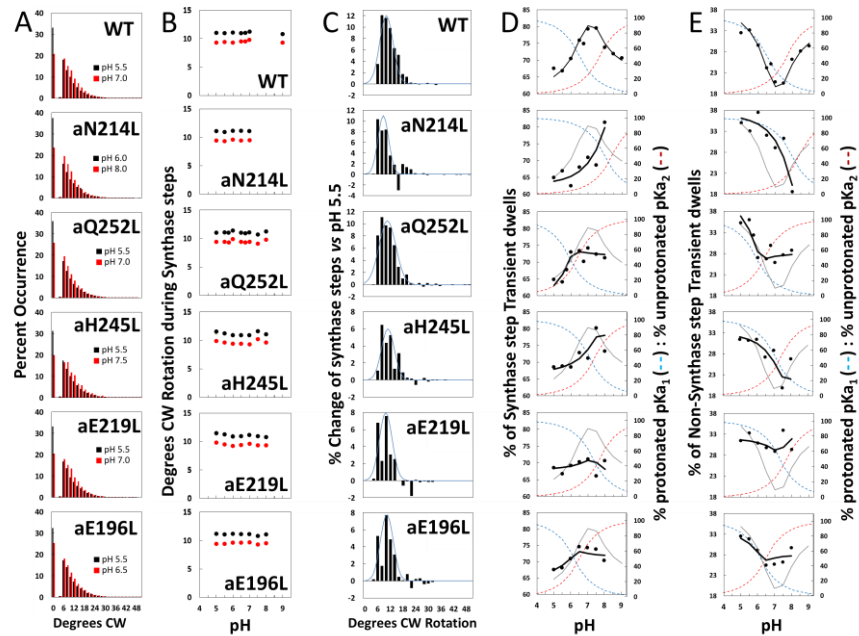
Figure 27. Effects of subunit-a mutations on the pH dependence of the extent of clockwise (CW) synthase-direction step rotation and fraction of transient dwells (TDs) containing synthase-direction steps. (A) Distributions of the extent of CW rotation in the ATP synthesis direction during transient dwells for WT and subunit-a mutants at the low (black) and high (red) pH values indicated. (B) Mean (black) and median (red) extents of CW rotation during a synthase-direction step versus pH. (C) Distributions of the difference in extent of CW synthase-direction step rotation between pH values in (A) when the percent of synthase-direction steps was maximum versus minimum where the blue line is the Gaussian fit. (D) Percent of TDs containing CW synthase-direction steps versus pH, where the data were fit to Equation 6 (black line). The fit for WT is shown as a gray line in the mutant plots. The fraction of protonated groups with pKa_1 (blue line), and unprotonated groups with pKa_2 (red line) versus pH was calculated from the pKa values of Table 2. (E) Percent of TDs that lack synthase-direction steps versus pH where the probability of forming a TD without a synthase-direction step (black line) was determined by Equation 5 from the fraction of protonated groups with pKa_1 (blue line), and unprotonated groups with pKa_2 (red line) versus pH calculated using pKa values from Table 2. The fit for WT is shown as a gray line in the mutant plots.

The extents of CW c-ring rotation during synthase events
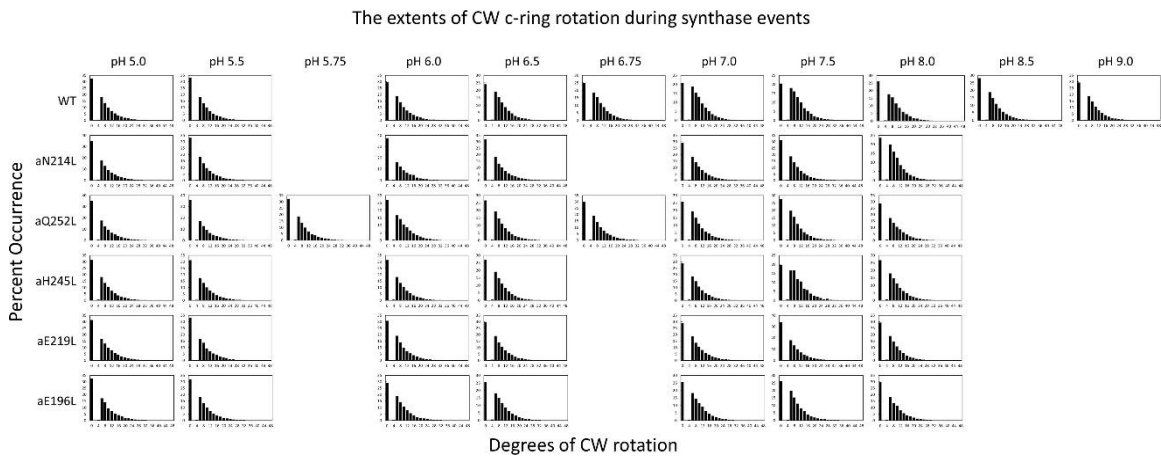
Figure 28. Distributions of the extent of clockwise (CW) rotation in the ATP synthesis direction during transient dwells for WT and subunit-a mutants versus pH.
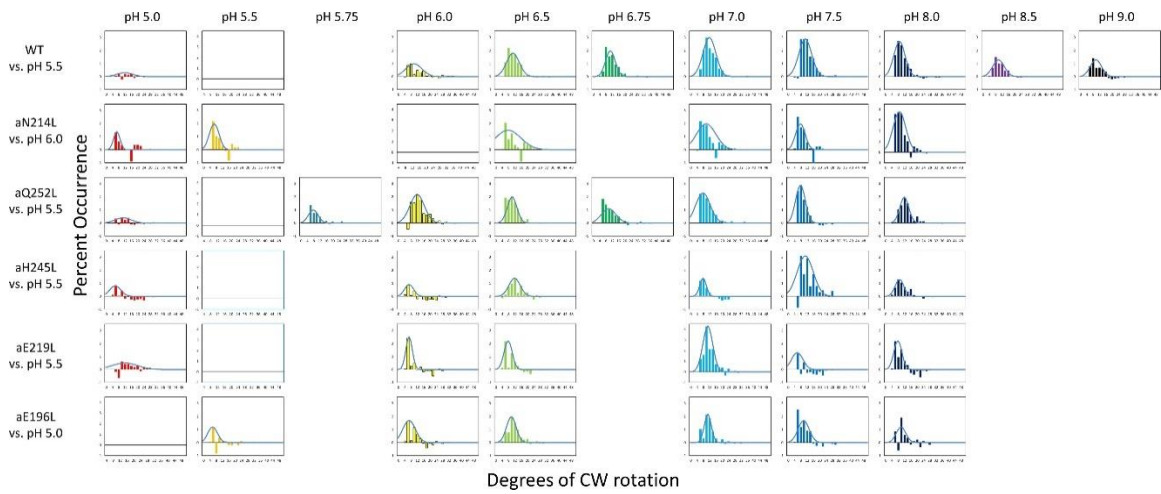
Figure 29. Distributions of the difference in extent of clockwise (CW) synthase-direction step rotation between pH values when the percent of synthase-direction steps was maximum versus minimum, where (—) is the Gaussian fit.

<u>Subunit-a mutations affect the proportion of TDs with synthase-direction steps</u>

We tested the hypothesis that synthase-direction steps result when both the input and output channels are in the correct protonation state to enable H^+ transfer to the carboxyl groups of the leading, and from the lagging c-subunits, respectively. If correct, the pH dependence of synthase-direction steps should follow the sum of the proportions of the protonated input and unprotonated output channels even when these pKa values change as the result of mutations. Alternatively, it was possible that the 11° rotations that we attribute to synthase-direction steps resulted instead from twisting of subunit-a and the c-ring as a single unit in response to the mismatch of the c-ring and catalytic dwell positions, which would not be subject to changes by subunit-a mutations.

The subset of TDs that forced the c-ring to rotate CW (synthase-direction steps) against the CCW force of F_1-ATPase rotation was pH dependent (**Figure 27D**). A maximum of 80% of TDs contained synthase-direction steps in WT at ~pH 7.3, and a minimum of 67% at pH 5.5. At pH values > 7.5, the proportion of synthase-direction steps decreased to 71% at pH 9.0.

Because a TD either contains (T_S) or lacks (T_N) a synthase-direction step, the pH dependence of TDs with a synthase-direction step (**Figure 27D**) was the inverse of that without a synthase-direction step (**Figure 27E**) per Equation 5.

$$T_S = 1 - T_N$$ Eq. 5

For WT, the minimum T_N of 20% at pH 7.5 increased 1.7-fold and 1.5-fold at pH 5.5 and at pH 9.0, respectively. At these extremes of low and high pH values, TD formation was dominated by groups where either pKa_1 is protonated or by unprotonated groups with pK_2. This conclusion is supported by the good fits of the pH dependencies of TDs without synthase-direction steps for WT and subunit-a mutants (**Figure 27E**) to Equation 6, where the probability of forming a TD without a synthase-direction step (T_N) is the sum of the probability (P_1) of the protonated group(s) with pKa_1 (X_1), and the probability (P_2) of unprotonated group(s) with pKa_2

(Y_2). Thus, these results support the conclusion that a TD without a synthase-direction step can result from a H$^+$ transfer event from the protonated group with pKa$_1$ or from a H$^+$ transfer event to the unprotonated group with pKa$_2$.

$$T_N = P_1(X_1) + P_2(Y_2)$$ Eq. 6

Fits of the pH dependence of TDs without synthase-direction steps from Equation 6 (black line) were based on the pKa values (**Figure 27E**), and probabilities summarized in Table 2. The WT data fit to probabilities of 38% and 33% for protonated groups (pKa$_1$ 6.5) and unprotonated groups (pKa$_2$ 7.7), respectively, such that the difference between the pKa values was 1.2 pH units. Consequently, T_N showed a minimum at ~pH 7.3, and maxima at high and low pH values when only the group(s) with either pKa$_1$ or pKa$_2$ were protonated and unprotonated, respectively.

As a result of the subunit-a mutations, P$_1$ values changed to a smaller extent (32–42%) than did P$_2$ values (5–35%). Except for aE219L, all mutations decreased P$_2$, including a >6-fold decrease with aN214L. The difference between pKa values observed with the mutants was from 0.3 to 0.5 pH units compared to the 1.2 pH unit difference of WT. Both pKa$_1$ and pKa$_2$ of aN214L increased by 1.5 and 0.7 pH units such that the minimum T_N of ~18% at pH 8.0 represented an increase of 0.7 pH units from that of WT. At pH 5.5, T_Ns comprised 38% of all TDs in aN214L. A similar but smaller shift of the minimum T_N occurrence to pH 7.5 was also observed for aH245L, which primarily resulted from an increase in pKa$_1$ by 0.8 pH units from WT. A striking effect of mutations aQ252L, aE219L, and aE196L was that they suppressed the pH dependence of synthase-direction step formation. Of these, aE219L was most suppressed where T_S varied between 66% and 71% of TDs over the pH range examined.

In all cases, the occurrence of synthase-direction steps reached a maximum at the crossover point between the fractions of protonated groups with pKa$_1$ and unprotonated groups with pKa$_2$. This is the point at which the largest fractions of both groups were in the correct

82

protonation state where H^+ transfer events could occur from the pKa_1 groups to the c-ring, and from the c-ring to the pKa_2 groups. These results eliminate the alternative hypothesis that synthase-direction steps result from the twisting of F_O relative to F_1 as the result of elastic energy from c_{10}-ring: catalytic dwell mismatches because the elastic energy resulting from the mismatch in rotary positions would not be affected by these mutations.

	pKa_1	P_1 (%)	pKa_2	P_2
WT	6.5	38	7.7	33
aN214L	8.0	37	8.4	5
aQ252L	5.9	42	6.4	28
aE219L	7.1	32	7.4	35
aH245L	7.3	33	7.7	22
aE196L	6.2	34	6.5	28

Table 2. pKa Values and Probabilities of Forming Transient Dwells (TDs) without Synthase-Direction Steps for WT and Subunit-a Mutants.

Discussion

The results presented here provide new insight into the mechanism by which the F_O motor uses the energy from H^+ translocation to generate CW rotational torque on the c-ring to catalyze ATP synthesis. These studies support the hypothesis that residues associated with the half-channels work together to support a water column that transfers protons across the membrane in a coherent manner coupled to c-ring rotation in lieu of transferring protons directly and independently. These single-molecule investigations also tested the hypothesis that c-rotation operates via a Brownian ratchet versus a power stroke mechanism, and the results provide the first direct evidence that synthase-direction steps can occur by both mechanisms. Finally, the results presented here show that the proton translocation-dependent synthase-direction rotation occurs in 11° steps. These results do not support the hypothesis that the function of the essential aR210 is to deprotonate cD61 because recent F_O structures show that the unprotonated lagging cD61 carboxyl is still 7.3 Å away from aR210 after an 11° c-ring rotation. Alternatively, an alternating two-step mechanism is proposed below to resolve this discrepancy.

F_O uses a Grotthuss mechanism to translocate protons through both half-channels

The results presented here support a Grotthuss mechanism in F_O where water columns in each half-channel communicate via rotation-dependent H^+ transfer to and from the leading and lagging c-ring cD61 carboxyls. The coherent behavior of the water columns enables the release of a H^+ to the cytoplasm concurrent with each H^+ that enters the subunit-a input channel from the periplasm. This conclusion is supported by observations that: (i) ATP synthase-direction steps were maximal in WT and mutants when the fractions of protonated groups and unprotonated groups with low and high pKa values, respectively, were optimal for H^+ transfer both from the lagging cD61 to the output channel and from the leading cD61 to the input channel; (ii) mutation of a residue from either the input or output channel altered both the low and high pKa values of TDs indicating that the channels communicate; (iii) all mutations changed the ability to form TDs,

indicating all the groups examined participate; and (iv) none of the mutations completely eliminated the ability to form TDs.

This conclusion is also consistent with the fact that participating residues aS199, aN214, and aQ252 are polar but not ionizable, and distances between channel residues that are too far apart for direct H^+ transfer but are positioned at distances able to support a water column. Although aQ252 is highly conserved (**Figure 30**), glycine or hydrophobic groups are naturally substituted: (i) for aN214 (*Toxoplasma gondii*, *Thermus thermophilus*); (ii) for aH245 (*Mycobacterium phlei*, *Tetrahymena thermophila*, *Acetobacter woodii*, *Toxoplasma gondii*, *Ilyobacter tartaricus*, *Fusobacterium nucleatum*, *Thermus thermophilus*); and (iii) for aE219 (*Tetrahymena thermophila*, *Euglena gracilis*, *Bacillus pseudofirmus* OF4, *Pichia angusta*, *Saccharomyces cerevisiae*, *Arthrospira platensis* PCC9438). Such mutations can be tolerated if the primary role of these groups was to support a water column that transferred protons.

A recent F_1F_O structure from bovine mitochondria was of sufficient resolution to observe density near the input channel residues consistent with Grotthuss-type water molecules in this half-channel (Spikes *et al.*, 2020). Unidentified electron densities near subunit-a input channel residues in F_1F_O structures from *E. coli* (Sobti *et al.*, 2020) and from *Polytomella* (Murphy *et al.*, 2019) also suggest the presence of bound waters. The observation of a water column in both half-channels of the V_O complex (Roh *et al.*, 2020) suggests that Grotthuss-based H^+ translocation is a commonly shared trait among the greater family of rotary ATPases.

Additional structural evidence that supports the existence of a Grotthuss H^+ translocation mechanism is the presence of an ~30 Å diameter funnel that is lined with carboxylate and imidazole residues as the funnel narrows (**Figure 31**). The aE219-carboxyl examined here, which we propose to be the start of the Grotthuss column is positioned at the apex of this funnel. A Grotthuss mechanism was first proposed to explain extremely high rates of F_O-dependent H^+ translocation across R. capsulatus membranes (Feniouk *et al.*, 2004). The rates were so fast that an ~40 Å diameter Coulomb cage of charged and polar groups was proposed to be required to serve as a H^+ 'antenna' to increase the delivery rate of protons from the aqueous solution to the

entrance of the input channel water column (Wraight, 2006). The results presented here indicate that multiple residues contribute to the pKa values that enable synthase-direction steps. The funnel extends the input channel from the residues investigated here that are located near the middle of the membrane to the periplasm, which provides the ultimate supply of protons to the c-ring. The charged and polar residues in the funnel are likely to contribute to the pKa value, and may also facilitate the protonation of the input channel relative to the output channel even though both half-channels are exposed to the same buffer as the result of the lipid bilayer nanodiscs employed. More work is necessary to address this issue.
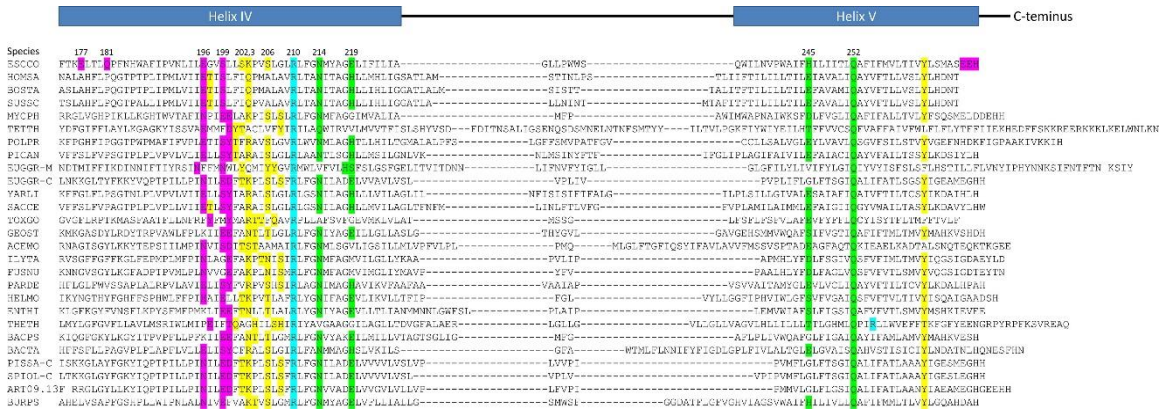
Figure 30. Sequence comparisons of the subunit-a helices that contact the c-ring. Sequences were aligned relative to essential Escherichia coli residues aR210 (blue) in the penultimate helix (helix IV), and with highly conserved aQ252 in the ultimate helix (helix V). Residues associated with the input channel (green), the output channel (pink), and the vestibule (yellow). Sequences are from the following species with their names indicated on the left: ESCCO, Escherichia coli; HOMSA, Homo sapiens; BOSTA, Bos taurus; SUSSC, Sus scrofa; MYCPH, Mycobacterium phlei; TETTH, Tetrahymena thermophila mitochondrial; POLPR, Polytomella sp. Pringsheim 198.80 mitochondrial; PICAN, Pichia angusta mitochondrial; EUGGR-M, Euglena gracilis mitochondrial; EUGGR-C, Euglena gracilis chloroplast; YARLI, Yarrowia lipolytica mitochondrial; SACCE, Saccharomyces cerevisiae mitochondrial; TOXGO, Toxoplasma gondii; GEOST, Geobacillus stearothermophilus; ACEWO, Acetobacterium woodii (Na+); ILYTA, Ilyobacter tartaricus (Na+); FUSNU, Fusobacterium nucleatum; PARDE, Paracoccus denitrificans; HELMO, Heliobacter modesticaldum unicellular photosynthetic; ENTHI, Enterococcus hirae (V/A-type Na+); THETH, Thermus thermophilus (V/A-type); BACPS, Bacillus pseudofirmus OF4 (Alkalihalobacillus pseudofirmus); BACTA, Bacillus sp. Strain TA2.A1 (thermoalkalophilic); PISSA-C, Pisum sativum chloroplast; SPIOL-C, Spinacia oleracea chloroplast, ART09.13F, Arthrospira sp. 09.13 F; BURPS, Burkholderia pseudomallei.

88
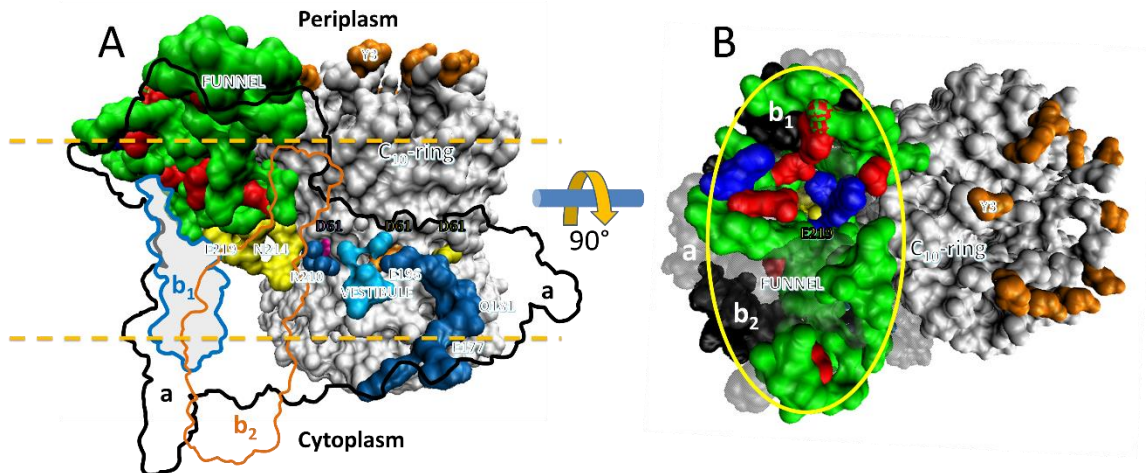
Figure 31. Aqueous funnel of charged and polar groups can serve as an antenna to supply protons to the input channel. (A) Transmembrane view of Escherichia coli F_O (pdb-ID 6OQR) showing the path of charged and polar residues across the membrane. Outlines indicate space occupied by hydrophobic residues in subunit-a (black line), subunit-b1 (blue line), and subunit-b2 (orange line). The inner surface of the funnel, which is lined with polar residues and loop regions (green), acidic groups (red), and histidines (blue) from subunit-a and the subunit-b1 N-terminus, is exposed to the periplasm at its wide end that narrows to aE219 (yellow) at the bottom. The input channel (yellow) extends from aE219 to aN214 and aQ252, which are proximal to aR210. Between aR210 and the output channel (dark blue) the leading (pink) and lagging (orange) cD61 groups rotate through a vestibule lined above and below the cD61 rotation plane by polar sidechains (light blue) that decrease the dielectric constant of the vestibule from that of the lipid bilayer. A protonated cD61 exposed to the lipid bilayer (yellow) is also visible. (B) Periplasmic surface of F_O showing the interior surface of the funnel (orange oval) lined with charged and polar groups from subunit-a and subunit-b1 as in A that narrows to aE219 (yellow) at the bottom where the input channel begins. Hydrophobic residues are shown of subunit-a (gray), subunits-b1 and -b2 (black), and the c-ring (white). The cY3 sidechains (orange) are shown to indicate the orientation of the periplasmic surface of the c-ring.

<u>F_O undergoes H^+ translocation-dependent 11° c-ring synthase-direction rotation steps</u>

The extent of rotation during ATP synthase-direction steps was unexpectedly found to rotate CW by 11° in the WT and all mutants. Evidence presented here supports the conclusion that synthase-direction steps result from protonation of the leading cD61 from the input channel and from deprotonation of the lagging cD61 to the output channel to rotate the c-ring relative to subunit-a. These results include that: (i) synthase-direction steps depend on a group of residues with a low pKa that must be protonated, and a second group with a high pKa that must be unprotonated; (ii) formation of synthase-direction steps reached a maximum at the pH when the fractions of protonated groups with the low pKa and unprotonated groups with the high pKa were optimal; and (iii) mutating subunit-a residues in either the input or output half-channels altered both high and low pKa values, and altered the extent and pH dependence of synthase-direction step formation. The effects of the subunit-a mutants on the synthase-direction steps rule out the possibility that these steps result from twisting the entire F_O relative to F_1.

During a CCW F_1-ATPase power stroke, TDs occur every 36°, which is equivalent to an interaction between subunit-a and each successive c-subunit in the *E. coli* c_{10}-ring. Since synthase-direction steps rotate by 11°, rotation by an additional 25° is required to advance the c-ring by one full c-subunit, which we observed in only 0.1% of the synthase-direction steps. Rotational sub-state structures (pdb-IDs 6OQR and 6OQS) of *E. coli* F_1F_O that differ by a 25° rotation of the c-ring relative to subunit-a were obtained by cryo-EM (Sobti *et al.*, 2020). Since advancing the c-ring by one c-subunit involves rotation by 36°, the difference between these sub-state structures also reveals information relevant to the 11° sub-step reported here.

The *E. coli* F_1F_O rotational sub-state structures that differ by the 25° rotation of the c-ring relative to subunit-a were obtained when the complex was inhibited by ADP (Sobti *et al.*, 2020). Similar 11° and 25° rotational sub-states have also been observed with ADP-inhibited F_1F_O from *B. taurus* (Zhou *et al.*, 2015) and from *M. smegmatis* (Guo *et al.*, 2021). In *M. smegmatis* F_1F_O, the binding of Bedaquiline stabilizes a rotational sub-state that is either 25° CW or 8° CCW from the equivalent rotational state in the absence of the drug (Guo *et al.*, 2021). The rotational

position of the c-ring in the cryo-EM structure of *S. cerevisiae* F_1F_O is also changed by ~9° when the inhibitor oligomycin is bound to F_O (Srivastava *et al.*, 2018).

Several structural features of *E. coli* F_O (Sobti *et al.*, 2020) are relevant to its ability to undergo synthase-direction steps, and in combination with the results presented here, they provide insight into the mechanism of sustained CW rotation to power ATP synthesis. A transmembrane view of subunit-a (**Figure 31**) shows that aE196, aS199, aR201, aN214, and aQ252 are aligned along the plane of cD61 rotation. This plane is surrounded by hydrophobic residues that form a vestibule. Between aS199 and aR210, polar groups line the vestibule above (aS202 and aS206) and below (aK203 and aY263) the cD61 rotation plane. Although these polar groups do not directly participate in H^+ translocation (Eya *et al.*, 1991), they enable water to access the vestibule (Angevine and Fillingame, 2003; Angevine *et al.*, 2003) to make it less hydrophobic than the lipid phase of the membrane. Residues that provide a possible path for the output channel from aE196 to the cytoplasm include aQ181, aE177, and the subunit-a C-terminal carboxyl, which span this distance at ~4 Å intervals (Sobti *et al.*, 2020), consistent with that needed to stabilize a Grotthuss water channel. More work is required to characterize this channel, especially since aE196 and aS199 are the only output channel residues conserved among other species (**Figure 30**).

A mechanism where F_O uses alternating 11° (**Figure 32A,B**) and 25° (**Figure 32B,C**) sub-steps to power c-ring rotation that drives ATP synthesis is consistent with the data presented here, and with *E. coli* F_1F_O structures 6OQR and 6OQS (Sobti *et al.*, 2020). In 6OQS (**Figure 32A**), the lagging cD61 (orange) is 3.5 Å from aS199, which enables H^+ transfer to aS199 and aE196 via bound water. The leading cD61 (pink) is 3.8 Å from the aR210-guanidinium, consistent with intervening water. This cD61 is also proximal to aN214 and aQ252, which positions it for protonation from the input channel via bound water. In our model, the pH-dependent 11° sub-step (**Figure 32A**) occurs upon H^+ transfer from water bound to aN214 and aQ252 to the leading cD61, and H^+ transfer from the lagging cD61 to aS199 and aE196.

The low, medium, and high efficiencies of TD formation reported here (**Figure 22C**) were attributed to torsional strain resulting from the asymmetry between 36° c_{10}-ring stepping, and the 120° F_1 power strokes (Yanagisawa and Frasch, 2017; Sielaff *et al.*, 2019). Based on this asymmetry observed in ADP-inhibited F_1F_O structures (Sobti *et al.*, 2016), high efficiency TD formation was proposed to occur (Sielaff *et al.*, 2019) in the rotary state comparable to that in which rotary sub-state structures PDB-IDs 6OQR and 6OQS were subsequently observed at 3.1 Å resolution (Sobti *et al.*, 2020). Sobti *et al.*, 2020, concurred that torsional strain contributed to their ability to resolve the 6OQR and 6OQS sub-state structures. However, in results presented here, catalytically active F_1F_O in lipid bilayer nanodiscs show successive 11° ATP synthase-direction steps every 36° including at the rotary position of the ATPase power stroke where ADP inhibits rotation (**Figure 22A**, dashed line). Because ATP synthase-direction steps can also occur with low efficiency when torsional strain decreases the probability of forming a synthase-direction step, it is clear that torsional strain is not the primary contributing factor to the ability of F_O to undergo 11° ATP synthase-direction steps.

After the 11° sub-step (**Figure 32B**), the distance of the now unprotonated lagging cD61 to the aR210-guanidinium decreased from ~11.5 to ~7.5 Å. These distances are inconsistent with the long-held belief that the role of aR210 is to displace the proton from the lagging cD61. Instead, we postulate that the electrostatic attraction between the negatively charged lagging cD61 and aR210 is sufficient to induce the 25° sub-step. As the result of this sub-step, the distance between these groups decreases from 7.5 to 3.8 Å (**Figure 32C**). As the 11° sub-step repeats, the subsequent loss of negative charge when the lagging cD61 is protonated by aN214 and aQ252 then allows this c-subunit to rotate away from aR210 into the lipid bilayer.
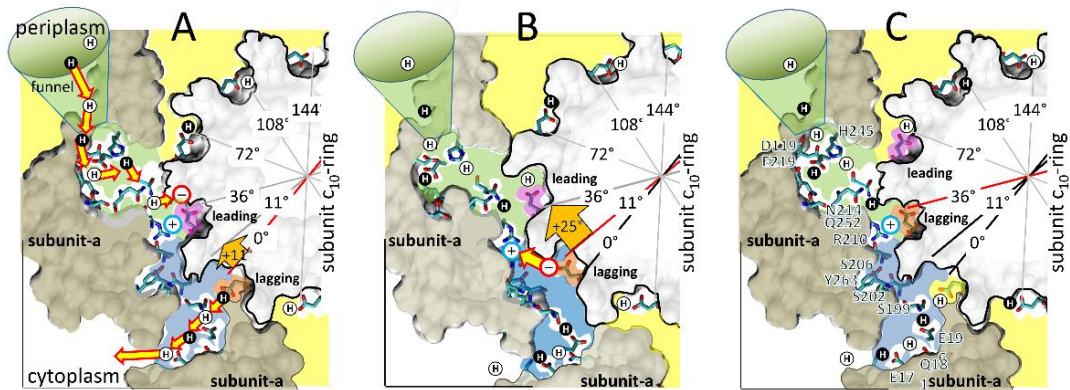
Figure 32. Alternating 11° and 25° sub-steps that power F_O c-ring ATP synthase-direction rotation. (A) The pH-dependent 11° sub-step occurs when H+ transfer from aN214/aQ25-bound water to the unprotonated leading cD61-carboxyl (pink), and from the protonated lagging cD61-carboxyl (orange) to aS199/aE196-bound water. Upon displacement from aR210 by protonation, leading cD61 adopts the closed conformation to enable rotation into the lipid bilayer (yellow). Due to coherent H+ movement in the Grotthuss column, each H+ entering the input channel (green) from the funnel causes a H+ to exit the output channel (blue) to the cytoplasm. Rotation occurs when lagging cD61 is deprotonated because the negatively charged carboxyl moves in response to the decrease in hydrophobicity from the lipid bilayer to the water-containing vestibule (blue), and from the electrostatic attraction to aR210. This decreases the distance between the lagging cD61 carboxyl and the aR210-guanidinium from ~11.5 to ~7.5 Å. (B) The 25° sub-step occurs primarily from the electrostatic interaction between the lagging cD61 carboxy (orange) and the aR210-guanidinium. (C) Electrostatic attraction decreases the distance between orange cD61 and aR210 from ~7.5 to ~3.5 Å to complete a 36° stepwise c-ring rotation, which positions the orange cD61 to become the leading carboxyl for the next pH-dependent 11° sub-step. Escherichia coli F_1F_O cryo-EM structures of rotary sub-states pdb-IDs 5OQS (A and C), and 5OQR (B) are shown as cross-sections of F_O with hydrophobic resides of subunit-a (brown) and the c-ring (gray) along the plane defined by cD61 groups as viewed from the periplasm. Protons are alternately colored black and white to show the progression of proton transfer events.

93

The probability that a TD occurs may appear to be stochastic. However, its occurrence depends on the kinetics and the energetics of the system. Slowing the angular velocity of the F_1 ATPase-driven power stroke increases TD occurrence at pH 8.0 (shown here to be suboptimal) indicating that the ability to form a TD depends on the rate that an interaction can form between subunit-a and each c-subunit relative to the angular velocity of F_1-ATPase- driven rotation (Ishmukhametov *et al.*, 2010).

Evidence supports the hypothesis that the energy for F_1-ATPase power strokes is derived from ATP binding-dependent closure of the β-subunit lever domain upon subunit-γ, which is initiated at ~36° after the catalytic dwell in *E. coli* F_1 (Martin *et al.*, 2014). Based on the K_D of ATP at 36° measured in *Geobacillus stearothermophilus* F_1, the energy available for the power stroke from ATP binding is ~13.5 k_BT (Adachi *et al.*, 2012).

The results here suggest that the energy required to power the 11° synthase-direction step is close to that of the F_1-ATPase power stroke including: (i) that some synthase-direction steps oscillate consistent with a Brownian ratchet, especially those steps that occur late in the F_1 power stroke when the affinity for ATP is the highest; and (ii) that TD formation efficiency is increased or decreased (high and low efficiencies) by the 0.4 k_BT of torsional energy from the ±14° rotary mismatch between F_1 and F_O calculated from Equation 7, where θ is the rotational displacement in radians using the spring constant, κ, of 12.6 k_BT radian–2 measured for *E. coli* F_1F_O (Sielaff *et al.*, 2008).

$$U = 0.5\kappa\theta^2 \qquad\qquad \text{Eq. 7}$$

Consequently, the F_O motor must have at least 13.5 k_BT available to cause a TD. Possible sources of energy for TDs in addition to the 0.4 k_BT of torsional energy include: (i) as much as 4.4 k_BT from the difference of pKa values between the input and output channels; (ii) 5.9 k_BT from the exclusion of the lagging charged cD61 carboxyl from the lipid bilayer into the aqueous vestibule, based on its measured desolvation energy (White and Wimley, 1999). The

energy penalty of 0.8 k_BT to insert the leading protonated cD61 carboxyl into the lipid bilayer is avoided by its conversion to the closed and locked position in the c-ring (Pogoryelov *et al.*, 2010); and (iii) as much as 38.1 k_BT from the electrostatic attraction of aR210 to unprotonated lagging cD61 at a distance of 11.5 Å when it is exposed directly to the lipid bilayer. The energy of this attractive force, which is highly dependent on the hydrophobicity of its environment, is calculated by the modified Coulomb Equation (Equation 7), where q_i and q_j are elementary charges, r_{ij} is the interatomic distance (in Ångstroms), and e is the dielectric constant, which is a measure of the hydrophobicity of the environment that ranges from 2 (lipid bilayer) to 80 (aqueous solvent). Although we do not yet know how wet the vestibule is, a dielectric constant of 13 and an 11.5 Å aR210-cD61 distance results in 3.8 k_BT, which when summed with the other energy sources totals 14.1 k_BT without input of torsional energy. Since F_1-ATPase rotation from the catalytic dwell to the point that ATP binds is powered by no more than 4 k_BT (Martin *et al.*, 2018), this explains why synthase-direction rotation at these rotational positions typically has power stroke characteristics.

$$U = \frac{1}{e}\left(\frac{q_i q_j}{r_{ij}}\right) 561 \; \kappa_B T \qquad\qquad\qquad \text{Eq. 7}$$

After the 25° rotation step when the unprotonated cD61-aR210 distance is 3.8 Å, the electrostatic force is 11.4 k_BT or 73.8 k_BT when the dielectric constant is 13 or 2, respectively. Thus, the electrostatic interaction in a hydrophobic environment would be far too strong for any rotation to occur. More work is required to quantify the energetics of these sub-steps in the ATP synthesis mechanism because, when understood in combination with the steady-state pmf values and the dissociation constants of ATP, ADP, and P_i versus rotary position, these energy contributions will determine the non-equilibrium ATP/ADP•P_i concentration ratio that can be maintained by F_1F_O at steady-state *in vivo*.

Chapter 4

EFFECTS OF F_O SUBUNIT C-RING MODIFICATION ON THE *E. coli* F_OF_1 ATP SYNTHASE

FUNCTION

Abstract

The stoichiometry of subunit-c in the proton-carrying c-ring of the F_OF_1 ATP synthase varies between species, but the bioenergetic consequences of c-ring size evolution are not well understood. Nine chimeric F_OF_1 were expressed in *E. coli* with the intent to modify c-ring stoichiometry using subunit-c protein sequence derived from various species that contain c_8 to c_{17}-ring, except for c_{16}-ring. Western blot, negative stain TEM, and cryo-EM results showed that changing the subunit-c sequence allowed the expression and full assembly of the enzyme complex. Overall, F_OF_1 with smaller anticipated c-ring size showed higher ATP synthesis rate, higher ATP hydrolysis rate, and higher coupling between the c-ring and subunit-a interface. The overall ATP synthase rate decreased with increasing anticipated c-ring size, with ATP synthase rates of small c-rings ($c_8 - c_{11}$) increasing significantly with a combination of ΔpH and $\Delta \psi$ compared to the rate driven by ΔpH alone. The c_{12} and c_{15}-ring chimeras that result in symmetrical rotational steps between the F_O and F_1 resulted in lower ATP synthesis activities, suggesting that asymmetry between the F_OF_1 motors contribute to the mechanism that generates torque to drive ATP synthesis. The differences between the growth rates of the chimeric cells in succinate medium was minimal despite the differences in ATP synthesis activities between the chimeric F_OF_1, suggesting compensatory mechanisms by the *E. coli* cells that allow them to overcome the loss of F_OF_1 function. The c_{17} chimera consistently showed poor enzymatic activities and poor growth in succinate medium. The very low coupling between the c-ring and subunit-a shown in this chimera suggests that c_{17}-ring is too large for the *E. coli* F_OF_1.

Introduction

The F_OF_1 ATP synthase is an enzyme that exists in virtually all organisms on Earth because of its vital role in the synthesis of ATP through oxidative phosphorylation. The F_OF_1 is found in the inner membrane of mitochondria, thylakoid membrane of chloroplast, and in the cell membrane in eubacteria, where it generates ATP by utilizing the proton gradient across the membrane generated by the electron transport chain (Kühlbrandt, 2019).

This enzyme complex is composed of two opposing molecular motors, which are the membrane-bound F_O motor and the extrinsic F_1 motor. These two motors are connected by a central rotor and a peripheral stalk, which enables the rotation of one motor to be transferred to the other. The F_O motor is responsible for generating the torque to turn the central rotor during ATP synthesis. The F_O contains subunit-a that functions as a stator to the subunit-c ring and facilitates the flow of protons across the membrane by its two proton half-channels that are exposed to either side of the membrane. These proton half-channels are not directly connected to each other, but are each connected to the subunit-c ring, which rotates as the individual c-subunits in the ring accepts a proton from the proton input half-channel and donates a proton to the proton output half-channel (Yanagisawa *et al.,* 2021).

The rotation of the F_O c-ring driven by the flow of protons is transferred to the central rotor, which forces conformational changes in the F_1 motor attached to the other side of the central rotor. The F_1 contains the $(αβ)_3$-ring composed of three subunit-α and -β heterodimers, each containing a catalytic site where ATP is synthesized. Each αβ heterodimer binds ADP and inorganic phosphate (P_i), synthesizes ATP, and releases ATP as the central rotor rotates 360°, and the three αβ heterodimers carry out these steps in an alternating fashion relative to each other. Due to the alternating catalysis carried out by each αβ heterodimer, the three sites are at different catalytic steps of ATP synthesis at any given moment. Therefore, one ATP molecule is produced every time the central rotor rotates 120°. The $(αβ)_3$-ring in the F_1 motor is conserved in all known species, implying that three ATP molecules are produced for every 360° rotation of the central rotor in all known species (Kühlbrandt, 2019).

When the F_OF_1 synthesizes ATP from ADP and P_i, it increases the [ATP] relative to [ADP] and [P_i] against the chemical equilibrium, and this disequilibrium powers the cellular functions that require ATP hydrolysis. This chemical equilibrium is described by Gibbs free energy of ATP synthesis (Equation 8) (Rosing *et al.*, 1972). However, the F_OF_1 can also hydrolyze ATP into ADP and P_i and pump the protons in the opposite direction when the [ATP] to [ADP][P_i] ratio is overwhelmingly large. This process is used by bacterial F_OF_1 to hydrolyze ATP and pump protons into the periplasm to maintain the necessary PMF during fermentation (Kühlbrandt, 2019).

$$\Delta G = \Delta G^\circ + RT \, \ln\left(\frac{[\text{ATP}]}{[\text{ADP}][\text{P}_i]}\right)$$
Eq. 8

The number of $\alpha\beta$ heterodimers in the F_1 motor is conserved among different species, but the number of c-subunits that comprise the c-ring in the F_O motor varies among species. The known sizes of the c-ring ranges from the c_8-ring of mammalian F_O (Collinson, *et al.*, 1996; Watt, *et al.*, 2010) to c_{17}-ring of *Burkholderia pseudomallei* (Schulz *et al.*, 2017). This means that the number of protons required for the c-ring to complete the 360° rotation varies among species. For example, the mammalian mitochondrial c_8-ring requires eight protons to rotate 360° (He *et al.*, 2018), but the c_{14}-ring found in the chloroplast ATP synthase in land plants requires 14 protons to make the same rotation (Vollmar *et al.*, 2009). The only c-ring stoichiometry between c_8 and c_{17} ring that has not been discovered to date is the c_{16} ring (assuming it exists). In mitochondria, a shift from c_{10} in the ancestral eukaryote to c_8 in the ancestral metazoan occurred, while chloroplasts underwent a shift from c_{10} to c_{14}. Although subunit-a is highly conserved, substantial variation now exists in the other subunits that comprise the peripheral stalk that connect the F_o and F_1 stator.

The number of c-subunits in the c-ring is determined by the protein sequence of subunit-c. It is thought that the alanine motif (AxAxA) at amino acid sequence positions 13, 19, 23 (Bovine positions) located at the N-terminus (inner helix) of subunit-c determines the size of the c-ring. These alanine residues are highly conserved in the animal phyla, in which most, if not all species

of F_OF_1 contains a c_8 ring. Other eukaryotes and bacteria that contain a larger c-ring have residues with a larger hydrophobic side chain such as Leu, Ile, Val, or Phe at these positions (Watt *et al.*, 2010).

It has also been proposed that the membrane protein-packing motif of repetitive glycine residues (xGxGxGxG) located near the alanine motif also contributes to the size of the c-ring. In this motif, Gly has a small sidechain and 'x' has a larger hydrophobic (Val, Iso, Phe) or a polar (Asn) sidechain, which closely packs the inner helices of the c-ring and makes the ring smaller (Vonck *et al.*, 2002). Mutating the Gly in this motif into Ala in *Ilyobacter tartaricus* have been shown to change the wild type c_{11}-ring into $c_{<11}$, c_{12}, c_{13}, c_{14}, and $c_{>14}$ rings (Pogoryelov *et al.*, 2012). Additionally, this glycine motif is replaced by alanine residues (AxAxAxA) in alkaliphilic *Bacillus* species that express a c_{13}-ring. Mutating the alanine into glycine residues in *Bacillus pseudofirmus* OF4 have been shown to change a portion of WT c_{13} ring to c_{12} (Preiss *et al.*, 2013).

The consequences of altering the F_O c-ring size in the remains elusive, as changing the c-ring stoichiometry in tobacco chloroplast F_OF_1 from a c_{14} to c_{15} has been shown to lower the expression level of the enzyme, but had no effect on growth and photosynthetic electron transport. However, it was shown that membrane potential was increased in the c_{15} mutant to ensure higher proton flux without unwanted low pH-induced feedback inhibition of the electron transport (Yamamoto *et al.*, 2023).

Because the number of c-subunits in the F_O c-ring can vary among different species while F_1 always synthesizes three ATP molecules from a complete 360° rotation, this implies that the H^+/ATP ratio is different for various species, which impacts the energetic output efficiency of the ATP synthase. The H^+/ATP ratio in F_OF_1 containing a c_8-ring and a c_{17}-ring would be 2.67 (8 H^+/3 ATP) and 5.67 (17 H^+/3 ATP), respectively, which differ by more than two-fold. The c_8-ring in mitochondria may be the most energy efficient and the c_8-ring may be the smallest possible size because of physical constraints (Kühlbrandt, 2019).

In addition to the H$^+$/ATP ratio, changes in the c-ring stoichiometry also implies an energetic cost difference in protein complex assembly. Why and how ATP synthase diversified to a wide range of energy efficiency is not well understood. It is not clear whether the diversification of the c-ring size was due to natural selection that favors a certain H$^+$/ATP ratio depending on the energy requirement of the organisms, or if selection did not play a role in the evolution of the c-ring diversity at all. Some suggest that increases in molecular complexity can result from constructive neutral evolution (CNE) with inconsequential or no change in physiological function because the cost of expanding the number of subunits in a protein complex is insignificant and does not influence natural selection (Stoltzfus, 1999).

The flow of protons that drives the rotation of the c-ring is derived from the proton motive force (PMF), which is composed of difference in pH across the membrane (ΔpH) and the membrane potential (Δψ) (Equation 8). Both ΔpH and Δψ depend on the proton gradient across the membrane and are thought to be thermodynamically equivalent. In mitochondria, the ΔpH across the inner membrane is <1, generating less than -60 mV of PMF, while the Δψ is approximately -150 mV, making the total PMF approximately -210 mV (Mitchell, 2011). Proteobacteria also generates more Δψ than ΔpH, with *E. coli* generating -135 mV Δψ and -35 mV ΔpH, making the total PMF -170 mV (Cheuk and Meier, 2021). However, in chloroplasts, the ΔpH is greater than the Δψ, with ΔpH of 2.5 (-150 mV) generated under intense light condition and Δψ of -30 mV, making the total PMF approximately -180 mV (Junesch and Gräber, 1991; Cruz *et al.*, 2001). Cyanobacteria has ΔpH and Δψ that are more equal, with *Synechococcus PCC7942* generating ΔpH of -100 mV and Δψ of -90 mV, making the total PMF -190 mV (Ritchie, 1991).

PMF (or μ_{H^+}) = Δψ – 60 · ΔpH (in units of mV)   Eq. 8

We have now constructed nine chimeras of the *E. coli* F$_O$F$_1$ ATP synthase in which the subunit-c sequence has been modified with the intent of changing the size of the c-ring. Modifying

only the subunit-c ring while maintaining the rest of the F_OF_1 as WT allowed for an apples-to-apples comparison of the different species of subunit-c on the performance of *E. coli* cells and of the F-ATP synthase. Here, we present the initial characterization of the impact of changing the c-ring stoichiometry on the function of the F_OF_1 ATP synthase in *E. coli*. This work provides the first direct comparison of the consequences of evolutionary divergence of the F_OF_1 ATP synthase.

Results

Nine chimeric F_OF_1 were expressed in *E. coli* cells, in which the inner helix of subunit-c that is thought to determine the c-ring size was derived from the subunit-c protein sequences of the species that express different c-ring sizes, while the sequence from the looped region to the outer helix that interacts with subunit-a was unaltered from WT *E. coli* sequence. The species of subunit-c sequences selected were *Bos Taurus* c_8, *Mycobacterium smegmatis* c_9, *Saccharomyces cerevisiae* c_{10}, *Fusobacterium nucleatum* c_{11}, *Paracoccus denitrificans* (strain Pd 1222) c_{12}, *Synechococcus elongatus* (strain PCC 7942 / FACHB-805) (aka *Anacystis nidulans* R2) c_{13}, *Spinacia oleracea* c_{14}, *Spirulina platensis* (aka *Arthrospira platensis*) c_{15}, and *Burkholderia pseudomallei* c_{17}. The *E. coli* strains generated using these sequences were designated as Bt-c8, Ms-c9, Sc-c10, Fn-c11, Pd-c12, Se-c13, So-c14, Sp-c15, and Bp-c17.

Comparisons of chimeric F_OF_1 expression levels in *E. coli*

To assess if the genetic modification to the subunit-c gene affected the expression level and the assembly of the ATP synthase in *E. coli*, a Western blot was made using an antibody against F_1 subunit-β to quantitate the amount of assembled F_OF_1 in cell membranes from the nine chimeric strains compared to that of the WT (**Figure 33**). The F_1 motor is a water-soluble portion of the enzyme that would only be anchored to the cell membrane if it is assembled with the transmembrane F_O motor. Because the primary antibody used for Western blot targeted the F_1, the results showed that altering the subunit-c inner helix still allowed the central rotor to dock to the subunit-c ring, connecting the F_1 to the F_O. These results showed that all nine F_OF_1 chimeras were expressed and assembled into the full enzyme complex.
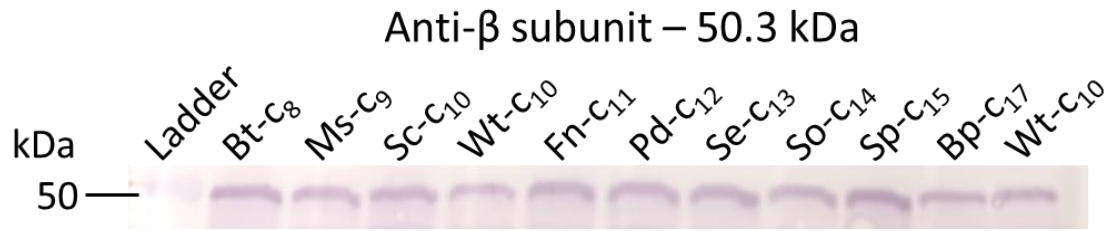
Figure 33. Western blot of the cell membrane from the nine chimeric *E. coli* strains using anti-

subunit-β primary antibody. The results showed the predicted 50.3 kDa band from all nine strains

of *E. coli*, indicating that chimeric F_OF_1 fully assembled in each strain.

Chimeric F_OF_1 was purified from Bt-c8, So-c14, and Sp-c15 cells by detergent solubilization, Ni-NTA affinity chromatography, and gel filtration chromatography. The purified F_OF_1 samples were imaged by negative-stain TEM, which showed fully assembled enzyme complexes (**Figure 34**). The purified F_OF_1 from Sp-c15 chimera was also imaged by cryo-EM, from which a reconstruction of the protein structure at approximately 7.6 Å resolution was generated from 2D class averages of approximately 36,000 particles (**Figure 35**). Although the resolution was not high enough to resolve the individual c-subunits, the electron density of the F_O motor suggested that the c-ring size has changed.
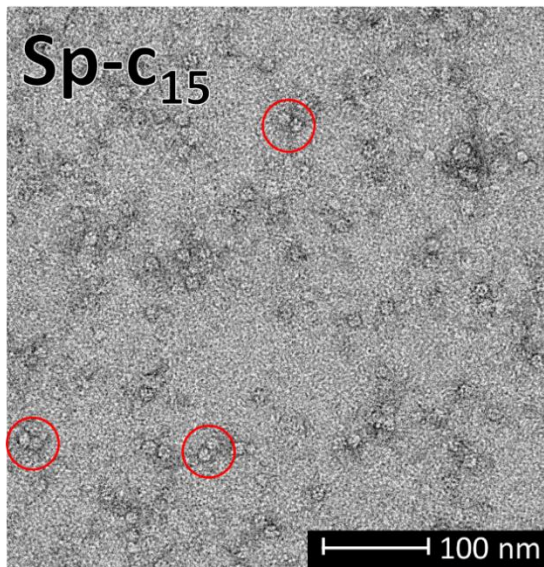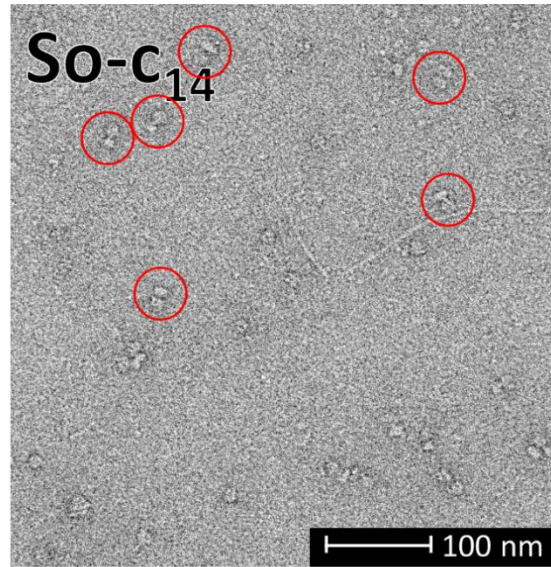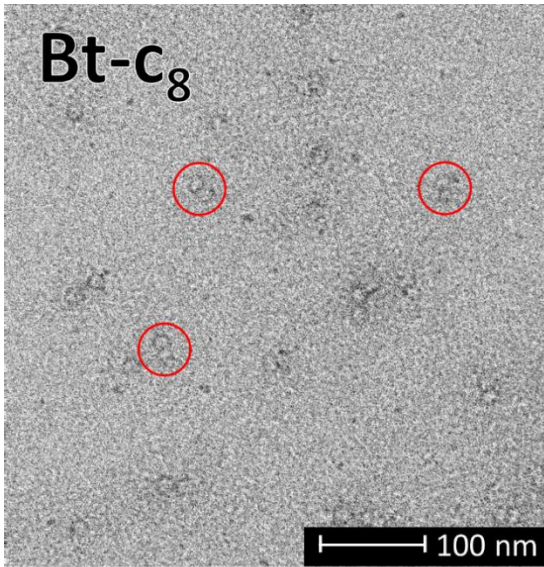
Figure 34. Negative-stained TEM images of F_OF_1 chimera purified from Bt-c8, So-c14, and Sp-c15. All chimeric ATP synthase samples showed fully assembled F_OF_1 complex.
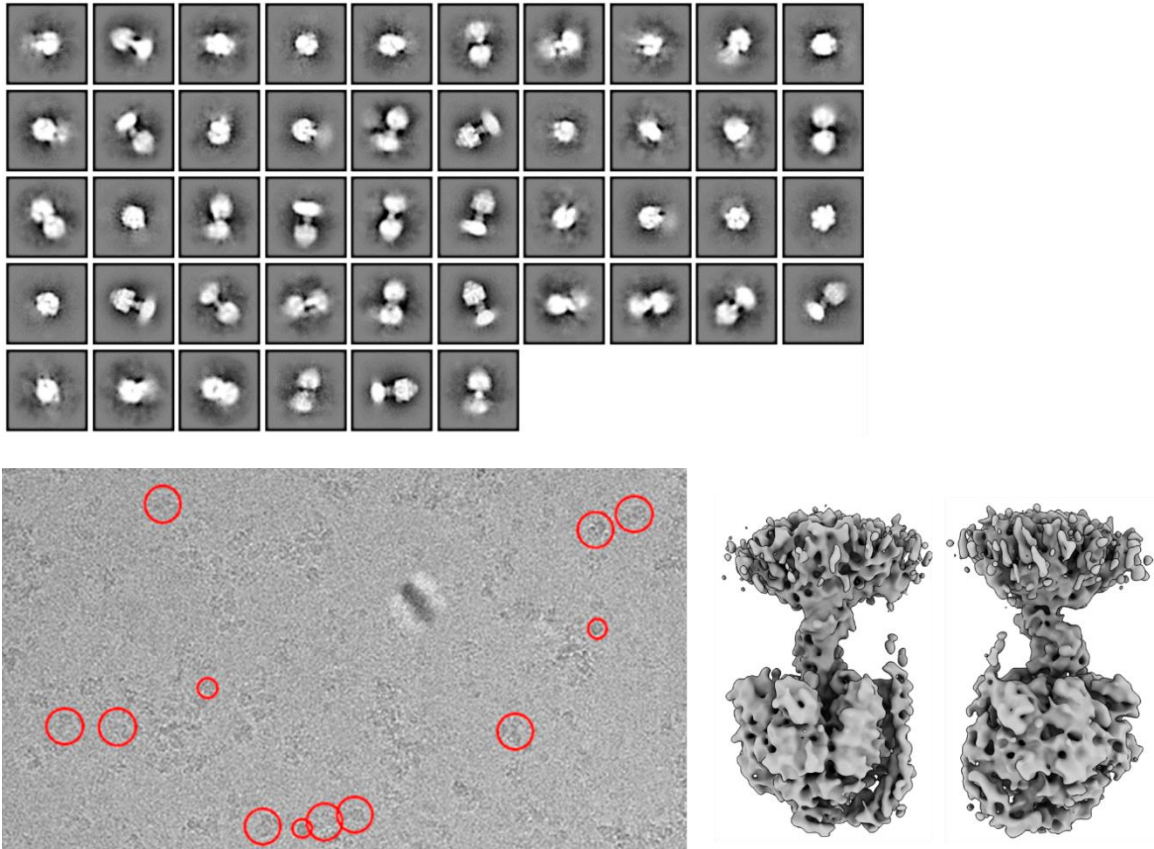
Figure 35. Classification of Cryo-EM images of Sp-c15 F_OF_1 chimera. Image-averaged structure of chimeric F_OF_1 at 7.6 Å resolution generated from approximately 36,000 particles.

<u>Growth rates of chimeric *E. coli* cells in succinate media</u>

The effect of altering the F_O c-ring on the cellular function of *E. coli* was determined by measuring the cell growth rate in succinate media at 37 °C. In succinate medium, cells require F_OF_1 to produce ATP necessary for cellular metabolism. Each strain containing the modified c-subunit sequence was monitored for growth by measuring the OD_{600} cell density from the time of inoculation with starter culture until the cells reached the stationary phase (**Figure 36**). Four replicates of the growth curves were measured for each chimera.

In succinate media, the Bt-c8 chimeric cells grew slower than WT for the first few hours, but the growth accelerated and reached the final cell density of ~1.2 OD_{600} after 8 hours, surpassing the WT cell density of ~1.0 OD_{600}. The Ms-c9 cells showed poor growth compared to WT, only reaching the OD_{600} of ~0.14. The Sc-c10 and Fn-c11 cells showed a very similar growth pattern as WT. The growth curves of Pd-c12, So-c14, and Sp-c15 overlapped with WT until hour 4, after which all three chimeras grew more than the WT until they all reached an OD_{600} of ~1.2 after 8 hours. The Se-c13 cells showed slightly less growth than WT. And the Bp-c17 cells showed very poor growth with a final OD_{600} of <0.1.

To further compare the succinate-dependent growth of each chimeric *E. coli* cells, the growth rates of each chimeric strain were determined from the growth curves by calculating the greatest increase in OD_{600}/hour during the exponential phase. The plot of the growth rate as a function of the anticipated c-ring size (**Figure 37**) did not show a significant trend. However, the Bt-c8 and So-c14 cells showed the highest growth rates of 0.34 and 0.33 OD_{600}/h, respectively. It was noted that the chimeras that contained the c-ring inner helix sequences derived from mitochondria and chloroplast F_OF_1 from multicellular eukaryotic organisms showed the highest growth rates. On the contrary, the Ms-c9 and Bp-c17 cells showed the lowest growth rate of all chimeras at 0.04 and 0.05 OD_{600}/h, respectively. The remaining strains did not show significant differences in the growth rates compared to the 0.24 OD_{600}/h from WT *E. coli* c10, with Sc-c10, Fn-c11, Pd-c12, Se-c13, and Sp-c15 cells growing at 0.27, 0.27, 0.30, 0.23, and 0.30 OD_{600}/h,

respectively. These results further indicated that the chimeric F_OF_1 fully assembled in the cells

and carried out ATP synthesis.
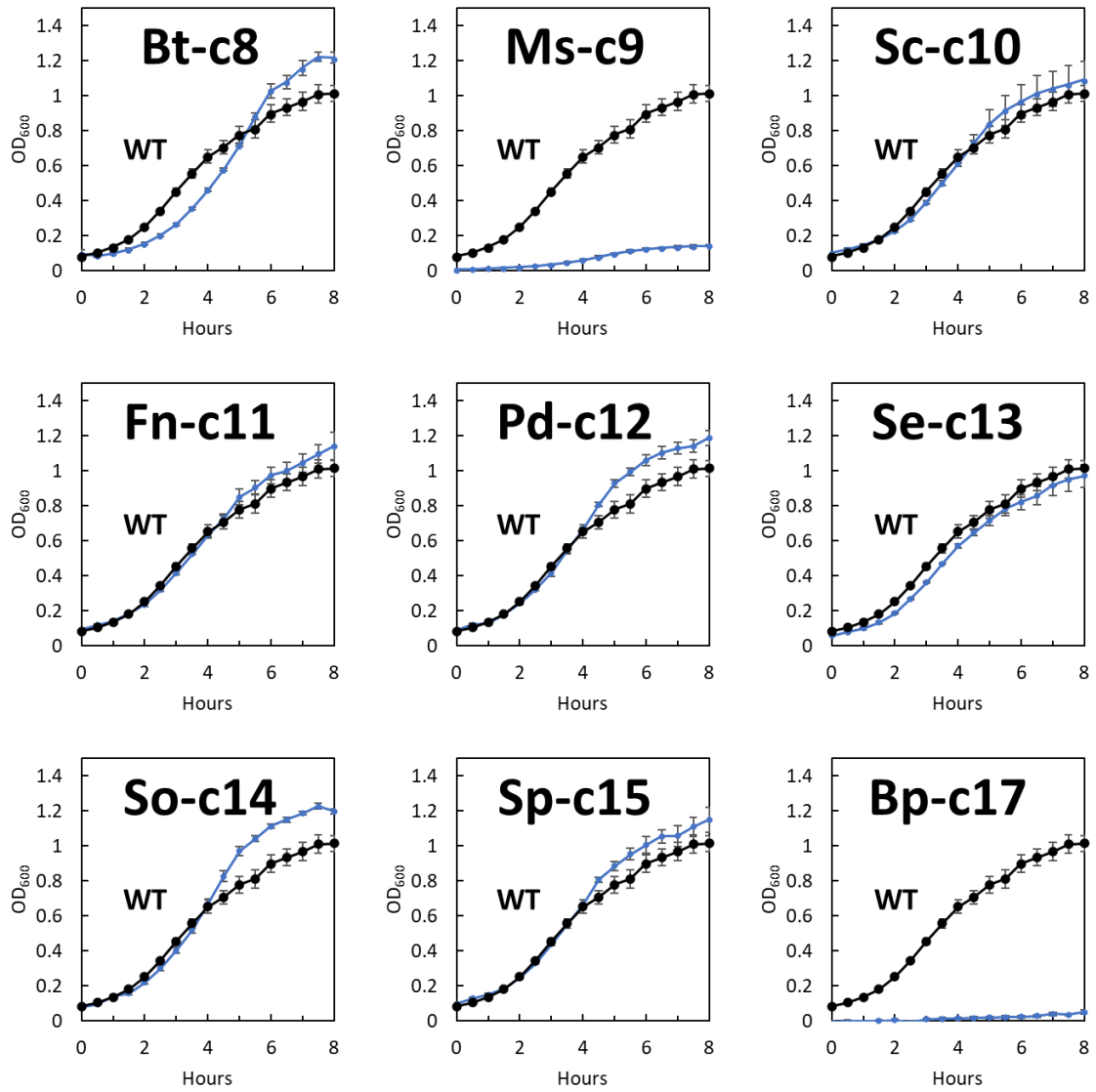
Figure 36. *E. coli* succinate-dependent growth curves for wild type (WT) versus chimera encoding a c-subunit that putatively forms a c-ring varying in size from c_8 to c_{17}. The colored line represents the chimeric F_OF_1 *E. coli* strains compared to the WT shown in black line.
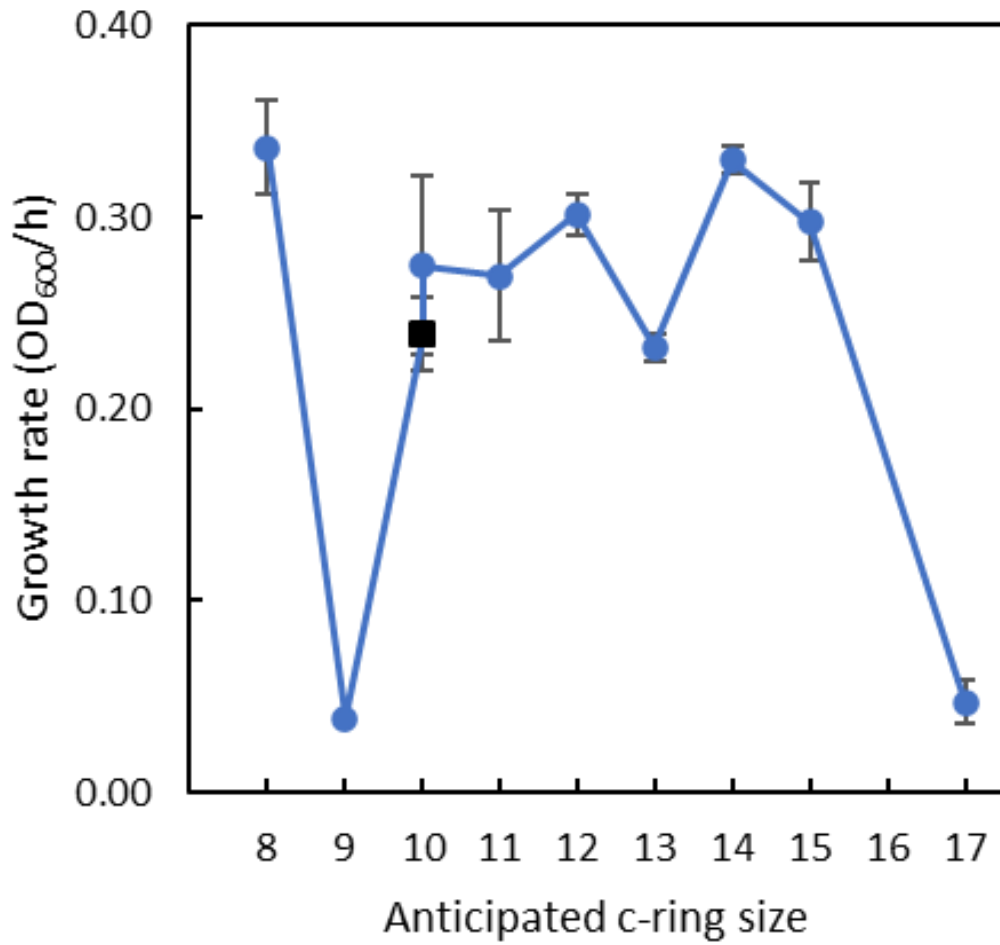
Figure 37. Summary of growth rates versus anticipated c-ring size. From each strain of *E. coli* cell growth curves, the fastest growth rate during the exponential phase was calculated in OD_{600}/hr. Black datapoint represents the WT *E. coli* with a c_{10}-ring.

<u>ATP synthesis rates of the chimeras</u>

The ability of the chimeric F_OF_1 to catalyze ATP synthesis was determined by the luciferin-luciferase assay using inverted membrane vesicles (IMVs) of the *E. coli* strains. Rates of ATP synthase activity was measured at a PMF of -210 mV that was composed of three different proportions of ΔpH and ΔΨ. The three proportions of ΔpH and ΔΨ were: (i) -210 mV and 0 mV; (ii) -150 mV and -60 mV; and (iii) -90 mV and -120 mV, where the ΔpH values in mV correspond to pH differences of 3.5, 2.5 and 1.5, respectively (**Figure 38**). These conditions made it possible to compare the contributions of ΔpH and ΔΨ on the ability of the chimeric F_OF_1 to synthesize ATP (**Figure 39**).

When the PMF was composed of ΔpH of -210 mV and 0 mV ΔΨ (**Figure 39A**), the data showed an overall trend of decreasing ATP synthesis rate with increasing c-ring size. However, peaks in ATP synthesis activity were observed from Fn-c11 and So-c14 IMV that deviated from the overall trend. The Bt-c8 chimera with the smallest c-ring had an ATP synthesis activity of 12.8 nmol ATP (mg protein·min)$^{-1}$, which declined to 10.8 with Ms-c9. The Sc-c10 IMV showed a further decline in ATP synthesis activity with 4.5 nmol ATP (mg protein·min)$^{-1}$, which was 58% lower activity compared to the rate of 10.6 seen from WT *E. coli* IMVs that contained the same sized c_{10}-ring. The ATP synthesis activity increased to 18.4 with Fn-c11, decreased to 8.7 and 8.6 with Pd-c12 and Se-c13, respectively, reached another peak of 14.4 with So-c14, then decreased back down to 6.0 and 0.9 with Sp-c15 and Bt-c17, respectively.

When the PMF was composed of -120 mV ΔΨ and -90 mV ΔpH, the data again showed a decreasing trend in ATP synthesis activity as the anticipated c-ring size increased (**Figure 39B**). Under this condition, a peak was seen from So-c14 again, but not from Fn-c11. The ATP synthesis rates from c_8 to c_{11} ring-chimera did not show a significant change, going from 12.6, 13.1, 10.4, 11.4, and 12.2 nmol ATP (mg protein·min)$^{-1}$ with Bt-c8, Ms-c9, Sc-c10, WT *E. coli* c10, and Fn-c11, respectively. Under this condition, the difference between the Sc-c10 and WT *E. coli* c_{10} was minimal. With a further increase in anticipated c-ring size with Pd-c12, the ATP synthesis rate showed a significant decrease to 0.7, and the rate increased to 6.9 with Se-c13. Then, the

So-c14 chimera showed the highest rate of all chimeras under this condition with 21.1 before the rates decreased again to 4.0 and 0.8 nmol ATP (mg protein·min)$^{-1}$ with Sp-c15 and Bp-c17 chimeras.

Among the three ΔpH and ΔΨ conditions, the highest ATP synthesis rates were seen when the ΔpH and ΔΨ were set to -150 and -60 mV, respectively (**Figure 39C**). Like the other two conditions, the overall trend showed a decreasing ATP synthesis rate with increasing c-ring size. However, only Fn-c11 showed the peak in this condition while So-c14 did not show a peak. Notably, So-c14 was the only chimera where this condition did not result in the highest rate compared to the other two ΔpH ΔΨ conditions. The Bt-c8 IMV showed a rate of 34.9 nmol ATP (mg protein·min)$^{-1}$, which increased slightly to 36.5 with Ms-c9. The activity of Sc-c10 was 20.4, which was a ~27% decrease in activity compared to 27.9 from WT *E. coli*. Then, the Fn-c11 chimera showed the highest ATP synthesis rate by far out of all chimeras with 48.4 nmol ATP (mg protein·min) $^{-1}$. After that point, the activity reached a valley with Pd-c12 chimera showing the rate of 11.9. The rate slightly increased to 17.9 with Se-c13, followed by a steady decrease by So-14, Sp-c15, and Bp-c17 showing the rates of 14.9, 8.9, and 0.4 nmol ATP (mg protein·min)$^{-1}$ respectively.

Overall, the chimeras with smaller anticipated c-ring showed a significantly higher ATP synthesis rate under the -60 mV ΔΨ, -150 mV ΔpH condition, while the activities under 0 mV ΔΨ, -210 mV ΔpH and -120 mV ΔΨ, -90 mV ΔpH conditions were similar to each other. As the anticipated c-ring size increased, the differences between the three ΔpH and ΔΨ conditions diminished, until Sp-c15 and Bp-c17 showed almost no difference at all between the three conditions (**Figure 39D**).

The three ΔpH ΔΨ conditions showed bigger differences between the highest and lowest ATP synthesis activities when the c-rings were relatively smaller, and the differences between the three conditions diminished with the larger c-rings. The differences between the highest and the lowest rates for Bt-c8, Ms-c9, Sc-c10, WT c10, and Fn-c11 were 22.4, 25.7, 15.9, 17.3, and 36.2

ATP (mg protein · min^{-1}), respectively, while the differences for Pd-c12, Se-c13, So-c14, Sp-c15, and Bp-c17 were 11.2, 11.0, 6.7, 4.9, and 0.5, respectively.

Overall, the ATP synthesis rates decreased as the anticipated c-ring size increased, and the Bt-c8 and So-c14 chimeras with the eukaryotic subunit-c showed one of the highest ATP synthesis rates.

These results again showed that the $F_O F_1$ can assemble and function when the inner helix is replaced with a different species. The differences in the ATP synthesis activities between the chimeric $F_O F_1$ provided evidence that the c-ring has been altered in ways that support alterations in c-ring size. Additionally, these results showed that efficient ATP synthesis by the $F_O F_1$ requires an optimal ratio of ΔpH and ΔΨ, which likely depend on the stoichiometry of the c-ring.
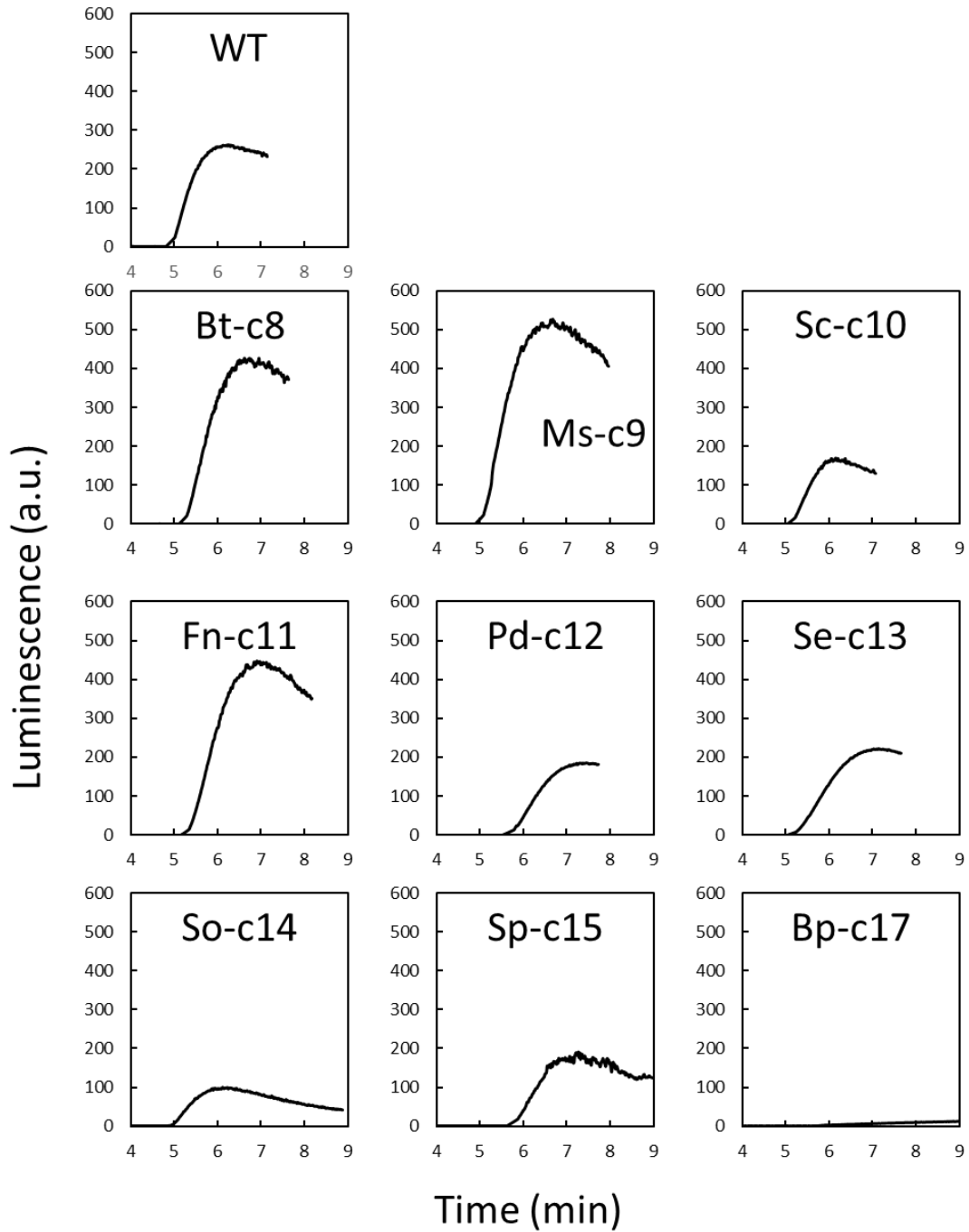
Figure 38. Examples of ATP synthesis rate measurements of the chimeric IMV by luciferin-luciferase bioluminescence assay. The ATP synthesis rate was determined by measuring the increase in the intensity of 562 nm luminescence. Data shown are examples of assays under 2.5 ΔpH (-150 mV) and -60 mV Δψ.
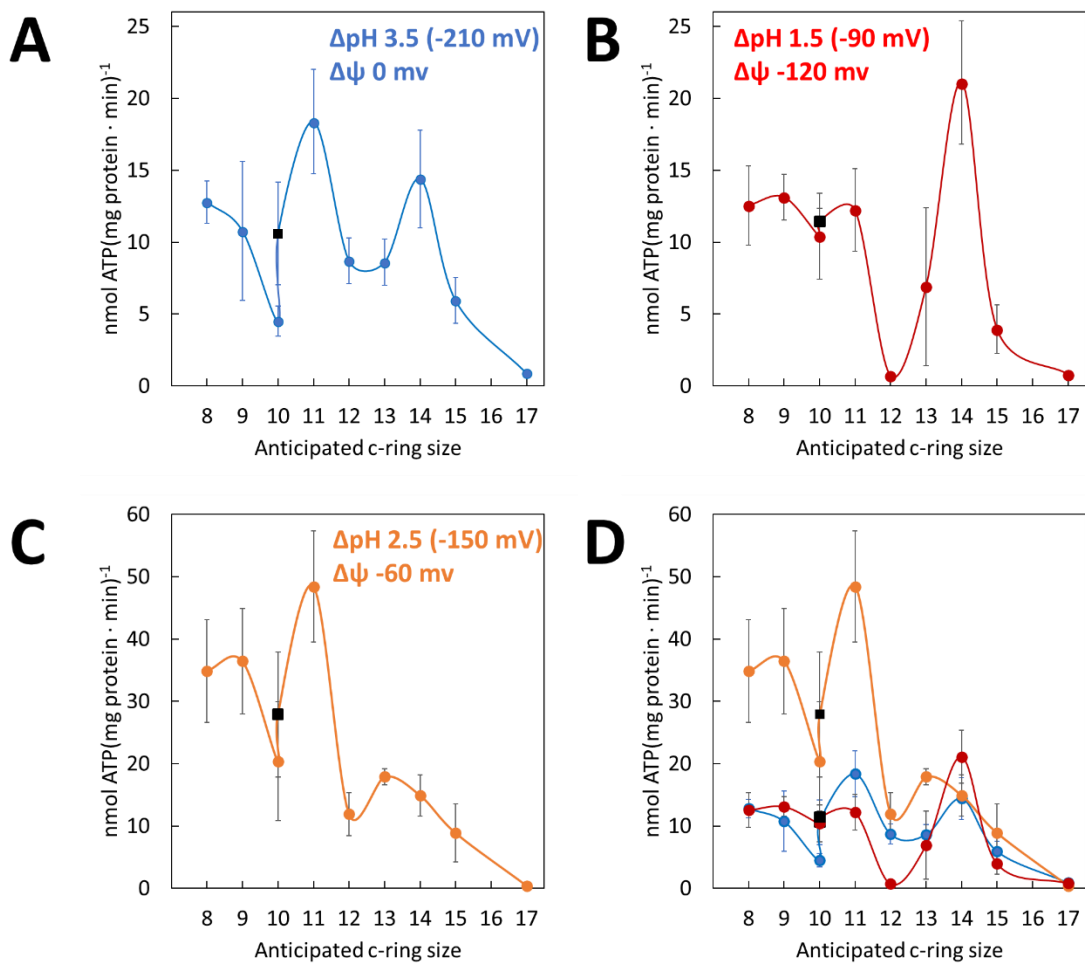
Figure 39. ATP synthesis rates versus anticipated c-ring size measured via luciferin-luciferase bioluminescence assays of IMVs. Three experimental conditions were set up to establish (A) -210 mV ΔpH and 0 mV ΔΨ (blue line), (B) -90 mV ΔpH and -120 mV ΔΨ (red line), and (C) -150 mV ΔpH and -60 mV ΔΨ (orange line. (D) shows the comparison between the three conditions. Black datapoint represents the WT *E. coli* with a c_{10}-ring.

ATP hydrolysis rates of the chimeras

 To measure the ability of the chimeric F_OF_1 to hydrolyze ATP, the ATP hydrolysis rates of the IMV containing the chimeric F_OF_1 were measured by NADH-coupled ATP hydrolysis assay (**Figure 40**). The data showed a slight negative correlation between the anticipated c-ring size and the ATP hydrolysis rate (**Figure 41**). Bt-c8 IMV showed a rate of 3.30 µmol ATP (mg protein·min)$^{-1}$, Ms-c9 showed a similar rate at 3.28, WT-c10 IMV showed one of the highest ATP hydrolysis rates of 4.35, while the Sc-c10 IMV that also contains a c_{10}-ring showed a lower rate of 2.92. The Fn-c11 showed a similar rate as the other chimeras with the smaller c-ring size with the rate of 3.13. Then, the ATP hydrolysis rate increased with the Pd-c12 IMV, showing the rate of 4.40. From this point, the rate steadily decreased with Se-c13, Sp-c14, So-c15, and Bp-c17 with 4.06, 2.27, 2.62, and 1.96 µmol ATP (mg protein·min)$^{-1}$, respectively, with Bp-c17 showing an activity of less than half compared to the WT. These results showed that although altering the c-ring caused a slight decrease in the ATP hydrolysis rate with an increase in anticipated c-ring size, the differences between the chimeras were not as dramatic compared to the differences in ATP synthesis rates between the chimeric F_OF_1.
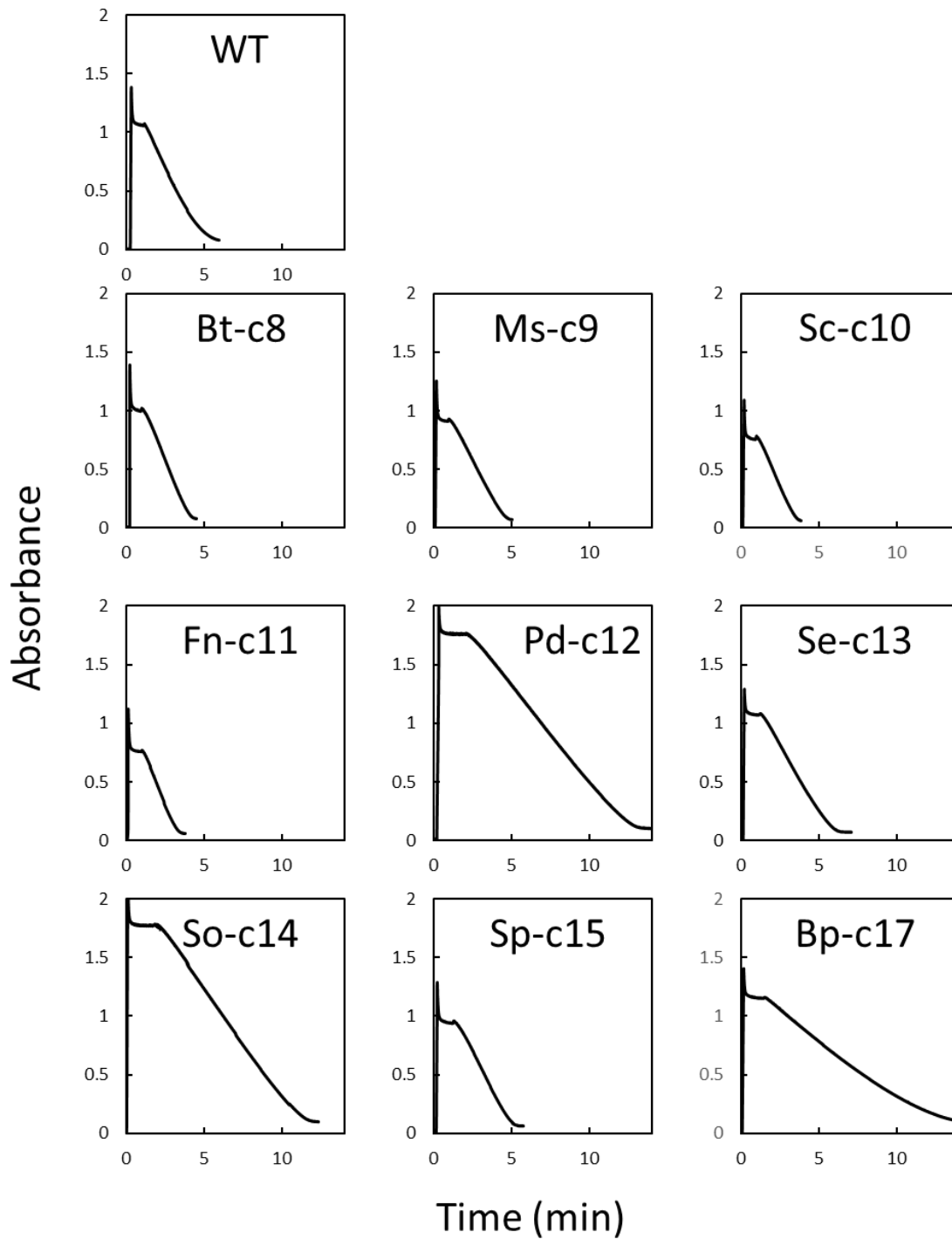
Figure 40. Examples of NADH-coupled ATP hydrolysis assay measurements. Decrease in absorbance at 340 nm was measured to determine the rate of ATP hydrolysis by chimeric *E. coli* IMVs.
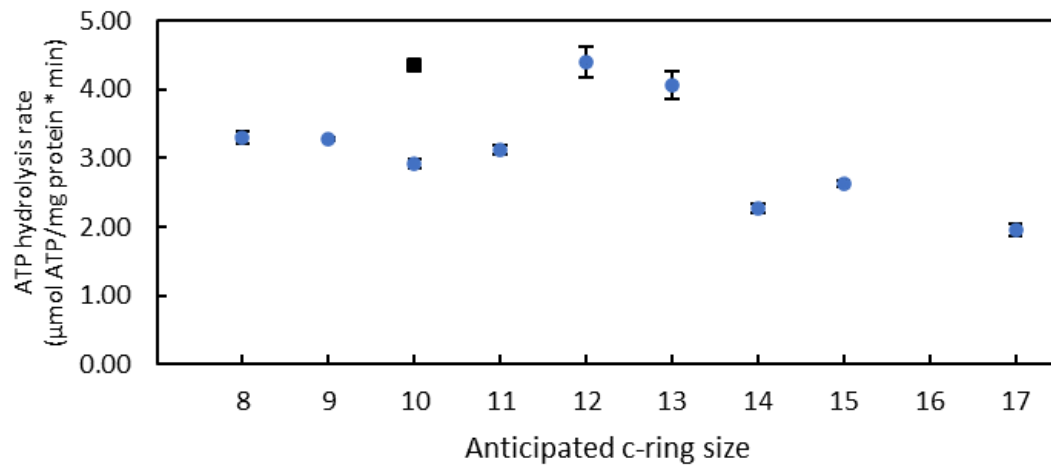
Figure 41. Summary of ATP hydrolysis rates of the chimeric *E. coli* IMV as a function of the anticipated c-ring size. Black square datapoint represents the WT *E. coli* with a c_{10}-ring.

<u>The coupling of the interface between the c-ring and subunit-a</u>

To measure the coupling of the interface between the c-ring and subunit-a in each chimeric F_OF_1, ACMA (9-amino-6-chloro-2-methoxyacridine) quenching assays were conducted using the chimeric IMVs (**Figure 42**). ACMA is a pH-sensitive fluorescent dye that accumulates inside the IMVs. Fluorescence intensity is high in the absence of a pH gradient across the membrane. However, conditions that decrease the internal pH of the IMVs quench the fluorescence. Differences in the ability of F_OF_1 to catalyze ATPase-dependent proton gradient formation in IMVs were compared between WT and the chimeras by ACMA fluorescence quenching. Addition of ATP induced a decrease in fluorescence intensity in all chimeras, which was restored upon addition of carbonyl cyanide p-chlorophenylhydrazone (CCCP) that rapidly collapses the pH gradient in the IMV. A loose coupling of the interface between the c-ring and subunit-a enables the protons to leak out of the IMV that decreases the extent of ACMA quenching.

The extent of quenching was observed to depend on the amount of IMVs in the assay, which was measured as µg protein. To establish a more quantitative measure of the extent of coupling by the chimera, the initial and quenched fluorescence intensities were plotted *versus* µg of protein (**Figure 43**). These data were fitted to trend lines, in which the difference between the initial and quenched trend lines represents the extent of ACMA quenching. The fluorescence quenching by WT IMV at 155 µg protein that showed the highest quenching among all measurements was designated to be 100% quenching. The percentage of ACMA quenching by each chimera was calculated relative to this 100% and plotted as a function of µg of protein (**Figure 44a**). Based on this plot, the percentage of quenching by each chimera at 119 µg IMV protein were calculated to compare the coupling of the c-ring and subunit-a in each chimera (**Figure 44b**). The 119 µg IMV protein was the highest amount of Bt-c8 IMV used in the experiments.

The results showed an overall trend of decreasing coupling as the anticipated c-ring size increased. At 119 µg IMV protein, Bt-c8 showed 93% quenching, Ms-c9 showed 84%, Sc-c10

showed 80%, WT *E. coli* c_{10} IMV showed 90%, Fn-c11 showed 87%, Pd-c12 showed 83%, Se-c13 showed a significant decrease in quenching at 46%, So-c14 showed 74%, Sp-c15 showed 74%, and Bp-c17 showed the lowest quenching at 10%. Based on these results, the extent of ATPase-dependent quenching in the c13 and c17 chimera were clearly less than that of the WT and other chimeras. These data are consistent with the change in the c-ring size as a result of the change in the inner helix sequence modification in the c-ring.
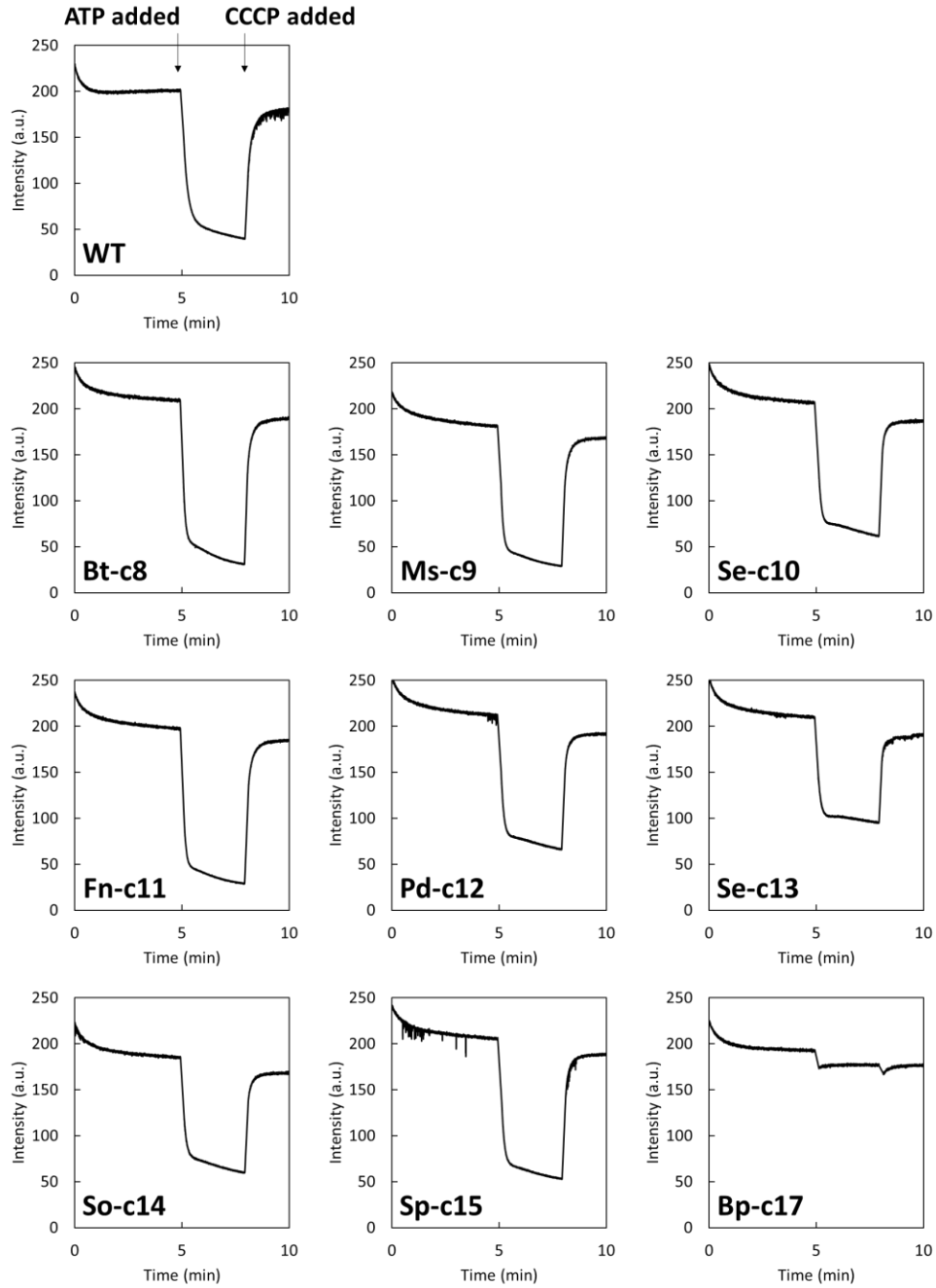
Figure 42. Measurement of proton gradient formation in the chimeric IMVs by ACMA quenching assay. (A) Examples of fluorescence measurements made for each chimera. The point at which ATP and CCCP were added to the reaction mixture are indicated in the WT plot. (B) Initial and quenched fluorescence levels as a function of IMV added to the reaction mixture in μg protein.
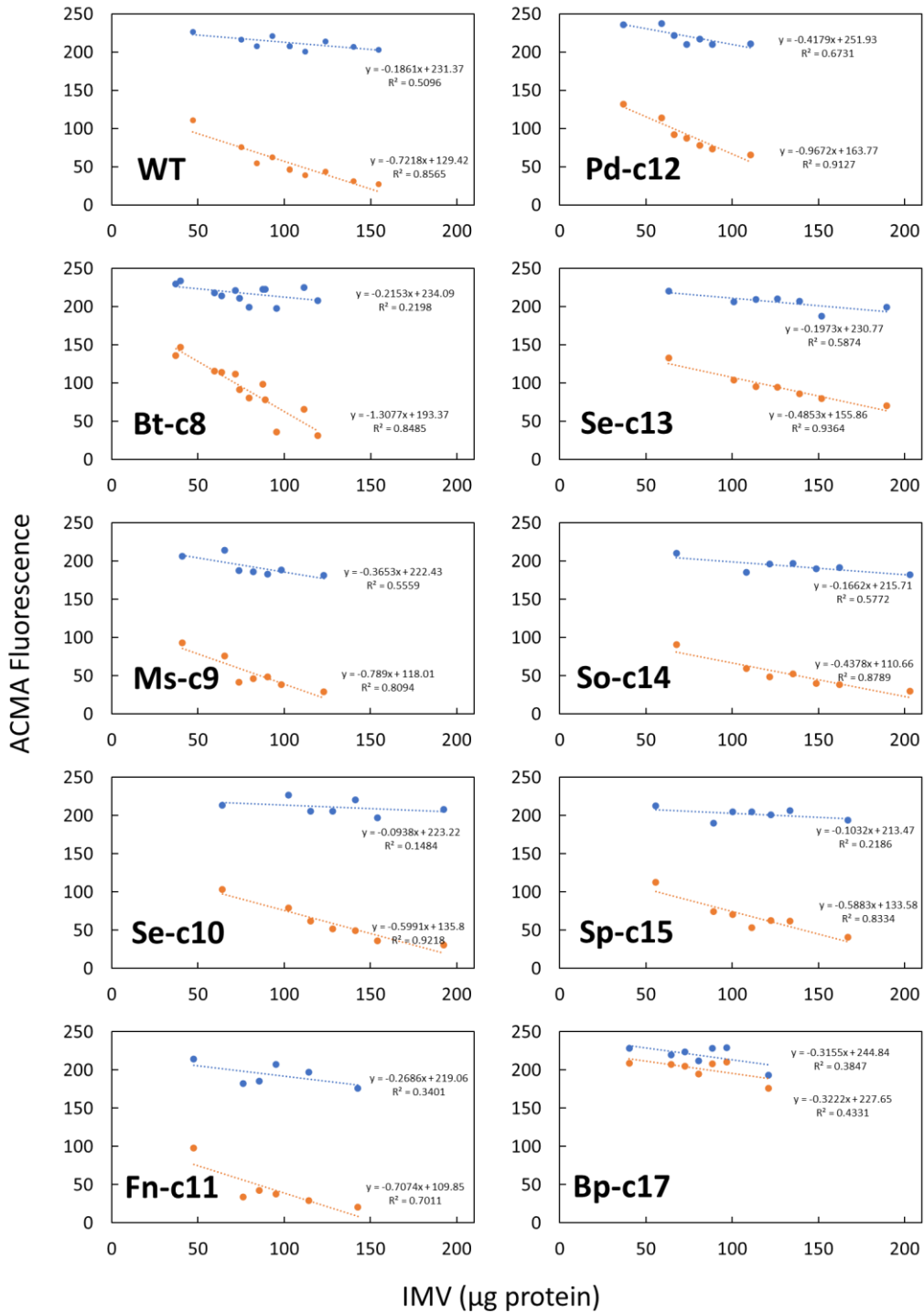
Figure 43. The initial and quenched ACMA fluorescence of the chimeric IMVs. The initial (blue) and quenched (orange) ACMA fluorescence are plotted as a function of the amount of IMV in µg protein. Linear trend lines are shown for each chimera as dotted lines.

121
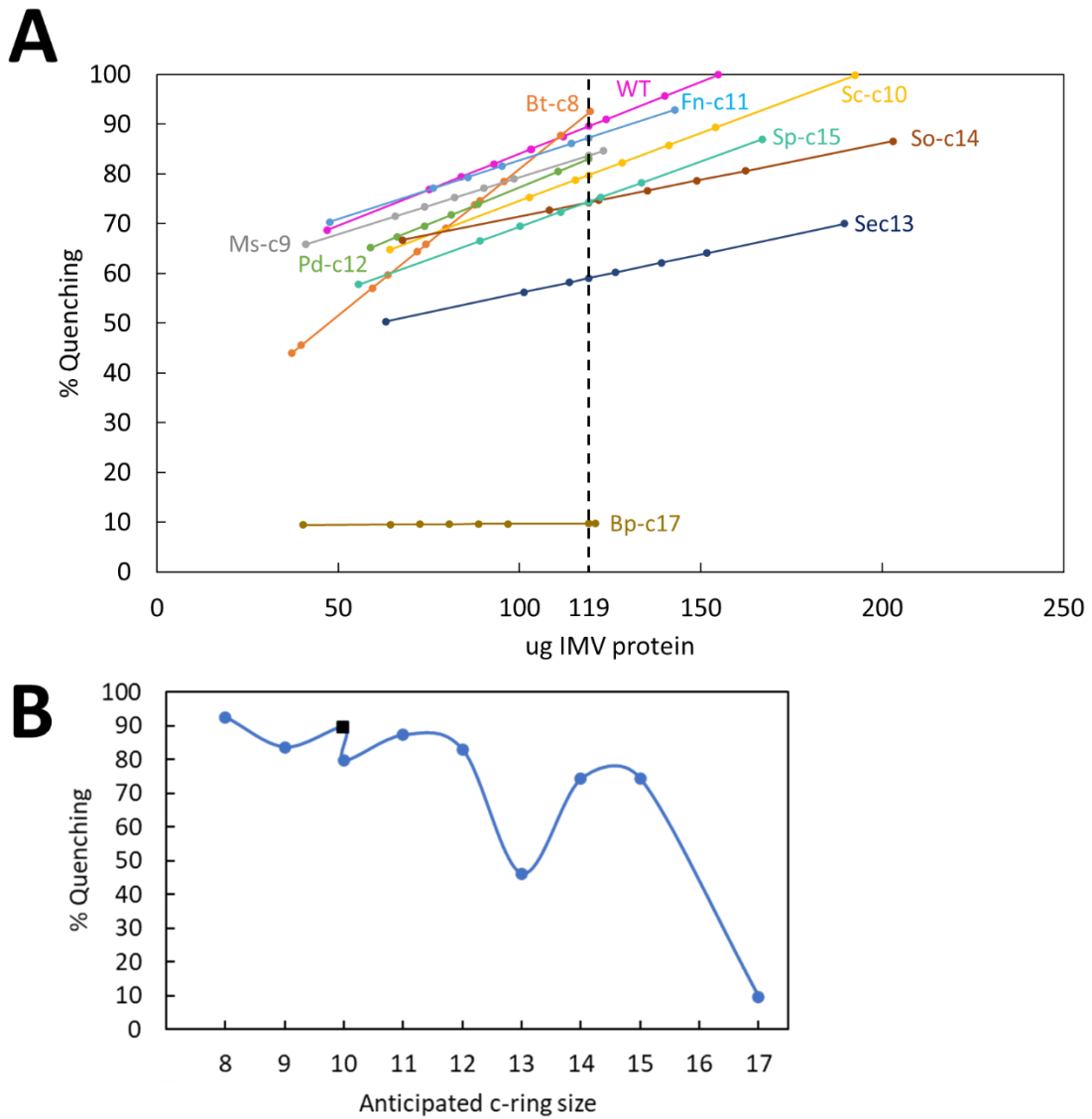
Figure 44. The % ACMA quenching of the nine chimeras. (A) The extent of quenching by each chimera relative to WT IMV at 155 μg protein as a function of μg IMV protein. Dotted line represents 119 μg protein, which was the highest amount of Bt-c8 IMV used in the experiments. (B) The % ACMA quenching of each chimeric IMV at 119 μg protein as a function of the anticipated c-ring size. Black datapoint represents the WT.

Discussion

Nine chimeras of the *E. coli* F_OF_1 ATP synthase were constructed using subunit-c sequences from organisms that contain c_8 to c_{17}-rings in F_OF_1, with exception of a c_{16}-ring, which has not been discovered to date. The inner (N-terminal) helix of the *E. coli* c-subunit was substituted, which contains the sidechains in contact with adjacent c-subunits that determine the number of c-subunits in the c-ring. Since the rest of the enzyme complex remained unchanged, these N-terminal helix substitutions provides a direct comparison of the effects of c-ring size on the performance of *E. coli* cells and on the F_OF_1 ATP synthase.

<u>All F_OF_1 chimeras assembled into functional complexes.</u>

The results presented here including negative stain TEM images and cryo-EM structures of the purified chimeric F_OF_1, as well as Western blots of isolated *E. coli* membranes that showed the presence of F_1 subunit-β, support the conclusion that the F_OF_1 complex assembles in the membrane in all chimeras (**Figures 33-35**). Evidence that the chimeric F_OF_1 complexes had assembled in a functional manner is shown by the growth of *E. coli* cells in succinate medium, as well as their ability to catalyze both ATP hydrolysis and ATP synthesis. Although it is noteworthy that the Bp-c17 chimera exhibited very low ATP synthase rates.

<u>Contributions of ΔpH and ΔΨ to ATP synthase activity</u>

The results presented here provide new insight into the impact of c-ring size on the relative contributions of ΔpH and ΔΨ as an energy source to drive ATP synthesis. When driven by -120 mV ΔpH and -60 mV ΔΨ, the ATP synthase rate decreased with increasing anticipated c-ring size. This is consistent with the H^+/ATP ratio that depends on the number of subunits in the c-ring. A smaller c-ring theoretically requires fewer H^+ to produce the same amount of ATP compared to a larger c-ring that requires more H^+ to make a full 360° revolution to synthesize 3 ATP molecules. However, when these results were compared to the dependence of the ATP synthesis rate driven only by ΔpH on c-ring size, it is clear that the small c-rings (c_8 – c_{11}) and

large c-rings (c_{13} – c_{17}) respond differently to ΔpH and ΔΨ. With large c-rings, ATP synthesis rates decreased with increasing c-ring size with ΔpH alone, and these rates were not significantly affected when driven by -120 mV ΔpH and -60 mV ΔΨ. However, ATP synthase rates with small rings increased significantly and proportionally to the inverse of c-ring size compared to the rate driven by ΔpH alone.

The results presented here indicate that the rate enhancement from ΔΨ with small c-rings, or lack thereof with large c-rings, results from the size of the c-ring. These results are consistent with the single-molecule rotation results of *E. coli* $F_O F_1$ that show that the F_O proton translocation-dependent step induces an 11° rotation in the ATP synthase direction (Yanagisawa and Frasch, 2021). The energy to drive rotation by 11° was proposed to result from deprotonation of the essential cD61 carboxyl group on the c-subunit, which forces the negatively charged carboxyl group from the hydrophobic lipid bilayer into the aqueous vestibule that exists at the interface between subunit-a and the c-ring. The remaining 25° of c-ring rotation to complete each 36° rotational step of the *E. coli* c_{10}-ring was postulated to result from the electrostatic attraction between subunit-a R210 and the unprotonated cD61 carboxyl group, where the strength of this attraction is a function of the hydrophobicity of the vestibule and the membrane potential (Yanagisawa and Frasch, 2021). This two-step mechanism suggests that the proton translocation-dependent sub-step remains 11° regardless of c-ring size so long as a tight interface between subunit-a and the c-ring is maintained at the point where deprotonation of subunit-c forces the charged carboxyl group to move from the hydrophobic lipid bilayer. The decreased coupling in the c_{17}-chimera evident by the small extent of ACMA fluorescence quenching may be the result of the inability of subunit-a to form a tight interface with such a large c-ring. Since rotational c-subunit stepping of a c_8-ring and a c_{15}-ring is 45° and 24°, respectively, the membrane potential-dependent step will be significantly larger for the smaller c-ring, which is consistent with the results presented here. Work is now underway to test this hypothesis directly using single-molecule rotation studies of the chimeric $F_O F_1$.

The results presented here conflict with chemiosmotic theory that assumes that ΔpH and ΔΨ are chemically and kinetically equivalent as energy sources for ATP synthesis in membranes from bacteria and photosynthetic thylakoids (Bokranz, *et al.*, 1985; Slooten and Vandenbranden, 1989; Junesch and Gräber, 1991; Turina *et al.*, 1991; Mitchell, 2011). However, work published before the size of c-rings was known to differ among species showed that *E. coli* F_OF_1 reconstituted into liposomes required both ΔpH and ΔΨ for high ATP synthase rates, while proteoliposomes containing chloroplast F_OF_1 achieved high synthase rates at a high ΔpH in the absence of ΔΨ, which also suggests that ΔpH and ΔΨ are not kinetically equivalent in driving ATP synthesis (Fischer and Gräber 1999).

In vivo steady-state levels of ΔpH and ΔΨ are now known to differ between *E. coli* (Meier and Cheuk, 2021) the stroma lamellae where chloroplast F_OF_1 is located (Junesch *et al.*, 1991; Cruz *et al.*, 2001), and in other organisms (Ritchie, 1991; Watt et al., 2010; Mitchell, 2011) as summarized in **Figure 45**. The small ΔpH relative to the ΔΨ in mitochondria and *E. coli* is thought to result because the intermembrane space of mitochondria and the periplasm of bacteria is so large that it is difficult to generate a significant ΔpH. Conversely, the F_OF_1 in the chloroplast resides mostly in the stroma lamella, which forms the small tubular connection between the thylakoids with a small volume. The small volume in the stroma lamella allows a larger ΔpH to be formed across the membrane more easily, even when a relatively small number of protons are pumped into the thylakoids (Kühlbrandt, 2019).

It is noteworthy that the condition with -90 mV ΔpH and -120 mV ΔΨ did not enhance the rate of ATP synthesis of chimeric F_OF_1 with smaller c-rings relative to that driven by ΔpH alone (**Figure 39**). This is remarkable since the values of ΔpH and ΔΨ used most closely match the *in vivo* steady-state values in bovine mitochondria and *E. coli* (**Figure 45**). First, this suggests that the *in vivo* ΔpH and ΔΨ levels have not evolved to optimize the rate of ATP synthesis in these organisms. Second, it suggests that the values of ΔpH and ΔΨ that enable the highest ATP synthase rates differ as a function of the size of the c-ring. This conclusion is supported by the

ATP synthase rate observed here with the c_{11} chimera driven by -120 mV ΔpH and -60 mV $\Delta\Psi$, which is higher than the overall trend in which the rate decreased with increasing c-ring size.
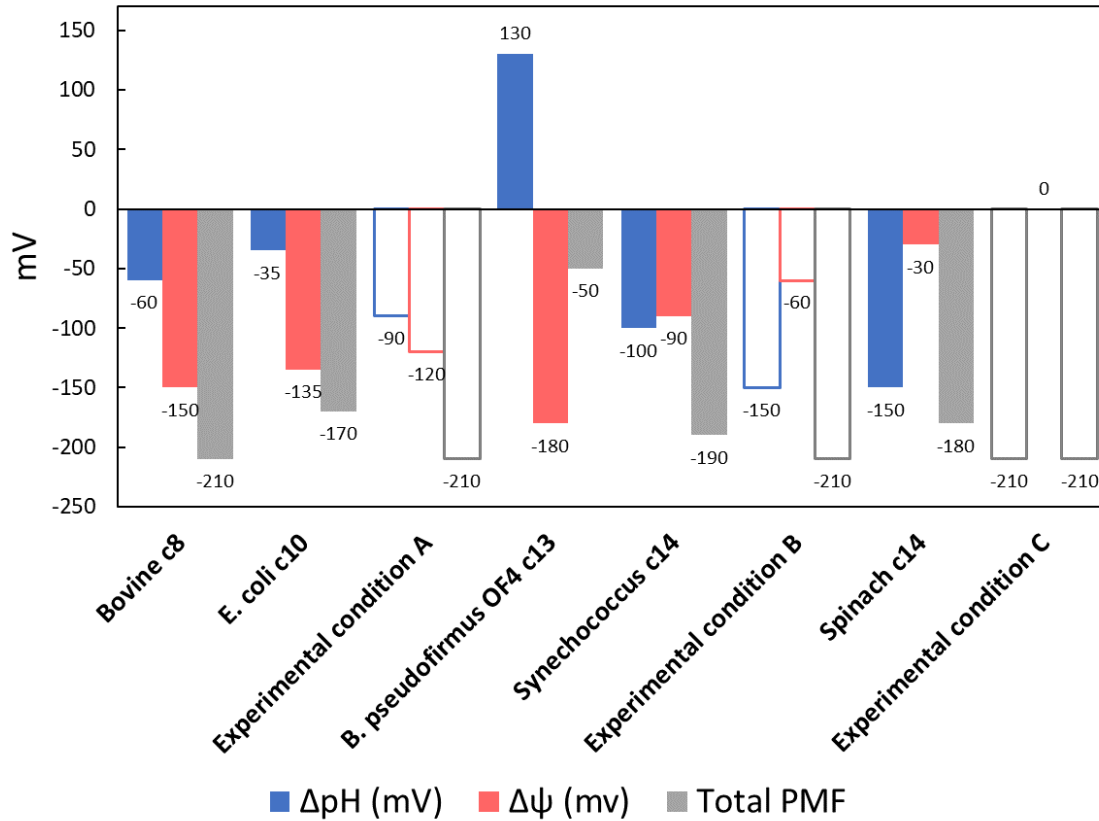
Figure 45. The PMF composition of different species and experimental conditions used. The ΔpH is shown in blue, Δψ is shown in red, and the total PMF is shown in gray for species with varying anticipated sizes of F_O c-ring. (Junesch et al., 1991; Ritchie, 1991; Seelert et al., 2000; Cruz et al., 2001; Jiang et al., 2001; Pogoryelov et al., 2007; Watt et al., 2010; Preiss et al., 2010; Mitchell, 2011).

127

<u>Symmetry between the c-ring stoichiometry and the F_1 120° rotations</u>

The ATP synthesis rates observed with chimeras Pd-c12 and Sp-c15 were disproportionally low (**Figure 39**). This may be because the number of subunits in their c-ring is a multiple of three, which matches the number of catalytic sites in F_1. When F_OF_1 rotates, the section of the γ-subunit that protrudes must fit through a tight space between the $(αβ)_3$-ring, subunit-a, and the peripheral stalk during one of the three 120° rotations to synthesize ATP. During this 120° rotation, extra energy is likely necessary to squeeze the γ subunit through the space, which is accommodated by an asymmetric stoichiometry between the three 120° rotations of the F_1 motor and the c-ring size that is not a multiple of 3. For example, the *E. coli* c_{10}-ring would rotate in 3, 3, and 4 c-subunit increments to complete the 360° rotation, which means that one of the three 120° rotations by the F_1 motor would be fueled by 4 H^+ rather than 3. In addition, there is evidence that the asymmetry between the F_1 and the c-ring stepping generates elastic energy that is stored in the central rotor and/or the peripheral stalk that can either promote or hinder the rotation of the c-ring towards ATP synthesis, depending on the alignment of the F_1 catalytic dwell to the subunit-c stepping (Yanagisawa *et al.* 2017, 2021; Sielaff *et al.*, 2019). The extra proton and the elastic energy from the structural asymmetry of the F_OF_1 are likely required for the γ-subunit to rotate through the tight space. Alternatively, the extra proton may be necessary to overcome the opposing elastic energy. Therefore, the low ATP synthesis activities from Pd-c12 and Sp-c15 chimeras suggest that their symmetric F_OF_1 lack the elastic energy and the extra proton to efficiently synthesize ATP.

However, the ATP synthesis rate of Ms-c9 was relatively high despite the anticipated lack of asymmetry between the F_O and F_1. This may be because F_OF_1 containing a small c-ring has a higher dependence on Δψ to drive ATP synthesis, as seen from the ATP synthesis assay results in which smaller c-ring chimeras achieved substantially higher ATP synthesis rates when ΔpH and Δψ were -150 and -60 mV, respectively. The Ms-c9 chimera may be able to efficiently synthesize ATP despite the lack of F_OF_1 asymmetry because of its higher dependence on the c-ring stepping during ATP synthesis caused by the electrostatic interaction between the

unprotonated cD61 and aR210, which is driven by $\Delta\psi$, over the proton translocation-dependent c-ring stepping (Yanagisawa *et al.*, 2021).

Growth rates indicate that *E. coli* can partially compensate for loss of F_OF_1 energy efficiency.

Succinate-dependent growth rates of *E. coli* strains containing chimeric F_OF_1 presented here had a much smaller dependence on c-ring size than would be expected based on the differences in ATP synthase activity. It is possible that the expression levels of F_OF_1 differ among the nine chimeric *E. coli* strains, which could enable the *E. coli* strains to compensate for the changes in efficiency of ATP synthesis catalyzed by the chimeric F_OF_1. The different expression levels between the WT and the chimeric F_OF_1 must be considered when analyzing the results of the bulk biochemical assays of ATP synthesis, ATP hydrolysis, and ACMA quenching. For example, the values obtained from the WT IMVs in the bulk assays may be underestimated if the WT IMV contained less F_OF_1 than the chimeric strains. The enzymatic activity per WT IMV may have been lower than the chimeras, even though the activity per individual molecule of WT enzyme may have been equal or higher than the chimeras.

The Bp-c17 chimera consistently showed the lowest performance in succinate medium growth rate, ATP synthesis activity, and ATP hydrolysis activity, and ACMA quenching activity among all chimeras tested in this study (**Figures 37, 39, 41, 44**) The ACMA quenching assay indicated that the coupling of the interface between the c-ring and subunit-a is poor in this chimera, which may be because a c_{17}-ring is too large for the *E. coli* F_OF_1 that contains a c_{10} ring in its wild-type form. Alternatively, the growth rate and the ATP synthesis rate may have been low for Bp-c17 because the c-subunit sequence used for this chimera originated from the *B. pseudomallei* N-type ATPase, as discussed earlier. This is consistent with the results showing 99% lower ATP synthesis rate (with ΔpH 2.5 and $\Delta\psi$ -60 mV) by Bp-c17 relative to the WT, while ATP hydrolysis was only 55% lower than the WT. These results are consistent with a c-ring that has evolved to be optimized for ATP hydrolysis-dependent proton pumping instead of ATP synthesis.

129

As discussed above, the *in vivo* steady-state levels of ΔpH and ΔΨ in wild type *E. coli* do not appear to be optimized for the rate of ATP synthase that F_OF_1 is capable of. Altering the expression of the electron transfer complexes to increase ΔpH and ΔΨ is another possible way that *E. coli* strains containing the chimera may have compensated for the loss of energetic efficiency of F_OF_1.

Another possible means that *E. coli* may have used to maintain the succinate-dependent growth rate despite the loss in bioenergetic efficiency due to the presence of chimeric F_OF_1 may be to undergo cell division at shorter time intervals. This would keep the cell size small to increase the surface to volume ratio, which increases the amount of ATP synthase relative to the cell volume. Work is underway to measure cell sizes of the *E. coli* strains as a function of c-ring size.

Conclusion

In conclusion, all nine chimeras assembled properly into full F_OF_1 complex. Difference in growth rates of the *E. coli* strains, ATP synthesis activities, ATP hydrolysis activities, and ACMA quenching activities suggest that the c-ring stoichiometry has indeed changed in these chimeras.

The growth rates of the chimeras did not show a significant trend as a function of anticipated c-ring size. However, the Bt-c8 and So-c14 chimeras that contained a c-ring inner helix sequences that derived from multicellular eukaryotic F_OF_1 grew at the fastest rate among all chimeras, while the bacterial chimeras grew at similar rates as the WT *E. coli*. The ATP synthesis rates of the chimeras showed an overall trend of decreasing ATP synthesis with increasing anticipated c-ring size. Additionally, the differences in ATP synthesis rates measured with varying conditions show that both ΔpH and ΔΨ are required to drive the F_OF_1, and the optimal ratio of the two variables may be different for each c-ring stoichiometry. This may explain the high rates observed with the Fn-c11 chimera.

The Bp-c17 chimera that showed very low growth rate and ATP synthesis activity suggest that the loss of energy coupling may contribute to the cellular function of the *E. coli*.

Quantitation of the expression levels of the chimeric F_OF_1 gave insight into how the cell compensated for the differences in the F_OF_1 activities between the chimeras.

Overall, this work shows that c-ring stoichiometry, ΔpH and $\Delta \psi$ conditions that determines the PMF, and the coupling between the subunit-c and subunit-a, all contribute to the efficiency at which F_OF_1 synthesizes ATP. More work needs to be done to determine the stoichiometry of the subunit-c ring in the structure of the chimeric F_OF_1 through cryo-EM.

Chapter 5

SUMMARY

The F_O motor of the F_OF_1 ATP synthase has been studied less extensively than the F_1, and the molecular mechanism behind its function is still not fully understood. Single-molecule gold nanorod experiments allow for the detailed analysis of the rotation of individual F_OF_1 molecules at the angular resolution of 0.02°–0.12° and a time resolution of 5 μs to elucidate the details of the mechanisms that cannot be resolved by bulk experiments. The results presented in the preceding three chapters and the appendix provide unique insights into the mechanism of how the F_O drives the CW rotation that powers ATP synthesis.

The pKa values of the subunit-a proton half-channels

The single-molecule gold nanorod assay of the nanodisc F_OF_1 allows for the detection of transient dwells (TDs) that occur during the ATPase-dependent 120° power strokes, in which the interactions between subunit-a and the c-ring halts the CCW ATP hydrolysis rotation and often rotate the c-ring in the CW, ATP synthesis direction. In chapter 2, the occurrences of transient dwells (TDs) during the 120° power strokes by *E. coli* F_OF_1 nanodisc were measured as a function of pH ranging from 5.0 to 9.0. The TD occurrence at pH 9.0 was 23% and did not change significantly when the pH decreased to 7.5 in 0.5 pH increments. However, the TD occurrences steadily increased to 48% when the pH was further decreased from 7.5 to 5.0. Because both F_O proton half-channels are exposed to the same pH in this experimental condition, the data showed that the pKa of each half-channels are different, and that the periplasmic half-channel is more easily protonated in a manner that halts ATPase-driven rotation by blocking ATPase-dependent proton pumping. This difference in pKa of the two half-channels has likely evolved to favor the flow of protons in the ATP synthesis direction over ATP hydrolysis.

Chapter 3 explored this further with the calculations of the pKa values of the two half channels. Single-molecule rotation measurements of *E. coli* F_OF_1 nanodisc with subunit-a

132

mutation aE196 on the proton output channel side and aN214, aE219, aH245, aQ252 in the

proton input channel side were made as a function of pH. The measurements of TD occurrences

as a function of pH with each mutant showed that these amino acid residues are involved in the

proton translocation mechanism that drives the rotation of the F_O motor. The results were used to

determine that the pKa values of subunit-a proton input and output channels in WT *E. coli* F_OF_1

are 5.6 and 7.5, respectively, which is consistent with the results shown in chapter 2 that showed

that periplasmic half-channel is more easily protonated than the cytoplasmic half-channel.

The Grotthuss mechanism drives the flow of protons through the subunit-a half-channels

        When the TD occurrences of subunit-a mutants were measured in chapter 3, it was

determined that a mutation in one proton half-channel resulted in the change of pKa in both half-

channels, which supported the hypothesis that proton translocation through the F_O motor involves

the Grotthuss mechanism, in which a column of single water molecules in each half-channel

linked by the c-ring facilitates a rapid flow of protons through the F_O motor. Because the c-ring

connects the two Grotthuss water columns in each half-channel, disruption of one water column

influences both proton half-channels.

        The Grotthuss mechanism hypothesis is also consistent with the fact that participating

residues aS199, aN214, and aQ252 are polar but not ionizable, and the distances between these

residues are too far apart for direct proton transfer. However, they are positioned at distances that

can support a water column. Although aQ252 is highly conserved, glycine or hydrophobic groups

naturally occur at positions aN214 (e.g., *T. gondii, and T. thermophilus*), aH245 (e.g., *M. phlei, T.*

thermophila, A. woodiii, T. gondii, I. tartaricus, F. nucleatum, and T. thermophilus) and for aE219

(e. g. *T. thermophila, E. gracilis, B. pseudofirmus $_OF4$, P. angusta, S. cerevisiae*, and *A. platensis*

PCC9438). Such mutations can be tolerated if the primary role of these groups is to support a

water column that transfers protons. Mutation of one residue may disrupt the Grotthuss water

column, but still allow it to function, albeit less efficiently.

The presence of a Grotthuss water column is also supported by 2.7-Å cryo-EM structures of yeast V_O that revealed ordered water molecules in the luminal half-channel (equivalent to ATP synthase proton input half-channel in F_O). The putative water molecules detected in the cryo-EM density were consistent with the statistically probable water clusters observed by near-atomic resolution cryo-EM structure–based molecular dynamics (MD) simulations. MD simulations showed a network of hydrogen-bonded water molecules that connects the proton-carrying subunit-c glutamates to a conserved glutamic acid (aE789 in yeast) located at the entry of the luminal half-channel. The MD simulations revealed that this "water wire" is disrupted after the subunit-c glutamate is deprotonated and aE789 in the luminal half-channel is protonated. This mechanism is postulated to prevent the protons from leaking back from the luminal half-channel into the interface between subunit-a and the c-ring (Roh *et al.*, 2020).

11° sub-step of the F_O c-ring in ATP synthesis direction

In chapter 3, the analysis of TDs revealed a pH-dependent 11° sub-step of the c-ring in the ATP synthesis direction that can overcome the opposing F_1-ATPase-dependent rotation. Measurements of the rotation of subunit-a mutants suggested that this 11° c-ring sub-step occurs when the protons are transferred from the subunit-a input channel with a low pKa to the c-ring, and when the protons are transferred from the c-ring to the output channel with a high pKa. TDs are most likely to occur when the protonation states of both half-channels are favorable for proton translocation between them and the c-ring.

These results support a mechanism in which 36° rotational stepping facilitated by individual c-subunits in the c-ring during ATP synthesis is dependent on an 11° sub-step caused by proton translocation between the cD61 residues on subunit-c and the subunit-a proton half-channels. The remaining 25° sub-step is postulated to result from an electrostatic interaction between the unprotonated, negatively charged cD61 that just donated a proton to the output half-channel, and the positively charged aR210 residue in subunit-a.

Chapter 2 and 3 discussed how the probability of TDs at each pH condition did not fit a single Gaussian curve, but instead fit three curves. This suggested that the asymmetry of the three ATPase-dependent 120° power strokes cause high, medium, and low efficiencies of c-ring stepping in CW (ATP synthase) direction, which were represented by the three probabilities of TD formation. The asymmetry of the three power strokes is likely to be caused by the misalignment between the F_O and F_1 rotations, as well as the relative positions of the central and peripheral stalks that changes between the three power strokes.

In Appendix A, the data shown in chapters 2 and 3 were corroborated by two other single-molecule measurements of the F_OF_1 rotation: fluorescence video-microscopy with attached actin filaments and Förster resonance energy transfer between pairs of fluorescence probes. When the dwell times of the F_OF_1 rotations were compared between the different methods, asymmetric rotational behavior was observed from all three techniques. The results showed that one dwell in the three-stepped rotary progression lasts longer than the other two by a factor of up to 1.6, which was consistent with the high, medium, and low probabilities of transient dwell formation shown in Chapter 2.

This rotational asymmetry was small, but it provided evidence that the structural asymmetry of the F_OF_1 influences its rotational dynamics and causes rotational asymmetry. The effect of structural asymmetry on the rotation was likely small because the internal elastic coupling between the F_1 and F_O motors by the flexibility of the peripheral stalk and the flexible interface between the c-ring and the central rotor dampens the effects of the structural asymmetry on the rotation.

Analyzing the cryo-EM structures of the F_OF_1 in the context of the three probabilities of TD occurrences described in chapters 2 and 3 and the asymmetric rotation of F_OF_1 shown in appendix A provided insight into the mechanism behind the asymmetric rotation of the F_OF_1. The Cryo-EM structures of *E. coli* F_OF_1 showing three states with different positions of the central stalk likely correspond to the three 120° rotary positions of the catalytic dwells (**Figure 46**).

Comparison of the c_{10}-ring rotary positions relative to subunit-a between State 1 (PDB-ID: 5T4O) and State 2 (5T4P) shows the c-ring shifted by four c-subunits, which is 144° apart (36° × 4). When State 2 and State 3 (5T4Q) are compared, they are three c-subunits apart in rotational positions, which is 108° apart (36° × 3). Finally, the difference between state 3 back to State 1 is also three c-subunits with 108° rotation.

It was concluded that the transition from State 3 to State 1 (denoted power stroke-3 in **Figure 46**) corresponds to the power stroke with a high probability of TD formation shown in chapter 2 because in state 3, the proton carrying cD61 residue on subunit-c (**Figure 46** chain P) is aligned with subunit-a residue aR210 (black line), and in state 1, the c-ring has rotated 108° relative to the state 3 (green line), which is less than the 120° rotation induced by the F_1 motor (red line). This 12° asymmetry between the c-ring rotation and the F_1 causes elastic energy to be stored between F_O and F_1 in a manner that promotes CW rotation of the c-ring in the ATP synthesis direction, which promotes the formation of TDs. The next transition from State 1 to state 2 (power stroke-1) would correspond to the power stroke with a low probability of TD formation because in state 2, the 120° rotational position of the F_1 lags behind the 144° rotational position of the subunit-c ring caused by the transfer of four protons by four c-subunits. Unlike the asymmetry between the F_O and F_1 during power stroke-3 that promotes the CW rotation of the c-ring, the misalignment here would discourage the CW rotation and would hinder the formation of TDs. Finally, the transition from state 2 to state 3 (power stroke-1) restores the alignment between F_O and F_1 rotations, which would not generate elastic energy and therefore would not promote or hinder the formation of TDs. This power stroke likely corresponds to the medium probability of TDs formation.

The cryo-EM structures also showed that during power stroke-1, a portion of γ-subunit that protrudes out from the central rotor must pass through the narrow gap created by the F_1 (αβ)$_3$-ring, the F_O c-ring, and the peripheral stalk. This is also the power stroke in which four protons are translocated instead of three. This extra proton translocated in this power stroke may be necessary to overcome the energy requirement for the γ-subunit to pass through the gap.

During power stroke-2, there is nothing in the central stalk that would have to fit through the same gap. And during power stroke-3, subunit-ε that also protrudes from the central rotor must pass through the gap. It may be possible that this contributes to the high probability of TD formation that is hypothesized to occur during power stroke-3.
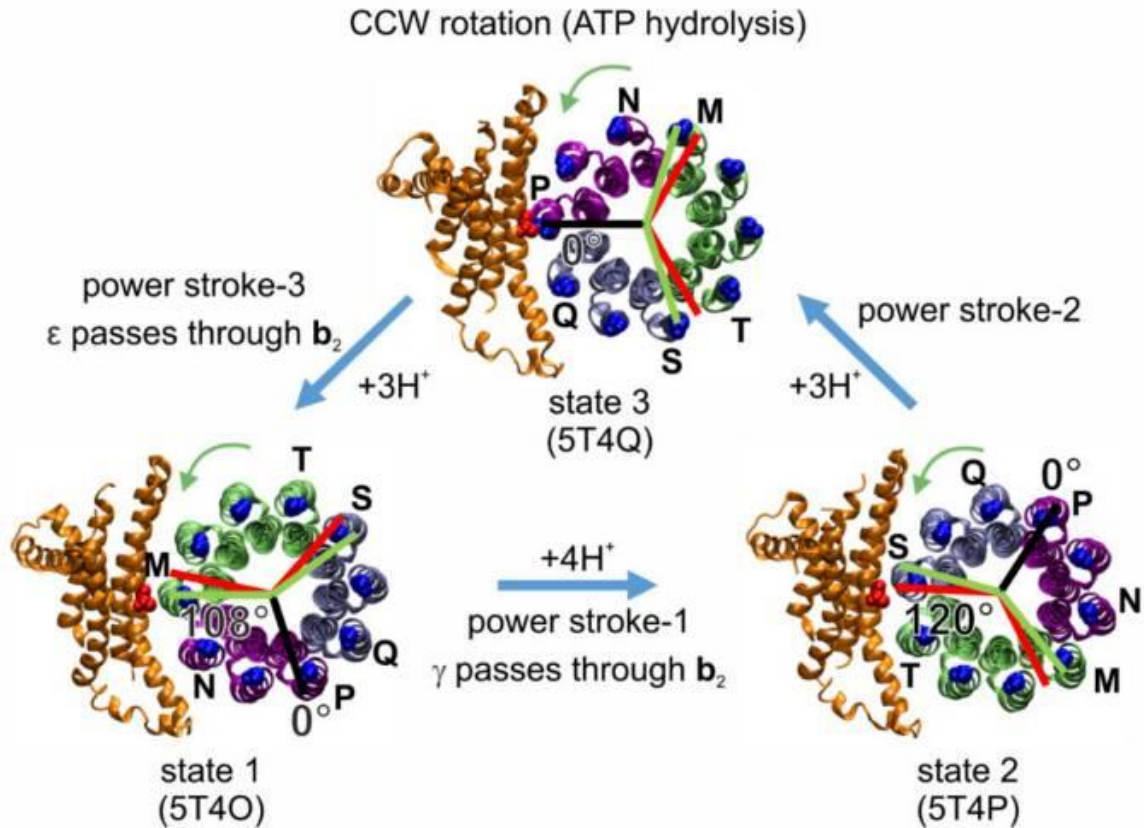
Figure 46. Asymmetry between the three F_1-ATPase power strokes of *E. coli* F_OF_1, as shown by the rotary positions of residue cD61 in each c-subunit (blue) relative to aR210 (red) in the three states of the *E. coli* F_OF_1 cryo-EM structures (viewed from the membrane side) designated by their PDB-ids (Sobti et al., 2016). In structure 5T4Q, cD61 of c-subunit chain P is closely aligned with aR210 (black line designates 0° of rotation). Assuming this state shows the alignment with a catalytic dwell position in F_1, red lines show the other two 120° rotational positions of the catalytic dwells in F_1 during subsequent power strokes. Green lines show the 108° rotations that result from the three proton-dependent CCW rotational steps (green arrows) of the c-ring that occur during the power strokes, which results in strain between the catalytic dwell positions of F_O and F_1. From state 3 to state 1 (three c-subunits, purple), and from state 2 to state 3, the c-ring rotates by 108° (three c-subunits, ice blue), whereas from state 1 to state 2, the c-ring rotates by 144° (four c-subunits, lime).

In Chapter 4, the subunit-c ring of the *E. coli* F_OF_1 was modified with the intent of changing the stoichiometry of c-ring, which would alter the number of protons that are translocated for each 120° power stroke of the F_1 motor. The chimeras Pd-c12, Sp-c15 with anticipated c-ring sizes of c_{12} and c_{15}, respectively, showed the lowest ATP synthesis rates along with the Bp-c17 chimera. These results are consistent with the hypothesis that structural and rotational asymmetry between the F_1 and F_O play an important role in the enzymatic function of the ATP synthase. The Pd-c12 and Sp-c15 F_OF_1 lack the asymmetry between the two motors, therefore they are not able to generate the extra energy in one of the three 120° F_1 power stroke necessary to overcome the energy barrier of subunit-γ squeezing though the narrow space. They may also lack the elastic energy generated from the asymmetry between the three F_1 power strokes and the F_O stepping, given that their c-ring stoichiometry is in the multiple of three subunits. However, the ATP synthesis rate of Ms-c9, which also lacks the asymmetry between F_OF_1, was relatively high. This may be because of a higher dependence on the Δψ to drive ATP synthesis by F_OF_1 containing a small c-ring. Small c-ring likely depend more on the c-ring stepping driven by the electrostatic interaction between the unprotonated cD61 and aR210 to drive ATP synthesis over the proton translocation-dependent stepping.

The effects of altering the c-ring stoichiometry on the function of the F_OF_1

In chapter 4, nine chimeras of the *E. coli* F_OF_1 were constructed using the inner (N-terminal) helix sequences of subunit-c derived from species of organisms that are known to contain a c_8 to c_{17}-ring in their F_OF_1. Western blot, growth curves, ATP synthesis assay, ATP hydrolysis assay, and ACMA quenching assay all showed that altering the inner helix of the c-ring allowed functional F_OF_1 to be expressed and assembled in the *E. coli* strains.

The growth curves of the *E. coli* strains were measured in succinate medium that forces the cells to rely on the F_OF_1 as the only source of ATP production. The results showed no significant overall trend in growth rate vs. anticipated c-ring size. However, the Bt-c8 and the So-c14 chimeras, in which the subunit-c sequences were derived from bovine mitochondrial F_OF_1

and spinach chloroplast F_OF_1, respectively, showed the highest growth rate of all *E. coli* strains. This suggested that ATP-producing organelles in eukaryotic cells have optimized the c-ring size to maximize ATP synthesis.

The ATP synthesis rates of the chimeras showed that as the anticipated c-ring size increased, the ATP synthesis rates decreased in a consistent manner with the H^+/ATP ratio of the anticipated c-ring sizes. Furthermore, the ATP synthesis rates of F_OF_1 with smaller c-ring sizes (c_8 – c_{11}) were dramatically increased when the PMF was composed of ΔpH and $\Delta\Psi$ of -150 and -60 mV, respectively, as opposed to when the PMF was composed of only ΔpH. However, this effect was not as significant with the larger c-ring sizes (c_{13} – c_{17}), in which the ATP synthesis activities were similar between the three ΔpH $\Delta\Psi$ conditions tested.

The results shown in chapter 4 suggest that higher ATP synthesis rate with smaller c-ring in the presence of $\Delta\Psi$ results from the membrane potential-dependent step of the c-ring following the proton translocation-dependent 11° step shown in chapter 3. The two-step c-ring rotation mechanism shown in chapter 3 suggests that the proton translocation-dependent sub-step remains 11° regardless of c-ring size so long as a tight interface between subunit-a and the c-ring is maintained at the point where deprotonation of subunit-c forces the charged carboxyl group to move from the hydrophobic lipid bilayer. The decreased coupling in the Bp-c17 chimera evident by the small extent of ACMA fluorescence quenching may be the result of the inability of subunit-a to form a tight interface with such a large c-ring. Since rotational c-subunit stepping of a c_8-ring and a c_{15}-ring is 45° and 24°, respectively, the membrane potential-dependent step will be significantly larger for the smaller c-ring, which is consistent with the results presented in chapter 4.

The effect of c-ring modification was much more dramatic on the ATP synthesis rates compared to the growth rates. Results here suggest that *E. coli* cells have a mechanism that allows it to compensate for the loss of ATP synthesis activity by increasing the expression level of the F_OF_1.

Chapter 6

METHODS

<u>Mutagenesis of F$_O$F$_1$ ATP Synthase</u>

The F$_O$ subunit-a mutant plasmids were constructed from the pNY1^{-Ase} or pNCcys plasmid containing the entire unc operon with a 6-His tag on the N-terminus of subunit-β and a cysteine inserted at the second position of subunit c (c2∇Cys), described previously by Ishmukhametov *et al.*, 2010. The aN214L, aQ252L, aH245L, aE219L, and aE196L mutations were made on the plasmid using QuikChangesII-XL Site-Directed Mutagenesis Kit (Agilent). *E. coli* strain DK8, which lacks the unc operon, was transformed with the mutant plasmid.

<u>Purification of F$_O$F$_1$ ATP Synthase</u>

To purify the F$_O$F$_1$, *E. coli* cells were grown in 8L of LB + 50 µg/mL ampicillin at 37° while being shaken in baffled flasks at 170 rpm, the cells were pelleted by centrifuging at 6k RPM for 10 min at 4°C and the cell pellet was stored at -80° C. All following steps were conducted at 4°C. The cell pellet was thawed, homogenized with French Press Buffer (200 mM Tris-HCl/pH 8.0, 100 mM KCl, 5 mM MgCl$_2$, 0.1 mM EDTA, and 2.5% (v/v) glycerol), and the cells were lysed by passing through the French Press twice. Cell lysate was spun at 7k RPM to pellet the cell debris and any cells that were not lysed. The supernatant was centrifuged at 50k RPM for 1 hour to pellet the cell membrane. The cell membrane was homogenized in F$_O$F$_1$ detergent solubilization buffer (50 mM Tris-HCl/pH 8.0, 100 mM NaCl, 5 mM MgCl$_2$, 15 mM β-DDM, 40 mM ε-aminocaproic acid, 15 mM 4-aminobenzamidine, and 200 mM sucrose) and incubated for 1 hour while gently rotating on a rotator drum. After incubation, the cell membrane was pelleted down by centrifuging at 50k RPM for 45 min. The supernatant was passed through a 5 mL Ni-NTA His-trap on an FPLC equilibrated with the Ni column wash buffer (50 mM Tris-HCl/pH 8.0, 100 mM NaCl, 5 mM MgCl$_2$, 1.5 mM β-DDM, and 30 mM imidazole) at 3 mL/min, the Ni column was washed with 60 mL of Ni column wash buffer, and the F$_O$F$_1$ was eluted with Ni column elution buffer (50

mM Tris-HCl/pH 8.0, 100 mM NaCl, 5 mM $MgCl_2$, 1.5 mM β-DDM, and 300 mM imidazole). The

eluted F_OF_1 was spin-concentrated using a 100 kDa MWCO spin-concentrator and ran through a

Superose6 size-exclusion column equilibrated with the SEC buffer (50 mM Tris-HCl/pH 8.0, 100

mM NaCl, 5 mM $MgCl_2$, and 0.02% (w/v) β-DDM). The fraction containing F_OF_1 was spin-

concentrated using a 0.5 mL 100 kDa MWCO spin-concentrator to a concentration of 5 to 10

mg/mL.

Preparation of Nanodisc F_OF_1

To form nanodiscs, membrane scaffold protein MSP-1E3D1 was used. The MSP was

prepared by removing the His-tag with overnight TEV protease digestion at room temperature (at

25:1 ratio, w/w). Cleaved MSP was purified by passing through a Ni-NTA column. To incorporate

the F_OF_1 into nanodiscs, a 1:4 molar ratio of F_OF_1:MSP was mixed with the addition of sodium

cholate to a concentration of 1%. To biotinylate the cysteine residue inserted at the N-terminus of

subunit-c, a 10-fold molar excess of biotin maleimide was added to the F_OF_1. The mixture was

gently shaken for 15 min to form biotinylated F_OF_1 nanodisc. The sample was desalted by running

through a Sephadex G-50 column equilibrated with Buffer A (50 mM Tris-HCl/pH 8.0, 100 mM

NaCl, 6% (v/v) glycerol, 4 mM 4-aminobenzamidine, and 5 mM $MgCl_2$). The sample was

aliquoted into 50 μL and quick frozen with liquid nitrogen until use. The presence of all F_OF_1

subunits and the MSP in each preparation was confirmed by SDS-PAGE.

Gold-Nanorod Single-Molecule Experiments

Rotation of individual nanodisc F_OF_1 molecules were observed by single-molecule

rotation assay. Purified nanodisc F_OF_1 were immobilized on a microscope slide by the His-tag on

subunit-β, unbound enzymes were washed off the slide with wash buffer (30 mM Tris, 30 mM

PIPES, 10 mM KCl, at the appropriate pH), 80 × 40 nm gold nanorod coated with avidin was

bound to the biotinylated c-ring of *E. coli* nanodisc F_OF_1, excess gold nanorod were washed off

with the wash buffer, and rotation buffer (1 mM Mg^{2+} ATP, 30 mM Tris, 30 mM PIPES, 10 mM

KCl, at the pH indicated) was added to the slide. The rotation of individual molecules was observed by measuring the change in intensity of polarized red light scattered from the gold nanorod using a single-photon detector. In each molecule observed, the rotation of the nanorod attached to an active nanodisc F_OF_1 complex was confirmed by the change in scattered light intensity as a function of the rotational position of the polarizing filter as described previously (Spetzler *et al.*, 2006; Hornung *et al.*, 2011). To make the measurement of nanodisc F_OF_1 undergoing power strokes, the orientation of the polarizing filter was adjusted to align with the minimum light intensity position that that corresponded to one of the three catalytic dwells. The sinusoidal change of polarized red light intensity was measured as the gold nanorod rotated from 0° to 90° relative to the catalytic dwell position. Measurements were taken in the form of 5 s data set at frame rate of 100 kHz. The occurrence of TDs in each subunit-a mutant was analyzed at varying pH from 5.0 to 8.0. TDs that occurred during the power strokes in the recorded data sets were analyzed by determining the $\arcsin^{1/2}$ of the intensity at each time point (Martin *et al.*, 2018; Martin *et al.*, 2015; Sielaff *et al.*, 2016).

Generating the c-ring Chimeras

To express the wild-type *E. coli* F_OF_1 ATP synthase for the experiments, *E. coli* strain DK8 that lacks the *Unc* operon, which encodes all the F_OF_1 subunits, was transformed with an expression vector *pNCcys* that contains the *Unc* operon and an ampicillin resistance gene. The *Unc* operon in this plasmid has been modified to remove all cysteine residues and insert a cysteine at the N-terminus of the subunit-c (c2▽C) to carry out the gold-nanorod single molecule experiments. In addition, a 6His-tag has been inserted to the N-terminus of subunit-β for purification and to carry out the gold-nanorod single molecule experiments as described previously (Ishmukhametov *et al.*, 2010).

To express the F_OF_1 ATP synthase with varying sizes of the c-ring, polypeptide sequences of subunit-c from various species that have been shown to express different sizes of c-rings were used. The species of subunit-c sequences selected were *Bos Taurus* c_8,

143

Mycobacterium smegmatis c_9, *Saccharomyces cerevisiae* c_{10}, *Fusobacterium nucleatum* c_{11}, *Paracoccus denitrificans* (strain Pd 1222) c_{12}, *Synechococcus elongatus* (strain PCC 7942 / FACHB-805) (aka *Anacystis nidulans* R2) c_{13}, *Spinacia oleracea* c_{14}, *Spirulina platensis* (aka *Arthrospira platensis*) c_{15}, and *Burkholderia pseudomallei* c_{17}. Chimeric *E. coli* generated using these sequences were denoted as Bt-c8, Ms-c9, Sc-c10, Fn-c11, Pd-c12, Se-c13, So-c14, Sp-c15, and Bp-c17.

To express these c-subunits in *E. coli*, the protein sequences were codon-optimized for *E. coli* and DNA fragments encoding the various subunit-c genes were synthesized. In all nine DNA fragments, a codon encoding a cysteine residue was inserted into position 2 to carry out the single-molecule experiments. Then, the WT c-subunit gene was removed from the *Unc* operon in the expression vector by introducing NotI and BspEI restriction sites to the 3' and 5' flanking regions of the subunit-c gene, respectively, and carrying out restriction digestion. Finally, the DNA fragment containing a foreign subunit-c gene (also digested with NotI and BspEI) was ligated into the plasmid. *E. coli* codon-optimization and DNA fragment synthesis was ordered on Integrated DNA Technologies.

The *E. coli* DK8 competent cells were transformed with the chimeric plasmids by heat shock and plated on LB agar + 50 µg/mL ampicillin. Colonies that grew in the presence of ampicillin were inoculated in LB + 50 µg/mL ampicillin, plasmid was purified from the cell culture and sequenced to confirm the successful transformation. Frozen permanent culture was made from the cell culture for further experiments.

To generate the Glu into Asp mutants, plasmid was purified from each chimeric *E. coli* cells and the H^+-carrying Glu residue (cD61 in WT *E. coli*) was substituted by the Asp residue by site-directed mutagenesis. The *E. coli* DK8 competent cells containing no plasmid was transformed with the mutated plasmid by heat shock and grown on LB agar + 50 µg/mL ampicillin to select for transformed cells. The mutation was confirmed by Sanger sequencing and permanent culture were made.

144

To generate the chimeras expressing a c-ring with a foreign inner helix and WT *E. coli* outer helix, DNA fragment was designed to contain the different species' inner helix sequence (codon optimized for *E. coli*) on the N-terminus side, followed by the *E. coli* "RQPD" looped region of and the outer helix sequence on the C-terminus side derived from the *E. coli* subunit-c. The DNA fragment was inserted into the expression vector and the competent *E. coli* cells were transformed as described above.

Then, the chimeric subunit-c DNA insert was modified so that only the inner helix that is thought to determine the c-ring size was of the foreign origin, and the sequence from the looped region to the outer helix that interacts with subunit-a was maintained as WT *E. coli* sequence.

TEM imaging

To image the purified F_OF_1 by negative staining TEM, the protein sample was diluted to 0.005, 0.002, and 0.001 mg/mL, applied to Holey Carbon Film CF-2/1-3C, 300 mesh Copper grids (Electron Microscopy Sciences), and stained with 2% uranyl acetate. The grids were imaged by Talos L120C TEM at 120 kV.

To image the F_OF_1 by cryo-EM, the protein samples were diluted to 3.0, 1.5, 0.6, and 0.3 mg/mL, loaded on Holey Gold Film R 2/2 on Gold 300 mesh grids (Electron Microscopy Sciences), and plunge frozen using Vitrobot Mark IV (Thermo Scientific). The plunge freezing condition was 22 °C, 100% humidity, 1 s blot time, and -1 blot pressure. The grids were imaged by Titan Krios 80/300 KeV.

Inverted Membrane Vesicles

Inverted membrane vesicles were generated form the chimeric *E. coli* cells to perform the western blot and the ensemble biochemical assays. The chimeric cells were grown in 50 mL LB + 50 µg/mL ampicillin overnight at 37°C, the cell culture was inoculated into 500 mL LB + 50 µg/mL ampicillin and grown for 3 hours, the cells were spun down at 6k RPM for 10 min at 4°C and the cell pellet was stored at -80° C. The cell pellet was thawed and homogenized in 25 mL French

Press Buffer (200 mM Tris-HCl/pH 8.0, 100 mM KCl, 5 mM $MgCl_2$, 0.1 mM EDTA, and 2.5% (v/v) glycerol), and the cells were inverted by passing through the French Press twice. The cell lysate was spun at 7k RPM to pellet the cell debris and any cells that were not lysed. The supernatant was centrifuged at 50k RPM for 1 hour to pellet the IMV. The IMV was homogenized in different volumes of different buffers depending on the experiments described below.

<u>Measurement of the F_OF_1 expression by Western blot</u>

The expression of F_OF_1 in each chimeric cell was measured by Western blot. The IMV pellet was homogenized in 1 mL of French Press buffer, the protein concentrations of the homogenized IMV for each chimera was measured by BCA assay, 10 μg protein worth of each IMV was ran on a 4-15% gradient SDS-PAGE gel. The proteins on the gel were transferred on a PVDF membrane and the bands were labeled using rabbit primary antibody against human ATP synthase subunit-β. The bands were labeled using goat anti-rabbit IgG-AP conjugate (Bio-Rad #1706518).

<u>ATP synthesis assays</u>

The ATP synthesis rates of the chimeric IMV were measured using ATP bioluminescence assay kit CLS II luciferin/luciferase system (Roche Diagnostics). The ΔpH and Δψ across the IMV membrane was established using resuspension buffer 1 and acidic buffer 2 that each contained 20 mM succinate, 20 mM tricine, 50 mM MES, 200 mM NaCl, 5 mM NaH_2PO_4, 5 mM $MgSO_4$, and alkaline buffer 3 that contained 200 mM tricine and varying concentrations of KCl and KOH. To vary the ΔpH, the pH inside the IMV was adjusted to 4.5, 5.5, and 6.5 by adjusting the pH of buffer 2, while the pH outside the IMV was maintained at 8.0 in order to set the ΔpH to 3.5, 2.5, and 1.5, respectively. To vary the Δψ, the [K^+] inside the IMV was adjusted to 20, 10, and 1 mM by adjusting the [KCl] and [KOH] in buffers 1 and 2 while the [K^+] outside the IMV was adjusted to 20, 200, and 200 mM by adjusting the [KCl] and [KOH] in buffer 3, in order to set the ΔΨ to 0, 60, and 120 mV, respectively. Prior to the measurements, the luciferin/luciferase mixture was dissolved in 10 ml of buffer 3. Freshly prepared IMV was resuspended in buffer 1 to a

concentration of ~15 mg protein/mL. For each assay, 30 μL of stock IMV was added to a cuvette that contained 280 μL of buffer 2, and 4 μL of 25 μM valinomycin, incubated for 5 min at 28 °C. Then, 330 μL of luciferin/luciferase mixture dissolved in buffer 3 and 16 μL of 2 mM ADP were added to the cuvette to initiate the ATP synthesis by the F_OF_1. The ATP synthesis rate was determined by measuring the increase in the intensity of 562 nm luminescence using the Cary Eclipse fluorescence spectrophotometer with the photomultiplier tube detector at 800 V and the slit width at 20 nm.

ATP hydrolysis assays

To measure the ATP hydrolysis rates of the chimeric IMV, ATP-regenerating NADH-coupled hydrolysis assays were conducted. The measurement was made with the final concentration of 50 mM Tris/HCl (pH 8.0), 10 mM KCl, 62.5 mM phosphoenolpyruvate, 0.3 mM NADH, 30 U pyruvate kinase, 30 U lactate dehydrogenase, 5 mM ATP, 5 mM $MgCl_2$, and 0.023 – 0.045 mg/mL IMV. The rate was determined as the change in absorbance at 340nm using a Cary 100 spectrophotometer with Peltier temperature control.

Proton Translocation-dependent Quenching of ACMA Fluorescence

The fluorescence of ACMA was excited at 410 nm and monitored at 480 nm using a Cary Eclipse fluorescence spectrometer. Fluorescence quenching was initiated by the addition of a final concentration of 0.8 mM ATP to IMVs suspended in a buffer containing 10mM HEPES (pH 8.0), 100 mM KCl, 5 mM $MgCl_2$, and 0.3 μg/ml of ACMA. The reaction was terminated by addition of carbonyl cyanide p-chlorophenylhydrazone to a final concentration of 5 μg/mL.

Growth curve measurements

To measure the ATP synthase- dependent growth of the chimeric *E. coli* cells, growth curve of each chimeric cells were determined by measuring the OD_{600} of the cells grown in 1L succinate medium containing 60 mM KH_2PO_4, 40 mM NaH_2PO_4, 15 mM $(NH_4)_2SO_4$, 30 mM

147

succinate, 0.6 g/L casein hydrolysate, adjusted to pH 7.3, 1 mM $MgSO_4$, 22 mg/L Uracil, Arg-Ent-Thi containing the final concentrations of 0.8 mM L-arginine, 40.1 µM Dihydrobenzoic acid, and 20 µM Thiamine-HCl, Trace elements with the final concentrations of, 14 µM $ZnSO_4$, 1.01 µM $MnSO_4$, 4.72 µM Boric acid, 0.7 µM $CaSO_2$, 2.5 µM $CaCl_2$, and 1.81 µM $FeCl_3$.

REFERENCES

Abrahams, J., Leslie, G., Lutter, J., and Walker, J. (1994). "Structure at 2.8 Å resolution of F_1-ATPase from bovine heart mitochondria." Nature 370: 621-628.

Adachi, K., Oiwa, K., Nishizaka, T., Furuike, S., Noji, H., Itoh, H., Yoshida, M., and Kinosita, K. (2007). "Coupling of rotation and catalysis in F_1-ATPase revealed by single-molecule imaging and manipulation." Cell 130: 309-321.

Adachi, K., Oiwa, K., Yoshida, M., Nishizaka, T., and Kinosita, K. (2012). "Controlled rotation of F_1-ATPAse reveals differential and continuous binding changes for ATP synthesis." Nat. Commun. 3: 1022.

Allegretti, M., Klusch, N., Mills, D. J., Vonck, J., Kühlbrandt, W., and Davies, K. M. (2015). "Horizontal membrane-intrinsic α-helices in the stator a-subunit of an F-type ATP synthase." Nature. 521: 237-240.

Andries, K., Verhasselt, P., Guillemont, J., Gohlmann, H. W., Neefs, J. M., Winkler, H., Van Gestel, J., Timmerman, P., Zhu, M., Lee, E., Williams, P., de Chaffoy, D., Huitric, E., Hoffner, S., Cambau, E., Truffot-Pernot, C., Lounis, N., and Jarlier, V. (2005). "A diarylquinoline drug active on the ATP synthase of Mycobacterium tuberculosis." Science. 307: 223-227.

Angevine, C. M. and Fillingame, R. H. (2003). "Aqueous access channels in subunit a of rotary ATP synthase." J. Biol. Chem. 278: 6066–6074.

Angevine, C. M., Herold, K. A. G., and Fillingame, R. H. (2003). "Aqueous access pathways in subunit a of rotary ATP synthase extend to both sides of the membrane." Proc. Natl. Acad. Sci. U. S. A. 100: 13179-13183.

Bason, J. V., Montgomery, M. G., Leslie, A. G., and Walker, J. E. (2014). "Pathway of binding of the intrinsically disordered mitochondrial inhibitor protein to F_1-ATPase." Proc. Natl. Acad. Sci. U. S. A. 111: 11305–10.

Bokranz, M., Mörschel, E., and Kröger, A. (1985). Structural and ATP-hydrolyzing properties of the ATP synthase isolated from *Wolinella succinogenes*." Biochim. Biophys. Acta. 810: 84-93.

Boltz, K., and Frasch, W. D. (2005). "Interactions of γT273 and γE275 with the β subunit PSAV segment that links the γ-subunit to the catalytic site Walker homology B aspartate are important to the function of *Escherichia coli* F_1Fo ATP synthase." Biochemistry. 44: 9497-9506.

Boltz, K., and Frasch, W. D. (2006). "Hydrogen bonds between the α and β subunits of the F_1-ATPase allow communication between the catalytic site and the interface of the β catch loop and the γ subunit." Biochemistry. 45: 11190-11199.

Boyer, P. D. and Kohlbrenner, W. E. (1981). "The present status of the binding-change mechanism and its relation to ATP formation by chloroplasts." In Energy Coupling in Photosynthesis, ed. BR Selman, S Selman-Reimer, pp. 231-41. Amsterdam: Elsevier

Bustamante, C., Marko, J. F., Siggia, E. D., and Smith, S. (1994). "Entropic elasticity of lambdaphage DNA." Science 265: 1599-1600.

Cabezon, E., Montgomery, M. G., Leslie, A. G., and Walker, J. E. (2003). "The structure of bovine F_1-ATPase in complex with its regulatory protein IF_1." Nat. Struct. Biol. 10: 744–50.

Cain B. D. and Simoni R. D. (1986). "Impaired proton conductivity resulting from mutations in the a subunit of F_1F_o ATPase in *Escherichia coli*." J. Biol. Chem. 261: 10043-50.

Cain, B. D. and Simoni, R. D. (1988). "Interaction between Glu-219 and His-245 within the a subunit of F_1F_0-ATPase in *Escherichia coli*." J. Biol. Chem. 263: 6606-6612.

Cain, B. D. and Simoni, R. D. (1989). "Proton translocation by the F_1F_0ATPase of *Escherichia coli* Mutagenic analysis of the a subunit." J. Biol. Chem. 264: 3292-3300.

Cingolani, G., and Duncan, T. M. (2011). "Structural basis for inhibition of bacterial ATP synthase by subunit epsilon of the rotor stalk." Nat. Struct. Mol. Biol. 18: 701-707.

Collinson, I. R., Skehel, J. M., Fearnley, I. M., Runswick, M. J., and Walker, J. E. (1996). "The F_1F_0-ATPase complex from bovine heart mitochondria: The molar ratio of the subunits in the stalk region linking the F1 and F0 domains." Biochemistry. 35:12640-12646.

Cook, P. F., and Cleland, W. W. (2007). "Enzyme kinetics and mechanism," in Fundamentals of Protein Structure and Function. ed. E. Buxbaum (London: Garland Science), 325–364.

Cukierman, S. (2006). "Et tu, Grotthuss! and other unfinished stories." Biochim. Biophys. Acta. 1757: 876-885.

Czub, J., and Grubmüller, H. (2011). "Torsional elasticity and energetics of F_1-ATPase." Proc. Natl. Acad. Sci. U. S. A. 108: 7408-7413.

Cruz, J. A., Sacksteder, C. A., Kanazawa, A., and Kramer, D. M. (2001). "Contribution of electric field ($\Delta\psi$) to steadystate transthylakoid proton motive force (pmf) in vitro and in vivo. Control of pmf parsing into $\Delta\psi$ and ΔpH by ionic strength." Biochemistry. 40: 1226–37.

Diez, M., Zimmermann, B., Börsch, M., Konig, M., Schweinberger, E., Steigmiller, S., Reuter, R., Felekyan S., Kudryavtsev V., Seidel, C. A. M., and Gräber, P. (2004). "Proton-powered subunit rotation in single membrane-bound F_0F_1-ATP synthase." Nature Struct. Mol. Biol. 11: 135-141.

Engelbrecht, S., Deckers-Hebestreit, G., Altendorf, K., and Junge, W. (1989). "Cross-reconstitution of the F_0F_1-ATP synthases of chloroplasts and *Escherichia coli* with special emphasis on subunit delta." Eur. J. Biochem. 181: 485-491.

Enoki, S., Watanabe, R., Iino, R. and Noji, H. (2009). "Single-molecule study on the temperature-sensitive reaction of F_1-ATPase with a hybrid F_1 carrying a single beta(E190D)." J. Biol. Chem. 284: 23169-23176.

Etzold, C., Deckers-Hebestreit, G., and Altendorf, K. (1997). "Turnover number of *Escherichia coli* F_0F_1 ATP synthase for ATP synthesis in membrane vesicles." Eur. J. Biochem. 243: 336-343.

Eya, S., Maeda, M., and Futai, M. (1991). "Role of the carboxyl terminal region of H^+-ATPase (F_0F_1) a subunit from *Escherichia coli*." Arch. Biochem. Biophys. 284: 71-77.

Feniouk, B., Koslova, M., Knorre, D., Cherepanov, D., Mulkidjanian, A., and Junge, W. (2004). "The proton-driven rotor of ATP synthase: ohmic conductance (10 fS) and absence of voltage gating." Biophys. J. 86: 4094-4109.

Fillingame, R. H., and Steed, P. R. (2014). "Half-channels mediating H^+ transport and the mechanism of gating in the F_O sector of Escherichia coli F_1F_O ATP synthase." Biochim. Biophys. Acta. 1837: 1063-1068.

Fillingame, R. H., Peters, L. K., White, L. K., Mosher, M. E., and Paule, C. R. (1984). "Mutations altering aspartyl-61 of the omega subunit (uncE protein) of Escherichia coli H+ -ATPase differ in effect on coupled ATP hydrolysis." J. Bacteriol. 158(3): 1078-83.

Fischer, S., Etzold, C., Turina, P., Deckers-Hebestreit, G., Altendorf, K., and Gräber, P. (1994). "ATP synthesis catalyzed by the ATP synthase of Escherichia coli reconstituted into liposomes." European Journal of Biochemistry. 225: 167-172.

Fischer, S. and Gräber, P. (1999). "Comparison of ΔpH and Δψ-driven ATP synthesis catalyzed by the H+-ATPases from Escherichia coli or chloroplasts reconstituted in liposomes". FEBS Lett. 457: 327-332.

Fischer, S., Graber, P., and Turina, P. (2000). "The activity of the ATP synthase from Escherichia coli is regulated by the transmembrane proton motive force." J. Biol. Chem. 275: 30157–30162.

Frasch, W. D. (2000a). "Vanadyl as a probe of the function of the F_1-ATPase-Mg^{2+} cofactor." J. Bioenergetics and Biomembranes. 32: 539-546.

Frasch, W. D. (2000b). "The participation of metals in the mechanism of the F_1-ATPase." Biochim. Biophys. Acta. 1458: 310-325.

Furuike, S., Nakano, M., Adachi, K., Noji, H., Kinosita, K., and Yokoyama, K. (2011). "Resolving stepping rotation in Thermus thermophilus H^+-ATPase/synthase with an essentially drag-free probe." Nat. Commun. 2: 233.

Gao, Y. Q., Yang, W., and Karplus, M. (2005). "A structure-based model for the synthesis and hydrolysis of ATP by F_1-ATPase." Cell. 123: 195-205.

Gledhill, J. R., Montgomery, M. G., Leslie, A. G., and Walker, J. E. (2007). "How the regulatory protein, IF_1, inhibits F_1-ATPase from bovine mitochondria." PNAS. 104: 15671–76.

Greene, M. D., and Frasch, W. D. (2003). "Interactions between γR268, γQ269 and the β subunit catch-loop of E. coli F_1-ATPase are critical for catalytic activity." J. Biol. Chem. 278: 51594-51598.

Guo, H., Courbon, G. M., Bueler, S. A., Mai, J., Liu, J., and Rubinstein, J. L. (2021). "Structure of mycobacterial ATP synthase bound to the tuberculosis drug bedaquiline." Nature. 589: 143-147.

Hahn, A., Vonck, J., Mills, D., Meier, T., and Kühlbrandt, W. (2018). "Structure, mechanism, and regulation of the chloroplast ATP synthase." Science. 360: eaat:4318.

Hartzog, P. E., and Cain, B. D. (1994). "Second-site suppressor mutations at glycine 218 and histidine 245 in the a subunit of F_1F0 ATP synthase in Escherichia coli." J. Biol. Chem. 269: 32313-32317.

Hayek, S. R., Rane, H. S., Karlett J Parra, K. J. (2019). "Reciprocal Regulation of V-ATPase and Glycolytic Pathway Elements in Health and Disease." Front. Physiol. 10: 127.

Hatch, L. P., Cox, G. B., and Howitt, S. M. (1995). "The essential arginine residue at position 210 in the alpha subunit of the *Escherichia coli* ATP synthase can be transferred to position 252 with partial retention of activity." J. Biol. Chem. 270: 29407-29412.

He, J. Y., Ford, H. C., Carroll, J., Douglas, C., Gonzales, E., Ding, S. J., Fearnley, I. M., and Walker, J. E. (2018). "Assembly of the membrane domain of ATP synthase in human mitochondria." Proc. Natl. Acad. Sci. U. S. A. 115: 2988–2993.

Hicks, D. B., Liu, J., Fujisawa, M., Krulwich, T. A. (2010). F_1F_0-ATP synthases of alkaliphilic bacteria: lessons from their adaptations. Biochim. Biophys. Acta. 1797(8): 1362-77.

Hilpert, W., Schink, B., and Dimroth, P. (1984). "Life by a new decarboxylation-dependent energy conservation mechanism with Na^+ as coupling ion." EMBO J. 3: 1665-1670.

Hornung, T., Ishmukhametov, R., Spetzler, D., Martin, J., and Frasch, W. D. (2008). "Determination of torque generation from the power stroke of *Escherichia coli* F_1-ATPase." Biochim. Biophys. Acta- Bioenergetics. 1777: 579-582.

Hornung, T., Martin, J., Ishmukhametov, R., Spetzler, D., and Frasch, W. D. (2011). "Microsecond   resolution of single molecule rotation catalyzed by molecular motors." Methods Mol. Biol. 778: 273-289.

Howitt, S. M. and Cox, G. B. (1992). "Second-site revertants of an arginine-210 to lysine mutation in the a-subunit of the FoF_1-ATPase from *Escherichia coli*: implications for structure." Proc. Natl. Acad. Sci. U. S. A. 89: 9799-803.

Howitt, S. M., Lightowlers, R. N., Gibson, F., and Cox, G. B. (1990). "Mutational analysis of the function of the a-subunit of the $F0F_1$-APPase of *Escherichia coli*." Biochim. Biophys. Acta. 1015: 264-268.

Hwang, W., and Karplus, M. (2019). "Structural basis for power stroke vs. Brownian ratchet mechanisms of motor proteins." Proc. Nat. Acad. Sci. USA. 116: 19777-19785.

Iida, T., Minigawa, Y., Ueno, H., Kawai, F., Murata, T., and Iino, R. (2019). "Single-molecule analysis reaveals rotational substeps and chemo-mechanical coupling scheme of enterococcus hirae V_1-ATPase." J. Biol. Chem. 294: 17017-17030.

Ishmukhametov, R., Hornung, T., Spetzler, D., and Frasch, W. D. (2010). "Direct observation of stepped proteolipid ring rotation in *E. coli* F_0F_1-ATP synthase." EMBO J. 29: 3911-3923.

Itoh, H., Takahashi, A., Adachi, K., Noji, H., Yasuda, R., Yoshida, M., and Kinosita, K. (2004) "Mechanically driven ATP synthesis by F_1-ATPase." Nature. 427: 465-468.

Jiang, W., Hermolin, J. and Fillingame, R. H. (2001) "The preferred stoichiometry of c subunits in the rotary motor sector of Escherichia coli ATP synthase is 10." Proc. Natl. Acad. Sci. U.S.A. 98: 4966-4971.

Junesch, U. and Gräber, P. (1987). "Influence of the redox state and the activation of the chloroplast ATP synthase on proton-transport-coupled ATP synthesis hydrolysis." Biochim. Biophys. Acta. 893: 275-88.

Junesch, U., and Gräber, P. (1991). "The rate of ATP-synthesis as a function of ΔpH and Δψ catalyzed by the active, reduced H+-ATPase from chloroplasts." <u>FEBS Lett.</u> 294: 275-278.

Junge, W., Sielaff, H., and Engelbrecht, S. (2009). "Torque generation and elastic power transmission in the rotary F_OF_1-ATPase." <u>Nature.</u> 459: 364-370.

Kayalar, C., Rosing, J., and Boyer, P. D. (1977). "An alternating site sequence for oxidative phosphorylation suggested by measurement of substrate binding patterns and exchange reaction inhibitions". <u>J. Biol. Chem</u>. 252(8): 2486-2491.

Koga, N., and Takada, S. (2006). "Folding-based molecular simulations reveal mechanism of the rotary motor F_1-ATPase." <u>Proc. Natl. Acad. Sci. U. S. A.</u> 103: 5367-5372.

Krulwich, T. A. (1995) "Alkaliphiles: 'basic' molecular problems of pH tolerance and bioenergetics." <u>Mol Microbiol.</u> 15(3): 403-10.

Kühlbrandt, W. (2019). "Structure and mechanism of F-type ATP synthases." <u>Annu. Rev. Biochem.</u> 88: 515-549.

Kushmerick, M. J., Meyer, R. A., and Brown, T. R. (1992a) "Regulation of oxygen consumption in fast- and slow-twitch muscle." <u>Am. J. Physiol.</u> 263: C598-606.

Kushmerick, M. J., Moerland, T. S., and Wiseman, R. W. (1992b) "Mammalian skeletal muscle fibers distinguished by contents of phosphocreatine, ATP, and P_i." <u>Proc. Natl. Acad. Sci. U. S. A.</u> 89: 7521-7525.

Lightowlers, R. N., Howitt, S. M., Hatch, L., Gibson, F., and Cox, G. B. (1987). "The proton pore in the *Escherichia coli* FoF1-ATPase: a requirement for arginine at position 210 of the a-subunit." <u>Biochim. Biophys. Acta.</u> 894: 399-406.

Lightowlers, R. N., Howitt, S. M., Hatch, L., Gibson, F., and Cox, G. B. (1988). "The proton pore in the *Escherichia coli* $F0F_1$-ATPase: substitution of glutamate by glutamine at position 219 of the alpha-subunit prevents F0-mediated proton permeability." <u>Biochim. Biophys. Acta.</u> 933: 241-248.

Lowry, D., and Frasch, W. D. (2005). "Interactions between β_D372 and γ-subunit N-terminus residues γK9 and γS12 are important for ATP synthase activity catalyzed by the *E. coli* F_OF_1 ATP synthase." <u>Biochemistry.</u> 44: 7275-7281.

Mark, J. E., Eisenberg, A., Graessley, W. W., Mandelkern, L., and Koenig, J. L. (1993). "Physical Properties of Polymers." American Chemical Society, (Washington, DC), 2nd Ed.

Martin, J., Hornung, T., Ishmukhametov, R., Spetzler, D., and Frasch, W. D. (2018). "Elastic coupling power stroke mechanism of the F_1-ATPase molecular motor." <u>Proc. Natl. Acad. Sci. U. S. A.</u> 115: 5750-5755.

Martin, J., Hudson, J., Hornung, T., and Frasch, W. D. (2015). "Fo-driven power stroke rotation occurs against the force of F1ATPase-dependent rotation in the F_OF_1 ATP synthase." <u>J. Biol. Chem.</u> 290: 10717-10728.

Martin, J., Ishmukhametov, R., Hornung, T., Ahmad, Z., and Frasch, W. D. (2014). "Anatomy of F_1-ATPase powered rotation." <u>Proc. Natl. Acad. Sci. U. S. A</u>. 111: 3715-3720.

Meier, T. and Cheuk, A. (2021). "Rotor subunits adaptations in ATP synthases from photosynthetic organisms." Biochem. Soc. Trans. 49(2): 541-550.

Meier, T., Polzer, P., Diederichs, K., Welte, W., and Dimroth, P. (2005). "Structure of the Rotor Ring of F-Type Na+-ATPase from *Ilyobacter tartaricus*. Science. 308: 659-662.

Mitchell, P. (1961). "Coupling of photophosphorylation to electron and hydrogen transfer by a chemiosmotic type of mechanism." Nature. 191: 144-48.

Mitchell, P. (2011). Chemiosmotic coupling in oxidative and photosynthetic phosphorylation. 1966. Biochim. Biophys. Acta. 1807: 1507-1538.

Morales-Rios, E., Montgomery, M. G., A, G., Waler, L., and Walker, J. E. (2015). "Structure of ATP synthase from *Paracoccus denitrificans* determined by X-ray crystallography at 4.0 Å resolution." Proc. Nat. Acad. Sci. USA. 112: 13231-13236.

Mukherjee, S., and Warshel, A. (2011). "Electrostatic origin of the mechanochemical rotary mechanism and the catalytic dwell of F_1-ATPase." Proc. Natl. Acad. Sci. U. S. A. 108: 20550-20555.

Mukherjee, S., and Warshel, A. (2015). "Dissecting the role of the γ-subunit in the rotary-chemical coupling and torque generation of F_1-ATPase." Proc. Natl. Acad. Sci. U. S. A. 112: 2746-2751.

Müller, M., Pänke, O., Junge, W., and Engelbrecht, S. (2002). "F_1-ATPase, the C-terminal end of subunit γ is not required for ATP hydrolysis-driven rotation." J. Biol. Chem. 277: 23308-23313.

Murphy, B. J., Klusch, N., Langer, J., Mills, D. J., Yildiz, Ö., and Kühlbrandt, W. (2019). "Rotary substates of mitochondrial ATP synthase reveal the basis of flexible F_1-F_O coupling." Science. 364: eaaw9128.

Nalin, C. M. and McCarty, R. E. (1984). "Role of a disulfide bond in the gamma subunit in activation of the ATPase of chloroplast coupling factor 1." J. Biol. Chem. 259: 7275-80.

Neukirch, S., Goriely, A., and Hausrath, A. C. (2008). "Chirality of coiled coils: elasticity matters." Phys. Rev. Lett. 100: 038105.

Noji, H., Yasuda, R., Yoshida, M., and Kinosita, K. (1997). "Direct observation of the rotation of F_1-ATPase." Nature. 386: 299-302.

O'Neal, C. C., and Boyer, P. D. (1984). "Assessment of the rate of bound substrate interconversion and of ATP acceleration of product release during catalysis by mitochondrial adenosine triphosphatase." J. Biol. Chem. 259: 5761-5767.

Oster, G., Wang, H., and Grabe, M. (2000). "How Fo-ATPase generates rotary torque." Philos. Trans. R. Soc. Lond., B, Biol. Sci. 355: 523-528.

Pänke, O., Cherepanov, D. A., Gumbiowski, K., Engelbrecht, S., and Junge, W. (2001). "Viscoelastic dynamics of actin filaments coupled to rotary F-ATPase: angular torque profile of the enzyme." Biophys. J. 81: 1220-1233.

Panyukov, S., and Rabin, Y. (2000). "Thermal fluctuations of elastic filaments with spontaneous curvature and torsion." <u>Phys. Rev. Lett.</u> 85: 2404-2407.

Pinke, G., Zhou, L., and Sazanov, L. (2020). "Cryo-EM structure of the entire mammalian F-type ATP synthase." <u>Nat. Struct. Molec. Bio.</u> 27: 1077-1085.

Pogoryelov, D., Klyszejko, A. L., Krasnoselska, G. O., Heller, E., Leone, V., Langer, J. D., Vonck, J.,Müller, D. J., Faraldo-Gómez, J. D., and Meier, T. (2012). "Engineering rotor ring stoichiometries in the ATP synthase." <u>Proc. Natl. Acad. Sci</u>. 109(25): E1599–E1608.

Pogoryelov, D., Krah, A., Langer, J. D., Yildiz, Ö., Faraldo-Gómez, J. D., and Meier, T. (2010). "Microscopic rotary mechanism of ion translocation in the F_O complex of ATP synthases." <u>Nat. Chem. Bio.</u> 6: 891-899.

Pogoryelov, D., Reichen, C., Klyszejko, A. L., Brunisholz, R., Muller, D. J., Dimroth, P., and Meier, T. (2007). "The oligomeric state of c rings from cyanobacterial F-ATP synthases varies from 13 to 15." <u>J. Bacteriol.</u> 189(16): 5895-902.

Preiss, L., Klyszejko, A. L., Hicks, D. B., Liu, J., Fackelmayer, O. J., Yildiz, Ö., Krulwich, T. A., and Meier, T. (2013). "The c-ring stoichiometry of ATP synthase is adapted to cell physiological requirements of alkaliphilic *Bacillus pseudofirmus* OF4." <u>Proc. Natl. Acad. Sci</u>. 110(19): 7874-7879.

Preiss, L., Yildiz, O., Hicks, D. B., Krulwich, T. A. and Meier, T. (2010) "A new type of proton coordination in an F1Fo-ATP synthase rotor ring." <u>PLoS Biol.</u> 8: e1000443.

Pu, J., and Karplus, M. (2008). "How subunit coupling produces the gamma-subunit rotary motion in F_1-ATPase." <u>Proc. Natl. Acad. Sci. U. S. A.</u> 105: 1192-1197.

Pullman, M. E., Penefsky H., and Racker E. (1958). "A soluble protein fraction required for coupling phosphorylation to oxidation in submitochondrial fragments of beef heart mitochondria." <u>Arch. Biochem. Biophys.</u> 76: 227-30.

Pullman, M. E. and Monroy, G. C. (1963). "A naturally occurring inhibitor of mitochondrial adenosine triphosphatase.) <u>J. Biol. Chem.</u> 238: 3762–69.

Ragunathan, R., Sielaff, H., Sundararaman, L., Biukovic, G., Sony, M., Manimekalai, S., Singh, D., Kundu, S., Wohland, T., Frasch, W., Dick, T., Grüber, G. (2017). "The uniqueness of subunit α of mycobacterial F-ATP synthases: An evolutionary variant for niche adaptation." <u>J. Biol. Chem.</u> 292: 11262-11279.

Rao, R. and Senior. A. E. (1987). "The properties of hybrid F1-ATPase enzymes suggest that a cyclical catalytic mechanism involving three catalytic sites occurs." <u>J. Biol. Chem.</u> 25: 17450-54.

Richter, M. L., Snyder, B., McCarty, R. E., and Hammes, G. G. (1985). "Binding stoichiometry and structural mapping of the epsilon polypeptide of chloroplast coupling factor 1." <u>Biochemistry.</u> 24: 5755-5763.

Ritchie, R. J. (1991.) "Membrane potential and pH control in the cyanobacterium Synechococcus R-2 (Anacystis nidulans) PCC 7942." <u>J. Plant Physiol.</u> 137: 409-418.

Roh, S.-H., Shekhar, M., Pintilir, G., Chipot, C., Wilkens, S., Singharoy, A., and Chiu, W. (2020). "Cryo-EM and MD infer water-mediated proton transport and autoinhibition of VO complex." Sci. Adv. 6: eabb9605.

Rosing, J., Slater, E. C. (1972). "The value of ΔG° for the hydrolysis of ATP". Biochim. Biophys. Acta. 267: 275–290.

Saita, E.-I., Suzuki, T., Kinosita, K., and Yoshida, M. (2015). "Simple mechanism whereby the F_1-ATPase motor rotates with near-perfect chemomechanical energy conversion." Proc. Natl. Acad. Sci. U. S. A. 112: 9626-9631.

Schulz, S., Wilkes, M., Mills, D. J., Kühlbrandt, W., Meier, T. (2017) "Molecular architecture of the N-type ATPase rotor ring from *Burkholderia pseudomallei*." EMBO Rep. 18(4): 526-535.

Seelert, H., Poetsch, A., Dencher, N. A., Engel, A., Stahlberg, H. and Müller, D. J. (2000). "Structural biology. proton-powered turbine of a plant motor." Nature. 405: 418-419.

Shimabukuro, K., Yasuda, R., Muneyuki, E., Hara, K., Kinosita, K., and Yoshida, M. (2003). "Catalysis and rotation of F_1 motor: cleavage of ATP at the catalytic site occurs in 1 ms before 40 degree substep rotation." Proc. Natl. Acad. Sci. U. S. A. 100: 14731-14736.

Sielaff, H., Martin, J., Singh, D., Biukovic, G., Grüber, G., and Frasch, W. D. (2016). "Power stroke angular velocity profiles of archaeal A-ATP synthase versus thermophilic and mesophilic F-ATP synthase molecular motors." J. Biol. Chem. 291: 25351-25363.

Sielaff, H., Rennekamp, H., Wächter, A., Xie, H., Hilbers, F., Feldbauer, K., Dunn, S. D., Engelbrecht, S., and Junge, W. (2008). "Domain compliance and elastic power transmission in rotary F_OF_1-ATPase." Proc. Natl. Acad. Sci. U. S. A. 105: 17760-17765.

Sielaff, H., Yanagisawa, S., Frasch, W., Junge, W., and Börsch, M. (2019). "Structural asymmetry and kinetic limping of single rotary F-ATP synthases." Molecules. 24: 504-529.

Slooten, L. and Vandenbranden, S. (1989). "ATP-synthesis by proteoliposomes incorporating Rhodospirillum rubrum F0F1 as measured with firefly luciferase: dependence on Δ and ΔpH." Biochim. Biophys. Acta. 976: 150-160.

Sobti, M., Smits, C., Wong, A. S. W., Ishmukhametov, R., Stock, D., Sandin, S., and Stewart, A. G. (2016). "Cryo-EM structures of the autoinhibited *E. coli* ATP synthase in three rotational states." eLife. 5: 21598.

Sobti, M., Walshe, J., Wu, D., Ishmukhametov, R., Zeng, Y. C., Robinson, C. V., Berry, R. M., and Stewart, A. G. (2020). "Cryo-EM structures provide insight into how *E. coli* F_1F_O ATP synthase accommodates symmetry mismatch." Nat. Commun. 11: 2615.

Spetzler, D., Ishmukhametov, R., Day, L. J., Hornung, T., Martin, J., and Frasch, W. D. (2009). "Single molecule measurements of F_1-ATPase reveal an interdependence between the power stroke and the dwell duration." Biochemistry. 48: 7979-7985.

Spetzler, D., Ishmukhametov, R., Hornung, T., Martin, J., York, J., Jin-Day, L., and Frasch, W. D. (2012). "Photosynthesis: plastid biology, energy conversion and carbon assimilation. Advances in Photosynthesis and Respiration," in Energy Transduction by the Two Molecular Motors of the F_1F_O ATP Synthase. Vol. 34. eds. J. J. Eaton-Rye, B. C. Tripathy and T. D. Sharkey (Dordrecht, The Netherlands: Springer), 561–590.

Spetzler, D., York, J., Lowry, D., Daniel, D., Fromme, R., and Frasch, W. D. (2006). "Microsecond time resolution of single molecule F_1-ATPase rotation." Biochemistry. 45: 3117-3124.

Spikes, T. E., Montgomery, M. G., and Walker, J. E. (2020). "Structure of the dimeric ATP synthase from bovine mitochondria. Proc. Natl. Acad. Sci. U. S. A. 117: 23519–23526.

Srivastava, A. P., Lou, M., Zhou, W., Symersky, J., Bai, D., Chambers, M. G., Faraldo-Gómez, J. D., Liao, M., and Mueller, D. M. (2018). "High-resolution cryo-EM analysis of the yeast ATP synthase in a lipid membrane." Science. 360: eaas9699

Steigmiller, S., Turina, P., and Gräber, P. (2008). "The thermodynamic H^+/ATP ratios of the H^+-ATP synthases from chloroplasts and *Escherichia coli*." PNAS. 105: 3745–3750.

Stock, D., Leslie, A. G., and Walker, J. E. (1999). "Molecular architecture of the rotary motor in ATP synthase." Science. 286: 1700-1705.

Stoltzfus, A. (1999). "On the possibility of constructive neutral evolution". J. Mol. Evol. 49: 169-181.

Tanigawara, M., Tabata, K. V., Ito, Y., Ito, J., Watanabe, R., Ueno, H., Ikeguchi, M., and Noji, H. (2012). "Role of the DELSEED loop in torque transmission of F_1-ATPase." Biophys. J. 103: 970-78.

Treloar, L. R. G. (1975). "The Physics of Rubber Elasticity." Oxford University Press, London.

Turina, P., Melandri, B.A. and Gräber, P. (1991). "ATP synthesis in chromatophores driven by artificially induced ion gradients." Eur. J. Biochem. 196: 225-229.

Turina, P., Samoray, D., and Gräber, P. (2003) "H^+/ATP ratio of proton transport-coupled ATP synthesis and hydrolysis catalysed by CF_OF_1-liposomes." EMBO J. 22: 418-426.

Usukura, E., Suzuki, T., Furuike, S., Soga, N., Saita, E., Hisabori, T., Kinosita, K., and Yoshida, M. (2012). "Torque generation and utilization in motor enzyme F_OF_1-ATP synthase: half-torque F_1 with short-sized pushrod helix and reduced ATP synthesis by half-torque F_OF_1." J. Biol. Chem. 287: 1884-1891.

Vik, S. B., Cain, B., Chun, K., and Simoni, R. (1988). "Mutagenesis of the a subunit of the F_1F_O-ATPase from *Escherichia coli*. Mutations at glu-196, pro-190, and ser-199." J. Biol. Chem. 263: 6599-6605.

Vollmar, M., Schlieper, D., Winn, M., Büchner, C., and Groth, G. (2009). "Structure of the c14 rotor ring of the proton translocating chloroplast ATP synthase." J. Biol. Chem. 284(27): 18228-35.

Vonck, J., von Nidda, T. K., Meier, T., Matthey, U., Mills, D. J., Kühlbrandt, W., and Dimroth, P. (2002). "Molecular architecture of the undecameric rotor of a bacterial Na+-ATP synthase". J. Mol. Biol. 321(2): 307-316.

Watanabe, R., Iino, R., and Noji, H. (2010). "Phosphate release in F1-ATPase catalytic cycle follows ADP release." Nat. Chem. Biol. 6: 814-820.

Watt, I. N., Montgomery, M. G., Runswick, M. J., Leslie, A. G., and Walker, J. E. (2010) "Bioenergetic cost of making an adenosine triphosphate molecule in animal mitochondria." Proc. Natl. Acad. Sci. U. S. A. 107(39): 16823-7.

White, S., and Whimley, W. C. (1999). "Membrane protein folding and stability: physical principals." Ann. Rev. Biophys. Biomol. Struct. 28: 319-365.

Wilke-Mounts, S., Weber, J., Grell, E., and Senior, A. E. (1994). "Tryptophan-free *Escherichia coli* F_1-ATPase." Arch. Biochem. Biophys. 309: 363-368.

Wolgemuth, C. W., and Sun, S. X. (2006). "Elasticity of alpha-helical coiled coils." Phys. Rev. Lett. 97: 248101.

Wraight, C. A. (2006). "Chance and design-proton transfer in water, channels and bioenergetic proteins." Biochim. Biophys. Acta. 1757: 886-912.

Yamamoto, H., Cheuk, A., Shearman, J., Nixon, P. J., Meier, T., and Shikanai, T. (2023). "Impact of engineering the ATP synthase rotor ring on photosynthesis in tobacco chloroplasts." Plant Physiol. 192(2): 1221-1233.

Yanagisawa, S., and Frasch, W. D. (2017). "Protonation dependent stepped rotation of the F-type ATP synthase c-ring observed by single-molecule measurements." J. Biol. Chem. 292: 17093-17100.

Yanagisawa, S., and Frasch, W. D. (2021). "pH-dependent 11° F_1F_O ATP synthase sub-steps reveal insight into the F_O torque generating mechanism." eLife. 10: e70016.

Yasuda, R., Noji, H., Yoshida, M., Kinosita, K., and Itoh, H. (2001). "Resolution of distinct rotational substeps by submillisecond kinetic analysis of F_1-ATPase." Nature. 410: 898-904.

Yasuda, R., Noji, H., Kinosita, K. Jr., and Yoshida, M. (1998). "F_1-ATPase is a highly efficient molecular motor that rotates with discrete 120° steps." Cell 93: 1117-1124.

Zarco-Zavala, M., Watanabe, R., McMillan, G. G., Suzuki, T., Ueno, H., Mendoza-Hoffmann, F., García-Trejo, J. J., and Noji, H. (2020). "The 3 x 120° rotary mechanism of *Paracoccus denitrificans* F_1-ATPase is different from that of the bacterial and mitochondrial F_1-ATPases." Proc. Natl. Acad. Sci. U. S. A. 117: 29647-29657.

Zhou, A., Rohou, A., Schep, D. G., Bason, J. V., Montgomery, M. G., Walker, J. E., Grigorieff, N., and Rubinstein, J. L. (2015). "Structure and conformational states of the bovine mitochondrial ATP synthase by cryo-EM." eLife. 4: e10180.

APPENDIX A

STRUCTURAL ASYMMETRY AND KINETIC LIMPING OF SINGLE ROTARY F-ATP

SYNTHASES

Structural Asymmetry and Kinetic Limping of Single Rotary F-ATP Synthases

Hendrik Sielaff [1],*, Seiga Yanagisawa [2], Wayne D. Frasch [2], Wolfgang Junge [3] and Michael Börsch [1]

[1]   Single-Molecule Microscopy Group, Jena University Hospital, Friedrich Schiller University, 07743 Jena, Germany; michael.boersch@uni-jena.de

[2]   School of Life Sciences, Arizona State University, Tempe, Arizona, AZ 85287, USA; seiga@asu.edu (S.Y.); frasch@asu.edu (W.D.F.)

[3]   Department of Biology & Chemistry, University of Osnabrück, 49076 Osnabrück, Germany; junge@uos.de

*   Correspondence: hendrik.sielaff@med.uni-jena.de; Tel.: +49-3641-9-396613

Abstract: F-ATP synthases use proton flow through the F_O domain to synthesize ATP in the F_1 domain. In *Escherichia coli*, the enzyme consists of rotor subunits $\gamma\varepsilon\mathbf{c}_{10}$ and stator subunits $(\alpha\beta)_3\delta\mathbf{ab}_2$. Subunits $\mathbf{c}_{10}$ or $(\alpha\beta)_3$ alone are rotationally symmetric. However, symmetry is broken by the $\mathbf{b}_2$ homodimer, which together with subunit $\delta\mathbf{a}$, forms a single eccentric stalk connecting the membrane embedded F_O domain with the soluble F_1 domain, and the central rotating and curved stalk composed of subunit $\gamma\varepsilon$. Although each of the three catalytic binding sites in $(\alpha\beta)_3$ catalyzes the same set of partial reactions in the time average, they might not be fully equivalent at any moment, because the structural symmetry is broken by contact with $\mathbf{b}_2\delta$ in F_1 and with $\mathbf{b}_2\mathbf{a}$ in F_O. We monitored the enzyme's rotary progression during ATP hydrolysis by three single-molecule techniques: fluorescence video-microscopy with attached actin filaments, Förster resonance energy transfer between pairs of fluorescence probes, and a polarization assay using gold nanorods. We found that one dwell in the three-stepped rotary progression lasting longer than the other two by a factor of up to 1.6. This effect of the structural asymmetry is small due to the internal elastic coupling.

Keywords: F_OF_1 ATP synthase; *Escherichia coli*; single-molecule fluorescence; symmetry; cryo-EM structure; subunit rotation; elasticity

1. Introduction

The F-ATP synthase is a highly flexible and robust motor enzyme [1–8]. ATP synthesis is coupled to the proton motive force (pmf) or ion motive force across the membrane. Under certain physiological conditions, the enzyme can work in reverse and build up an electrochemical potential by hydrolyzing ATP. In *Escherichia coli* (*E. coli*), the F-ATP synthase (EcF$_O$F$_1$) consists of eight different subunits. The eight subunits either belong to the membrane embedded and proton translocating F_O domain ($\mathbf{a}$:$\mathbf{b}_2$:$\mathbf{c}_{10}$), or to the soluble and ATP synthesizing/hydrolyzing F_1 domain (α_3:β_3:γ:δ:ε). Structural details of the EcF$_O$ domain were revealed by NMR [9,10], and the structure of the EcF$_1$ domain was solved by X-ray crystallography [11]. The structure of the holoenzyme (EcF$_O$F$_1$) has recently been solved by cryogenic electron microscopy (cryo-EM), and is shown in Figure 1 [12]. The F$_1$ domain of this EcF$_O$F$_1$ structure is similar to the first crystal structure of the F$_1$ domain of bovine mitochondrial ATP synthase solved by Abrahams et al. [13] that was followed by a series of structures that showed the F$_1$ domain in different conformations [14–22]. Recent cryo-EM structures [23] of various ATP synthases [12,24–29] revealed the symmetric and asymmetric features of this enzyme. In *E. coli* [12], the main body in the F$_1$ domain consists of alternating α and β subunits. Each of the three β subunits

at the interface with the adjacent homologous α subunits carries a catalytic nucleotide-binding site, while the respective nucleotide binding site in subunit α is non-catalytic. Each αβ heterodimer forms a catalytic unit, and faces a different side of the central stalk subunit γ. These three αβ heterodimers sequentially cycle through three different conformations, as revealed by the first crystal structure of bovine mitochondrial F_1 ATP synthase [13]. The $(αβ)_3$-ring surrounds the helices of the C-terminal domain (CTD) and the N-terminal domain (NTD) of subunit γ that forms a curved coiled-coil, which asymmetrically interacts with the β subunits. Distal from the N- and C-termini, the globular domain of subunit γ protrudes from the $(αβ)_3$-ring, where it docks with the globular NTD of subunit ε and the membrane-embedded ring of **c** subunits of F_O. Subunits γ, ε, and the **c**-ring form the central rotor stalk. The symmetry of the central stalk is distorted by the eccentric binding of subunit ε and the curved shaft of subunit γ.
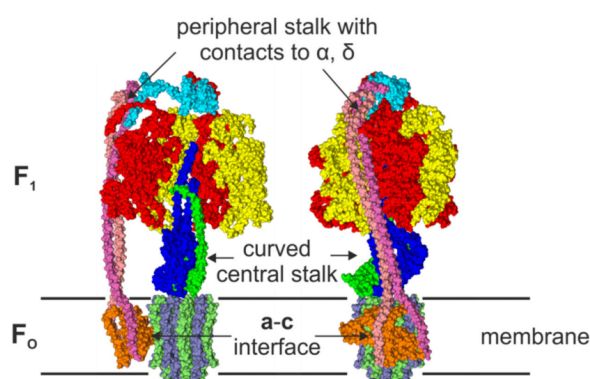
Figure 1. Front view (**left**) and side view (**right**) of a surface representation of the cryo-EM EcF_OF_1 structure (PDB-id: 5T4O) [12] in the membrane. One αβ-pair is omitted in the front view to reveal the conformation of the central stalk. The structure shows the asymmetric features, i.e., the peripheral stalk that is connected to subunit δ and one subunit α, the interface of the **c**-ring and subunit **a** with its two half-channels, and the curved central shaft composed of subunits γε. The subunits are colored in red (α), yellow (β), blue (γ), cyan (δ) green (ε), orange (**a**), pink, and mauve (**b₂**), and ice blue/lime (**c**-ring).

The F_O and F_1 domains are also connected by a peripheral, eccentric stalk. In eubacteria, this stalk is composed of a homodimer of **b** subunits that forms a right-handed coiled-coil [30–32], which is tethered to the δ subunits, and docks to subunit **a** that serves as the interface with the c_{10}-ring. Subunit δ binds to the N-termini of all α subunits at the top of the F_1-head. This rigid stator stalk [33–35] is the most obviously asymmetric feature in F-ATP synthases.

The F_O domain is located within the inner membrane of bacteria. This bioenergetic coupling membrane separates two phases, one that is acidified and electro-positively charged by the respective proton pump (P-side), and the opposite one that is more alkaline and electro-negative than the former (N-side). Within the F_O domain, subunit **a** forms two non-collinear half-channels that connect to either the P-side or the N-side of the membrane, respectively, to provide access for protons and enable protonation of the opposed carboxyl group in each **c** subunit (D61 in *E. coli*), which is located in the middle of the hydrophobic membrane. The number of **c** subunits in the **c**-ring varies between species from 8 to 15 [36–52], but is conserved within species and reflects an adaptation to their environment. In *E. coli*, the ring consists of 10 **c** subunits [53–56].

Functionally, this enzyme consists of two coupled motors, the multi-step motor in F_O (depending on the number of **c** subunits) and the three-step motor in F_1, which are elastically coupled [5,57–60].

In the active enzyme, the stator subunits $(\alpha\beta)_3\delta\mathbf{ab}_2$ and the rotor subunits $\gamma\varepsilon\mathbf{c}_{10}$ rotate against each other. The torque that is generated by the pmf-dependent rotation induced by F_O is used to synthesize ATP in F_1. In reverse, ATP hydrolysis-dependent rotation by F_1 can pump protons through F_O to generate a pmf. The rotation mechanism was coined "binding-change mechanism", and its principals were first described by Boyer [61,62]. He noticed that the release of ATP, but not its formation, requires energy input. Since then, the mechanism has been confirmed by a series of single molecule rotation experiments, first with the F-ATP synthase [56,63–71], and subsequently with the A-ATP synthase and the V-ATPase [72–77]. During ATP hydrolysis, the counterclockwise (CCW) rotation (when viewed from the membrane side) of the central stalk ($\gamma\varepsilon\mathbf{c}_{10}$) progresses in three major steps of $120°$. The constant pauses between steps are characterized by the hydrolysis of ATP and release of Pi, and were coined catalytic dwells [71,78–80]. At low ATP concentrations, a second dwell position appeared, thereby dividing the $120°$ steps into two sub-steps of $80°$ and $40°$ in the $\alpha_3\beta_3\gamma$-complex of Bacillus PS3 [79]. As its duration depended on the ATP concentration, it was named the ATP binding/waiting dwell, accordingly. This second dwell was also found in other bacterial F-ATP synthases, like EcF_OF_1, but not in A/V-type enzymes, where the two dwells are at the same rotor position [73–76,81]. On the other hand, in human mitochondrial F-ATP synthases, and perhaps in all F-ATP synthases of eukaryotic mitochondrial origin as well, a third sub-step was found and associated with the release of Pi [82]. The details of the rotation mechanism have been reviewed elsewhere [2,3,5–8,83,84]

The rotation of central stalk subunit $\gamma\varepsilon$ in the F_1-head is coupled to the rotation of the **c**-ring in F_O. During rotation, each **c** subunit is protonated when it passes one of the two half-channels in subunit **a**. Protons from the P-side can enter one half-channel and in *E. coli* are passed to **c**D61 via **a**R210, thereby neutralizing the negatively charged **c**D61. Due to electrostatic constraints, rotation of the **c**-ring is then required to deliver the proton to the other half-channel to complete translocation of the proton across the membrane to the N-side. This alternating protonation/deprotonation of **c** subunits induces a clockwise rotation that is linked to the rotation of the central stalk subunits γ and ε, resulting in ATP synthesis in the catalytic nucleotide-binding sites. In contrast, during ATP hydrolysis, the γ subunit is forced to rotate CCW and protons are pumped in the opposite direction from the N-side to the P-side, accordingly. This protonation and deprotonation of the **c**-ring works like a Brownian ratchet [85–87] and provides an almost frictionless rotation of the **c**-ring against the stator to ensure high efficiency and high turnover rates [4].

Similar to the F-type are the A-type ATP synthases of archea and V-type ATPases of vacuoles. Although they differ in structure, the fundamental physical and biochemical principals of ATP synthesis/hydrolysis are the same [88,89]. Crystal structures have revealed that they possess two or three peripheral stalks, respectively, that are formed by a heterodimer and do not enter the membrane and do not contact subunit **a** [90–96]. Other differences include a collar-like structure formed by subunit C, located perpendicular to the membrane, which serves as an anchor for the peripheral and central stalks and establishes the contact with the **c**-ring [96,97], as well as the central stalk subunits DF. A structural comparison suggests that the coiled-coil domain of subunit D and the globular domain of subunit F are a structural homolog to the γ subunit of F-ATP synthases, while there is no counterpart of the F-type ε subunit [98–100]. In addition, subunit F acts as an activator for ATP hydrolysis [101].

In total, the various structural data of F-ATP synthases showed several asymmetric elements that are related to the two stalks. Here, we asked whether structural symmetry breaking caused rotary limping of the active enzyme. In order to correlate structural and rotational asymmetry, we studied actively rotating single EcF_OF_1 complexes by three distinct single-molecule fluorescence microscopy techniques.

2. Asymmetric Elements in the F-ATP Synthase

The structural data of the F-ATP synthases and rotation experiments with single molecules revealed a fundamental asymmetry in the composition and function of this enzyme. In summary,

the static asymmetric structural elements of F-ATP synthases, of which variations can also be found in A-type ATP synthases and V-type ATPases, are as follows: (i) the different conformations and nucleotide occupancies of the three β subunits in the F_1-head at any moment; (ii) the interface of the **c**-ring with the eccentric subunit **a** including its two half-channels; (iii) the eccentric position of the peripheral stalk consisting of subunits **a**, δ, and **b**$_2$; (iv) the interaction between the curved central stalk (especially subunit γ) and each αβ heterodimer at any moment; and (v) the portions of subunits γ and ε that extend beyond the diameter of the **c**-ring might impose a drag on rotation when passing the peripheral stalk. In addition, (vi) in the active enzyme, the catalytic dwell times are different for each dwell position.

2.1. The F_1 Domain

The α and β subunits in the F_1-head fold the same way with an N-terminal β-barrel domain, an open α/β domain that forms the catalytic site in subunit β, and a C-terminal helical lever domain. The N-terminal β-barrel domain of these subunits forms a crown around the $(αβ)_3$-ring that stabilizes the complex as rotation-dependent conformational changes in the β subunits occur. In all structures in all types of ATP synthases, the three pairs of catalytic subunits (subunits αβ in F-type, subunits AB in A/V-type complexes) are present in three asymmetric conformations and have different MgATP/MgADP occupancies, reflecting the various states of catalytic reaction. In addition, each αβ-pair has different interfaces with each of the two other αβ-pairs, as each of the three αβ-pairs is in a different catalytic state, even in the absence of the central rotor stalk [102]. This is consistent with the observation that the three catalytic sites bind nucleotides with low, medium, and high affinity only in the presence of Mg^{2+} [103]. It appears that binding of Mg-nucleotides induces conformational changes in the enzyme that are required for its activity. The asymmetric subunits were coined according to their nucleotide occupancy in the first crystal structure from bovine mitochondrial F_1-ATP synthase [13], namely α/β$_{TP}$ for the site with a bound AMP-PNP (a non-hydrolysable ATP analog) with high binding affinity, α/β$_{DP}$ for the site with a bound ADP and medium binding affinity, and α/β$_E$ for an empty and open site with low binding affinity [104]. During catalysis, the three αβ heterodimers unidirectionally cycle through all three conformations with transition states that are represented by different crystal structures. The conformations of the β subunits are coordinated by their position relative to the curved γ subunit via electrostatic interactions. During this process, not only are single domains of subunits moving, but the entire F_1-head is rocking [12]. In total, although the chemical reactions in each nucleotide-binding site are symmetric in the time average, the overall structure of the F_1-head is asymmetric at any particular moment.

2.2. The F_O Domain

In the F_O domain, proton flux across the membrane is realized by the ring of **c** subunits and the peripheral subunit **a** that provides two half-channels for protons to access the **c**-ring. In *E. coli*, each of the ten **c** subunits consists of a hairpin structure with two α-helices that spans the membrane, with an essential D61 that can bind a proton. Together they form a symmetric **c**-ring. At the interface with subunit **a**, the **c**-ring faces the two half-channels, with the essential residue R210 in subunit **a** that mediates proton transport from the medium to subunit **c**. Although the interface is located asymmetrically on one side, each c subunit is exposed to the same conditions when passing the interface, therefore rotational symmetry is maintained. However, as the central stalk subunits γ and ε bind asymmetrically to the **c**-ring, each **c** subunit is unique. Neither is the **c**-ring rotating symmetrically in synthesis and hydrolysis directions, as the two α-helices of each **c** subunit are different.

Cryo-EM structures from different organisms revealed that the two transmembrane helices that comprise the half-channels in subunit **a** cross the membrane at an oblique angle to cover one site of the **c**-ring [105]. When viewed from the membrane side, the two half-channels are asymmetrically arranged: the right semi-channel turns towards the P-side of the membrane, while the left semi-channel faces the N-side, to ensure obliged proton translocation into one direction only that is linked to the

rotation of the central stalk and the catalysis reaction in F_1 [106,107]. Recent experiments have shown that access to the two half-channels is not the same from both sides of the membrane [108].

The ratio of **c** subunits or translocated protons to $\alpha\beta$ heterodimers or catalyzed nucleotides, respectively, is not an integral number. In EcF_OF_1, the ratio is 10/3, i.e., 3.3 protons are translocated to synthesize one ATP molecule. In a rigid coupling of the two motors, a varying number of 3 to 4 protons would be translocated during ATP synthesis that would be the basis for an asymmetric rotation. However, the **c**-ring is elastically coupled to the central shaft in F_1 [58] to provide a smooth rotation [57].

2.3. The Peripheral Stalk

F-ATP synthases have one eccentric peripheral stalk that covers almost the whole complex, i.e., a distance of more than 10 nm. This stalk is the most prominent asymmetric feature of the F-ATP synthase. The $\mathbf{b}_2$ homodimer that forms the main body of this stalk is an intrinsic asymmetric structure, as each individual **b** subunit forms different contacts with other subunits. The helix of one monomer ($\mathbf{b}_N$) that is skewed toward the N-terminus forms contacts with subunit δ at the top and with the N-terminus of one subunit α on the side of the F_1-head. The helix of the other monomer ($\mathbf{b}_C$) is skewed towards the C-terminus and was found in close proximity to one β subunit. The $\mathbf{b}_2$ homodimer interacts with the $\alpha\beta$ heterodimer at a location close to the non-catalytic nucleotide-binding site [109,110], such that it is unlikely to impact nucleotide binding or release at the catalytic site. The $\mathbf{b}_2$ homodimer bifurcates just above the membrane to dock to subunit **a** at two locations [12]. On the other side, subunit δ docks the peripheral stalk via one **b** subunit to the N-termini of the three α subunits. However, the α-δ contact region is different for each α subunit [12], and the $\alpha\beta$-pair that faces $\mathbf{b}_2\delta$ is therefore different than the other two. These structural features all contribute to the asymmetrical nature of the peripheral stalk.

In contrast, A-type and V-type complexes have two and three peripheral stalks, respectively, formed by heterodimers that are structural homologues of the F-type stalk [90–92]. The stalks are asymmetric, as each stalk contacts different subunits and adopts a unique bend that depends on the rotational state of the complex. The two stalks of A-ATP synthases are not directly opposite to each other, but are on each side of one AB-pair [96]. In contrast, the three peripheral stalks in V-ATPases make nearly indistinguishable contacts with the V_1 head, but have different contacts with the collar-like structure [111]. As the ration of AB-pairs to peripheral stalks is 1:1 in V-ATPases, it would be interesting to investigate if this is reflected in a different kind of asymmetry in the rotation pattern of the central stalk subunit DF compared to that of F-ATP synthases.

2.4. The Central Stalk

The central stalk consists of subunits γ and ε in the F_1 and the **c**-ring in the F_O domain. It was revealed by the first crystal structure of the bovine mitochondrial F_1 domain [13] that the curved shaft formed by the coiled-coil double helix of subunit γ interacts at two locations with the β subunits. First, within the cavity of the F_1-head, residues γR268 and γQ269 form a "catch" with a loop in subunit β_E that encompasses residues β297–305. This catch-loop results from salt bridges and H-bond interactions and is important for the activity of the complex [112]. Second, residues γ80–90 form a bulge near the orifice of the central cavity of F_1 that interact with residues β394-400 (DELSEED-loop) at the end of the lever-domain of subunit β_{TP} [13]. In addition, the top of subunit γ forms a swivel joint that can unwind during ATP hydrolysis [113]. On the F_O side, the globular domains of subunits γ and ε form an asymmetric interface with the **c**-ring that breaks its intrinsic symmetry. These elements provide asymmetry to the central shaft that connects the biochemical events in the nucleotide-binding sites to the proton flow in the F_O domain, and are important for unidirectional rotation with high kinetic efficiency, although slow hydrolytic reactions can occur also in the shaft-less $(\alpha\beta)_3$-ring [102,114].

The regulatory subunit ε, which docks to the globular domain of subunit γ, comprises a β-barrel at the NTD, and a helix-turn-helix motive at the CTD. The NTD is located eccentrically on top of the membrane bound **c**-ring, where it rotates together with the globular domain of subunit γ. The CTD of

subunit ε can extend into the $(\alpha\beta)_3$-ring of F_1 and form several contacts with subunits α, β, and γ [11]. In this extended conformation, it acts as an intrinsic inhibitor of ATP hydrolysis. The mechanism of subunit ε inhibition has been reviewed in detail elsewhere [115–117].

During rotation, subunit ε comes close to the $\mathbf{b}_2$ homodimer of the peripheral stalk once every full turn. However, as there is no cryo-EM or crystal structure available when subunit ε and the $\mathbf{b}_2$ homodimer are in closest proximity, it is unknown if the peripheral stalk imposes any steric hindrance on the rotation of subunit ε. This question can be answered only by single molecule experiments of the actively rotating F-ATP synthase. Any strong interaction would be revealed by one extended dwell or rotational step, with reduced velocity. In A-ATP synthases, two such events would be expected.

2.5. Rotational Catalysis

The rotary mechanism of the F-ATP synthase during ATP hydrolysis follows an alternating site binding-change mechanism [62]. At concentrations of ATP that saturate the rate of ATP hydrolysis activity ([ATP] > k_M), the ATP hydrolysis-dependent rotation occurs in $120°$ power strokes [58,118,119] that occur on a μs time scale [120], and are interrupted by catalytic dwells with a duration on the order of a few ms [78]. During each catalytic dwell of eubacterial F-ATP synthases, ATP is hydrolyzed at the catalytic site that corresponds to β_{DP} [22], and the dwell ends upon release of Pi to create an empty site β_E [70,71,79]. Rotation of subunit γ during the ensuing $120°$ power stroke undergoes a series of accelerations and decelerations that have been divided into two $60°$ phases [60,121]. The binding of ATP to the empty catalytic site occurs during phase-2 [60].

When the ATP concentration becomes rate-limiting ([ATP] < k_M), an ATP-binding dwell is observed that interrupts the power stroke at some point during phase-1, and occurs most frequently $34°$–$40°$ after the catalytic dwell [60,78]. The duration of ATP-binding dwells vary inversely with ATP concentration. Although the power stroke of the A-ATP synthase is closely similar to that of F-ATP synthases, ATP-binding dwells are not observed at rate-limiting ATP concentrations, such that ATP binding is believed to occur during the catalytic dwell [73,76,122]. The dissociation of ADP from β_{DP} typically occurs during phase-2 [71,121]. As the power stroke ends, the conformations of the catalytic sites change, such that β_E changes to β_{TP}, β_{TP} changes to β_{DP}, and β_{DP} changes to β_E.

As a result of each power stroke, subunit γ rotates by an amount equivalent to one αβ heterodimer in the $(\alpha\beta)_3$-ring, and involves the net binding of one ATP and release of one ADP and one Pi. Consequently, each complete rotation of subunit γ requires the consumption of an ATP at each catalytic site in the $(\alpha\beta)_3$-ring for a total of three ATP. This alternating site mechanism is supported by structural evidence [12–22], by nucleotide-binding studies [123–126], and by single-molecule studies that have visualized rotation directly using visible probes attached to the rotor. These probes include actin filaments [58,63,118,127], gold/polystyrene/magnetic beads [70,71,78,79], and gold nanorods [60,76,120,121,128], as well as single-molecule Förster resonance energy transfer (smFRET) measurements [55,59,67–69,129–134].

3. Single Molecule Rotation Experiments

The first rotation experiments with the F_1 domain from the thermophilic *Bacillus* PS3 were described in 1997 by Noji et al. [63]. They immobilized the $(\alpha\beta)_3$-ring on a glass surface, attached a fluorescent actin filament to subunit γ and observed its rotation after addition of ATP. Since then, a variety of rotation experiments with F_1 or F_OF_1 from different organisms have been performed. In addition to actin filaments, polystyrene beads, gold beads, magnetic beads, and gold nanorods have been used as a probe for rotation. Recently, the rotation of A/V-type complexes have also been examined. Here, we focus on the *E. coli* F-ATP synthase to investigate the rotary asymmetry in the holoenzyme. We have reevaluated our previously published data [58,108,119,130,133] to search for persistent asymmetric patterns. In each study, the use of a complete EcF_OF_1 complex was confirmed by SDS-PAGE [56,130,135], and by the rotation experiments that were designed such that rotation was only visible in the presence of the F_1 and the F_O domain. ATP hydrolysis driven rotation of the

rotor subunits was observed via an attached fluorescent actin filament or gold nanorod (AuNR) to the **c**-ring, or via smFRET between donor and acceptor fluorophores on individual stator and rotor subunits (Figure 2). ATP concentrations above the k_M of 45 μM for *E. coli* [136] ensured continuous rotation in 120° steps with catalytic dwells in between.
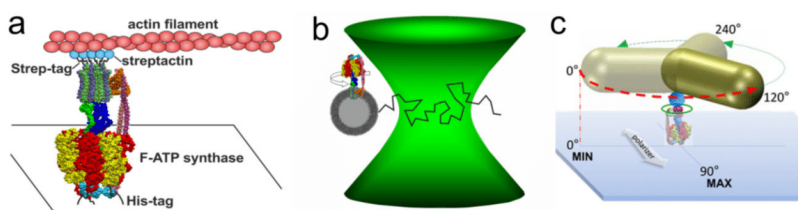
Figure 2. Single-molecule experiments with EcF_OF_1. (**a**) EcF_OF_1 was attached via His-tags in each β subunit to a cover glass. A fluorescently labelled actin filament, which was attached via streptactin and Strep-tags to the **c**-ring, served as a reporter for rotation during ATP hydrolysis [58]. (**b**) Fluorescently labelled EcF_OF_1 reconstituted in a liposome was diffusing through the confocal laser focus in a smFRET setup. Rotation of the central shaft during ATP hydrolysis was observed after addition of ATP, or ATP synthesis was powered by pmf [130]. (**c**) Immobilized EcF_OF_1 with an attached AuNR is rotating in 120° steps at saturating ATP concentrations, and intensities of the scattered light from the nanorod that were observed through a polarizer progressed sinusoidal and reached a maximum after 90° rotation [108].

3.1. Rotation Experiments with Actin Filaments

For the kinetic analysis of rotating EcF_OF_1 with actin filaments, we have reevaluated some previously unpublished data and data published by Sielaff et al. [58,119]. Single molecules of EcF_OF_1 were immobilized via His-tags in each β subunit on a Ni-NTA covered glass surface. A fluorescent actin filament (length: 0.5–0.9 μm) coupled to the **c**-ring via a Strep-tag served as a reporter to observe the ATP (0.05–5 mM) hydrolysis driven CCW rotation of the central stalk via micro-videography (Figure 2a). The rotational rate and dwell times were independent of the filament length and ATP, respectively (Figure 3a). The progression of a stepwise rotating filament is shown in Figure 3b. Histograms of the angular dependent probability distribution with three peaks representing the three catalytic dwells were fitted with Gaussians to determine the center of the peak (Figure 3c), whereas the mean dwell time of the complex at each of the three positions was determined with a monoexponential fit (Figure 3d). The propensity to reside in any out of the three positions differed, resulting in varying peak highs and dwell times. As the absolute orientation of the enzyme could not be determined, we estimated the maximum possible asymmetry between peaks and dwell times by aligning the peaks with the highest dwell time of each complex (Figure 3e). This resulted in one large peak, which area was 55–59% larger than that of the two other peaks. The averaged dwell times (τ) of the three peaks were 0.3 ± 0.2 s, 0.2 ± 0.15 s, and 0.2 ± 0.12 s, i.e., one long and two short dwells. The dwell times show a high standard deviation due to the fast rotational velocity and the short recording time of some filaments. The dwell times of the largest peak were on average 1.5 times longer than the other two. These results indicate a rotational asymmetry of the complex. However, the position of the peripheral stalk in relation to the orientation of the central stalk remained unknown. Therefore, these results are only supportive to the following experiments.
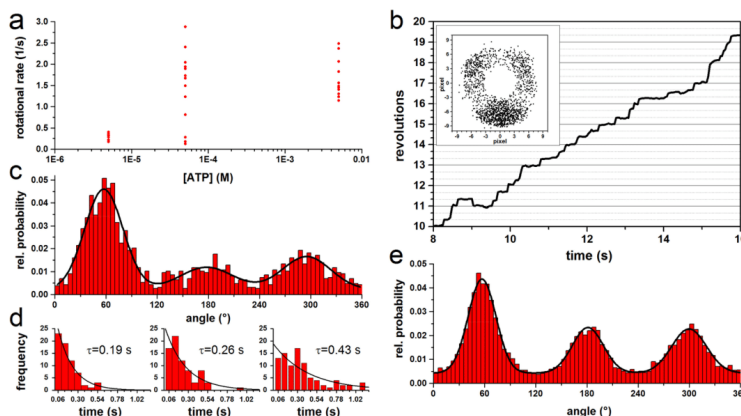
Figure 3. Properties of rotating actin filament-EcF$_O$F$_1$ complexes during ATP hydrolysis. (**a**) Rotational rate versus ATP. For short actin filaments ($\leq$1 μm), the rotational rate is independent of the ATP concentration and the filament length. (**b**) Trajectory of a typical rotating complex at 100 μM ATP in steps of 120$°$. The inset shows the endpoints of the 0.8 μm actin filament. (**c**) Normalized histogram of the angular probability distribution of the complex in **b**, where the three peaks, separated by 120$°$, were fitted with a Gaussian. (**d**) Dwell time histograms of each peak in c fitted with monoexponential decay. The dwell times (τ) are given for each histogram. (**e**) Combined normalized histogram of the angular distribution of rotating actin filament from 13 single molecules at 50–5000 μM ATP with 513 to 2174 frames per molecule. Each dataset was fitted with three Gaussians to determine the area of each peak. The datasets were aligned by positioning the largest peak at 60$°$.

3.2. Rotation Experiments with smFRET

In another set of single-molecule fluorescence measurements, smFRET was applied to investigate subunit rotation in liposome-reconstituted EcF$_O$F$_1$ during ATP hydrolysis and ATP synthesis [55,59,67–69,130,131,133,134]. To monitor the rotary motion of subunit ε during catalysis, the FRET donor fluorophore tetramethylrhodamine–C$_5$–maleimide was bound to a cysteine in subunit ε (εH56C) and the FRET acceptor fluorophore Cy5bis–C$_5$–maleimide was coupled to crosslink the two **b** subunits of the peripheral stalk (**b**Q64C). Single molecules of EcF$_O$F$_1$ were observed in freely diffusing liposomes using a confocal microscope setup (Figure 2b). The rotation of the rotor subunit ε relative to the static **b**$_2$ homodimer was recorded for ATP-driven ATP hydrolysis at saturating ATP concentrations (1 mM) and for proton-driven ATP synthesis at a high proton motive force, i.e., comprising an initial proton concentration difference of 4.1 pH units and an electric membrane potential. Excitation of the donor fluorophore resulted in photon bursts with different donor and acceptor intensities. The observation time of the freely diffusing proteoliposomes was limited to a few hundred milliseconds, and one, two, or three FRET efficiency levels could be discriminated in each photon burst. As before, these FRET levels corresponded to the catalytic dwells in between power strokes. The length of each dwell for the three distinct FRET levels was plotted in a histogram in order to calculate the mean dwell time for each FRET level separately. For the kinetic analysis, the first and last FRET level of a photon burst were omitted, as their actual duration before entering and after leaving the confocal detection volume remained unknown. For both ATP hydrolysis and ATP synthesis, three FRET levels were observed representing the three distances between the FRET labels or the relative orientation of the subunits, respectively, during the 120$°$ rotation in EcF$_O$F$_1$. Average dwell times for the three orientations were 12.7 $\pm$ 1.0 ms (medium FRET efficiency, M-level), 17.6 $\pm$ 1.4 ms (low FRET efficiency, L-level), and 15.8 $\pm$ 1.7 ms (high FRET efficiency, H-level) during ATP hydrolysis

(Figure 4a), and 15.4 ± 1.0 ms (M-level), 24.0 ± 4.4 ms (L-level), and 19.5 ± 2.2 ms (H-level) for ATP synthesis (Figure 4b). In both cases, kinetic analysis yielded an asymmetric distribution of FRET level dwells. The M-level had a significantly shorter dwell time than the L- and H-level, and the short and long dwell times differed by factors of 1.39 and 1.56 for ATP hydrolysis and synthesis, respectively [130].
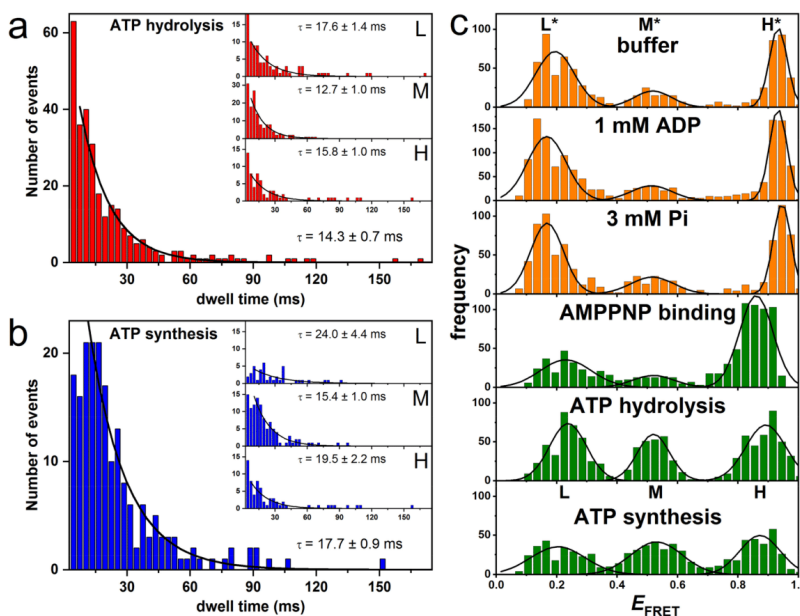
Figure 4. FRET histograms and dwell time histograms of subunit ε rotation in single FRET-labeled EcF$_O$F$_1$ during catalysis. (**a**) Dwell time histogram for all FRET levels during ATP hydrolysis. The insets show the individual dwell times for each of the three FRET levels. (**b**) Dwell time histogram for all FRET levels during ATP synthesis. The insets show the individual dwell times for each of the three FRET levels. (**c**) FRET histograms showing the three FRET levels L*, M*, H* (orange), and levels L, M, H (green) from measurements at different conditions at pH 8. See text for details. (Modified from [130]).

We also compared the occurrence of each FRET level in the dwell time histograms and found a higher occurrence of the M-level based on photon bursts with three or four FRET levels. This is in line with the shorter dwell time of the M-level and was confirmed by Monte-Carlo simulations, in which the abundance of each FRET level with the experimentally determined dwell times during ATP hydrolysis was examined using the experimentally determined dwell times for each orientation [131]. In case of three-level photon bursts, the following FRET sequences were found in the experiment/simulations, respectively: H-M-L 63.3%/38.4%, M-L-H 23.3%/33.6%, and L-H-M 13.3%/28.0%. The simulations with 10000 bursts and 1000 repetitions were statistically consistent and qualitatively reproduced the asymmetry in the experimental FRET level distribution with a strongly preferred intermediary M-level. However, the experimental data sets were limited to less than 300 molecules or photon bursts, respectively.

In subsequent smFRET experiments, the FRET donor EGFP was fused to the C-terminus of subunit **a** and the acceptor fluorophore Alexa568 to subunit ε at position ε56 [133]. Dwell times of 9 ± 1 ms (L-level), 11 ± 1 ms (M-level), and 10 ± 1 ms (H-level) were observed during ATP hydrolysis.

All dwells were similar within the error margin. When the FRET acceptor was coupled to subunit γ at position γ106 instead, the dwell times changed to 20 ± 3 ms (L-level), 20 ± 1 ms (M-level), and 16 ± 1 ms (H-level). Here, the dwell time of the H-level was shorter than the other two, but overall the difference between them was less than a factor of 1.25. The total number of photon bursts analyzed for dwell times in this study was similarly low, i.e., less than 400 enzymes for smFRET between subunits **a** and ε.

3.3. Rotation Experiments with Gold Nanorods

In this assay, instead of an actin filament, an 80 × 40 nm AuNR was attached to the **c**-ring of EcF_OF_1 as a visible probe, and ATP hydrolysis driven rotation of EcF_OF_1 was measured. The ability to acquire data at speeds equivalent to 100 k frames per s in combination with an AuNR substantially improved the time resolution to 10 µs, and increased the accuracy of determining rotational position to a standard error of 0.02°–0.12° [56]. When passed through a polarizing filter and measured by an avalanche photo diode, the polarized red light scattered from an AuNR of these dimensions changed in a sinusoidal manner as a function of the rotary position of the AuNR versus the polarizer direction. For each dataset, the polarizer was aligned with each AuNR-EcF_OF_1 complex to minimize the scattered red light intensity during one of the three catalytic dwells. The light intensity data collected from the subsequent 120° power stroke resulted in an increase from a minimum through a maximum, at which point the AuNR has rotated 90° [56]. These power strokes were selected for further analysis from the total of three successive power strokes that are required to complete 360° of rotation (Figure 5a).

After EcF_OF_1 embedded lipid bilayer nanodiscs (n-EcF_OF_1) were attached to a glass slide via His_6-tags on the N-termini of the β subunits, ATP hydrolysis-dependent rotation of an AuNR attached to the c_{10}-ring of n-EcF_OF_1 was examined in the presence of saturating concentrations of ATP (1 mM MgATP) at different pH. Under these conditions, transient dwells were observed to occur at ~36° intervals between the catalytic dwells of the ATP hydrolysis-dependent CCW power stroke. The transient dwells were shown to result from an interaction in EcF_O between subunit **a** and successive **c** subunits in the c_{10}-ring, which is consistent with their occurrence every 36°. This interaction was not only able to cancel the force of the ATP hydrolysis-driven CCW **c**-ring rotation, but over 70% of the time was able to push the rotor backwards in CW (i.e., ATP synthesis) direction by as much as one **c** subunit [137]. The average duration of transient dwells ranged from 50 µs to 175 µs [56], which is on the same time scale as proton gradient-dependent rotational stepping of **c** subunits during ATP synthesis under typical in vivo conditions (Figure 5b).

Each rotational data set analyzed from an n-EcF_OF_1 complex contained ~300 power strokes that increased from a minimum through a maximum intensity, which were examined for the presence of transient dwells. Between pH 9.0 and 7.5, about 23% of the power strokes analyzed from each data set contained transient dwells (Figure 5b). As the pH decreased below pH 7.5, the percentage of power strokes containing transient dwells increased inversely with pH to a maximum average of 50% at pH 5.0 (Figure 5d) [108]. For any given molecule, there is an equal probability that the power stroke analyzed corresponds to the rotation that originates from one of the three structural states (see below). This was corroborated by the fit of the distribution in Figure 5c with three Gaussian curves. The probability of forming transient dwells in each dataset was either low (blue line), medium (red line), or high (green line). The measured distribution at each pH (gray bars) was well fitted by the sum of the three Gaussians (black line).
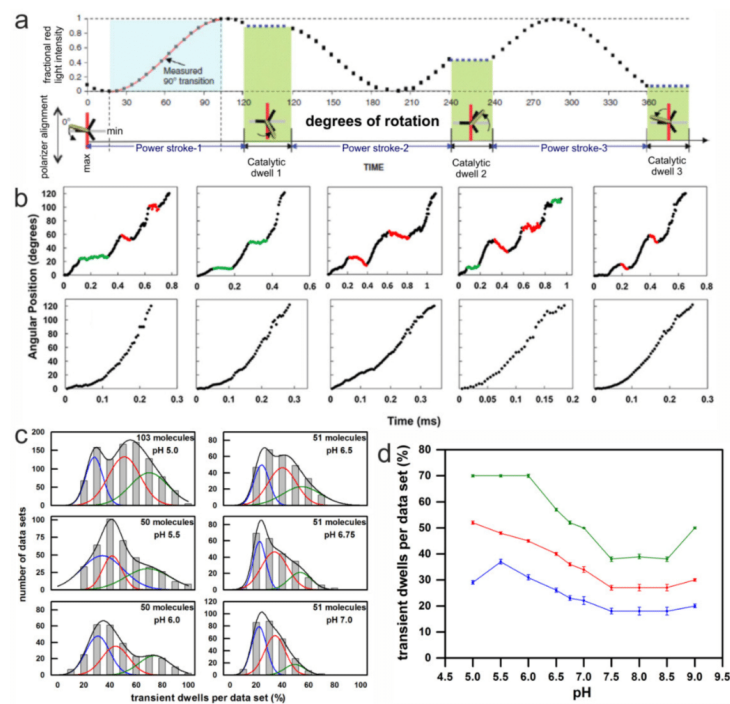
Figure 5. Method and results of single-molecule rotation experiments with AuNR attached to the **c**-ring of immobilized EcF_OF_1 during ATP hydrolysis. (**a**) Theoretical plot of the intensity of scattered red light from a nanorod during one complete revolution that involves three consecutive power strokes and three consecutive catalytic dwells separated by exactly $120°$. The nanorod is initially positioned almost—but not exactly—perpendicular to the orientation of the polarizer, such that the scattered light intensity goes through a minimum then a maximum prior to catalytic dwell 1. A transition includes the data between the minimum and maximum intensities representing $90°$ of the $120°$ of rotation. For analysis transitions from power stroke-1 to dwell 1 were selected. (Modified from [56]) (**b**) Examples of time-dependent changes in rotational position of n-EcF_OF_1 during F_1-ATPase–dependent power strokes at pH 5.0, where transient dwells, either present (**top**) or absent (**bottom**), are shown. Transient dwells where rotation was halted or contained CW rotation are colored green and red, respectively. (**c**) The distribution of single-molecule n-EcF_OF_1 power stroke data sets as a function of the percentage of the occurrence of transient dwells per data set, which were binned to each 10% (gray bar graphs). Each data set contained ~300 power strokes, derived from the indicated number of molecules. The data were fitted to the sum of three Gaussians (black line), where the probability of forming transient dwells was low (blue line), medium (red line), and high (green line). (**d**) The pH dependencies of the average percent of transient dwells per data set, with standard errors derived from the three Gaussians. (Modified from [108]).

The pH dependence of transient dwell formation observed with n-EcF_OF_1 was comparable to the pH range that powers proton gradient-driven ATP synthesis that occurs when the cytoplasmic and periplasmic half-channels in subunit **a** are exposed to pH 8.5 and 5.5, respectively. However, when EcF_O is embedded in a nanodisc, both proton half-channels are exposed to the same pH. The pH dependence of transient dwell formation shows that the periplasmic half-channel is more easily protonated in

a manner that halts ATP hydrolysis-driven rotation by blocking ATP hydrolysis-dependent proton pumping. The distribution of the percentage of transient dwells formed per data set did not fit to a single Gaussian at any of the pH values examined. In several data sets at pH values between 5.0 and 6.0, transient dwells were observed in 90–100% of the power strokes. The fits of the distributions of power strokes containing transient dwells improved substantially when the sum of three Gaussian distributions was used (Figure 5c). Each of the three Gaussians represents the ability to form transient dwells during the ATP hydrolysis driven power stroke, which occurred with a high, medium, or low probability, respectively. The overall formation of transient dwells increased with an increase in acidic environment (Figure 5d). For example, when the data were fit in this manner at pH 5.0, the high, medium, and low probabilities averaged 70%, 53%, and 29% of transient dwells formed per data set, respectively.

4. Discussion

In *E. coli* F-ATP synthase, rotation of the central shaft subunits γ and ε progresses in steps of $120°$ during ATP hydrolysis. At high (mM) ATP concentrations, the dwells of the rotor between steps are associated with the hydrolysis reaction of ATP. Here, we compared the dwell times of single enzymes measured by three different single-molecule techniques and found asymmetric rotational behavior with all three approaches. In experiments with actin filaments and large beads, it could be argued that an apparent rotational asymmetry originated from the drag of the probe or its interaction with the surface. However, asymmetric dwell times were also present when these surface effects were minimized in single-molecule experiments with nanorods, or even completely absent in smFRET measurements in solution.

4.1. Asymmetry Corroborated from Single-Molecule Rotation Experiments

In the rotation assay with actin filaments, we found one long (300 ms) and two short dwell times (200 ms). The areas of the Gaussians associated with these dwells differed by a factor of about 2, while the dwell times differed by a factor of 1.5. However, the significance of these findings is limited, because the rotary movement is damped by the viscous drag of the actin filament and the uncertainty of the angular position of the filament due to its inherent flexibility. The existence of one longer dwell time seemed to be plausible in view of the peripheral stalk subunits $\mathbf{b}_2$ that might affect the conformational dynamics of the nearest catalytic binding site or the progression of the central shaft when the bulge of subunits γ or ε pass by. In contrast, in smFRET experiments, the rotation is not hampered by a viscous drag of the marker of rotation, and the F-ATP synthase can rotate at maximum speed under non-limiting ATP concentrations. Different dwell times and ratios were measured depending on the labeling positions for the FRET donor and acceptor fluorophores. However, the dwell times differed not more than by a factor of 1.56, which is in the same order of magnitude as for the rotation assay with actin filament.

Other research groups also reported on asymmetric rotation with different types of ATP synthases in single-molecule experiments with immobilized complexes. Similar to the rotation experiments described here, small gold beads (40–80 nm) [138,139] or magnetic beads (200 nm) [140] were attached to immobilized F-type ATP synthases to reduce the viscous drag of the probe. The rotation of the central stalk subunits, DF in A/V-type complexes of *Thermus thermophiles* (TtA_OA_1) [74] and *Enterococcus hirae* [141] was investigated with 40 nm gold beads. In all studies, the histograms of angular orientation showed peaks with different heights and widths, similar to data shown here in Figure 3. From these data we draw two conclusions. From the broad width of the peaks, we deduce that the rotation of the central shaft was not always perfectly C3-symmetric. Instead, individual steps could be larger or smaller than $120°$, although one full rotation was always $360°$. The different heights indicate that the catalytic dwell times vary from each for the three positions. The variety of these data confirms that asymmetric rotation is not an artifact but a common feature of this flexible enzyme.

4.2. Comparison of Cryo-EM Structures

Structural evidence for the asymmetric distribution of rotor orientations with respect to the peripheral stator stalk has been provided recently by several cryo-EM structures of distinct ATP synthases. These studies resolved three different conformations of the F-type ATP synthase with the central shaft rotated by approximately $120°$ in each of them. The structures were classified according to the orientation of the central stalk, i.e., the bulge of subunit γ in relation to the peripheral stalk. The three structural states appeared as different subpopulations of the enzymes on the cryo-EM grid. For EcF_OF_1, Sobti et al. [12] reported a ratio for the three rotor orientations of 46.3%, 30%, and 23.7% for state 1, state 2, and state 3, respectively (Figure 6). Different subpopulations and ratios were also found for the *Bacillus* PS3 F-ATP synthase (BPF_OF_1) [29], the spinach chloroplast enzyme (CF_OF_1) [27], the yeast vacuolar V-ATPase (YV_OV_1) [94], and TtA_OA_1 [96]. However, almost no differences were found for the subpopulations of the three states of the bovine mitochondrial F-ATP synthase (MF_OF_1) [24]. Table 1 summarizes the occurrence of the three rotor orientations for the different enzymes. The relative ratios are similar for the two bacterial F-ATP synthases, with state 1 being the most abundant. In contrast, in CF_OF_1 the most abundant rotor orientation was found >10 times more often in state 3 than in the other two states. In addition, the rotary angles of the central stalk between the three states were $103°$, $112°$, and $145°$, which deviates significantly from the expected $120°$ angles. As TtA_OA_1 and YV_OV_1 have two and three peripheral stalks, respectively, their structures cannot be aligned with the F-type ATP synthases. Still, the ratios of the three states are similar to the ones of CF_OF_1 and BPF_OF_1, respectively.
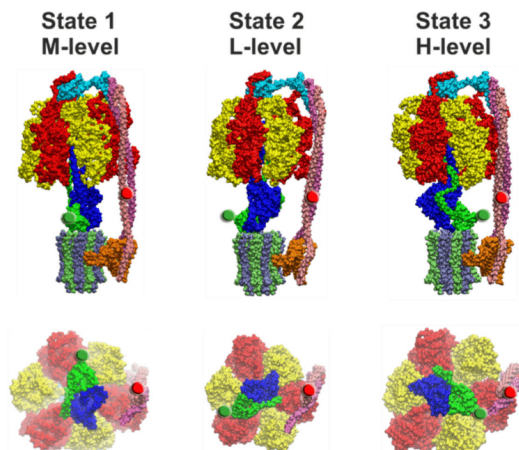
Figure 6. Side view (top row) and view from the membrane side with the **c**-ring and subunit **a** omitted of the three cryo-EM structural states of EcF_OF_1 [12]. State 1 (PDB-id: 5T4O, left), state 2 (PDB-id: 5T4P, middle), and state 3 (PDB-id: 5T4Q, right) correspond to FRET levels M, L, and H, respectively (as in Figure 4). In each image, the FRET-donor position at ε56 is marked with a green sphere and the FRET-acceptor position at **b**64 is marked with a red sphere. The portions of subunit ε and γ that extends beyond the diameter of the **c**-ring must pass through the narrow gap created by the peripheral stalk during rotation from state 3 to state 1, and during rotation from state 1 to state 2, respectively. The subunit coloring is the same as in Figure 1.

Table 1. Distribution of the three different states/rotor orientations of the F/A/V-type complexes that were found in cryo-EM studies. The F_OF_1 structures were aligned according to the orientation of the central stalk in relation to the peripheral stalk. As A_OA_1 and V_OV_1 have two and three peripheral stalks, respectively, it is not possible to align their states with the F_OF_1 structures.

Structure	State 1	State 2	State 3	Nucleotide Occupancy	Reference
EcF_OF_1	46.3%	30.0%	23.7%	ADP in $\alpha\beta_{closed}$	[12]
BPF_OF_1	45.3%	35.1%	19.6%	Mg-ADP in $\alpha\beta_{TP}$, Pi in $\alpha\beta_E$	[29]
CF_OF_1	8.1%	7.5%	84.4%	Mg-ADP in $\alpha\beta_{DP}$ and $\alpha\beta_{TP}$	[27]
MF_OF_1	31.3%	35.0%	33.7%	Unknown	[24]
TtA_OA_1	72.5%	18.7%	8.8%	ADP in AB_{closed} and $AB_{semi-closed}$	[96]
YV_OV_1	47%	36%	17%	unknown	[94]

4.3. Correlation of Cryo-EM Structures with smFRET Data

The questions remains of how the different dwell times found in single-molecule FRET experiments can be related to the three structures of EcF_OF_1 (Figure 6). FRET efficiencies for EcF_OF_1 labeled at rotor subunit ε56 and stator subunit **b**64 corresponded to fluorophore distances of 8.3 nm (L*-level), 6.4 nm (M*-level), and 4.0 nm (H*-level) in the absence of any added nucleotides, or in the presence of 1 mM ADP and/or 3 mM Pi. In the presence of 1 mM ATP during catalysis, the respective distances were 7.8 nm (L-level), 6.3 nm (M-level), and 4.6 nm (H-level) [130]. In the three EcF_OF_1 cryo-EM structures [12], distances between the Cα atoms of these two residues were 8.2/8.6 nm (PDB-id: 5T4P, state 2), 6.1/7.2 nm (PDB-id: 5P4O, state 1), and 3.5/3.4 nm (PDB-id: 4T4Q, state 3), respectively, depending on the position of **b**64 in each **b** subunit (Figure 6). The cryo-EM structures do contain only one bound ADP in one closed catalytic binding site, while the other two sites are empty and open. Therefore, the apparent agreement with the smFRET data in the absence of nucleotides or in the presence of ADP/Pi is excellent and approaches the current "state-of-the-art" of single-molecule FRET-based precise distance calculations [142]. However, given the uncertainties of the additional linker length for the fluorophores, limited mobility of the fluorophores in their local environment on the enzyme, and errors in fluorescence quantum yield determination in our smFRET data, the FRET distances obtained during catalysis and subunit rotation are also similar to the cryo-EM enzyme structures trapped in non-catalytic states.

The cryo-EM structures were based on more than 10,000 enzymes for each state [12,24]. The population of states was 46% for state 1, 30% for state 2, and 24% for state 3 (Table 1). They correspond to the medium (M*- or M-level), low (L*- or L-level), and high (H*- or H-level) FRET efficiencies, respectively (Figure 6). In contrast, in smFRET data in the absence of nucleotides or in the presence of ADP/Pi, the relative number of M*-level found was only 15%. Most of the non-active enzymes were found with the rotor orientation associated with the L*-level (50%). The H*-level occurred in 35% of cases (Figure 4c) [130]. About 1000 enzymes contributed to each smFRET data set, i.e., significantly less than in the cryo-EM data set. The catalytically active EcF_OF_1 showed a nearly uniform distribution of L, M, and H-level, based on only a few hundred enzymes. Thus, the asymmetric distributions found in cryo-EM structures and in smFRET data do not match.

This might be explained in part by the constraints of the smFRET analysis using freely diffusing proteoliposomes, but also by a potential bias of particles that can adsorb to the cryo-EM grid in a preferred orientation [143,144]. The relative occurrence of the L-, M-, and H-level during ATP hydrolysis is correlated to the dwell time of the respective FRET level [131]. To add a FRET level to the dwell time distribution requires a photon burst with at least three FRET levels, because the first and last FRET level cannot be included. The diffusion time of proteoliposomes through the confocal detection volume, i.e., the time for the occurrence of three consecutive FRET levels in a photon burst, was less than 1 s. The minimal dwell time that could be assigned in the smFRET time traces was about 5 ms, and the shortest photon burst analyzed was 20 ms. Therefore, to be added to the dwell time

histograms, photon bursts had to contain short dwells as intermediate FRET levels. For both ATP hydrolysis and ATP synthesis conditions, the dwell times of the M-level were shorter than for the L- and H-level. Accordingly, the M-level were most abundant in the dwell time distributions. However, Monte-Carlo simulations for the relation of dwell time and occurrence of a FRET level revealed that more than 10,000 FRET photon bursts with three and more subsequent FRET levels are required for a compelling correlation between them. In the smFRET experiments, dwell times had to be analyzed based on less than 100 dwells per FRET level.

Alternatively, the observation times of proteoliposomes in solution have to be prolonged to obtain more consecutive FRET levels within one photon burst. One approach to extend observation times in confocal smFRET measurements is the "anti-Brownian electrokinetic trap" (ABEL trap) invented by Cohen and Moerner [145–155]. A confocal laser pattern with correlated and localized photon detection is used to determine the position of a fluorescent particle within thin microfluidics. By applying electric fields, the fluorescent molecule is pushed back to the center of the laser focus pattern. In preliminary experiments, FRET-labeled EcF_OF_1 could be held and analyzed for up to 4 s in the absence of ATP until photobleaching of the dyes [156–159]. The limiting 1 µm thickness of the microfluidics and the uniform illumination by a fast moving laser focus yields constant fluorescence intensity from a single trapped molecule. Well-known smFRET artefacts, like red-fluorescent liposomes without a labeled enzyme or the existence of multiple enzymes within a single liposome, can be identified and omitted from subsequent smFRET analysis. Improved fluorophores for smFRET (brightness, photostability, monoexponential fluorescence lifetime, restricted blinking, and spectral fluctuations) will enable the recording of appropriate large numbers of FRET levels in order to corroborate the differing dwell times for the FRET levels, or the asymmetric distribution of rotor subunit orientations, respectively, in active and non-active F-ATP synthases.

4.4. Asymmetry in c-Ring Rotation

Cryo-EM structures of EcF_OF_1 exist in three states (Figure 6) that differ by the asymmetric positions of subunits γ and ε in relation to the peripheral stalk [12]. These structures likely correspond to the three 120° rotary positions of the catalytic dwells. However, the rotary positions of the c_{10}-ring relative to subunit **a** in the three states were 108°, 108°, and 144° apart. These rotary positions are consistent with the mismatch between the orientation of the three catalytic sites in the EcF_1 domain and the orientation of the c_{10}-ring in EcF_O domain. The structure implies that the synthesis/hydrolysis of one particular ATP requires four **c** subunit steps ($4H^+ \times 36° = 144°$), while for each of the other two ATPs synthesized/hydrolyzed, three proton translocation-dependent single **c** subunit steps ($3H^+ \times 36° = 108°$) must occur (Figure 7). The three cryo-EM structures of the *Bacillus* PS3 F-ATP synthase show a similar asymmetry for the rotational states of the **c**-ring [29].

As a result of the asymmetric binding of subunits γ and ε to the **c**-ring, each **c** subunit is unique, such that residue **a**R210 is positioned between two adjacent **c**D61 residues of adjacent **c** subunit chains designated M and N in state 1 (PDB-id: 5T4O), chains S and T in state 2 (PDB-id: 5T4P), and chains P and Q in state 3 (PDB-id: 5T4Q). The three successive 120° ATP hydrolysis-driven power strokes rotate the **c**-ring between the three catalytic dwell positions that correspond to the three structures. During power stroke 1, **c** subunits M, V, U, T rotate past subunit **a**, while in power stroke 2 and power stroke 3, **c** subunits S, R, Q, and subsequently P, O, N rotate past subunit **a**, respectively. These power strokes are unique from each other, first because power stroke 1 translocates $4H^+$, while the other two each translocate $3H^+$. Second, a portion of subunit γ that extends beyond the diameter of the **c**-ring must pass through the narrow gap created by the peripheral stalk during power stroke 1. A portion of subunit ε that also extends beyond the **c**-ring diameter must pass through this gap during power stroke 3, whereas power stroke 2 is not affected in this manner (Figure 6). However, from the static cryo-EM structures, it is unclear how c_{10}-ring rotation might be affected. Third, the position of **a**R210 relative to the **c**D61 residues of the adjacent **c** subunits varies significantly among the three cryo-EM states. In structure 5T4Q, which serves as a reference structure for the 0° rotational position in our

model shown in Figure 7, **a**R210 is extremely close to **c**D61 of chain P (4.5 Å). This state 3, that is formed after power stroke 2 and precedes power stroke 3, is equally separated from the other two states by the rotation of three **c** subunits (108°). However, in the 4 **c** subunit, power stroke 1 from state 1 to state 2, represented by structures 5T4O and 5T4P, respectively, there is a symmetry mismatch between the 144° **c**-ring rotation in F_O (i.e., the angle between the two green lines) and the 120° F_1 rotation (i.e., the angle between the two red lines). In state 1, the rotary position of the **c**-ring relative to **a**R210 is closer to a green line and F_O dominates the formation of a dwell position, while in state 2 this distance is closer to a red line and F_1 dominates the formation of a dwell position.
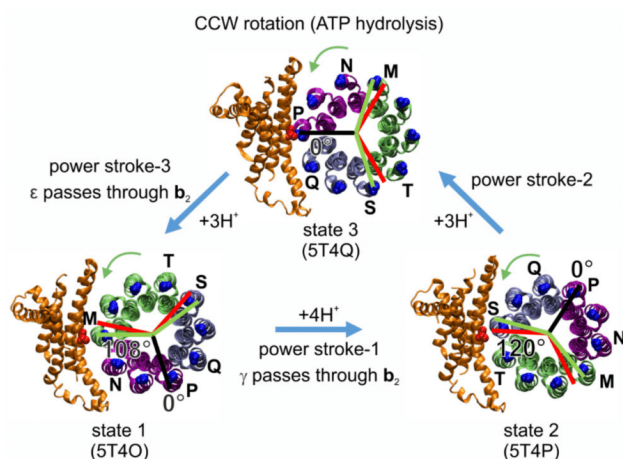
Figure 7. Asymmetry between the three F_1-ATPase power strokes of EcF_OF_1, as shown by the rotary positions of residue **c**D61 in each **c** subunit (blue) relative to **a**R210 (red) in the three states of the EcF_OF_1 cryo-EM structures (viewed from the membrane side as in Figure 6) designated by their PDB-ids [12]. In structure 5T4Q, **c**D61 of **c** subunit chain P is closely aligned with **a**R210 (black line designate 0° of rotation). Assuming that this state shows the alignment with a catalytic dwell position in F_1, red lines show the other two 120° rotational positions of the catalytic dwells in F_1 during subsequent power strokes. Green lines show the 108° rotations that result from the three proton-dependent CCW rotational steps (green arrows) of the **c**-ring that occur during the power strokes, which results in strain between the catalytic dwell positions of F_O and F_1. From state 3 to state 1 (3 **c** subunits, purple), and from state 2 to state 3, the **c**-ring rotates by 108° (3 **c** subunits, ice blue), whereas from state 1 to state 2, the **c**-ring rotates by 144° (4 **c** subunits, lime).

We proposed that the high, medium, and low probabilities of transient dwell formation (Figure 5c) depend on the rotary position of the ATP hydrolysis-dependent power stroke relative to the peripheral stalk [108]. It is likely that power stroke 3 represents the data sets with a high probability to form transient dwells, i.e., there is a high probability for subunit **a** to stop F_1-ATP hydrolysis-driven CCW rotation or even to push the **c**-ring CW after a 120° rotation. This is because structure 5T4O is in a rotary position comparable to that of a transient dwell after a 108° rotation of the **c**-ring (green line in Figure 7), instead of a 120° rotation (red line in Figure 7) as induced by the catalytic events in F_1. In contrast, power stroke 1 may be responsible for the data sets with a low probability of transient dwell formation, because in the structure 5T4P, the **c**-ring is in a position in line with a 120° rotation induced by F_1 (red line), where a transient dwell has not been formed. In the third case, transient dwells may be formed before power stroke 2, as in the structure 5T4P residue D61 of the **c** subunit closest to **a**R210 is not in an optimal position to receive a proton, in comparison with structure 5T4Q, which can be compensated by thermal fluctuation. The drag imposed on power strokes 1 and 3, when

the lobes of subunit γ and ε pass through the narrow gap created by the peripheral stalk, respectively, may also contribute to the probability of forming transient dwells during power strokes 1 and 3.

In contrast, measurements of the spring constant of the central stalk elements and smFRET data [59,134] revealed that the **c**-ring is elastically coupled to the $\gamma\varepsilon$-shaft, with the softest part being the interface between F_O and F_1 [58]. Elastic power transmission between F_O and F_1 is a central element in the coupling of the two nanomotors and allows the enzyme to run with high kinetic efficiency and with the same mechanism even if the number of **c** subunits varies between species [57]. The three structures in Figures 6 and 7 represent three energy-minimized snapshots of the subunit ε inhibited enzyme. These structures occur only transiently in the active enzyme. For the chloroplast enzyme it was shown that F_O alone can rotate $10\times$ faster than F_1 [160,161], i.e., during ATP synthesis it can run ahead of F_1 and build up and store elastic energy in the central shaft, depending on the stochastic binding of protons to **c**D61 in this Brownian ratchet. Accordingly, the orientation of **c**D61 towards **a**R210 during the same power stroke can vary in the active enzyme. Nevertheless, it is within the scope of this model that the step size is not always $120°$ but can be as small as $108°$ or as large as $144°$.

5. Conclusions

Our results on the rotation of single $F_O F_1$ ATP synthases suggest that its asymmetric structure is reflected in its rotational dynamics and breaks rotational symmetry. This is corroborated by three different single-molecule techniques applied here, and by the fact that other research groups studying the ATP synthase from different organisms and with different techniques found similar static and dynamic behavior. Table 2 summarizes the experimental differences found for the *E. coli* $F_O F_1$ ATP synthase.

Table 2. Dynamic and static differences of measurements with $EcF_O F_1$. The top part shows the dynamic differences in dwell times for the three catalytic dwells found in our single-molecule fluorescence experiments. For comparison, the bottom row shows the static distribution of the three different states in the cryo-EM measurement. (* FRET-levels do not apply to this method.)

FRET-Level Method	M, Dwell Time 1 (ms)	L, Dwell Time 2 (ms)	H, Dwell Time 3 (ms)	Direction of Rotation
rotation assay[*]	300.0	200.0	200.0	ATP hydrolysis
smFRET ε56/**b**64	12.7	17.6	15.8	ATP hydrolysis
smFRET ε56/**b**64	15.4	24.0	19.5	ATP synthesis
Conformation	**State 1**	**State 2**	**State 3**	
cryo-EM[*]	47%	30%	24%	N.A.

We found that during ATP hydrolysis in the F_1 domain one dwell time is by a factor 1.5 longer than the other two in rotation experiments with actin filaments. In contrast, the results of smFRET experiments indicate that one dwell time is shorter than the other two by a factor of 1.4 or 1.6 during ATP hydrolysis or synthesis, respectively. When the donor fluorophore was placed at a different position, this factor was even smaller (1.3). In addition, our experiments with gold nanorods suggests that there is rotational asymmetry also present in the F_O domain, as the two half-channels in subunit **a** seem to have different accessibilities for protons. At this state, the origin of the different patterns is unknown, because it is unclear which structural elements contribute mostly to this asymmetry. It could be that the effects of the asymmetric elements vary due to the elastic flexibility of the enzyme. One also has to consider that it is not clear how these differences are, at least partially, caused by the short observation times in the smFRET experiments or the drag imposed by the actin filament or any other probe that is coupled to an immobilized enzyme complex. Yet, overall the differences in dwell times were small and do not impede the high kinetic efficiency (i.e., the high turnover rate under load) of the enzyme [57,162].

In conclusion, the maximum difference between the dwell times for three rotor orientations was less than 1.6. This shows that the overall effect of the asymmetric structural features on the rotational

dynamics and dwell times is small. Of the asymmetric elements discussed, the ones that involve the $\mathbf{b}_2$ homodimer are the most likely candidates to prolong some, but not all, of the catalytic dwells, because the $\mathbf{b}_2$ homodimer is asymmetrically placed on one side of the $(\alpha\beta)_3$-ring. Together, these subunits form a stiff element with a torsional stiffness of $\kappa \approx 700$ pNnm [35]. On the other hand, the central rotor stalk itself is designed to store elastic energy during power transmission between the F_O and F_1 parts [57,59,134,163]. The interface between F_1 and F_O, involving subunits γ, ε, and the $\mathbf{c}$-ring, respectively, is at least one order of magnitude more elastic than the stator ($\kappa \approx 20$ pNnm). The flexible lever on subunit β adds a similar amount of elastic flexibility, reducing the effective spring constant of the active enzyme to about 35 pNnm [35,58]. Thus, transient flexibility in parts of the enzyme allows reducing kinetic limping. It remains for future experiments to investigate the details and effects of the asymmetric elements on the catalytic activity of the different types of ATP synthases.

Author Contributions: H.S., S.Y., W.D.F., W.J., and M.B. carried out design, conducted experiments, and analyzed data. H.S., W.D.F., W.J., and M.B. wrote the manuscript.

Conflicts of Interest: The authors declare no conflict of interest.

References

1. Boyer, P.D. ATP synthase-past and future. *Biochim. Biophys. Acta* **1998**, *1365*, 3–9. [CrossRef]
2. Senior, A.E.; Weber, J. Happy motoring with ATP synthase. *Nat. Struct. Mol. Biol.* **2004**, *11*, 110–112. [CrossRef] [PubMed]
3. Junge, W.; Sielaff, H.; Engelbrecht, S. Torque generation and elastic power transmission in the rotary F_OF_1-ATPase. *Nature* **2009**, *459*, 364–370. [CrossRef] [PubMed]
4. Von Ballmoos, C.; Wiedenmann, A.; Dimroth, P. Essentials for ATP synthesis by F1F0 ATP synthases. *Annu. Rev. Biochem.* **2009**, *78*, 649–672. [CrossRef] [PubMed]
5. Sielaff, H.; Börsch, M. Twisting and subunit rotation in single F_OF_1-ATP synthase. *Philos. Trans. R. Soc. Lond. B Biol. Sci.* **2013**, *368*, 20120024. [CrossRef]
6. Walker, J.E. The ATP synthase: The understood, the uncertain and the unknown. *Biochem. Soc. Trans.* **2013**, *41*, 1–16. [CrossRef] [PubMed]
7. Junge, W.; Nelson, N. ATP synthase. *Annu. Rev. Biochem.* **2015**, *84*, 631–657. [CrossRef]
8. Noji, H.; Ueno, H.; McMillan, D.G.G. Catalytic robustness and torque generation of the F_1-ATPase. *Biophys. Rev.* **2017**, *9*, 103–118. [CrossRef]
9. Girvin, M.E.; Rastogi, V.K.; Abildgaard, F.; Markley, J.L.; Fillingame, R.H. Solution structure of the transmembrane H$^+$-transporting subunit c of the F_1F_O ATP synthase. *Biochemistry* **1998**, *37*, 8817–8824. [CrossRef]
10. Dmitriev, O.; Jones, P.C.; Jiang, W.; Fillingame, R.H. Structure of the membrane domain of subunit b of the *Escherichia coli* F_OF_1 ATP synthase. *J. Biol. Chem.* **1999**, *274*, 15598–15604. [CrossRef]
11. Cingolani, G.; Duncan, T.M. Structure of the ATP synthase catalytic complex (F_1) from *Escherichia coli* in an autoinhibited conformation. *Nat. Struct. Mol. Biol.* **2011**, *18*, 701–707. [CrossRef] [PubMed]
12. Sobti, M.; Smits, C.; Wong, A.S.W.; Ishmukhametov, R.; Stock, D.; Sandin, S.; Stewart, A.G. Cryo-EM structures of the autoinhibited *E. coli* ATP synthase in three rotational states. *eLife* **2016**, *5*, 21598. [CrossRef] [PubMed]
13. Abrahams, J.P.; Leslie, A.G.; Lutter, R.; Walker, J.E. Structure at 2.8 Å resolution of F_1-ATPase from bovine heart mitochondria. *Nature* **1994**, *370*, 621–628. [CrossRef]
14. Abrahams, J.P.; Buchanan, S.K.; Van Raaij, M.J.; Fearnley, I.M.; Leslie, A.G.; Walker, J.E. The structure of bovine F_1-ATPase complexed with the peptide antibiotic efrapeptin. *Proc. Natl. Acad. Sci. USA* **1996**, *93*, 9420–9424. [CrossRef] [PubMed]
15. Van Raaij, M.J.; Orriss, G.L.; Montgomery, M.G.; Runswick, M.J.; Fearnley, I.M.; Skehel, J.M.; Walker, J.E. The ATPase inhibitor protein from bovine heart mitochondria: The minimal inhibitory sequence. *Biochemistry* **1996**, *35*, 15618–15625. [CrossRef] [PubMed]

16. Orriss, G.L.; Leslie, A.G.; Braig, K.; Walker, J.E. Bovine F$_1$-ATPase covalently inhibited with 4-chloro-7-nitrobenzofurazan: The structure provides further support for a rotary catalytic mechanism. *Structure* **1998**, *6*, 831–837. [CrossRef]

17. Braig, K.; Menz, R.I.; Montgomery, M.G.; Leslie, A.G.; Walker, J.E. Structure of bovine mitochondrial F$_1$-ATPase inhibited by Mg^{2+} ADP and aluminium fluoride. *Structure* **2000**, *8*, 567–573. [CrossRef]

18. Gibbons, C.; Montgomery, M.G.; Leslie, A.G.; Walker, J.E. The structure of the central stalk in bovine F$_1$-ATPase at 2.4 Å resolution. *Nat. Struct. Biol.* **2000**, *7*, 1055–1061.

19. Menz, R.I.; Walker, J.E.; Leslie, A.G. Structure of bovine mitochondrial F$_1$-ATPase with nucleotide bound to all three catalytic sites: Implications for the mechanism of rotary catalysis. *Cell* **2001**, *106*, 331–341. [CrossRef]

20. Kagawa, R.; Montgomery, M.G.; Braig, K.; Leslie, A.G.; Walker, J.E. The structure of bovine F$_1$-ATPase inhibited by ADP and beryllium fluoride. *EMBO J.* **2004**, *23*, 2734–2744. [CrossRef]

21. Kabaleeswaran, V.; Puri, N.; Walker, J.E.; Leslie, A.G.; Mueller, D.M. Novel features of the rotary catalytic mechanism revealed in the structure of yeast F$_1$ ATPase. *EMBO J.* **2006**, *25*, 5433–5442. [CrossRef] [PubMed]

22. Bowler, M.W.; Montgomery, M.G.; Leslie, A.G.; Walker, J.E. Ground state structure of F$_1$-ATPase from bovine heart mitochondria at 1.9 Å resolution. *J. Biol. Chem.* **2007**, *282*, 14238–14242. [CrossRef]

23. Guo, H.; Rubinstein, J.L. Cryo-EM of ATP synthases. *Curr. Opin. Struct. Biol.* **2018**, *52*, 71–79. [CrossRef] [PubMed]

24. Zhou, A.; Rohou, A.; Schep, D.G.; Bason, J.V.; Montgomery, M.G.; Walker, J.E.; Grigorieff, N.; Rubinstein, J.L. Structure and conformational states of the bovine mitochondrial ATP synthase by cryo-EM. *eLife* **2015**, *4*, 10180. [CrossRef] [PubMed]

25. Vinothkumar, K.R.; Montgomery, M.G.; Liu, S.; Walker, J.E. Structure of the mitochondrial ATP synthase from *Pichia angusta* determined by electron cryo-microscopy. *Proc. Natl. Acad. Sci. USA* **2016**, *113*, 12709–12714. [CrossRef] [PubMed]

26. Klusch, N.; Murphy, B.J.; Mills, D.J.; Yildiz, O.; Kühlbrandt, W. Structural basis of proton translocation and force generation in mitochondrial ATP synthase. *eLife* **2017**, *6*, 33274. [CrossRef] [PubMed]

27. Hahn, A.; Vonck, J.; Mills, D.J.; Meier, T.; Kühlbrandt, W. Structure, mechanism, and regulation of the chloroplast ATP synthase. *Science* **2018**, *360*, 4318. [CrossRef]

28. Srivastava, A.P.; Luo, M.; Zhou, W.; Symersky, J.; Bai, D.; Chambers, M.G.; Faraldo-Gomez, J.D.; Liao, M.; Mueller, D.M. High-resolution cryo-EM analysis of the yeast ATP synthase in a lipid membrane. *Science* **2018**, *360*, 9699. [CrossRef]

29. Guo, H.; Suzuki, T.; Rubinstein, J.L. Structure of a bacterial ATP synthase. *bioRxiv* **2018**. [CrossRef]

30. Dunn, S.D.; McLachlin, D.T.; Revington, M. The second stalk of *Escherichia coli* ATP synthase. *Biochim. Biophys. Acta* **2000**, *1458*, 356–363. [CrossRef]

31. Del Rizzo, P.A.; Bi, Y.; Dunn, S.D. ATP synthase b subunit dimerization domain: A right-handed coiled coil with offset helices. *J. Mol. Biol.* **2006**, *364*, 735–746. [CrossRef] [PubMed]

32. Colina-Tenorio, L.; Dautant, A.; Miranda-Astudillo, H.; Giraud, M.F.; Gonzalez-Halphen, D. The Peripheral Stalk of Rotary ATPases. *Front. Physiol.* **2018**, *9*, 1243. [CrossRef] [PubMed]

33. Dickson, V.K.; Silvester, J.A.; Fearnley, I.M.; Leslie, A.G.; Walker, J.E. On the structure of the stator of the mitochondrial ATP synthase. *EMBO J.* **2006**, *25*, 2911–2918. [CrossRef] [PubMed]

34. Rees, D.M.; Leslie, A.G.; Walker, J.E. The structure of the membrane extrinsic region of bovine ATP synthase. *Proc. Natl. Acad. Sci. USA* **2009**, *106*, 21597–21601. [CrossRef] [PubMed]

35. Wächter, A.; Bi, Y.; Dunn, S.D.; Cain, B.D.; Sielaff, H.; Wintermann, F.; Engelbrecht, S.; Junge, W. Two rotary motors in F-ATP synthase are elastically coupled by a flexible rotor and a stiff stator stalk. *Proc. Natl. Acad. Sci. USA* **2011**, *108*, 3924–3929. [CrossRef] [PubMed]

36. Stock, D.; Leslie, A.G.; Walker, J.E. Molecular architecture of the rotary motor in ATP synthase. *Science* **1999**, *286*, 1700–1705. [CrossRef]

37. Seelert, H.; Poetsch, A.; Dencher, N.A.; Engel, A.; Stahlberg, H.; Muller, D.J. Structural biology. Proton-powered turbine of a plant motor. *Nature* **2000**, *405*, 418–419. [CrossRef]

38. Stahlberg, H.; Muller, D.J.; Suda, K.; Fotiadis, D.; Engel, A.; Meier, T.; Matthey, U.; Dimroth, P. Bacterial Na$^+$-ATP synthase has an undecameric rotor. *EMBO Rep.* **2001**, *2*, 229–233. [CrossRef]

39. Mitome, N.; Suzuki, T.; Hayashi, S.; Yoshida, M. Thermophilic ATP synthase has a decamer c-ring: Indication of noninteger 10:3 H$^+$/ATP ratio and permissive elastic coupling. *Proc. Natl. Acad. Sci. USA* **2004**, *101*, 12159–12164. [CrossRef]

178

40. Meier, T.; Polzer, P.; Diederichs, K.; Welte, W.; Dimroth, P. Structure of the rotor ring of F-Type Na$^+$-ATPase from *Ilyobacter tartaricus*. *Science* **2005**, *308*, 659–662. [CrossRef]

41. Pogoryelov, D.; Yu, J.; Meier, T.; Vonck, J.; Dimroth, P.; Muller, D.J. The c$_{15}$ ring of the Spirulina platensis F-ATP synthase: F$_1$/F$_0$ symmetry mismatch is not obligatory. *EMBO Rep.* **2005**, *6*, 1040–1044. [CrossRef] [PubMed]

42. Meier, T.; Morgner, N.; Matthies, D.; Pogoryelov, D.; Keis, S.; Cook, G.M.; Dimroth, P.; Brutschy, B. A tridecameric c ring of the adenosine triphosphate (ATP) synthase from the thermoalkaliphilic *Bacillus* sp. strain TA2.A1 facilitates ATP synthesis at low electrochemical proton potential. *Mol. Microbiol.* **2007**, *65*, 1181–1192. [CrossRef] [PubMed]

43. Pogoryelov, D.; Reichen, C.; Klyszejko, A.L.; Brunisholz, R.; Muller, D.J.; Dimroth, P.; Meier, T. The oligomeric state of c rings from cyanobacterial F-ATP synthases varies from 13 to 15. *J. Bacteriol.* **2007**, *189*, 5895–5902. [CrossRef] [PubMed]

44. Meier, T.; Krah, A.; Bond, P.J.; Pogoryelov, D.; Diederichs, K.; Faraldo-Gomez, J.D. Complete ion-coordination structure in the rotor ring of Na$^+$-dependent F-ATP synthases. *J. Mol. Biol.* **2009**, *391*, 498–507. [CrossRef] [PubMed]

45. Pogoryelov, D.; Yildiz, O.; Faraldo-Gomez, J.D.; Meier, T. High-resolution structure of the rotor ring of a proton-dependent ATP synthase. *Nat. Struct. Mol. Biol.* **2009**, *16*, 1068–1073. [CrossRef] [PubMed]

46. Vollmar, M.; Schlieper, D.; Winn, M.; Büchner, C.; Groth, G. Structure of the c14 rotor ring of the proton translocating chloroplast ATP synthase. *J. Biol. Chem.* **2009**, *284*, 18228–18235. [CrossRef] [PubMed]

47. Watt, I.N.; Montgomery, M.G.; Runswick, M.J.; Leslie, A.G.; Walker, J.E. Bioenergetic cost of making an adenosine triphosphate molecule in animal mitochondria. *Proc. Natl. Acad. Sci. USA* **2010**, *107*, 16823–16827. [CrossRef]

48. Preiss, L.; Klyszejko, A.L.; Hicks, D.B.; Liu, J.; Fackelmayer, O.J.; Yildiz, O.; Krulwich, T.A.; Meier, T. The c-ring stoichiometry of ATP synthase is adapted to cell physiological requirements of alkaliphilic Bacillus pseudofirmus OF4. *Proc. Natl. Acad. Sci. USA* **2013**, *110*, 7874–7879. [CrossRef]

49. Matthies, D.; Zhou, W.; Klyszejko, A.L.; Anselmi, C.; Yildiz, O.; Brandt, K.; Muller, V.; Faraldo-Gomez, J.D.; Meier, T. High-resolution structure and mechanism of an F/V-hybrid rotor ring in a Na(+)-coupled ATP synthase. *Nat. Commun.* **2014**, *5*, 5286. [CrossRef]

50. Preiss, L.; Langer, J.D.; Hicks, D.B.; Liu, J.; Yildiz, O.; Krulwich, T.A.; Meier, T. The c-ring ion binding site of the ATP synthase from Bacillus pseudofirmus OF4 is adapted to alkaliphilic lifestyle. *Mol. Microbiol.* **2014**, *92*, 973–984. [CrossRef]

51. Preiss, L.; Langer, J.D.; Yildiz, O.; Eckhardt-Strelau, L.; Guillemont, J.E.; Koul, A.; Meier, T. Structure of the mycobacterial ATP synthase Fo rotor ring in complex with the anti-TB drug bedaquiline. *Sci. Adv.* **2015**, *1*, 1500106. [CrossRef] [PubMed]

52. Mazhab-Jafari, M.T.; Rohou, A.; Schmidt, C.; Bueler, S.A.; Benlekbir, S.; Robinson, C.V.; Rubinstein, J.L. Atomic model for the membrane-embedded VO motor of a eukaryotic V-ATPase. *Nature* **2016**, *539*, 118–122. [CrossRef] [PubMed]

53. Jiang, W.; Hermolin, J.; Fillingame, R.H. The preferred stoichiometry of c subunits in the rotary motor sector of *Escherichia coli* ATP synthase is 10. *Proc. Natl. Acad. Sci. USA* **2001**, *98*, 4966–4971. [CrossRef] [PubMed]

54. Ballhausen, B.; Altendorf, K.; Deckers-Hebestreit, G. Constant c$_{10}$ ring stoichiometry in the *Escherichia coli* ATP synthase analyzed by cross-linking. *J. Bacteriol.* **2009**, *191*, 2400–2404. [CrossRef] [PubMed]

55. Düser, M.G.; Zarrabi, N.; Cipriano, D.J.; Ernst, S.; Glick, G.D.; Dunn, S.D.; Börsch, M. 36 degrees step size of proton-driven c-ring rotation in FoF$_1$-ATP synthase. *EMBO J.* **2009**, *28*, 2689–2696. [CrossRef]

56. Ishmukhametov, R.; Hornung, T.; Spetzler, D.; Frasch, W.D. Direct observation of stepped proteolipid ring rotation in *E. coli* F$_O$F$_1$-ATP synthase. *EMBO J.* **2010**, *29*, 3911–3923. [CrossRef]

57. Junge, W.; Pänke, O.; Cherepanov, D.A.; Gumbiowski, K.; Müller, M.; Engelbrecht, S. Inter-subunit rotation and elastic power transmission in F$_0$F$_1$-ATPase. *FEBS Lett.* **2001**, *504*, 152–160. [CrossRef]

58. Sielaff, H.; Rennekamp, H.; Wächter, A.; Xie, H.; Hilbers, F.; Feldbauer, K.; Dunn, S.D.; Engelbrecht, S.; Junge, W. Domain compliance and elastic power transmission in rotary F$_O$F$_1$-ATPase. *Proc. Natl. Acad. Sci. USA* **2008**, *105*, 17760–17765. [CrossRef]

59. Ernst, S.; Düser, M.G.; Zarrabi, N.; Dunn, S.D.; Börsch, M. Elastic deformations of the rotary double motor of single FoF$_1$-ATP synthases detected in real time by Forster resonance energy transfer. *Biochim. Biophys. Acta* **2012**, *1817*, 1722–1731. [CrossRef]

60. Martin, J.L.; Ishmukhametov, R.; Spetzler, D.; Hornung, T.; Frasch, W.D. Elastic coupling power stroke mechanism of the F_1-ATPase molecular motor. *Proc. Natl. Acad. Sci. USA* **2018**, *115*, 5750–5755. [CrossRef]

61. Cross, R.L. The Mechanism and Regulation of Atp Synthesis by F_1-Atpases. *Annu. Rev. Biochem.* **1981**, *50*, 681–714. [CrossRef] [PubMed]

62. Boyer, P.D. The binding change mechanism for ATP synthase—Some probabilities and possibilities. *Biochim. Biophys. Acta* **1993**, *1140*, 215–250. [CrossRef]

63. Noji, H.; Yasuda, R.; Yoshida, M.; Kinosita, K., Jr. Direct observation of the rotation of F_1-ATPase. *Nature* **1997**, *386*, 299–302. [CrossRef] [PubMed]

64. Sambongi, Y.; Iko, Y.; Tanabe, M.; Omote, H.; Iwamoto-Kihara, A.; Ueda, I.; Yanagida, T.; Wada, Y.; Futai, M. Mechanical rotation of the c subunit oligomer in ATP synthase (F_0F_1): Direct observation. *Science* **1999**, *286*, 1722–1724. [CrossRef] [PubMed]

65. Pänke, O.; Gumbiowski, K.; Junge, W.; Engelbrecht, S. F-ATPase: Specific observation of the rotating c subunit oligomer of EFoEF1. *FEBS Lett.* **2000**, *472*, 34–38. [CrossRef]

66. Tsunoda, S.P.; Aggeler, R.; Yoshida, M.; Capaldi, R.A. Rotation of the c subunit oligomer in fully functional F1Fo ATP synthase. *Proc. Natl. Acad. Sci. USA* **2001**, *98*, 898–902. [CrossRef] [PubMed]

67. Börsch, M.; Diez, M.; Zimmermann, B.; Reuter, R.; Gräber, P. Stepwise rotation of the gamma-subunit of $EFoF_1$-ATP synthase observed by intramolecular single-molecule fluorescence resonance energy transfer. *FEBS Lett.* **2002**, *527*, 147–152. [CrossRef]

68. Börsch, M.; Diez, M.; Zimmermann, B.; Trost, M.; Steigmiller, S.; Gräber, P. Stepwise rotation of the γ-subunit of $EFoF_1$-ATP synthase during ATP synthesis: A single-molecule FRET approach. *Proc. SPIE* **2003**, *4962*. [CrossRef]

69. Diez, M.; Zimmermann, B.; Börsch, M.; Konig, M.; Schweinberger, E.; Steigmiller, S.; Reuter, R.; Felekyan, S.; Kudryavtsev, V.; Seidel, C.A.; et al. Proton-powered subunit rotation in single membrane-bound FoF_1-ATP synthase. *Nat. Struct. Mol. Biol.* **2004**, *11*, 135–141. [CrossRef]

70. Nishizaka, T.; Oiwa, K.; Noji, H.; Kimura, S.; Muneyuki, E.; Yoshida, M.; Kinosita, K., Jr. Chemomechanical coupling in F_1-ATPase revealed by simultaneous observation of nucleotide kinetics and rotation. *Nat. Struct. Mol. Biol.* **2004**, *11*, 142–148. [CrossRef]

71. Watanabe, R.; Iino, R.; Noji, H. Phosphate release in F_1-ATPase catalytic cycle follows ADP release. *Nat. Chem. Biol.* **2010**, *6*, 814–820. [CrossRef] [PubMed]

72. Hirata, T.; Iwamoto-Kihara, A.; Sun-Wada, G.H.; Okajima, T.; Wada, Y.; Futai, M. Subunit rotation of vacuolar-type proton pumping ATPase: Relative rotation of the G and C subunits. *J. Biol. Chem.* **2003**, *278*, 23714–23719. [CrossRef] [PubMed]

73. Imamura, H.; Takeda, M.; Funamoto, S.; Shimabukuro, K.; Yoshida, M.; Yokoyama, K. Rotation scheme of V_1-motor is different from that of F_1-motor. *Proc. Natl. Acad. Sci. USA* **2005**, *102*, 17929–17933. [CrossRef] [PubMed]

74. Furuike, S.; Nakano, M.; Adachi, K.; Noji, H.; Kinosita, K., Jr.; Yokoyama, K. Resolving stepping rotation in *Thermus thermophilus* H^+-ATPase/synthase with an essentially drag-free probe. *Nat. Commun.* **2011**, *2*, 233. [CrossRef] [PubMed]

75. Minagawa, Y.; Ueno, H.; Hara, M.; Ishizuka-Katsura, Y.; Ohsawa, N.; Terada, T.; Shirouzu, M.; Yokoyama, S.; Yamato, I.; Muneyuki, E.; et al. Basic properties of rotary dynamics of the molecular motor Enterococcus hirae V_1-ATPase. *J. Biol. Chem.* **2013**, *288*, 32700–32707. [CrossRef] [PubMed]

76. Sielaff, H.; Martin, J.; Singh, D.; Biukovic, G.; Grüber, G.; Frasch, W.D. Power Stroke Angular Velocity Profiles of Archaeal A-ATP Synthase Versus Thermophilic and Mesophilic F-ATP Synthase Molecular Motors. *J. Biol. Chem.* **2016**, *291*, 25351–25363. [CrossRef]

77. Singh, D.; Sielaff, H.; Börsch, M.; Grüber, G. Conformational dynamics of the rotary subunit F in the A_3B_3DF complex of Methanosarcina mazei Gö1 A-ATP synthase monitored by single-molecule FRET. *FEBS Lett.* **2017**, *591*, 854–862. [CrossRef]

78. Yasuda, R.; Noji, H.; Yoshida, M.; Kinosita, K., Jr.; Itoh, H. Resolution of distinct rotational substeps by submillisecond kinetic analysis of F_1-ATPase. *Nature* **2001**, *410*, 898–904. [CrossRef]

79. Shimabukuro, K.; Yasuda, R.; Muneyuki, E.; Hara, K.Y.; Kinosita, K., Jr.; Yoshida, M. Catalysis and rotation of F_1 motor: Cleavage of ATP at the catalytic site occurs in 1 ms before $40°$ substep rotation. *Proc. Natl. Acad. Sci. USA* **2003**, *100*, 14731–14736. [CrossRef]

80. Adachi, K.; Oiwa, K.; Nishizaka, T.; Furuike, S.; Noji, H.; Itoh, H.; Yoshida, M.; Kinosita, K., Jr. Coupling of rotation and catalysis in F_1-ATPase revealed by single-molecule imaging and manipulation. *Cell* **2007**, *130*, 309–321. [CrossRef]

81. Arai, S.; Saijo, S.; Suzuki, K.; Mizutani, K.; Kakinuma, Y.; Ishizuka-Katsura, Y.; Ohsawa, N.; Terada, T.; Shirouzu, M.; Yokoyama, S.; et al. Rotation mechanism of *Enterococcus hirae* V_1-ATPase based on asymmetric crystal structures. *Nature* **2013**, *493*, 703–707. [CrossRef] [PubMed]

82. Suzuki, T.; Tanaka, K.; Wakabayashi, C.; Saita, E.; Yoshida, M. Chemomechanical coupling of human mitochondrial F1-ATPase motor. *Nat. Chem. Biol.* **2014**, *10*, 930–936. [CrossRef] [PubMed]

83. Börsch, M.; Duncan, T.M. Spotlighting motors and controls of single FoF_1-ATP synthase. *Biochem. Soc. Trans.* **2013**, *41*, 1219–1226. [CrossRef] [PubMed]

84. Börsch, M. Microscopy of single FoF_1-ATP synthases—The unraveling of motors, gears, and controls. *IUBMB Life* **2013**, *65*, 227–237. [CrossRef] [PubMed]

85. Junge, W.; Lill, H.; Engelbrecht, S. ATP synthase: An electrochemical transducer with rotatory mechanics. *Trends Biochem. Sci.* **1997**, *22*, 420–423. [CrossRef]

86. Wang, H.; Oster, G. Ratchets, power strokes, and molecular motors. *Appl. Phys. A* **2002**, *75*, 315–323. [CrossRef]

87. Leone, V.; Pogoryelov, D.; Meier, T.; Faraldo-Gomez, J.D. On the principle of ion selectivity in Na^+/H^+-coupled membrane proteins: Experimental and theoretical studies of an ATP synthase rotor. *Proc. Natl. Acad. Sci. USA* **2015**, *112*, E1057–E1066. [CrossRef]

88. Grüber, G.; Wieczorek, H.; Harvey, W.R.; Müller, V. Structure-function relationships of A-, F- and V-ATPases. *J. Exp. Biol.* **2001**, *204*, 2597–2605.

89. Yamato, I.; Kakinuma, Y.; Murata, T. Operating principles of rotary molecular motors: Differences between F_1 and V_1 motors. *Biophys. Physicobiol.* **2016**, *13*, 37–44. [CrossRef]

90. Cross, R.L.; Müller, V. The evolution of A-, F-, and V-type ATP synthases and ATPases: Reversals in function and changes in the H^+/ATP coupling ratio. *FEBS Lett.* **2004**, *576*, 1–4. [CrossRef]

91. Muench, S.P.; Trinick, J.; Harrison, M.A. Structural divergence of the rotary ATPases. *Q. Rev. Biophys.* **2011**, *44*, 311–356. [CrossRef] [PubMed]

92. Stewart, A.G.; Sobti, M.; Harvey, R.P.; Stock, D. Rotary ATPases: Models, machine elements and technical specifications. *Bioarchitecture* **2013**, *3*, 2–12. [CrossRef] [PubMed]

93. Grüber, G.; Manimekalai, M.S.; Mayer, F.; Müller, V. ATP synthases from archaea: The beauty of a molecular motor. *Biochim. Biophys. Acta* **2014**, *1837*, 940–952. [CrossRef] [PubMed]

94. Zhao, J.; Benlekbir, S.; Rubinstein, J.L. Electron cryomicroscopy observation of rotational states in a eukaryotic V-ATPase. *Nature* **2015**, *521*, 241–245. [CrossRef] [PubMed]

95. Davies, R.B.; Smits, C.; Wong, A.S.W.; Stock, D.; Christie, M.; Sandin, S.; Stewart, A.G. Cryo-EM analysis of a domain antibody bound rotary ATPase complex. *J. Struct. Biol.* **2017**, *197*, 350–353. [CrossRef]

96. Nakanishi, A.; Kishikawa, J.I.; Tamakoshi, M.; Mitsuoka, K.; Yokoyama, K. Cryo EM structure of intact rotary H^+-ATPase/synthase from Thermus thermophilus. *Nat. Commun.* **2018**, *9*, 89. [CrossRef] [PubMed]

97. Iwata, M.; Imamura, H.; Stambouli, E.; Ikeda, C.; Tamakoshi, M.; Nagata, K.; Makyio, H.; Hankamer, B.; Barber, J.; Yoshida, M.; et al. Crystal structure of a central stalk subunit C and reversible association/dissociation of vacuole-type ATPase. *Proc. Natl. Acad. Sci. USA* **2004**, *101*, 59–64. [CrossRef]

98. Numoto, N.; Hasegawa, Y.; Takeda, K.; Miki, K. Inter-subunit interaction and quaternary rearrangement defined by the central stalk of prokaryotic V_1-ATPase. *EMBO Rep.* **2009**, *10*, 1228–1234. [CrossRef]

99. Saijo, S.; Arai, S.; Hossain, K.M.; Yamato, I.; Suzuki, K.; Kakinuma, Y.; Ishizuka-Katsura, Y.; Ohsawa, N.; Terada, T.; Shirouzu, M.; et al. Crystal structure of the central axis DF complex of the prokaryotic V-ATPase. *Proc. Natl. Acad. Sci. USA* **2011**, *108*, 19955–19960. [CrossRef]

100. Kishikawa, J.; Ibuki, T.; Nakamura, S.; Nakanishi, A.; Minamino, T.; Miyata, T.; Namba, K.; Konno, H.; Ueno, H.; Imada, K.; et al. Common evolutionary origin for the rotor domain of rotary ATPases and flagellar protein export apparatus. *PLoS ONE* **2013**, *8*, 64695. [CrossRef]

101. Singh, D.; Sielaff, H.; Sundararaman, L.; Bhushan, S.; Grüber, G. The stimulating role of subunit F in ATPase activity inside the A-complex of the Methanosarcina mazei Gö1 A_1A_O ATP synthase. *Biochim. Biophys. Acta* **2016**, *1857*, 177–187. [CrossRef] [PubMed]

102. Uchihashi, T.; Iino, R.; Ando, T.; Noji, H. High-speed atomic force microscopy reveals rotary catalysis of rotorless F1-ATPase. *Science* **2011**, *333*, 755–758. [CrossRef] [PubMed]

103. Senior, A.E.; Nadanaciva, S.; Weber, J. The molecular mechanism of ATP synthesis by F_1F_0-ATP synthase. *Biochim. Biophys. Acta* **2002**, *1553*, 188–211. [CrossRef]

104. Mao, H.Z.; Weber, J. Identification of the betaTP site in the x-ray structure of F_1-ATPase as the high-affinity catalytic site. *Proc. Natl. Acad. Sci. USA* **2007**, *104*, 18478–18483. [CrossRef] [PubMed]

105. Allegretti, M.; Klusch, N.; Mills, D.J.; Vonck, J.; Kühlbrandt, W.; Davies, K.M. Horizontal membrane-intrinsic alpha-helices in the stator a-subunit of an F-type ATP synthase. *Nature* **2015**, *521*, 237–240. [CrossRef]

106. Nesci, S.; Trombetti, F.; Ventrella, V.; Pagliarani, A. The a subunit asymmetry dictates the two opposite rotation directions in the synthesis and hydrolysis of ATP by the mitochondrial ATP synthase. *Med. Hypotheses* **2015**, *84*, 53–57. [CrossRef]

107. Nesci, S.; Trombetti, F.; Ventrella, V.; Pagliarani, A. Opposite Rotation Directions in the Synthesis and Hydrolysis of ATP by the ATP Synthase: Hints from a Subunit Asymmetry. *J. Membr. Biol.* **2015**, *248*, 163–169. [CrossRef]

108. Yanagisawa, S.; Frasch, W.D. Protonation-dependent stepped rotation of the F-type ATP synthase c-ring observed by single-molecule measurements. *J. Biol. Chem.* **2017**, *292*, 17093–17100. [CrossRef]

109. McLachlin, D.T.; Coveny, A.M.; Clark, S.M.; Dunn, S.D. Site-directed cross-linking of b to the alpha, beta, and a subunits of the *Escherichia coli* ATP synthase. *J. Biol. Chem.* **2000**, *275*, 17571–17577. [CrossRef]

110. Brandt, K.; Maiwald, S.; Herkenhoff-Hesselmann, B.; Gnirss, K.; Greie, J.C.; Dunn, S.D.; Deckers-Hebestreit, G. Individual interactions of the b subunits within the stator of the *Escherichia coli* ATP synthase. *J. Biol. Chem.* **2013**, *288*, 24465–24479. [CrossRef]

111. Benlekbir, S.; Bueler, S.A.; Rubinstein, J.L. Structure of the vacuolar-type ATPase from Saccharomyces cerevisiae at 11-Å resolution. *Nat. Struct. Mol. Biol.* **2012**, *19*, 1356–1362. [CrossRef] [PubMed]

112. Greene, M.D.; Frasch, W.D. Interactions among gamma R268, gamma Q269, and the beta subunit catch loop of Escherichia coli F1-ATPase are important for catalytic activity. *J. Biol. Chem.* **2003**, *278*, 51594–51598. [CrossRef] [PubMed]

113. Hilbers, F.; Junge, W.; Sielaff, H. The torque of rotary F-ATPase can unfold subunit gamma if rotor and stator are cross-linked. *PLoS ONE* **2013**, *8*, 53754. [CrossRef] [PubMed]

114. Iino, R.; Noji, H. Rotary catalysis of the stator ring of F_1-ATPase. *Biochim. Biophys. Acta* **2012**, *1817*, 1732–1739. [CrossRef] [PubMed]

115. Feniouk, B.A.; Suzuki, T.; Yoshida, M. The role of subunit epsilon in the catalysis and regulation of F_OF_1-ATP synthase. *Biochim. Biophys. Acta* **2006**, *1757*, 326–338. [CrossRef]

116. Krah, A.; Zarco-Zavala, M.; McMillan, D.G.G. Insights into the regulatory function of the varepsilon subunit from bacterial F-type ATP synthases: A comparison of structural, biochemical and biophysical data. *Open Biol.* **2018**, *8*, 170275. [CrossRef]

117. Sielaff, H.; Duncan, T.M.; Börsch, M. The regulatory subunit epsilon in *Escherichia coli* F_OF_1-ATP synthase. *Biochim. Biophys. Acta-Bioenerg.* **2018**, *1859*, 775–788. [CrossRef]

118. Adachi, K.; Yasuda, R.; Noji, H.; Itoh, H.; Harada, Y.; Yoshida, M.; Kinosita, K., Jr. Stepping rotation of F_1-ATPase visualized through angle-resolved single-fluorophore imaging. *Proc. Natl. Acad. Sci. USA* **2000**, *97*, 7243–7247. [CrossRef]

119. Sielaff, H.; Rennekamp, H.; Engelbrecht, S.; Junge, W. Functional halt positions of rotary F_OF1-ATPase correlated with crystal structures. *Biophys. J.* **2008**, *95*, 4979–4987. [CrossRef]

120. Spetzler, D.; York, J.; Daniel, D.; Fromme, R.; Lowry, D.; Frasch, W. Microsecond time scale rotation measurements of single F_1-ATPase molecules. *Biochemistry* **2006**, *45*, 3117–3124. [CrossRef]

121. Martin, J.L.; Ishmukhametov, R.; Hornung, T.; Ahmad, Z.; Frasch, W.D. Anatomy of F_1-ATPase powered rotation. *Proc. Natl. Acad. Sci. USA* **2014**, *111*, 3715–3720. [CrossRef] [PubMed]

122. Iino, R.; Ueno, H.; Minagawa, Y.; Suzuki, K.; Murata, T. Rotational mechanism of *Enterococcus hirae* V-ATPase by crystal-structure and single-molecule analyses. *Curr. Opin. Struct. Biol.* **2015**, *31*, 49–56. [CrossRef] [PubMed]

123. Senior, A.E.; Weber, J.; al-Shawi, M.K. Catalytic mechanism of *Escherichia coli* F_1-ATPase. *Biochem. Soc. Trans.* **1995**, *23*, 747–752. [CrossRef] [PubMed]

124. Weber, J.; Senior, A.E. Catalytic mechanism of F1-ATPase. *Biochim. Biophys. Acta* **1997**, *1319*, 19–58. [CrossRef]

125. Weber, J.; Nadanaciva, S.; Senior, A.E. ATP-driven rotation of the gamma subunit in F_1-ATPase. *FEBS Lett.* **2000**, *483*, 1–5. [CrossRef]

126. Weber, J.; Muharemagic, A.; Wilke-Mounts, S.; Senior, A.E. Analysis of sequence determinants of F_1Fo-ATP synthase in the N-terminal region of alpha subunit for binding of delta subunit. *J. Biol. Chem.* **2004**, *279*, 25673–25679. [CrossRef] [PubMed]

127. Hirono-Hara, Y.; Noji, H.; Nishiura, M.; Muneyuki, E.; Hara, K.Y.; Yasuda, R.; Kinosita, K., Jr.; Yoshida, M. Pause and rotation of F_1-ATPase during catalysis. *Proc. Natl. Acad. Sci. USA* **2001**, *98*, 13649–13654. [CrossRef]

128. Hornung, T.; Ishmukhametov, R.; Spetzler, D.; Martin, J.; Frasch, W.D. Determination of torque generation from the power stroke of *Escherichia coli* F_1-ATPase. *Biochim. Biophys. Acta* **2008**, *1777*, 579–582. [CrossRef]

129. Börsch, M.; Gräber, P. Subunit movement in individual H^+-ATP synthases during ATP synthesis and hydrolysis revealed by fluorescence resonance energy transfer. *Biochem. Soc. Trans.* **2005**, *33*, 878–882. [CrossRef]

130. Zimmermann, B.; Diez, M.; Zarrabi, N.; Gräber, P.; Börsch, M. Movements of the epsilon-subunit during catalysis and activation in single membrane-bound H^+-ATP synthase. *EMBO J.* **2005**, *24*, 2053–2063. [CrossRef]

131. Zarrabi, N.; Zimmermann, B.; Diez, M.; Gräber, P.; Wrachtrup, J.; Börsch, M. Asymmetry of rotational catalysis of single membrane-bound FoF_1-ATP synthase. *Proc. SPIE* **2005**, *5699*. [CrossRef]

132. Düser, M.G.; Zarrabi, N.; Bi, Y.; Zimmermann, B.; Dunn, S.D.; Börsch, M. 3D-localization of the alpha-subunit in FoF_1-ATP synthase by time resolved single-molecule FRET. *Proc. SPIE* **2006**, *6092*. [CrossRef]

133. Düser, M.G.; Bi, Y.; Zarrabi, N.; Dunn, S.D.; Börsch, M. The proton-translocating a subunit of F_OF_1-ATP synthase is allocated asymmetrically to the peripheral stalk. *J. Biol. Chem.* **2008**, *283*, 33602–33610. [CrossRef]

134. Ernst, S.; Düser, M.G.; Zarrabi, N.; Börsch, M. Three-color Förster resonance energy transfer within single F_0F_1-ATP synthases: Monitoring elastic deformations of the rotary double motor in real time. *J. Biomed. Opt.* **2012**, *17*, 011004. [CrossRef] [PubMed]

135. Gumbiowski, K.; Pänke, O.; Junge, W.; Engelbrecht, S. Rotation of the c subunit oligomer in EF_0EF_1 mutant cD61N. *J. Biol. Chem.* **2002**, *277*, 31287–31290. [CrossRef]

136. Weber, J.; Wilke-Mounts, S.; Lee, R.S.; Grell, E.; Senior, A.E. Specific placement of tryptophan in the catalytic sites of *Escherichia coli* F_1-ATPase provides a direct probe of nucleotide binding: Maximal ATP hydrolysis occurs with three sites occupied. *J. Biol. Chem.* **1993**, *268*, 20126–20133. [PubMed]

137. Martin, J.; Hudson, J.; Hornung, T.; Frasch, W.D. Fo-driven Rotation in the ATP Synthase Direction against the Force of F_1 ATPase in the FoF_1 ATP Synthase. *J. Biol. Chem.* **2015**, *290*, 10717–10728. [CrossRef] [PubMed]

138. Ueno, H.; Suzuki, T.; Kinosita, K., Jr.; Yoshida, M. ATP-driven stepwise rotation of FoF_1-ATP synthase. *Proc. Natl. Acad. Sci. USA* **2005**, *102*, 1333–1338. [CrossRef] [PubMed]

139. Watanabe, R.; Tabata, K.V.; Iino, R.; Ueno, H.; Iwamoto, M.; Oiki, S.; Noji, H. Biased Brownian stepping rotation of FoF_1-ATP synthase driven by proton motive force. *Nat. Commun.* **2013**, *4*, 1631. [CrossRef] [PubMed]

140. Toei, M.; Noji, H. Single-molecule analysis of F_0F_1-ATP synthase inhibited by *N,N*-dicyclohexylcarbodiimide. *J. Biol. Chem.* **2013**, *288*, 25717–25726. [CrossRef]

141. Ueno, H.; Minagawa, Y.; Hara, M.; Rahman, S.; Yamato, I.; Muneyuki, E.; Noji, H.; Murata, T.; Iino, R. Torque generation of *Enterococcus hirae* V-ATPase. *J. Biol. Chem.* **2014**, *289*, 31212–31223. [CrossRef] [PubMed]

142. Hellenkamp, B.; Schmid, S.; Doroshenko, O.; Opanasyuk, O.; Kuhnemuth, R.; Rezaei Adariani, S.; Ambrose, B.; Aznauryan, M.; Barth, A.; Birkedal, V.; et al. Precision and accuracy of single-molecule FRET measurements-a multi-laboratory benchmark study. *Nat. Methods* **2018**, *15*, 669–676. [CrossRef] [PubMed]

143. Noble, A.J.; Wei, H.; Dandey, V.P.; Zhang, Z.; Tan, Y.Z.; Potter, C.S.; Carragher, B. Reducing effects of particle adsorption to the air-water interface in cryo-EM. *Nat. Methods* **2018**, *15*, 793–795. [CrossRef] [PubMed]

144. Noble, A.J.; Dandey, V.P.; Wei, H.; Brasch, J.; Chase, J.; Acharya, P.; Tan, Y.Z.; Zhang, Z.; Kim, L.Y.; Scapin, G.; et al. Routine single particle CryoEM sample and grid characterization by tomography. *eLife* **2018**, *7*, 34257. [CrossRef]

145. Cohen, A.E.; Moerner, W.E. Method for trapping and manipulating nanoscale objects in solution. *Appl. Phys. Lett.* **2005**, *86*, 093109. [CrossRef]

146. Cohen, A.E.; Moerner, W.E. The anti-Brownian electrophoretic trap (ABEL Trap): Fabrication and software. *Proc. SPIE* **2005**, *5699*. [CrossRef]

147. Cohen, A.E.; Moerner, W.E. Suppressing Brownian motion of individual biomolecules in solution. *Proc. Natl. Acad. Sci. USA* **2006**, *103*, 4362–4365. [CrossRef] [PubMed]

148. Cohen, A.E.; Moerner, W.E. Internal mechanical response of a polymer in solution. *Phys. Rev. Lett.* **2007**, *98*, 116001. [CrossRef]

149. Cohen, A.E.; Moerner, W.E. Controlling Brownian motion of single protein molecules and single fluorophores in aqueous buffer. *Opt. Exp.* **2008**, *16*, 6941–6956. [CrossRef]

150. Jiang, Y.; Wang, Q.; Cohen, A.E.; Douglas, N.; Frydman, J.; Moerner, W.E. Hardware-based anti-Brownian electrokinetic trap (ABEL trap) for single molecules: Control loop simulations and application to ATP binding stoichiometry in multi-subunit enzymes. *Proc. SPIE* **2008**, *7038*. [CrossRef]

151. Goldsmith, R.H.; Moerner, W.E. Watching conformational- and photo-dynamics of single fluorescent proteins in solution. *Nat. Chem.* **2010**, *2*, 179–186. [CrossRef] [PubMed]

152. Bockenhauer, S.; Fürstenberg, A.; Yao, X.J.; Kobilka, B.K.; Moerner, W.E. Conformational dynamics of single G protein-coupled receptors in solution. *J. Phys. Chem. B* **2011**, *115*, 13328–13338. [CrossRef]

153. Wang, Q.; Moerner, W.E. An Adaptive Anti-Brownian Electrokinetic Trap with Real-Time Information on Single-Molecule Diffusivity and Mobility. *ACS Nano* **2011**, *5*, 5792–5799. [CrossRef] [PubMed]

154. Wang, Q.; Moerner, W.E. Lifetime and Spectrally Resolved Characterization of the Photodynamics of Single Fluorophores in Solution Using the Anti-Brownian Electrokinetic Trap. *J. Phys. Chem. B* **2013**, *117*, 4641–4648. [CrossRef] [PubMed]

155. Bockenhauer, S.D.; Duncan, T.M.; Moerner, W.E.; Börsch, M. The regulatory switch of F_1-ATPase studied by single-molecule FRET in the ABEL Trap. *Proc. SPIE* **2014**, *8950*. [CrossRef]

156. Su, B.; Düser, M.G.; Zarrabi, N.; Heitkamp, T.; Starke, I.; Börsch, M. Observing conformations of single FoF$_1$-ATP synthases in a fast anti-Brownian electrokinetic trap. *Proc. SPIE* **2015**, *9329*. [CrossRef]

157. Dienerowitz, M.; Ilchenko, M.; Su, B.; Deckers-Hebestreit, G.; Mayer, G.; Henkel, T.; Heitkamp, T.; Börsch, M. Optimized green fluorescent protein fused to FoF$_1$-ATP synthase for single-molecule FRET using a fast anti-Brownian electrokinetic trap. *Proc. SPIE* **2016**, *9714*. [CrossRef]

158. Dienerowitz, M.; Heitkamp, T.; Gottschall, T.; Limpert, J.; Börsch, M. Confining Brownian motion of single nanoparticles in an ABELtrap. *Proc. SPIE* **2017**, *10120*. [CrossRef]

159. Dienerowitz, M.; Dienerowitz, F.; Börsch, M. Measuring nanoparticle diffusion in an ABELtrap. *J. Opt.* **2018**, *20*, 034006. [CrossRef]

160. Lill, H.; Engelbrecht, S.; Schönknecht, G.; Junge, W. The proton channel, CF0, in thylakoid membranes—Only a low proportion of CF$_1$-lacking CF$_0$ is active with a high unit conductance (169 fS). *Eur. J. Biochem.* **1986**, *160*, 627–634. [CrossRef]

161. Schönknecht, G.; Junge, W.; Lill, H.; Engelbrecht, S. Complete tracking of proton flow in thylakoids-the unit conductance of CF$_0$ is greater than 10 fS. *FEBS Lett.* **1986**, *203*, 289–294. [CrossRef]

162. Pänke, O.; Cherepanov, D.A.; Gumbiowski, K.; Engelbrecht, S.; Junge, W. Viscoelastic dynamics of actin filaments coupled to rotary F-ATPase: Angular torque profile of the enzyme. *Biophys. J.* **2001**, *81*, 1220–1233. [CrossRef]

163. Cherepanov, D.A.; Mulkidjanian, A.Y.; Junge, W. Transient accumulation of elastic energy in proton translocating ATP synthase. *FEBS Lett.* **1999**, *449*, 1–6. [CrossRef]

APPENDIX B

PERMISSION TO PUBLISH

I, Seiga Yanagisawa, have communicated with and have received permission to include the published works contained herein from those individuals that are co-authors with me.